NANYANG TECHNOLOGICAL UNIVERSITY

EXPERIMENTAL AND ANALYTICAL STUDY OF REINFORCED CONCRETE SUBSTRUCTURES SUBJECTED TO A LOSS OF GROUND CORNER COLUMN SCENARIO

QIAN KAI

SCHOOL OF CIVIL AND ENVIRONMENTAL ENGINEERING

2012

EXPERIMENTAL AND ANALYTICAL STUDY OF REINFORCED CONCRETE SUBSTRUCTURES SUBJECTED TO A LOSS OF GROUND CORNER COLUMN SCENARIO

QIAN KAI

School of Civil and Environmental Engineering

A thesis submitted to the Nanyang Technological University

in fulfillment of the requirement for the degree of

Doctor of Philosophy

2012

ACKNOWLEDGMENTS

The research work reported in this thesis, on the performance of reinforced concrete substructures for progressive collapse caused by losing a ground corner column, was carried out in the School of Civil and Environmental Engineering, Nanyang Technological University, Singapore. It is difficult to use a single page to express my appreciation to all those who have contributed to the success of my research over the last four years. Herein, I would like to take this opportunity to thank those whose contributions to the research were indispensable.

I wish to express my deepest gratitude to my supervisor, Associate Professor Li Bing, for his patient guidance, warm encouragement, and stimulus throughout this research. His unwavering enthusiasm and constant interesting in scientific research is much appreciated and unforgettable. It is a great benefit and honor to work with him.

I would like to thank to the technicians at the protective engineering laboratory of NTU for their constructive suggestions and advice helped tremendously during the experimental work. Appreciation must also be given to my fellow graduate students for their support and friendship during the time of my studies; Anand Nair and Yap Sim Lim are two members need to be given distinguished honors in my list of acknowledgements. Their time and effort has helped astoundingly into making this study a reality.

Finally, I would like to give special thanks to my wife, Deng Xiao Fang and my parents for their encouragement, understanding and support during the past years. Thank you, sincerely!

TABLE OF CONTENT

LIST OF FIGURES

LIST OF TABLES

LIST OF SYMBOLS

CHAPTER 3

D_1 is the vertical displacement

E_0 is the initial stiffness

$f_c^{'}$ is the concrete compressive strength

f_t is the concrete tensile strength

h is the distance between the transducers at segment 1

H_1 is the horizontal movement of the joint just above the damaged column

k is a constant

S_t is the width of segment 1

TV is the total vertical distance between the center of steel box and the center of corner joint when specimen has vertical displacement of D_1

V is the vertical distance between the center of steel box and the center of corner joint at beginning of the test

$\overline{V}$ is the average vertical distance between two steel pins in each direction

ε_0 is the concrete ultimate strain

σ_c is the concrete compressive stress at any compressive strain ε_c

σ_t is the concrete tensile stress

δ is the difference between the diameter of the hole and the steel pin

δ_t is the displacement measured by the top transducer at hinge 1

δ_b is the displacement measured by the bottom transducer at hinge 1

λ is a constant

ϕ is the design rotation of the steel column

CHAPTER 5

A_g is the gross area of the beam cross-section

A_l is the total area of bottom longitudinal reinforcement at the beam end near the corner joint at PL3

A_{js} is the total area of horizontal transverse reinforcement crossing the diagonal plane from corner to corner of the joint

A_{sb} is the shear area was recommended by Calvi *et al*. [C1]

a is the strut width

b_w is the beam width

b_{eff} is the average of the beam and column width

C_1 is a constant

C_2 is a constant

C_3 is a constant

C_{bc} is the compression force provided by beam concrete

C_{bs} is the compression force provided by beam reinforcement

C_{cc} is the compression force provided by column concrete

C_{cs} is the compression force provided by column reinforcement

D is the compression force of the joint diagonal strut

d_b is the depth of the beam cross-section

d_l is the bar diameter of the longitudinal reinforcement

d is the effective depth of the beam

$f_c^{'}$ is the compressive strength of concrete

f_{yv} is the tensile strength of the transverse reinforcement

E_s is the elastic modulus of the steel

E_c is the elastic modulus of the concrete

F_{FF} is the residual strength at final failure stage (PL6)

F_t is the residual strength at PL5

$F_u^{measured}$	is the measured ultimate capacity of the substructures
$F_u^{cantilever}$	is the predicted ultimate capacity by cantilever model ($\xi = 0.0$)
F_u^{full}	is the predicted ultimate capacity by full constraint model ($\xi = 1.0$)
$F_u^{partial}$	is the predicted ultimate capacity by partial constraint model ($\xi = 0.65$)
$F_u^{predicted}$	is the predicted ultimate capacity of the substructures
$F_y^{cantilever}$	is the predicted yield strength by cantilever model ($\xi = 0.0$)
F_y^{full}	is the predicted yield strength by full constraint model ($\xi = 1.0$)
$F_y^{partial}$	is the predicted yield strength by partial constraint model ($\xi = 0.70$)
$F_y^{predicted}$	is the predicted yield strength of the substructures
G_c	is the shear modulus
H	is the height of the wall
jd_b	is the distance from the centroid of the compressive forces in the steel and concrete to the centroid of tension in the beam section
jd_c	is the distance from the centroid of compressive forces in the steel and concrete to the centroid of tension in the column section
kd_b	is the neutral axial depth of the beam section
kd_c	is the neutral axial depth of the column section
K_{NF1}	is the slope of the descending branch between PL3 to PL4
K_{NF2}	is the slope of the descending branch between PL4 to PL5
K_v	is the shear stiffness of beam per unit length after cracks
l_n	is the clear span of the beam
l_w	is the wall length
L_{sp}	is the plastic hinge length
L_{spy}	is the equivalent plastic hinge length to account for strain penetration
M_a	is the allowable moment in the BENC
M_u	is the ultimate moment in the BENF
N_b	is the beam axial force

N_b^m	is the measured axial force applied on the beam at PL3
n	is the modular ratio
T_{bs}	is the tensile force in the beam longitudinal reinforcement
T_{cs}	is the tensile force in the column longitudinal reinforcement
V_c	is the shear force in the upper column
V_{cd}	is the design shear force resistance of the concrete in a joint
V_{cr}	is the shear force when the beam onset of shear cracking
V_{jd}	is the total joint shear strength
$V_j^{measured}$	is the measured joint shear strength
$V_j^{predicated}$	is the predicted joint shear strength by proposed strut-and-tie model
V_n	is shear force demand at first yield
V_{sd}	is the design shear force resistance of the transverse reinforcement
α	is the inclination of the compression struts with respect to the element axis
β	is the angle between the transverse reinforcement and the horizontal axis
ρ_v	is the transverse reinforcement ratio
ρ_{BL}	is the beam longitudinal reinforcement ratio
ξ	is the constraint effective factor
ε_s^m	is the measured tensile strain of the bottom longitudinal reinforcement
θ	is the angle between the beam axial and the strut center line
ν	is the compressive effectiveness strength factor that is less than unity, 0.34 was suggested in Schlaich *et al.* [S7]
ϕ	is the designed rotation of the steel column
φ_u	is the ultimate curvature
φ_A	is the curvature at point A
φ_B	is the curvature at the point B
φ_u	is the ultimate curvature which is typically determined from strain limits
φ_x	is the curvature at the point, x away from B

φ_y is the yield curvature at point A

Δ_{FF} is the displacement at final failure stage (PL6)

Δ_{NF} is the displacement at normal failure stage (PL4)

Δ_{NF}^{f} is the flexural displacement at normal failure stage (PL4)

Δ_{NF}^{P} is the plastic displacement at normal failure stage (PL4)

Δ_{NF}^{S} is the shear deformation at normal failure stage (PL4)

Δ_t is the displacement at PL5

Δ_{y}^{full} is the yield displacement excluded strain penetration by full constraint model

$\Delta_{y}^{cantilever}$ is the yield displacement excluded strain penetration by cantilever model

$\Delta_{y}^{partial}$ is the yield displacement excluded strain penetration by partial constraint model

$\Delta_{y.f}^{partial}$ is the yield displacement included strain penetration by partial constraint model

$\Delta_{y.f}^{full}$ is the yield displacement included strain penetration by full constraint model

$\Delta_{y.f}^{cantilever}$ is the yield displacement included strain penetration by cantilever model

$\Delta_{y.s}$ is the shear displacement at the first yield (ductility equal to 1)

Δ_{s1} is the shear displacement when the beam onset of shear cracking

CHAPTER 6

N is the number of sampling points in the acceleration time series

$u(t)$ is the displacement time series

$\dot{u}(t)$ is the velocity time series

$\ddot{u}(t)$ is the recorded acceleration time series

$\Delta\tau$ is the integral time step

CHAPTER 7

α is the strain hardening ratio

c_e is the equivalent viscous damping

$DUS_{SDOF}^{\tau=0.0}$ is the dynamic ultimate strength of the test specimens obtained from SDOF method excluded the residual strength

$DUS_{SDOF}^{\tau=0.5}$ is the dynamic ultimate strength of the test specimens obtained from SDOF method included partial of the residual strength

$DUS_{CC}^{\tau=0.0}$ is the dynamic ultimate strength of the test specimens obtained from capacity curve method excluded the residual strength

$DUS_{CC}^{\tau=1.0}$ is the dynamic ultimate strength of the test specimens obtained from capacity curve method included the residual strength

k_e is the effective stiffness

m_e is the equivalent mass

m_k is the concentrate mass k at location of z_k

$m(z)$ is the distributed mass function

$P(t)$ is the applied force

$P_{CC}(u)$ is the capacity function at the displacement demand u

$P_{NS}(u)$ is the nonlinear static loading estimated at the displacement demand u

$R(t)$ is the reaction force

u_d is the displacement demand

x is the displacement of the mass

$\dot{x}$ is the velocity of the mass

$\ddot{x}$ is the acceleration of the mass

$\psi(z)$ is the shape function

$\psi(z_k)$ is the shape function value at point z_k

θ_P is the allow plastic rotation

θ_y is the member yield rotation

ζ is the damping ratio

τ is the stiffness reduction ratio

Δ_{max} is the maximum displacement

CHAPTER 8

A_s is the area of tension steel per unit width

d_c is the width of the corner column

$f_c^{'}$ is the compressive strength of concrete

f_{si} is the tensile stress of the i^{th} rebar numbered from the adjacent column

f_y is the yield strength of the reinforcement

$F_{membrane}$ is the predicted tensile membrane resistance in the slab

F_{ix} is the tensile force of the i^{th} rebar perpendicular with x direction

F_{ixv} is the vertical component of the tensile force of the i^{th} rebar perpendicular with x direction

F_{iy} is the tensile force of the i^{th} rebar perpendicular with y direction

F_{iyv} is the vertical component of the tensile force of the i^{th} rebar perpendicular with y direction

F_u^{flange} is the ultimate strength of the RC frame included the flange effect of the slab

$F_u^{measured}$ is the measured ultimate strength of the S-series specimens

$F_u^{predicted}$ is the predicted ultimate strength of the S-series specimens based on the proposed theoretical model

$F_u^{yield-line}$ is the flexural strength of the RC slab itself, which was determined by yield-line method

F_{xv} is the total vertical components in the slab rebar perpendicular with x direction

F_{yv}	is the total vertical components in the slab rebar perpendicular with y direction
M_a	is the allowable bending moment of in the BENC
M_u^{flange}	is the ultimate bending moment of in the BENF including the flange
m_u	is the ultimate bending moment per unit width
m_{un}	is the ultimate bending moment per unit width at a yield line
l_{nx} , l_{ny}	are the clear span of the beam in x and y direction respectively
l_x , l_y	are the span of the beam in x and y direction respectively
l_0	is the length of the yield line
l	is the span of the slab
l_n	is the clear span of the beam
S	is the spacing of the slab reinforcement
W_u	is the total load on a segment of the yield line pattern
Δ	is the downward movement of the centroid of a segment
δ	is the virtual small displacement in the direction of the load
θ_n	is the relative rotation about the yield line of the two segments
ξ	is the rotational constraint effective factor, here ξ=0.65

LIST OF ABBREVIATIONS

ATTB	Allowable Tie Force in the Transverse Beam
ATLB	Allowable Tie Force in the Longitudinal Beam
Beam-T	Transverse Beam
Beam-L	Longitudinal Beam
BENAC	Beam End Near the Adjacent Column
BENC	Beam End Near the Corner Joint
BENF	Beam End Near the Fixed Support
DIF	Dynamic Increase Factors
DLIF	Dynamic Load Increase Factors
DoD	Department of Defense
DUS	Dynamic Ultimate Strength
FE	Finite Element
FF	Final Failure Stage
GSA	General Services Administration
LHR	Longitudinal Horizontal Reaction
LIF	Load Increase Factors
LS	Linear Static Analysis
LVDT	Linear Variable Differential Transducers
MC	Maximum Compressive Force
MBM	Maximum Bending Moment
MCHR	Maximum Compressive Horizontal Reaction
MT	Maximum Tensile Force
MTTB	Measured Tie Force in the Transverse Beam
MTLB	Measured Tie Force in the Longitudinal Beam
ND	Nonlinear Dynamic Analysis
NS	Nonlinear Static Analysis
NF	Normal Failure Stage
PL	Performance Level
RTTB	Required Tie Force in the Transverse Beam
RTLB	Required Tie Force in the Longitudinal Beam

SDOF	Single Degree of Freedom
SUS	Static Ultimate Strength
Span-T	Span in the Transverse Direction
Span-L	Span in the Longitudinal Direction
TDR	Tip Displacement Ratio
THR	Transverse Horizontal Reaction

ABSTRACT

Damage from abnormal loading such as explosion, bombing, and sudden vehicle impacts on frame elements can result in a loss of individual elements or total collapse of the whole structure. Progressive collapse has been a concern for many decades, but recent attacks of terrorism including the destruction of the Murrah Federal Building and World Trade Center have reignited the demand for a deeper understanding of the performance of structures under these circumstances.

The ultimate objective of this dissertation is to experimentally and analytically evaluate the performance of the reinforced concrete (RC) structures under the loss of a corner column scenario. While various numerical studies have examined this issue, no related three-dimensional (3D) experimental studies have been conducted on this subject to date. In this study, three series of tests were designed and conducted at NTU, Singapore. In the first series of tests, seven RC beam-column substructures were tested under quasi-static loading regime to investigate their quasi-static behavior for progressive collapse. In the second series of tests, six RC beam-column substructures with similar dimensions and reinforcement details as the specimens tested in the first series were tested under dynamic loading regime to investigate their dynamic performance. In the third series of tests, three additional specimens incorporating RC slabs were tested to study the slab effects on the behavior of the substructures in resisting progressive collapse. In addition, the dynamic effects due to sudden removal of a critical column suggested by the UFC guidelines were evaluated by comparing the quasi-static and dynamic response of the substructures.

Supplementary analytical analyses were conducted in order to better understand the performance of RC structures under the scenario of the loss of a corner column. A series of equations were derived in an attempt to replicate the quasi-static behavior of the specimens under a quasi-static loading regime. Moreover, in order to quickly and effectively evaluate the vulnerability of RC structures for progressive collapse, the accuracy of the simplified analytical models–single degree freedom model and capacity curve model were validated by comparisons with the experimental results.

Finally, simplified analytical models were proposed to predict the tensile membrane action developed in RC slab in resisting progressive collapse that caused by the loss of a corner column. After experimental and analytical investigations, the author hopes to attain a more comprehensive understanding of the behavior of RC substructures during progressive collapse caused by the loss of a ground corner column, thereby providing the urgently needed data to refine existing design guidelines for the prevention of progressive collapse.

CHAPTER 1

INTRODUCTION

1.1 Problem Statements

With the increasing number of terrorist attacks launched against important government and commercial buildings in the world, the community of engineer continues to improve the design of buildings to make them safer and less vulnerable to terrorist attacks. One of the aspects considered in designing safer buildings and structures is their ability to prevent total collapse after the loss of load-bearing elements due to a terrorist attack (progressive collapse).

The American Society of Civil Engineering (ASCE) standard ASCE 7-10 [A5] defines "progressive collapse" as "the spread of an initial local failure from element to element, which eventually results in the collapse of an entire structure or a disproportionately large part of it." In less technical terms, the idea of progressive collapse is often thought of as a domino effect.

Progressive collapse is a relatively low probability event. However, the consequences of a building with progressive collapse could be catastrophic. For example, in the Oklahoma City bombing in 1995, 42 % of the Alfred P. Murrrah Federal Building was destroyed by progressive collapse and only 4 % by the explosion. This attack claimed 168 lives and left 800 injured (Corley [C4]).

In the past decade, several design guidelines (DoD [D1] and GSA [G1]) have been developed and a number of numerical research studies (Kaewkulchai and Williamson [K1], Bao *et al.* [B2], and Marjanishvili [M1]) have been conducted for progressive collapse. However, experimental studies on the performance of RC frame for progressive collapse are relatively fewer. Moreover, majority of the previous experimental tests were focused on the response of buildings under the scenario of the

loss of an interior or exterior column. It must be emphasized that the loss of a corner column in the event of a terrorist attack is more prone to trigger progressive collapse due to the inability to redistribute the additional loadings to surrounding elements. In addition, the corner bay (perimeter components) has a much higher possibility of being targeted in a terrorist act. Thus, it is an urgent need to experimentally investigate the performance of RC frames in resisting progressive collapse caused by the loss of a corner column.

In-situ tests are the first choice to experimentally study the ability of RC frames in resisting progressive collapse. However, the tremendous costs of the in-situ tests means that it is impossible to systematically investigate the performance of RC frames against progressive collapse via this method. Previous research studies had indicated that the upper and lower floors will operate in tandem as a unit as long as the dimensions and reinforcement details of the frame element in the upper and lower floors are identical. Thus, the behavior of multi-storey frames could be simplified to a single storey substructure with proper boundary conditions.

In order to capture in detail the quasi-static performance and cracking development of the substructure under the scenario of the loss of a corner column, a series of 3-dimensional RC beam-column substructures (F-series specimens) were subjected to a quasi-static loading regime. It should be pointed out that progressive collapse events are dynamic phenomena. Thus, in order to capture the dynamic performance of the beam-column substructures and to evaluate the dynamic effects due to the sudden removal of a corner column, six beam-column substructures (DF-series specimens) with similar dimensions and reinforcement details as the specimens tested in the first series were tested under the dynamic loading regime. Furthermore, in typical cast-in-situ construction, beams, columns and slabs are cast simultaneously and therefore act as a single structural unit. Ignoring the effect of the slab on the stiffness and strength of the beams will most likely result in a significant underestimation of the vertical force resistance capacity. Therefore, another series of tests (S-series specimens) were conducted in this study to investigate the quasi-static performance of the RC substructures with RC slab for progressive collapse. By comparing the failure mechanisms and load-displacement response of S-series specimens with the

corresponding F-series specimens, the effect of the slabs on the performance of the RC substructures can be determined.

Considering that limited specimens and parameters have been taken into account in this study and continuing to conduct experimental tests for this issue is a lengthy task, it is necessary to conduct further analytical studies to come out with design-oriented guidelines for progressive collapse. Thus, supplementary analytical analyses were also carried out in this study.

1.2 Objectives and Scopes of Research

The ultimate goal of the present work is to contribute to improve the understanding of the performance of RC substructures under the scenario of the loss of a corner column. In this perspective, the specific objectives of the research are:

- To understand the overall performance of the RC beam-column substructures without slab under the scenario of the loss of a corner column and to quantify the contribution of the beam catenary effects in resisting progressive collapse.

- To develop an analytical model, including a set of equations for predicting the load-displacement curve of the RC beam-column substructures. The various parameters can be studied by using the proposed model.

- Through experimental tests, to better understand the dynamic performance of the RC beam-column substructures without slab under the scenario of the loss of a corner column.

- To evaluate the accuracy of the simplified analytical models (Single Degree of Freedom model and capacity curve model) to predict the dynamic response of RC beam-column substructures for progressive collapse.

- To evaluate the accuracy of the dynamic increase factors provided in the DoD

[D1] by comparing the results obtained from the quasi-static tests with the corresponding dynamic tests.

- To quantify the slab contribution and tensile membrane action to resist progressive collapse by comparing the response of specimens with and without slab.

1.3 Organization of Thesis

The introduction of the problems, the objectives and the scopes of this study are described in this chapter. **Chapter 2** presents the background information and a literature review of progressive collapse. Past research as well as current code requirements regarding progressive collapse of building are discussed. In **Chapter 3**, the details of the experimental program of the RC beam-column substructures without slab subjected to quasi-static load are presented. **Chapter 4** presents the test results of the seven RC beam-column substructures without slab subjected to quasi-static load. The test results include the crack pattern, load-displacement curve, bending moment and local strain gauge results. In **Chapter 5**, an analytical model was developed to predict the load-displacement curves of the test specimens introduced in **Chapter 4**. The validated analytical model was utilized to conduct parametric study. **Chapter 6** presents the dynamic results of the dynamic specimens including the final crack pattern, acceleration, velocity and displacement response, as well as the histories of the bending moment, vertical and horizontal reaction forces. In **Chapter 7**, the accuracy of the analytical models (SDOF and capacity curve method) to predict the vulnerability of test specimens are evaluated and the dynamic effects attained from experimental and analytical analyses were compared with the value provided in the design guideline. Slab effects on the performance of the RC substructures for progressive collapse were investigated in **Chapter 8** by comparing the static performance of specimens with and without slabs. Finally, the conclusions are stated in **Chapter 9**, where some recommendations for future research studies are also proposed.

CHAPTER 2

BACKGROUND AND LITERATURE REVIEW

2.1 Introduction

This chapter consists of three sections. The first section provides an overview of the progressive collapse phenomenon. The second section gives details on current building codes and provisions related to progressive collapse. The third section covers past research studies including analytical and experimental studies for progressive collapse.

2.2 History of Progressive Collapse

Throughout the past decades, many events have indicated the importance of mitigation against progressive collapse to practicing engineers and design agencies. Since then, changes in building practices by the engineering communities and work groups for design standards have been made to address what is so called low probability/high consequence events. The following part of this chapter highlights some of the past events that clearly demonstrate the progressive collapse phenomena.

2.2.1 Ronan Point Apartment, 1968

The collapse that took place at Ronan Point Apartment first attracted the attention of public for progressive collapse. On May 16, 1968, a gas explosion occurred on the 18^{th} floor of the 22-storey pre-cast panel construction supported by cast in place concrete structure. The explosion blew out a load bearing pre-cast wall panel near the exterior corner of the building, which caused a loss of support for the 19^{th} to 22^{nd} storeys of the building. Subsequently, debris from the upper floors caused each floor

below to progressively collapse. **Fig. 2.1** shows the Ronan Point Apartment after the collapse.

Although the failure of the Ronan Point structure was not one of the larger building disasters of recent decades, the magnitude of the collapse was shockingly out of proportion compared to the trigger event. Thus, this type of sequential and domino-effect failure has since been of great concern to engineers.

Fig. 2.1: Ronan Point Apartment after collapse

2.2.2 Murrah Federal Building, 1995

On April 19, 1995, a truck loaded with an ammonium nitrate and fuel oil bombs caused the collapse of one-half of the total area of the Murrah Federal Building. The Murrah Federal Building was a 9-storey, conventionally reinforced, one-way slab system designed in early 1970. It had a transfer girder on the third floor supporting intermediate columns, providing a clear span for the first two levels of about 12.2 m.

Analyses based on the approximate blast loading indicated that the column nearest to the explosion would have failed by brisance or shattering. The columns on either side of this column were found to have exceeded their shear strength and failed in shear. The loss of these three supporting columns resulted in an increased span length of the transfer girder to about 48.8 m. The increased bending moment associated with the increased span caused it to fail, which led to the progressive collapse of all of the floors above. The extent of damage included most of the north half of the footprint and 10.0 m into the building. Approximately half of the occupiable space within the Murrah Federal Building collapsed. **Fig. 2.2** shows the Murrah Federal Building after the collapse.

For the Murrah Federal Building, most agree that a change in its design by eliminating transfer girder, added continuity and ductility would have reduced the extent of the damage.

Fig. 2.2: Murrah Federal Building after collapse
(http://en.wikipedia.org/wiki/Oklahoma_City_bombing)

2.2.3 World Trade Center, 2001

On September 11, 2001, both of the Twin Towers of the World Trade Center (WTC) in New York collapsed. A Boeing 767 jetliner crashed into the upper part of the tower at high speed, damaging the structure near the point of impact and causing an intense fire within the building. The structure lost its ability to support the weight of the members above the impact zone and it eventually led to the collapse of the upper storeys. This in turn resulted in a progression of failure to the entire building. **Fig. 2.3** shows the progressive collapse of the World Trade Center.

Ironically, the events on that day show that progressive collapse can be averted in many cases. The towers were able to withstand the initial impact loading by the high speed airplane and only collapsed later due the weakening of the structure due to the fire.

This event led to the greatest public exposure of the potential of the inherent weakness in structures when exposed to unexpected or extreme loadings when compared to the previous recorded events.

Fig. 2.3: World Trade Center under progression collapse
(http://www.solcomhouse.com/Worldtradecenter.htm)

2.2.4 Pentagon, 2001

On the very same day as collapse of WTC, an aircraft crashed into the Pentagon. The structural system as a whole showed great ability to redistribute load with only a small area of local collapse. This is unlike all the previous cases mentioned earlier that suffered progressive collapse.

The collapse was limited in this case due to several factors. The Pentagon was built with a certain degree of redundancy. Alternate load paths of the beam and the girder framing system together with the short spans between columns helped in preventing a global collapse. Furthermore, there was substantial continuity of beam and girder bottom reinforcement through support. The column design had provided significant residual load capacity through spiral reinforcements and having the exterior wall to act as transfer girders greatly reduced the possibility for a global collapse. **Fig. 2.4** presents the aftermath of the attack.

Fig. 2.4: Pentagon after attack

2.3 Standards and Codes Provisions

2.3.1 Introduction

The Ronan Point Apartment collapse in 1968 triggered the rise of a new view in the design philosophy of structures. Since then, many codes and standards have attempted to provide guidelines to address progressive collapse. Although this issue can be addressed either implicitly or explicitly, most codes and standards contain explicit provisions. The following sections within this chapter will highlight some of the standards and codes.

2.3.2 ACI 318-08 [A3] on Structural Integrity Requirement

ACI 318-08 [A3] addresses progressive collapse indirectly through its structural integrity provisions. Section 7 of ACI 318-08 [A3] specifies that structures should be detailed such that in the event of damage to a major structural element or an abnormal loading event, the resulting damage will be confined to a relatively small area and the structure will have a better chance of maintaining its overall stability. This is presumed to be accomplished by establishing integrity within reinforcement that helps to tie the structure together. Structural integrity provisions for other systems are given in Chapter 13 (two-way slabs), 16 (pre-cast concrete) and 18 (pre-stressed concrete).

The deficiencies of the ACI 318-08 [A3] against progressive collapse are as follows:

- ACI provisions are not sufficient as they do not explicitly address the type of structure, loading or strength requirements; all of which are important in the evaluation of the potential of the progressive collapse of a structure.

- Stability issues which may arise as a result of loss of some key member/members of the structure are not addressed.

- Providing minimum integrity reinforcement as recommended by the code is not sufficient for detailed evaluation and analysis that is necessary to understand the redistribution of loads, alternate load path/paths and the ultimate structure behavior under a particular loading situation.

2.3.3 ASCE 7-10 [A5]

ASCE 7-10 [A5] is the only mainstream standard which explicitly addresses the issue of progressive collapse. Section C1.4 of ASCE 7-10 [A5] on general structural integrity outlines the need to protect structures against blasts which can result in progressive collapse. It also gives the factors that contribute to the risk of damage propagation in modern structures. ASCE 7-10 [A5] gives the following two design alternatives to investigate and design for progressive collapse:

2.3.3.1 Direct Design

This explicitly considers resistance to progressive collapse during the design process through either:

Alternate load path: a method that allows local failure to occur but seeks to provide alternate load paths so that damage is absorbed and major collapse averted, or

Specific local resistance: a method that seeks to provide sufficient strength to resist failure at the element level.

2.3.3.2 Indirect Design

This involves implicit consideration of resistance of progressive collapse during the design process through the provisions of minimum levels of strength, continuity and ductility.

2.3.4 DoD (Department of Defense) Guidelines [D1]

The DoD [D1] was recently revised and a number of significant improvements were implemented, particularly with regard to the direct and indirect design approaches. During the revision of DoD [D1], the effectiveness of the indirect and direct design methods used in existing design requirements was evaluated and research was performed to improve these approaches.

2.3.4.1 Tie Forces

A common criticism towards the tie force approach in the old version of DoD [D1] was directed towards the inability of steel connections and some RC members and connections to carry the tie force magnitude after being subjected to significant rotation. In the updated DoD [D1], the horizontal tie forces (internal and peripheral) are no longer permitted to be concentrated in the beams, girders and spandrels (unless the designer can show that these members are capable of carrying the tensile loads while undergoing large deformations and rotations). The horizontal tie forces are instead carried in the floor.

2.3.4.2 Alternate Path Analysis Procedures

In the Alternate path method, the designer must show that the structure is capable of bridging over a removed structural element and that the resulting extent of damage does not exceed the damage limits. In the updated DoD [D1], the analysis procedures and accepted criteria employed in ASCE 41-06 [A4] were adopted and modified.

2.3.4.3 Load and Dynamic Increase Factors

Three analytical procedures may be employed for progressive collapse analysis: Linear Static (LS), Nonlinear Static (NS) and Nonlinear Dynamic (ND). Typically, ND gives the most rigorous result, but is more complicated and expensive to apply. For preliminary designs or for simple structural systems, designers often choose LS and NS for analysis. However, as progressive collapse is a dynamic and nonlinear event, the applied load cases for the static procedures require the use of load increase factors (to account for inertial and nonlinear effects) or dynamic increase factors (to only account for inertial effects) in LS and NS, procedures respectively.

The procedure to determine the load increase factors (LIF) and dynamic increase factors (DIF) consists of 3 steps:

Step 1: Starting with a baseline model design using conventional design loads, a ND analysis was performed using the 1.2DL+0.5LL case combination; the values of plastic rotation and displacement at the column removal location were recorded.

Step 2: Using the same design and model from step1, a NS analysis was performed, with a trial DIF applied to the extreme load case (DIF×(1.2DL+0.5LL)). The DIF was adjusted and the model was re-run until the maximum plastic rotation matched the rotation or displacement measured in step1.

Step 3: Using the same design and model from Step1, a LS analysis was performed. A trial LIF was applied to the extreme load case (LIF×(1.2DL+0.5LL)). The LIF was adjusted and the model was re-run until the maximum displacement match the displacement measured in step1.

2.3.5 General Services Administration [G1]

The GSA [G1] publishes guidelines that include recommendations to address the potential for progressive collapse in federal buildings. A flow chart methodology is

provided to identify whether the structure under consideration must be evaluated for the potential of progressive collapse, hence, require a detailed analysis.

General structural integrity is achieved through a performance-based design approach. The document provides the methodology and performance criteria for these determinations without prescribing the exact manner of design and analysis. The designer is allowed to use nonlinear finite element analysis. A table of maximum allowable ductility and/or rotation limits for many structural components of various construction types is given to evaluate the survivability of the structure. The analysis and design of progressive collapse are described for both new construction as well as existing construction.

For new and existing structures, guidance is given for analysis of "typical" and "atypical" structure systems. For typical systems, designers can use linear elastic static analysis. In case of bearing wall buildings, the length of wall assumed to be removed in each case is the width of a bay or 30 feet, whichever is smaller.
The assumed gravity load is:

$$2(1.0DL+0.25LL) \qquad (2\text{-}1)$$

Structures with a combination of structural systems, vertical discontinuities, variations in bay size, extreme bay sizes, plan irregularities and closely spaced columns are designated as atypical structures. The section on existing construction provided an outline for assessing the potential of progressive collapse in existing structures and then incorporating the findings into project-specific risk assessment. Guidelines for analysis techniques, criteria and considerations, material properties, and modeling are provided.

The actual potential for progressive collapse is determined by the calculation of the Demand Capacity Ratio (DCR) for each primary and secondary structural element. A material strength increase of 5% for structural steel and 25% for reinforced concrete is allowed. The facilities are judged to have a high potential for progressive collapse if any of the primary or secondary structural elements outside of the allowed collapse area has the following:

DCR>2.0 for typical structures

DCR>1.5 for atypical structures

2.3.6 ISC Security Criteria [I1]

The purpose of ISC [I1] is to develop long-term construction standards for location requiring blast resistance or other specialized security measures. The problem of progressive collapse is handled indirectly through reference to the ASCE 7-95 [A6]. The design to prevent progressive collapse is to be based on dead load plus a realistic estimate of the live load which could be as low as 25% of the code prescribed live load. The document also has good engineering practice guidelines to mitigate the effects of blast on structures:

- Use of elasto-plastic analysis to absorb blast energy.
- Provide reinforcement in other than primary member design direction.
- Lap splices should be staggered and able to develop full reinforcement capacity.
- Connections should be ductile with adequate moment capacity.
- Special shear reinforcement should be provided for inelastic energy absorption.
- Transfer girders and other sources of point failures that can lead to widespread damage should be avoided.
- Redundancy and alternate load path should be encouraged.
- Column spacing should be reduced so that reasonably sized members can be designed to assist the design loads and increase the redundancy of the system.

- Floor-to-floor height should be minimized.

2.3.7 National Building Code of Canada [N1]

The National Building Code of Canada (NBC) [N1] is one of the codes that has addressed progressive collapse in some form for decades. The earlier version of NBC [N1] had provisions for abnormal loading, ductility of connections, design of members to prevent them from failure and provisions for alternate load paths. Several ways of ensuring alternate load path were mentioned including good floor plan, returns on walls, allowing floor slabs to be able to span with low factor of safety perpendicular to their primary span direction, providing internal load bearing partitions, designing for catenary action and considering beam action in wall design to allow walls to span over areas of damage. These elaborated provisions were modified in 1977 [N2] and taken out in the 1980 [N3] edition of the NBC. The current integrity provisions of the Canada code look something similar to the integrity provision of ACI 318-08 [A3].

2.4 Numerical Studies

Several numerical tools have been developed to simulate the performance of progressive collapse of buildings (Kaewkulchai and Williamson [K1] and Bao *et al.* [B2]) and the adequacy of existing commercial software to perform collapse simulations (Marjanishvili [M1] and Fu [F1]).

2.4.1 Kaewkulchai and Williamson [K1]

Kaewkulchai and Williamson [K1] developed a computer program for analyzing dynamic progressive collapse of planar frames where member failure is simulated by the modification of stiffness and the release of end forces. That research reported that:

- From cases considering dynamic load redistribution, dynamic effects appeared to

have significant impact on the response behavior of the frames.

- Damage appeared to be contained only within the collapsing bay.

- There was little difference in the response of frames whether or not the analysis starts from a deformed or an un-deformed configuration at the time of column failure.

2.4.2 Bao *et al.* [B2]

Bao *et al.* [B2] has proposed macro-models of beam-column sub-assemblies that attempt to capture the key local and global response characteristics by calibrating to results obtained from detailed finite element analyses. That research revealed that:

- Compared with elastic joint models, inelastic joint models are found to more accurately characterize the nonlinear behavior associated with the transfer of forces through the beam-column joint which provides the capability to capture the large deformation response associated with progressive collapse.

- Simplified macro-model approaches are a viable alternative to detailed finite-element analysis if careful calibration and validation of the macro-models are carried out prior to utilizing them in nonlinear dynamic simulations.

- Frames designed for high seismic region perform better and are less vulnerable to progressive collapse than frames designed for low to moderate seismic regions. This is attributed to both the section stiffness and strength and also the detailing requirements which enable larger demands to be transmitted through the joints.

2.4.3 Marjanishvili [M1]

Marjanishvili [M1] compared the four analysis procedures (LS, NS, LD, and ND) to discuss the advantages and disadvantages of each method. That research revealed that:

- Simpler analysis procedures (LS) use more conservative response evaluation criteria than more elaborated analysis procedures (ND).

- In order to determine the likelihood of a structure for progressive collapse, a structure's response is evaluated by starting with simpler static methodology. If simpler static methodology indicated that the structure had high possibility for progressive collapse, more complex analysis methods should be carried out for more accurately evaluate the vulnerability of the structures for progressive collapse.

2.4.4 Fu [F1]

Fu [F1] developed a 3-D model to simulate the performance of multi-storey buildings under sudden column removal. That research concluded that:

- The dynamic response of the structure is mainly related to the affected loading area after the column removal, which determines the amount of energy to be absorbed by the building.

- All the structural members at the possible column removal level should also be designed to at least twice the static axial force obtained when applying the 1.0 DL+0.25 LL load combination.

- The beam to column connection at the column removal level should also be designed to have at least twice the static axial force acting on the connections under the 1.0 DL+0.25 LL load combination.

- Under the same general conditions, a column removal at a higher level will induce larger vertical displacement than a column removal at ground level. This is because when the column is removed at the ground floor, more floors will participate in absorbing the released energy than that occurred at a higher level.

Moreover, the cross-section of the beams at a higher level was smaller than that at ground level.

2.5 In-Situ Tests

Several in-situ tests were performed on existing concrete buildings by Sasani *et al*. [S1] and Sasani [S2]. Both of the above tests were conducted by sudden removal of one or more exterior or corner columns at the first floor level. Although the deformations of these buildings after removal of the columns are limited, these tests revealed the system behavior of the buildings to resist progressive collapse. The valuable conclusions obtained from in-situ tests provided the evidence to perform laboratory tests for progressive collapse.

2.5.1 Sasani *et al*. [S1]

Sasani *et al*. [S1] had experimentally and analytically evaluated the potential progressive collapse of real structure in America. The test results indicated that:

- Vierendeel action was identified as the major mechanism for the redistribution of the loads in that structure. This is, because of moment connections, the beams and columns above the removed column deform in double curvature.

- The concrete modulus of the rupture would affect the whole behavior of the structure significantly. That is, because the beam at the sections where the top bars were cut-off experience large tension bending moments. If the demand for bending moments in these sections had been larger than their cracking bending moments, brittle flexural failure would have occurred. Such failure would have reduced the strength and stiffness associated with the Vierendeel action, leading to larger vertical deformations.

- Considering the significant contribution of Vierendeel action in resisting progressive collapse and potential brittle flexural failure in some beam sections,

the importance of proper anchorage of a portion of beam bottom reinforcement into exterior joints is described.

The deficiencies of that study were pointed out as follows:

- The tested structure did not reach the failure stage because the additional dead load and live load was removed before conducting the test.

- The column was not completely removed by the bomb. Thus, it was difficult to analyze the results.

- The strain and stress of the reinforcement were not monitored.

- The accuracy of the material properties used in the analytical study was poor because the structure was constructed 50 years ago.

2.5.2 Sasani [S2]

Sasani [S2] recorded the response of a six-storey reinforced concrete infilled-frame structure after sudden removal of two adjacent exterior columns (one of which was a corner column). Then, analytical models of the structure using commercial software and the Applied Element Method were utilized to determine the global and local deformations. The findings were pointed as follows:

- Bi-directional Vierendeel action of transverse and longitudinal frames with the participation of infill walls is identified as the major mechanism for redistribution of loads in that structure.

- One of the potential failure modes was failure of the anchorage of the bottom beam reinforcement at the face of the removed column due to moment reversal occurring in the region.

- The mechanism for propagation of deformation over the height of the structure is analytically described. It is shown that soon (about $1/20^{th}$ of the time required for the structure to reach the peak displacement) after column removal, axial forces in the columns above the removed columns reduce to almost zero and then different floors practically move together.

- The analytical results show that the joints above a removed column in two different floors move almost identically. This provides the evidence for current setup design.

The deficiencies of that study were pointed out as follows:

- The tested structure did not reach the failure stage, because of this experimental test was conducted on a real structure. The additional dead load and live load was removed before conducting the test.

- The instrumentation of the test was limited, such as the strain profile variation of the rebar could not be properly measured. The load redistribution of the structure could not be directly evaluated (as described in Sasani [S2], only qualitatively observe the increment of axial force in the column nearby the lost columns).

2.6 Laboratory Tests

In-situ tests are the first choice to experimentally study the behavior of RC frames to resist progressive collapse. However, it is impossible to systematically investigate the performance of RC frames against progressive collapse via this method due to the huge time and cost required. Thus, it is necessary to conduct substructure tests in laboratory to study the equivalent performance of whole frame for progressive collapse. Laboratory tests of large scale substructures or sub-assemblages are present, though relatively scarce in the literature.

2.6.1 Yi *et al.* [Y1]

Yi *et al*. [Y1] conducted a four-bay and three-storey one-third scale experimental model in China. The test results indicated that:

- Failure resulting from the progressive collapse of the RC concrete frame was ultimately controlled by the rupture of the longitudinal beam reinforcement.

- The effect of catenary action could not be ignored in order to design the RC frame under column loss scenario. The test results showed that after plastic mechanism formed, the beam catenary mechanism can be considered as an alternative load path and can resist additional loads.

The deficiencies of that study were pointed out as follows:

- That study was a small scale testing and could not represent well the response of real structure.

- That experimental program did not consider the effect of top beam reinforcement cut-off on the whole behavior of the frame. Sasani *et al*. [S1] had shown that the cut-off section was in the tension moment after loss of the column. If the concrete modulus of rupture was not large enough the cracking in the cut-off section would prevent development of the catenary mechanism.

- The loading process was different from the real structure under loss of column scenario. In that study, the third floor was applied 109 kN, which was the static loading of the first floor. The third floor should be less than that the value in the real situation.

- There was just one specimen in that study because construction of such a frame was very expensive. Thus, a parametric study was impossible.

- Quasi-static tests were conducted. However, the nature of the progressive collapse event is a dynamic phenomenon.

- Slab contribution to resist progressive collapse was not included in the tests.

2.6.2 Orton *et al.* [O1]

Orton *et al*. [O1] conducted seven half-scale beam-column assemblages which represented two spans of a RC frame with a center column removed by blast.

In that study, the longitudinal reinforcement was discontinuous. Some of the specimens were strengthened by using CFRP (carbon fiber-reinforced polymer) to study the efficiency of CFRP providing continuity in RC beams. The greatest contribution of that study is it provided a way to improve the resistance of government or important commercial old building to survive the terrorist attacks.

The test results indicated that:

- Beams without continuous reinforcement were only able to reach 73 % of the load required by the GSA [G1] provisions if catenary action is developed. Such beams may survive progressive collapse situations if additional strength is available from the slab or upper-storey columns.

- CFRP sheets were used to provide continuity of the positive moment reinforcement, and 55 % and 60 % of the GSA [G1] required load was reached. However, limited rotation capacity of the positive moment sections led to the fracture of reinforcing bars. Therefore, providing continuity through the positive moment reinforcement may not lead to improved progressive collapse resistance if the beam does not have sufficient rotational ductility to reach catenary action.

- CFRP sheets were used to provide continuity of the negative moment reinforcement, and 108 % of the GSA [G1] required load was reached. The

behavior improved due to development of hinges at the more ductile sections, leading to an improved rotational ductility that allowed the beam to reach catenary action. Deflection at peak load, however, was 11 % of the double span length.

The deficiencies of that study were identified as follows:

- The calculated load based on GSA [G1] provisions was too conservative. The dynamic amplification factor can only reach '2' when the beam is in the linear elastic region.

- The behavior of existing buildings in the seismic zone had not been studied in that investigation.

- In that study, the boundary condition of the specimens was assumed to be fixed end. This assumption needs to be evaluated by experimental or analytical analysis.

- Similar as Yi *et al*. [Y1], dynamic characteristics of the progressive collapse and slab effect were not involved in that study.

2.6.3 Su *et al*. [S4]

Su *et al*. [S4] tested twelve beam-column assemblages representing two spans of a RC frame with a center column removed.

Twelve specimens representing reinforced concrete frame beams were tested to investigate their load-carrying capacity against progressive collapse. In that study, twelve specimens were divided into three series to study the effect of reinforcement ratio, span-depth ratio and loading rate on the arch action development.

The test results indicated that:

- The compressive arch action due to longitudinal restraint can significantly enhance the flexural strength of a beam subjected to vertical loads. For the specimens tested in this study, the compressive arch action resulting from axial restraint contributed 50 to 160 % extra loading capacity beyond the capacity estimated without considering axial restraining forces.

- The compressive arch action was observed to be a function of flexural reinforcement ratio and ratio of beam span to depth. The tests indicated that the effects of compressive arch action increased with a decrease of the beam span-depth ratio and flexural reinforcement ratio.

- Under faster loading rate, the compressive arch effect could still be developed but the effect of loading rate could be neglected.

The deficiencies of that study were pointed out as follows:

- Majority of the specimens in that study developed only arch action while the catenary effect of the specimen with large deflection was not included.

- For series C, it was concluded that the loading rate has no effect on the response of specimens. This needs to be further studied because the loading rate in series C might not be as fast as real situation.

- The existing slab will change the mechanism of failure mode and needs to be included in future study.

2.6.4 Yap [Y2]

Yap [Y2] tested six exterior beam-column joints under monotonic static loading to study the response of exterior joints with the loss of an exterior column.

Six exterior beam-column joints divided into two series (non-seismically detailing and limited-seismic detailing) were conducted in the protective engineering laboratory of NTU, Singapore. This experimental study was the first laboratory tests regarding the RC frame with exterior column loss scenario.

The test results indicated that:

- In the experimental study, test specimens were loaded monotonically beyond their service loading until failure was observed. Test results obtained were satisfactory in terms of strength under monotonic loading, simulating gravity load from the floor service loading. Better performance was due to the provision of transverse reinforcement in the joint region as well as the additional longitudinal beam bars, as evidenced from the test results.

- The increase in the percentage of transverse reinforcement in the joint region improved the strength of the joint through the development of the truss mechanism. However, test results from the specimens of the improved design (LS series) showed that joint shear failure was still the dominant failure mode and was independent of the amount of joint transverse reinforcement.

- Premature bond failure was observed in the bottom beam bars in all NS series specimens. It was suggested that the additional bottom beam longitudinal reinforcement could prevent such failure.

- Test results on the increase in provision of transverse reinforcement in the beam and column elements adjacent to the joint panel showed no significant influences on the strength of the exterior beam-column sub-assemblages. However, total deformations were significantly reduced.

The deficiencies of that study were pointed out as follows:

- Only exterior beam-column sub-assemblages were tested. In order to better

understand the performance of the RC frame after the exterior column removed, the behavior of the whole cantilevered bay should be investigated.

- The possible existing beam-axial force with large deflection will affect the response of exterior beam column joint while this effect could not be included in that set-up.

- The flange of slab could provide additional strength and stiffness on the joint and might change the failure mode of the joint.

- The nature of progressive collapse was dynamic and this was ignored by these tests.

2.7 Summary

Based on the systematic literature review, the common deficiencies of existing researches for progressive collapse are shown below:

1. Many analytical studies have investigated the behavior of structures under the scenario of instant loss of columns. However, few studies involved the case of losing a ground corner column.

2. Although several in-situ tests had investigated the dynamic performance of RC structures after losing exterior or corner column scenario, live load and part of dead load of the structures was removed before the tests for safety reason.

3. Existing laboratory tests were conducted quasi-statically to simulate the equivalent dynamic performance of the frames for progressive collapse.

4. Existing laboratory tests focused only on the frame behavior following the removal of interior or exterior columns.

5. Existing laboratory tests only modeled the two-dimensional (2D) planar frame behavior after the removal of the columns.

6. Existing laboratory tests do not include the load resistance contribution of RC slab on the performance of the frame for progressive collapse.

Therefore, in order to further develop the database of laboratory test for progressive collapse and to provide reference for design of new building and rehabilitation of existing buildings in resisting progressive collapse, three series of tests were conducted in this study. For the first series of tests, seven RC beam-column substructures with different design detailing, span aspect ratio and design span length were tested under quasi-static loading regime. For the second series of tests, six beam-column substructures with similar dimension and reinforcement details as the specimens tested in the first series were conducted under dynamic loading regime to study their dynamic performance and to evaluate the dynamic effects. For the third series of tests, three beam-column-slab substructures were designed to evaluate the slab effects on the performance of the beam-column substructure in resisting progressive collapse. The specimen design, the experimental setup design and experimental results are described in the following chapters.

CHAPTER 3

EXPERIMENTAL PREPARATION AND TEST PROCEDURE FOR QUASI-STATIC TESTS

3.1 Introduction

Progressive collapse has been of great concern to structural engineers, considering the widely publicized collapses. Reviewing the previous research studies (refer to **Chapter 2**, it was found that very few experimental studies have been conducted on RC frames against progressive collapse caused by the loss of a corner column. In order to understand the quasi-static behavior of RC substructures for progressive collapse, seven one-third scale beam-column substructures were tested quasi-statically. This chapter describes the details of the test specimens, the preparatory works and the test setup design of the quasi-static test program. The instrumentations used for load and displacement measurements are also described in detail.

3.2 Experimental Setup Design

3.2.1 Introduction

Previous studies (Sasani *et al.* [S1] and Sasani [S2]) had indicated that all floors above the lost column deformed almost simultaneously and the axial force of the column above the lost column reduced to zero in very short time (within 0.01 s). Moreover, the damage of the floor in different storeys was similar after the removal of a corner column. Thus, all floors worked together to redistribute the total axial force in the ground corner column after the removal of a corner column. Moreover, if the dimensions and reinforcement details of beams and slab in each floor were identical and the load condition in each floor was similar, it could be assumed that the beams connected to the corner joint in each floor would just need to redistribute the loading initially carried by its own floor. Therefore, the progressive collapse performance of a

multi-storey frame could be equivalently studied by a series of single-storey substructure with proper boundary conditions (as shown in **Fig. 3.1)**. The main differences between the ground substructure, middle substructure, and roof substructure are the boundary conditions applied on the corner joint. The ground floor substructure is one of the most critical cases when the frame subjected to the scenario of the loss of a corner column. Thus, it was investigated in this study. As suggested in Qian and Li [Q1], a substructure can be further simplified by representing the interior beam-column sub-assemblages as an equivalent fixed support (refer to **Fig. 3.2**). However, designing proper boundary conditions on the corner column had become a challenge in this study. Both numerical and experimental studies (Sasani [S2], Sasani and Sagiroglu [S3]) indicated that the direction of the bending moment in the beam end near the corner joint (BENC) changed and resulted in a considerable increase in bending moment (tensile at the bottom) in the BENC due to Vierendeel action (refer to **Fig. 3.3**). Thus, it was necessary to design a steel assembly (as shown in **Fig. 3.2**) to be applied on the corner joint to simulate the effects of the Vierendeel action on the test specimens. However, from the deformation shape of the corner joint observed by Sasani and Sagiroglu [S3], a slight horizontal movement accompanied the vertical movement of the corner joint after the removal of a ground corner column (refer to **Fig. 3.4**) and this indicated that the rotational constraint in the BENC was not full. In other words, the designed steel assembly (as shown in **Fig. 3.2**) in the test setup not only applies rotational constraints on the corner joint, but also allows the corner joint to move horizontally as that in the prototype frames. It was understandable that the extent of the horizontal constraints was related to the allowable horizontal movement of the corner joint. In this study, the author first predicts the relationship of the horizontal movement and vertical displacement in the prototype frames via finite element (FE) analysis. Then, the steel assembly (as shown in **Fig. 3.2**) was designed to allow the corner joint in the test specimens achieve similar relationship as that in the prototype frames.

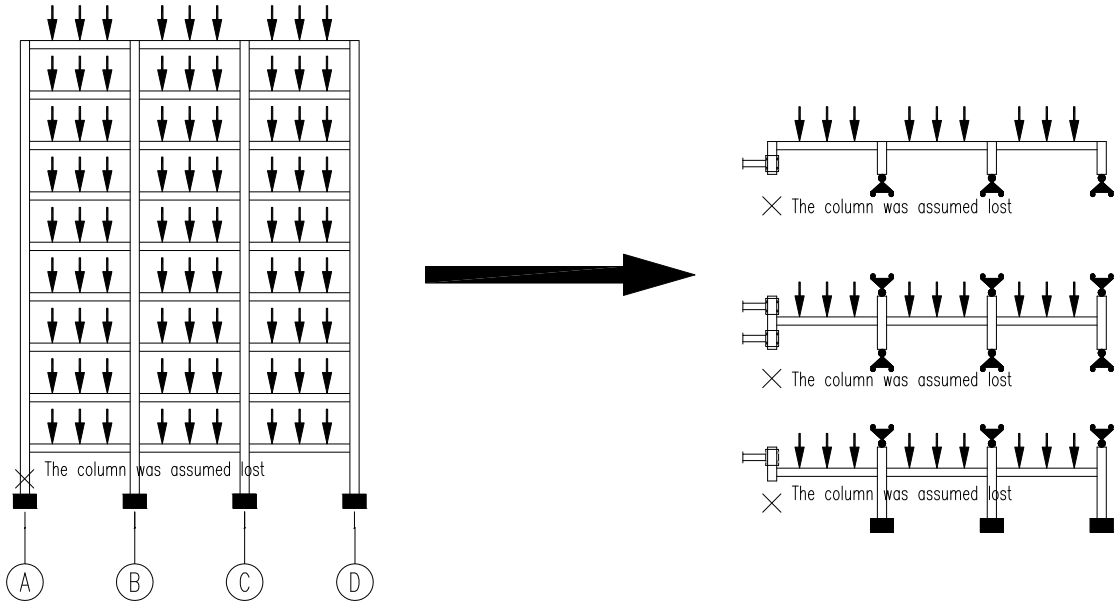

Fig. 3.1: Substructures tests to represent whole frame test

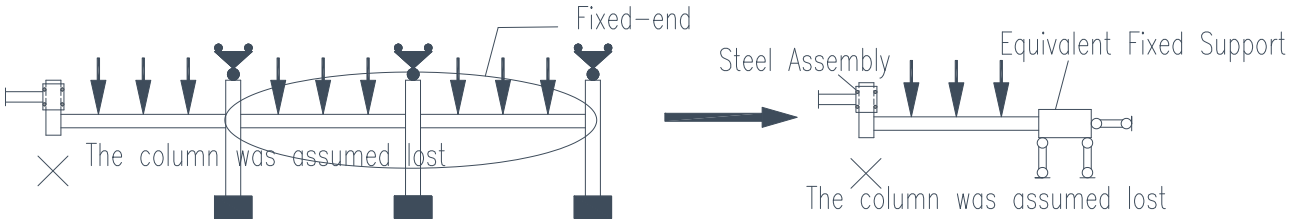

Fig. 3.2: Fixed support to simulate interior beam-column sub-assemblages of the substructures

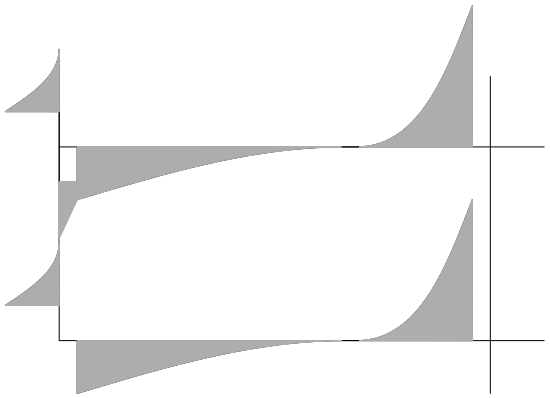

Fig. 3.3: Bending moment diagram of the substructures after the removal of a corner column

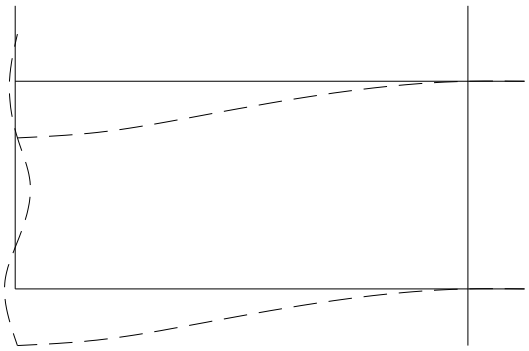

Fig. 3.4: Deformed shape of the substructures after the removal of a corner column

In order to predict the relationship of the horizontal movement and vertical displacement of the corner joint in the prototype frame, nonlinear fiber based FE models were utilized. In-situ dynamic test conducted by Sasani *et al*. [S1] was utilized to validate the FE models.

3.2.2 Validate Finite Element Model

In order to validate the proposed model, a 10-storey RC frame was built as shown in **Fig. 3.5**. The model replicated the in-situ testing of a RC building by Sasani *et al*. [S1]. **Fig. 3.6** schematically shows the typical plan of the building. The frame size, slab thickness and boundary conditions were similar to the in-situ test by Sasani *et al*. [S1] and are given in **Table 3.1**. The slab was indirectly considered by simulating the beam as T-beam or L-beam with effective flange width of 1/4 of the span (ACI 318-08 [A3]).

Table 3.1: Summary of the Frame Member Dimensions in Sasani *et al*. [S1]

Elements	Depth (mm)	Width (mm)	Thickness (mm)	Reinforcement Ratio (%)
Beam	510	510	N/A	1.0
Column	510	510	N/A	2.0
Slab	N/A	N/A	203	0.2

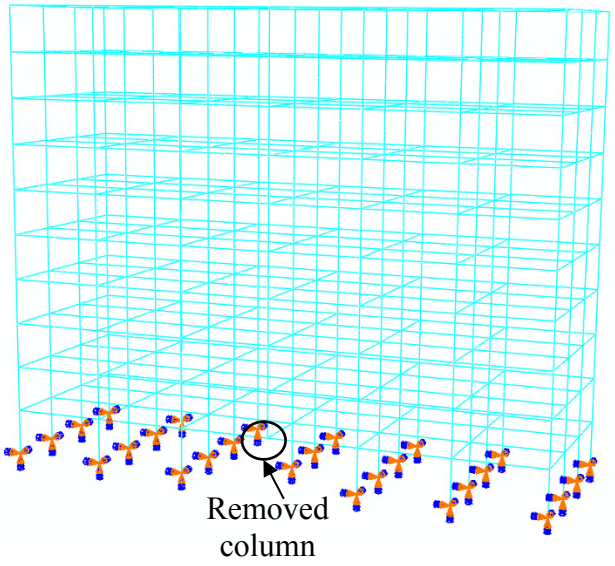

Fig. 3.5: The numerical validation model using ABAQUS [A2]

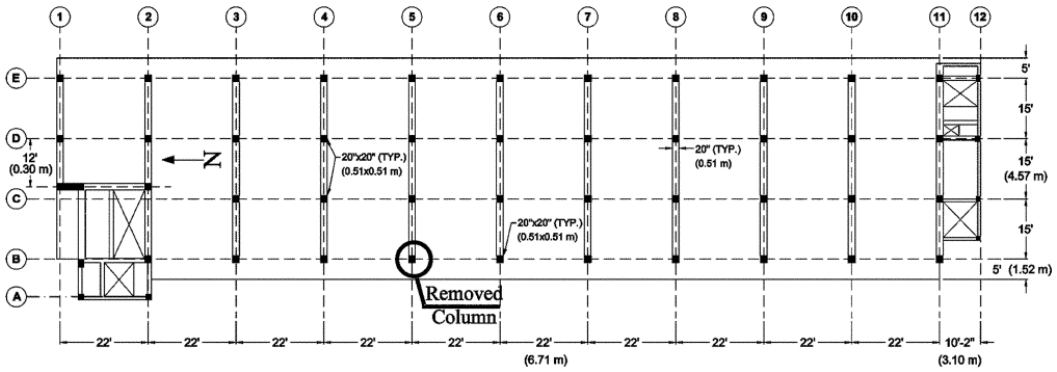

Fig. 3.6: In-situ test by Sasani *et al.* [S1]

3.2.2.1 Beam Element for Beam and Column

The beam and column were modeled using 3-node quadratic Euler-Bernoulli beam elements B32. The details of the beam element formulation can refer the theory manual of ABAQUS [A2]. Only a brief introduction is presented as follows:

First, input the beam properties by defining the relevant cross-section shape from the pre-defined ABAQUS cross-section library. At each increment of the analysis, the

stress over the cross-section is numerically integrated to define the beams response as the analysis proceeds. This allows the analysis to follow the development of the full elastic-plastic behavior of the section at each integration point along the beam. The longitudinal reinforcement in the beam element is defined by modifying the input file manually as the keyword *REBAR for beam element is not supported by the CAE of ABAQUS [A2].

3.2.2.2 Material Model

Reinforcement Material Model

A bilinear stress-strain relationship was used to model the uniaxial material property for steel bars. **Fig. 3.7** shows the analytical stress-strain model for steel. The density, modulus of elasticity and Poisson's ratio of the steel reinforcement are $7850\,kg/m^3$, 200,000 MPa and 0.3, respectively. The yield and ultimate strength of the steel reinforcement are 331 MPa and 503 MPa, respectively.

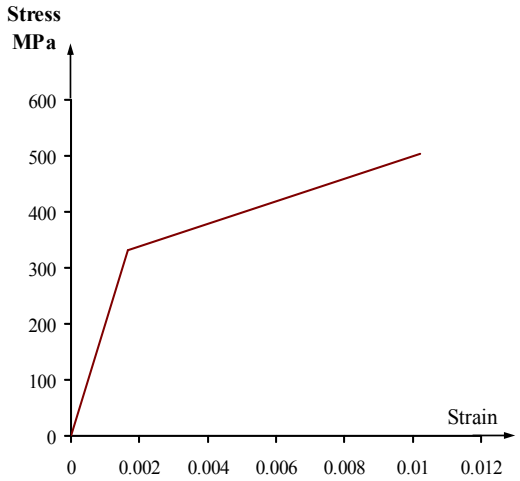

Fig. 3.7: Bilinear stress-strain curves for steel rebar

Concrete Material Model

The concrete was modeled using a smeared crack model from ABAQUS [A2]. The model does not track individual macro cracks. Constitutive calculations are performed independently at each integration point of the finite element model, and the presence of cracks enters into these calculations in the manner that the cracks affect the stress and the material stiffness associated with the model.

Constitutive Model of Concrete

The density and Poisson's ratio of concrete were assumed 2450 kg/m^3 and 0.2 respectively in this study. The compression hardening behavior of the concrete was defined based on Saenz. [S5] 's suggestions as:

$$\sigma_c = \frac{E_0 \varepsilon_c}{1 + (R + R_E - 2)(\frac{\varepsilon_c}{\varepsilon_{cc}^{'}}) - (2R - 1)(\frac{\varepsilon_c}{\varepsilon_{cc}^{'}})^2 + R(\frac{\varepsilon_c}{\varepsilon_{cc}^{'}})^3} \qquad (3\text{-}1)$$

where $\varepsilon_{cc}^{'}$ is the strain corresponding confined concrete ultimate strength $f_{cc}^{'}$; ε_c is the concrete compressive strain; σ_c is the concrete compressive stress at any compressive strain ε_c;

$$E_0 = 4700\sqrt{f_{cc}^{'}} \text{ (MPa)} \qquad (3\text{-}2)$$

$$R = \frac{R_E(R_\sigma - 1)}{(R_\varepsilon - 1)^2} - \frac{1}{R_\varepsilon} \qquad (3\text{-}3)$$

$$R_E = \frac{E_0 \varepsilon_{cc}^{'}}{f_{cc}^{'}} \qquad (3\text{-}4)$$

and constants $R_\sigma = 4, R_\varepsilon = 4$ can be used (Hu and Schnobrich [H2]). Eq. 3-1 is taken as the equivalent uniaxial stress-strain curve for concrete when $\varepsilon_c < \varepsilon_{cc}^{'}$. When $\varepsilon_c \geq \varepsilon_{cc}^{'}$, a linear descending line is used to model the softening behavior of concrete. $f_c = 0.75 f_{cc}^{'}$ when $\varepsilon_c = \varepsilon_u^{'}$.

Tension Stiffness

The sub-option tension stiffness is utilized to control the phenomenon of the concrete to carry tension even after cracking. The tension stiffening sub-option improves the accuracy of the finite element models in representing cracks and improves the numerical stability of the solution. **Fig. 3.8** illustrates the concrete tensile stress-strain curves which are frequently used in the simulation practice. They are stepped unloading response, gradually unloading response and discontinuous unloading response after cracking (Gilbert and Warner [G2], Gupta and Maestrini [G3]). The previous studies (Williams [W1], Clark and Speirs [C3]) indicated that the tensile stiffness is related to the reinforcement ratio, rebar size and concrete strength. In the smeared crack model of ABAQUS [A2], the tensile stiffness model can be simplified as linear descending or bi-linear descending. As shown in **Fig. 3.9**, we assumed the concrete tensile strength decreases to zero when the tensile strain reaches $\alpha\varepsilon_{cr}$. The value of α is in the range of 5 to 25 (Prakhya and Morley [P7]). ABAQUS [A2] suggests the value of α to be 10. Considering the crack strain of the concrete as $\frac{f_t}{E_c}$, no tensile strength can be provided by concrete when strain exceeded $10 \times \frac{f_t}{E_c}$. The sensitivity of the numerical results for tensile stiffness model will be studied in the validation section.

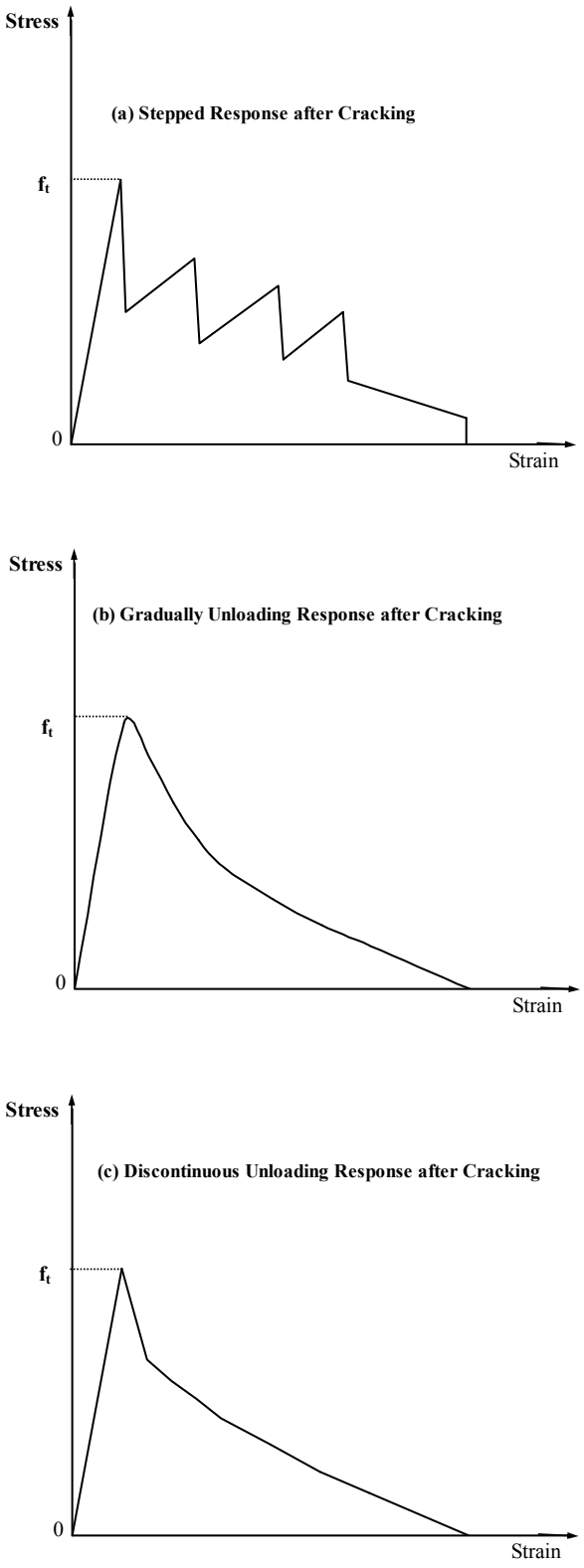

Fig. 3.8: The typical concrete tensile stress-strain curves

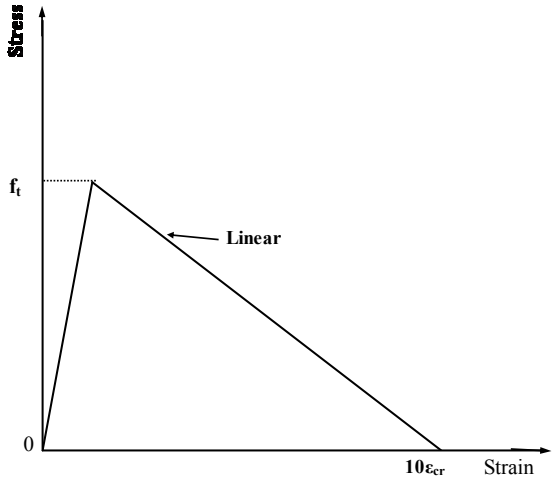

Fig. 3.9: The simplified linear tensile stress-strain curve of concrete

Shear Retention

As the concrete cracks, its shear stiffness is diminished. This sub-option in ABAQUS [A2] defines the reduction of the shear modulus associated with crack surfaces in a concrete model as a function of the tensile strain across the crack. The shear modulus after cracking is defined as:

$$G_{crack} = \rho G \qquad (3\text{-}5)$$

where G is elastic shear modulus of the uncracked concrete, ρ is a multiplying factor.

The shear retention model assumes that the shear stiffness of open cracks reduces linearly to zero as the crack opening increases.

$$\rho = \begin{cases} (1 - \varepsilon / \varepsilon^{\max}) & \text{for } \varepsilon < \varepsilon^{\max} \\ 0 & \text{for } \varepsilon \geq \varepsilon^{\max} \end{cases} \qquad (3\text{-}6)$$

where ε is direct strain across the crack and $\varepsilon^{\max}$ is the user-specified value.

Fig. 3.10 presents the relationship of the multiplying factor and concrete tensile strain.

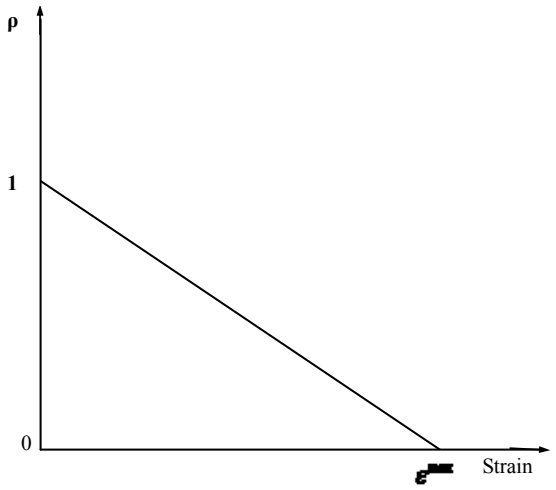

Fig. 3.10: The relationship of the multiplying factor and concrete tensile strain

3.2.2.3 Loading Process

The initial local failure as a result of the removal of a column was modeled by a sudden release of the resultant end forces of the column. The loading process of the analytical simulation is shown as follows:

- The structure was analyzed under the gravity loads as specified in Sasani *et al.* [S1] and the end forces of the column to be removed were determined.

- The floor corner column was removed and, instead, the reaction force in the ground corner column was applied on the structure. Note that the results of such analysis are identical to those of the previous analysis where the column was not removed.

- When all of the gravity loads were applied on the frame and the analysis was stable, the reaction force was suddenly reduced to zero (1 millisecond). This is to model the sudden removal of the column and a dynamic analysis was conducted.

Fig. 3.11 illustrates the comparisons of the numerical results with the experimental results conducted by Sasani *et al*. [S1]. As shown in the figure, the finite element model predicts the first peak displacement very well. However, significant displacement oscillation is observed in the finite element results after reaching the first peak displacement while the oscillation was limited in the test recording. This was possibly due to the column not being totally destroyed in the test of Sasani *et al*. [S1] which resulted in large damping in the test.

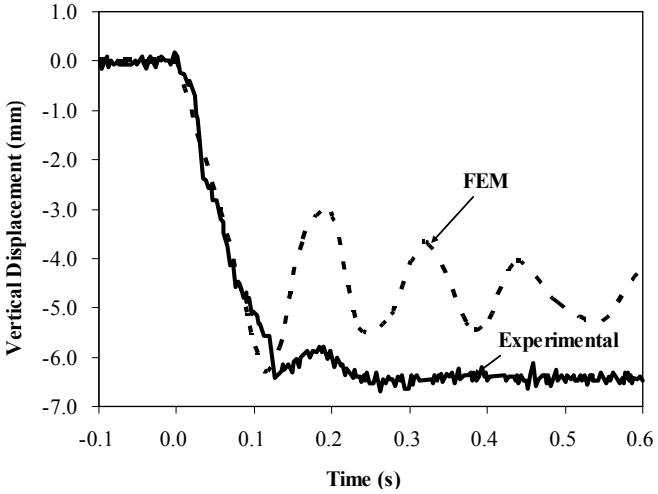

Fig. 3.11: Experimental and analytical vertical displacements of Joint B5 in fifth floor of Sasani *et al*. [S1]

3.2.3 Predict the Horizontal Movement of the Corner Joint with Increasing the Vertical Displacement

The RC moment resisting frames (prototype frames) having similar details of the tested specimens were utilized to predict the relationship of the horizontal movement and the vertical displacement of the corner joint after removal of a ground corner column. The detailing of each specimen is shown in the next section. **Fig. 3.12** illustrates the dimensions and reinforcement details of the control frame. The distributed dead load on the prototype structure due to gravity load of 210.0 mm thick slab was 5.1 kPa. The super imposed dead load due to ceiling weight was assumed to be 1.0 kPa. The equivalent additional dead load due to the weight of in-fill wall and beam were 2.25 kPa and 1.59 kPa, respectively. The live load was assumed to be 2.0 kPa. Since the slab was not included in this FE model, the pressure applied on the slab

was transferred into the beams. Two load procedures were conducted in the models (nonlinear dynamic procedure (ND) and nonlinear static (NS) procedure). For ND, gravity loads (1.2DL+0.5LL) were applied gradually within 3 second. After that, the pre-determined reaction force in the corner column was suddenly decreased to zero (1 millisecond). For NS, the damaged corner column was removed first. Then gravity load 2(1.2DL+0.5LL) was gradually applied on the structures. The relationship of vertical displacement and horizontal movement of the corner joint is shown in **Fig. 3.13**. As shown in **Fig. 3.13**, the horizontal movement increased with increasing vertical displacement for specimens in both procedures. The maximum horizontal movement of the corner joint (7.2 mm) was reached in Specimen F5 when the vertical displacement was 180 mm. However, the horizontal movement of the corner joint of Specimen DF5 in the ND procedure was 6.9 mm, which was slightly less than the horizontal movement obtained from the NS procedure. It should be noted that Specimens F5 and DF5 had similar dimensions and reinforcement details while they were subjected to the quasi-static and dynamic load regimes respectively. The dimensions and reinforcement details of Specimens F5 and DF5 are given in **Tables 3.2** and **6.2**, respectively. To be conservative, the maximum horizontal movement of 7.2 mm was utilized in the designing of the steel assembly.

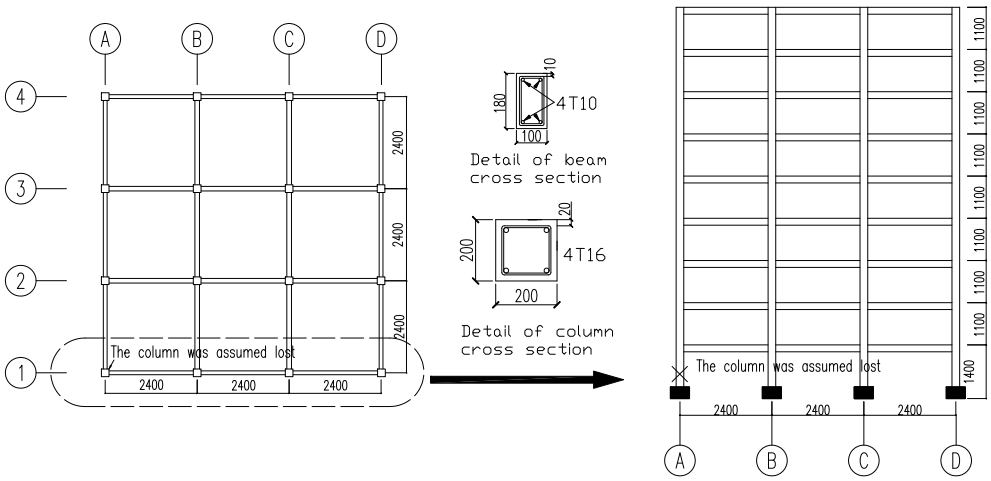

Fig. 3.12: The plan and elevation views of the scaled frame

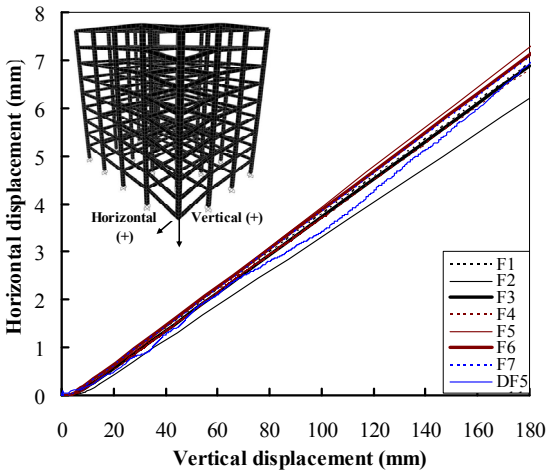

Fig. 3.13: The relationship of the vertical displacement and horizontal movement

3.2.4 Design the Allowance between the Pin and the Hole

After obtaining the relationship of the horizontal movement and vertical displacement of the corner joint in the prototype frame, the extent of the allowance in between the steel pin and hole in the steel assembly (as shown in **Fig. 3.14**) was specially designed to make sure the corner joint in the test specimen could achieve similar horizontal constraints as that in the prototype frame. As shown in **Fig. 3.14** (Item 5 in **Fig. 3.15**), the total length of the corner stub was about 1800.0 mm. In order to easily control the accuracy of the setup and to avoid the inconvenience of casting and transportation, part of the RC column was replaced by steel column. In order to make sure the corner joint of the tested specimen has similar horizontal movement (H_1) as that in the prototype frame when the vertical displacement reached 180 mm. The allowance between the steel pin and the hole was designed as follows:

$$\phi = \frac{H_1}{TV} = \frac{H_1}{V + D_1} = \frac{7.2}{625 + 180} = 8.9 \times 10^{-3} \qquad (3\text{-}7)$$

$$\delta = \frac{\overline{V} \times \phi}{2} = \frac{350 \times 8.9 \times 10^{-3}}{2} = 1.56 \qquad (3\text{-}8)$$

where ϕ is the design rotation of the steel column (Unit: rad); H_1 is the horizontal movement of the joint just above the damaged column; TV is the total vertical distance between the center of steel box and the center of corner joint when specimen has vertical displacement of D_1; V is the vertical distance between the center of steel box and the center of corner joint at beginning of the test; D_1 is the vertical displacement; $\overline{V}$ is the average vertical distance between two steel pins; δ is the difference between the diameter of the hole and the steel pin (Unit: mm).

Thus, the diameter of the steel pin was 40 mm while the diameter of the hole in the steel box was designed to be 43 mm as shown in **Fig. 3.14**.

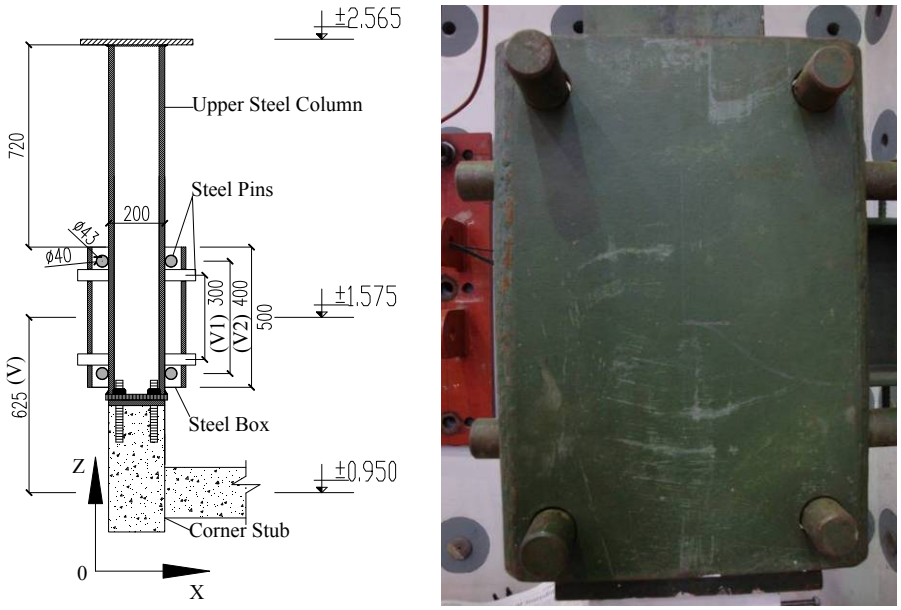

Fig. 3.14: An elevation view of the designed steel assembly (Item 5 in Fig. 3.15a)

3.2.5 Quasi-Static Test Setup Erected in the Laboratory

The erected test setup for quasi-static tests is shown in **Figs. 3.15a** and **3.15b**. The setup can be separated into three components. In component 1, vertical, axial and rotational constraints were provided at the adjacent columns to simulate fixed boundary condition provided by the surrounding structural elements. In component 2, axial loading in the corner column before damage was simulated by applying

downward displacements at the corner column stub through a hydraulic jack with 600 mm stroke. In component 3, partial rotational and horizontal constraints were applied to the corner column by a steel assembly (Item 5 in **Fig. 3.15**).

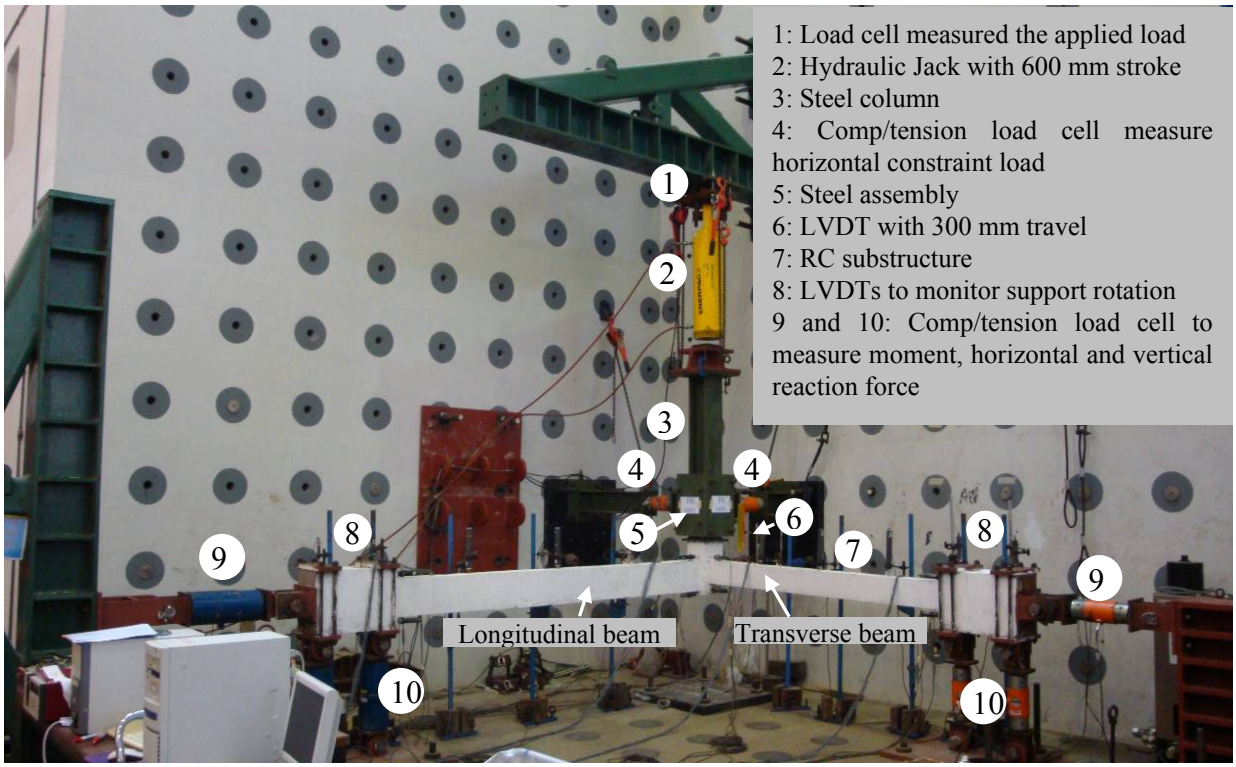

Fig. 3.15a: An overview of a specimen in position ready for testing (quasi-static tests)

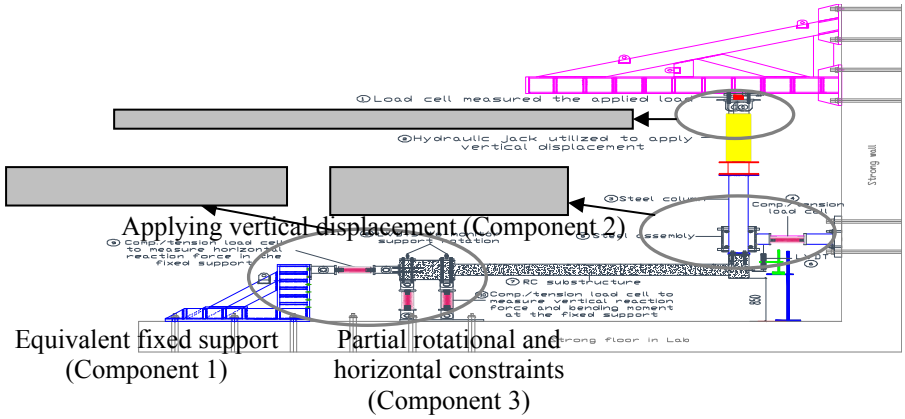

Fig. 3.15b: A 2D elevation view of a specimen in position ready for testing

3.3 Description of Test Specimens

3.3.1 Details of Test Specimens

Seven one-third scale RC beam-column substructures with different details were tested to investigate the quasi-static behavior of these substructures. The non-seismically detailed prototype RC moment resisting frames were designed according to Singapore Standard CP 65 [C2] while the seismically detailed prototype frame was designed according to ACI 318-08 [A3]. For non-seismically detailed prototype frames, the live load was taken to be 2.0 kPa at each storey level. Moreover, 1.0 kPa additional dead load, which accounts for items such as partitions, ceiling, mechanical ductwork, electrical items, plumbing, was assumed applied on each floor. Because Singapore is a low-seismicity zone, the prototype frame with seismic detailing (corresponding to F2) was designed by assuming it was located on a site class of D, stiff soil profile. The design spectral response acceleration parameters for seismic, S_{DS} and S_{D1}, were 0.47 and 0.32, respectively. As one-third scale tests were conducted in this study, the span and dimensions of the test specimens were scaled down proportionally. The span and dimensions of structural components of the prototype frames and test substructures were given in **Table 3.2.** The reinforcement details of the test substructures are summarized in **Table 3.3**. Based on static analysis, the design axial force in the corner column of each specimen as specified by DoD [D1] is determined and listed in **Table 3.3**. As illustrated in **Fig. 3.16**, each test substructure consisted of two doubly reinforced beams connected to a column stub at the corner and two enlarged columns at the edges where the rotational and horizontal restraints on beams were applied. The corner column stub representing the removed column was 200 mm square for all specimens. **Fig. 3.16** illustrates the reinforcement details of test specimens. The longitudinal reinforcement of corner column in all test specimens consisted of 4-T16 bars (16 mm diameter deformed bar) while the transverse reinforcement in the corner column were R6@55. The concrete cover in the column and beam were 20 mm and 10 mm, respectively. For beam longitudinal reinforcement, F2 was installed 4-T13 bars (13 mm diameter deformed bar). However, for the remaining specimens, 4-T10 bars (10 mm diameter deformed bar) were placed for

longitudinal reinforcement. The transverse reinforcement in F2 was hoop stirrups with 135° bends and transverse reinforcement were provided in the joint region. For the remaining specimens, non-seismic detailing was provided, transverse reinforcement was hoop stirrups with 90° bends and no transverse reinforcement was installed in the joint region. It should be emphasized that doubly continuous longitudinal rebar was installed in the beam because the specimens were scaled down in this study. Moreover, the anchorage failure of the bottom longitudinal reinforcement in the BENC due to the changed direction of the bending moment was prevented in the current study by using hooked anchorages instead of the compression development lengths. The development length of the hooked beam top longitudinal reinforcement into the fixed support was greater than the ACI 318-08 [A3] required development length. The detailing of the anchorage details is also illustrated in **Fig. 3.16**.

Table 3.2: Basic Configuration of Prototype and Model Frame (Unit: mm)

Test	Prototype frames				Model frames			
	Span-T	Span-L	Beam-T Dimensions	Beam-L Dimensions	Span-T	Span-L	Beam-T Dimensions	Beam-L Dimensions
F1	7200	7200	540×300	540×300	2400	2400	180×100	180×100
F2	7200	7200	540×300	540×300	2400	2400	180×100	180×100
F3	7200	7200	540×300	540×300	2400	2400	180×100	180×100
F4	7200	7200	540×300	540×300	2400	2400	180×100	180×100
F5	9000	9000	720×300	720×300	3000	3000	240×100	240×100
F6	7200	9000	540×300	720×300	2400	3000	180×100	240×100
F7	7200	9000	540×300	630×300	2400	3000	180×100	210×100

Note: Span-T and Span-L represent span in the transverse and longitudinal direction, respectively
Beam-T and Beam-L represent transverse beam and longitudinal beam, respectively.

Table 3.3: Specimen Properties (Quasi-static Tests)

Test	Elements		Longitudinal rebar		Transverse rebar			Design axial load (kN)
	Beam-T	Beam-L	Beam-T	Beam-L	Joint	Beam-T	Beam-L	
F1	Type a*	Type a*	4 - T10	4 - T10	None	R6@250	R6@250	18.6
F2	Type a*	Type a*	4 - T13	4 - T13	R6@55	R6@60	R6@60	18.6
F3	Type a*	Type a*	4 - T10	4 - T10	None	R6@180	R6@180	18.6
F4	Type a*	Type a*	4 - T10	4 - T10	None	R6@80	R6@80	18.6
F5	Type b*	Type b*	4 - T10	4 - T10	None	R6@160	R6@160	29.1
F6	Type a*	Type b*	4 - T10	4 - T10	None	R6@180	R6@160	23.2
F7	Type a*	Type c*	4 - T10	4 - T10	None	R6@180	R6@160	23.2

Note: Type a*: Clear length=2175 mm, cross-section=180 mm x 100 mm;
Type b*; Clear length =2775 mm, cross-section=240 mm x 100 mm;
Type c*: Clear length =2775 mm, cross-section=210 mm x 100 mm
Beam-T; Transverse beam; Beam-L; Longitudinal beam

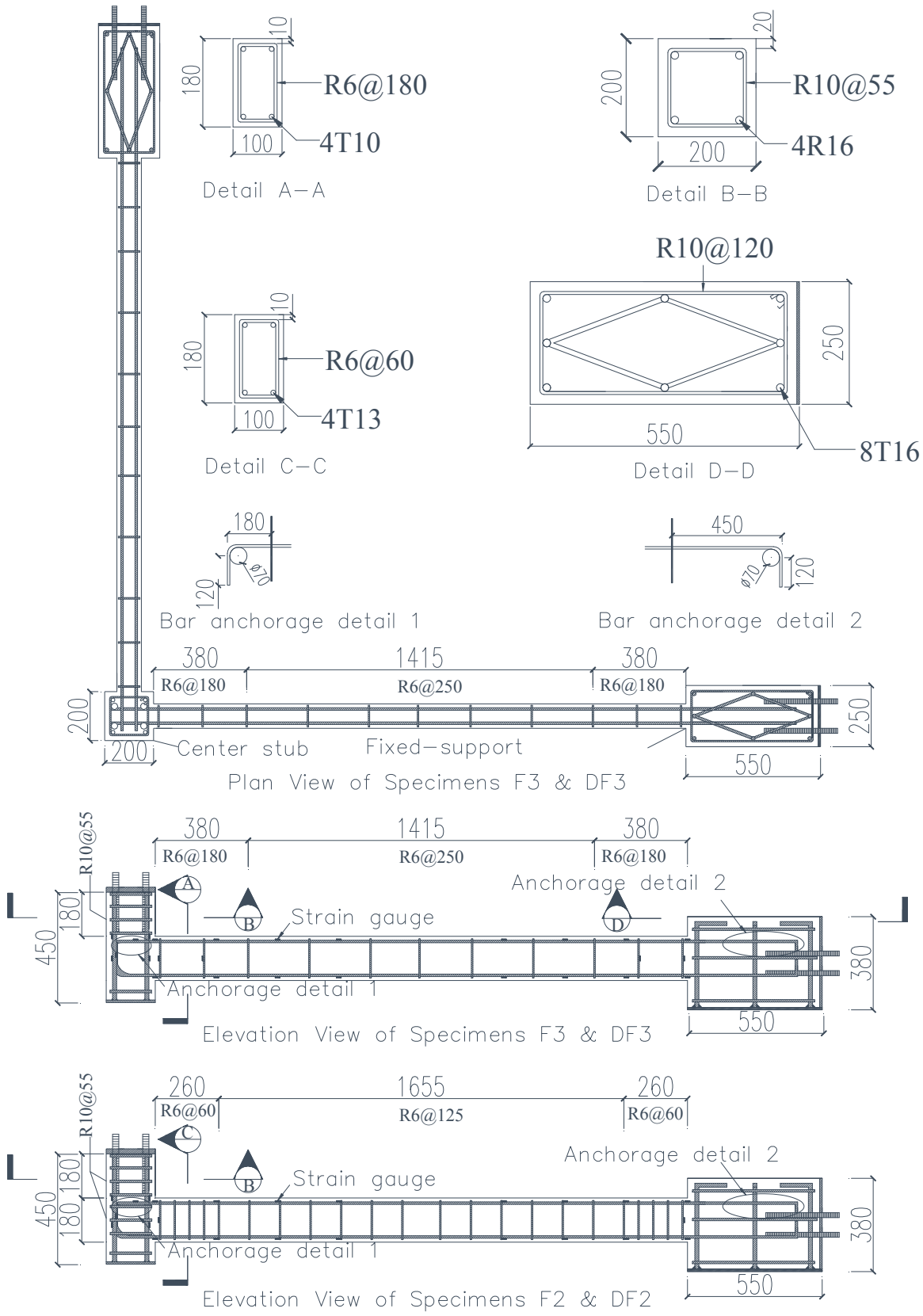

Fig. 3.16: Reinforcement details of typical specimens F3 and F2 (in mm)

3.3.2 Material Properties

In order to achieve more reliable results, the properties of materials used were determined through various tests. It is to be emphasized that the actual strength of the material supplied by the contractor deviated from that required.

3.3.2.1 Reinforcing Steel Bars

The steel bars used in all specimens were the hot-rolled type. Grade 250 (R6) and Grade 460 (T16, T13 and T10) steel bars were used as transverse and longitudinal reinforcement, respectively. Tensile tests were carried out on sample reinforcing bars to determine their true mechanical tensile properties. **Table 3.4** gives the measured tensile properties of the bars used in the tests.

Table 3.4: Properties of Reinforcing Steel

Types	Yield strength f_y (MPa)	Yield strain ε_y (10^{-6})	Ultimate strength f_u (MPa)	Ratio of elongation
R6	530	2650	613	20.3 %
T10	575	2895	695	21.7 %
T13	520	2595	637	22.6 %
T16	556	2897	635	21.1 %

Notes: R6= Plain round bar of 6 mm diameter; T10 = Deformed bar of 10 mm diameter
T13 = Deformed bar of 13 mm diameter; T16 = Deformed bar of 16 mm diameter

3.3.2.2 Concrete

Ready-mix concrete was utilized to cast the test specimens. The specified concrete compressive strength at 28 days was 30 MPa with the maximum specified aggregate size of 10 mm for all specimens. Six 150 mm diameter by 300 mm high concrete cylinders were utilized to determine the compressive strength of the concrete of each specimen at 28 days and on the day of test. **Table 3.5** gives the concrete strengths of the seven specimens at 28 days and on the day of testing.

Table 3.5: Compressive Strength of Concrete

Test	Compressive strength at 28 days f_c' (MPa)	Compressive strength on the day of testing f_c' (MPa)
F1	29.9	31.5
F2	30.6	32.1
F3	30.4	31.9
F4	30.7	32.5
F5	31.1	33.1
F6	31.0	32.8
F7	30.9	33.3

3.3.3 Construction Process

The construction of the test specimens was tendered to a construction company due to space limitations in the laboratory. The construction process consisted of several stages, including reinforcing cages, formworks, strain gauging, and casting and curing of the specimens. Details of each stage will be provided in the following sections.

3.3.3.1 Reinforcing Cages

All the longitudinal reinforcement and transverse reinforcement were cut to length and bent by the construction company. The installation of the strain gauges only took place after the completion of the reinforcing cages. This eliminates possible damage to gauges that could occur during the process of tying the reinforcing cages. **Fig. 3.17** illustrates a completed reinforcing cage of the beam-column substructures without slab.

3.3.3.2 Formwork

In the construction, wooden formwork was utilized. Before the placement of the reinforcing cages, the surfaces of the formwork were oiled so that the formwork can be easily removed and the surface of specimens will not be damaged. Special care

was taken to maintain the verticality of the two beams since small errors would result in failure to install the specimen on the loading rig. Before the casting process, 10 mm thick concrete spacer blocks were placed on the underside as well as the side faces of the transverse reinforcements to ensure a clear concrete cover of 10 mm was achieved. Lifting hooks were installed at various locations of the specimens to facilitate the lifting process. **Fig. 3.18** shows the constructed formwork with reinforcing cages prior to casting.

Fig. 3.17: Typical reinforcing cages

Fig. 3.18: Formwork with reinforcing cages

3.3.3.3 Casting and Curing

Chipping aggregates with a maximum size of 10 mm were used in the mix to ensure better flow of the concrete due to the limiting concrete cover spacing of 10 mm in the

beam. The specimens were cast in the upright position to simulate the real situation. After casting, all of the specimens were cured for two weeks with damp hessian fabrics. The specimens were then transported to the laboratory for the test setup.

3.4 Test Procedure

Before commencement of any loading sequence, the test specimen was painted with a thin coat of white-wash to allow better observation of cracks. All instrumentation (as will be described in the following sections) was calibrated in position and initialized. Before reaching first peak ultimate capacity, the vertical load was under force controlled steps (2 kN interval). After that, the vertical load was under displacement controlled steps with 10 mm interval.

3.5 Instrumentation of the Test

The test specimens had been extensively installed or mounted with measuring devices both internally and externally. Amongst those measurements recorded were vertical load and displacement imposed at the top of the corner column stub, redistributed vertical reaction and bending moment at the fixed support, the horizontal constraint measured in the fixed support and the constraint close to the corner column, shear and flexural deformations at the critical regions of the specimen, rigid body rotation and also the strains in the steel bars.

3.5.1 Measurement of Loads and Moments

The load cell (Item 1 in **Fig. 3.15**) beneath the hydraulic jack was used to measure the applied vertical load on the corner stub of the specimens. The tension/compression load cells (Item 4 in **Fig. 3.15**) connected with the steel assembly and tension/compression load cells (Item 9 in **Fig. 3.15**) horizontally connected to the fixed supports with the reaction frames were utilized to measure the horizontal reaction force developing during the tests. Another four tension/compression load cells (Item 10 in **Fig. 3.15**) vertically installed at the fixed supports were utilized to

measure the redistributed force and the moment developed in the fixed support during the tests.

3.5.2 Measurement of Deformation Shape of the Beams

The deformation shape of the beams during the test procedure was recorded by Linear Variable Differential Transducers (LVDTs) attached to magnetic stands, which were mounted on steel frames. **Fig. 3.19** presents the arrangement of LVDTs for deformation shape measurement on the test specimen.

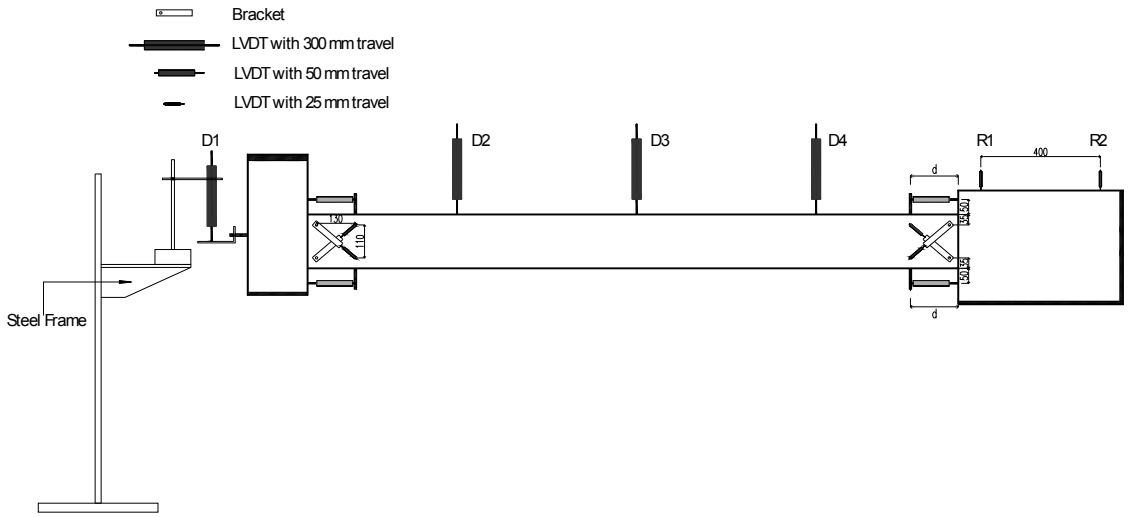

Fig. 3.19: Typical arrangements of LVDTs for deformation shape, flexure and shear deformations measurement (Unit: mm)

3.5.3 Measurement of Shear and Flexure Deformations

A series of LVDTs were placed at various locations of the specimen to measure the shear and flexure deformations. The LVDTs were attached on 3 mm thick steel plates and were mounted onto 8 mm steel rods embedded in the concrete. Such measurement devices were not applied to the full span of the beam, but only in locations where potential deformations were likely to occur.

The readings from pairs of LVDTs along the beam were used to measure flexure deformations of the test specimens. Shear distortions were measured by using LVDTs

arranged in a cross-like manner. It is to be noted that near normal failure stage, defined by a drop of the load resistant capacity by 25% of the ultimate capacity of the specimen, crushing and spalling of concrete induced false reading on the measurement devices. The affected LVDTs were then removed as they no longer served any purpose and to prevent them from being damaged. The overall arrangement of the instrumentation is shown in **Fig. 3.19**. Methods for calculation of shear and flexural deformations are presented as follows:

3.5.3.1 Flexural Deformation

The flexural deformations of beams were estimated from the discrete rotations in each segment along the beams, which were measured from pairs of LVDTs. The derivation of the following equations was based on Bernoulli hypothesis, which states that plane sections remain plane after deformation. With reference to **Fig. 3.20**, the rotation of segment 1 due to flexural (θ_{s1}) is given by:

$$\theta_{s1} = \frac{\delta_t - \delta_b}{h_t} \qquad (3\text{-}9)$$

where δ_t and δ_b are the displacement measured by the top and bottom transducer at hinge 1, respectively; and h is the distance between the transducers at segment 1 as illustrated in **Fig. 3.20**.

The corresponding average curvature (ϕ_{s1}) can be derived by:

$$\phi_{s1} = \frac{\theta_{s1}}{S_t} \qquad (3\text{-}10)$$

where S_t is the width of segment1 as illustrated in **Fig. 3.20**.

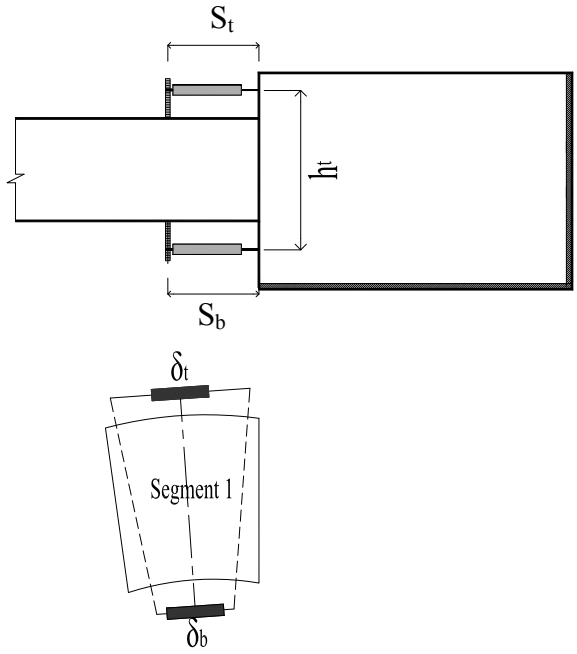

Fig. 3.20: Evaluation of the flexural deformations

3.5.3.2 Shear Deformation

The shear deformations of beams were measured by using pairs of LVDTs arranged in a cross-liked manner as described in the previous section. With reference to **Fig. 3.21**, the average shear distortion at segment 1 (r_{S1}) is evaluated as follows:

$$r_{S1} = \frac{\delta_{S1} - \delta'_{S1}}{2L_{S1}}(\tan\alpha_{S1} + \frac{1}{\tan\alpha_{S1}}) \qquad (3\text{-}11)$$

where δ_{S1} and δ'_{S1} are the changes in length of the diagonal; L_{S1} is the initial length of the diagonals; and α_{S1} is the angle between the diagonals and the vertical as shown in **Fig. 3.21**.

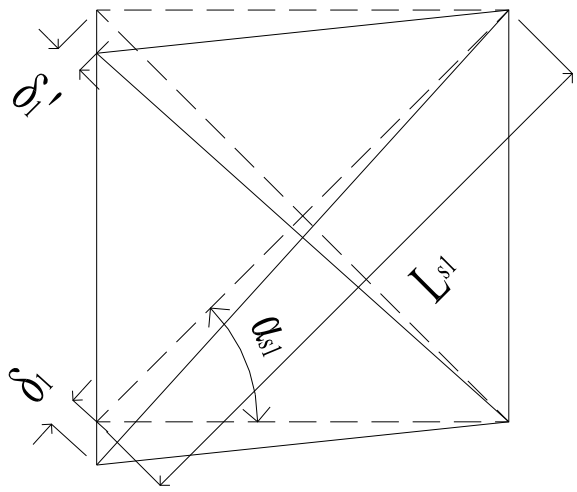

Fig. 3.21: Evaluation of the shear deformations

3.5.4 Measurement of Strains in Reinforcing Bars

Strain gauges were used to measure the local strains in the reinforcing steel bars. All strain gauges were of the KFG type with 3 mm gauge length, 120 Ω resistance and nominal gauge factor of 2.13. Soldering to the terminals was not required because these strain gauges had been pre-attached with 10 m long of 3 parallel vinyl-insulated lead wires. Due to the limited amount of available strain gauges, only reinforcing bars at critical locations (similar to that of the external measuring devices) were installed with gauges. Details on the preparation and installation of the strain gauges will not be presented in this report as the standard procedure was well documented elsewhere. The locations of the strain gauges for each test specimen are shown in **Fig. 3.16**.

3.5.5 Measurement of Rigid Body Rotation at the Fixed Supports

As described in the section of 3.2.5, a fixed boundary condition was assumed in the adjacent exterior column. However, movement of the assumed fixed support was observed due to gaps in the setup. In order to monitor the rotation of the "fixed support" and account for the effect of this rotation on the stiffness of the test specimens, two LVDTs (R1&R2 in **Fig. 3.19**) were installed before conducting the tests. The vertical displacement at the corner column due to this rotation of the fixed support was evaluated by assuming the beams as cantilever beams. It should be noted

that the error is negligible for this cantilever beam assumption due to the fact that the measured rigid rotation of the fixed support was limited.

3.6 Summary

This chapter describes an experimental program on seven one-third scale RC beam-column substructures for progressive collapse caused by losing a ground corner column. The following provides a summary of the chapter:

1. The validated finite element models help to design the experimental setup for the quasi-static tests.

2. The construction details of the seven one-third scale RC beam-column substructures for quasi-static tests were described together with details on the loading rig.

3. Instrumentation was installed at various locations for measurement and thereafter good understanding of the global performance of each specimen.

4. The derivations of formula to estimate shear and flexure deformations based on the data obtained from the instrumentation were described in detail.

CHAPTER 4

TEST RESULTS OF THE SUBSTRUCTURES WITHOUT SLAB UNDER QUASI-STATIC LOAD

4.1 Introduction

This chapter presents the experimental results of the substructures without slabs subjected to a quasi-static load regime. Experimental results include the measured load-displacement curve, beam horizontal reaction force versus vertical displacement at the corner column, the observed cracking patterns, the strain readings from the reinforcing bars, and bending moment response in the fixed support.

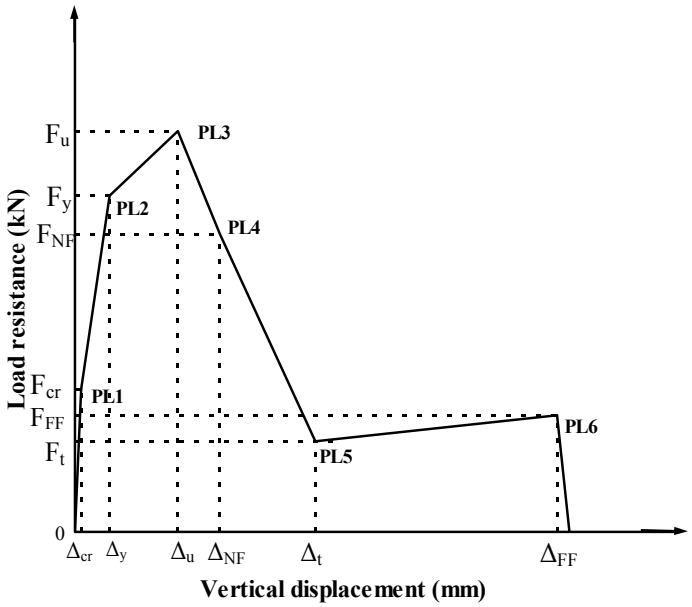

Fig. 4.1: Definition of the performance levels

The results of all test specimens will be presented together with performance levels as shown in **Fig. 4.1**. Six performance levels at six significant parts of the test were identified. They were the vertical displacement at which the first cracking load (F_{cr}) is attained (PL1); vertical displacement at which the yield force (F_y) was reached

(PL2); vertical displacement at which the ultimate resistant capacity (F_u) was attained (PL3); vertical displacement at normal failure stage (F_{NF}), which corresponded to a 25 % reduction in the ultimate capacity on the descending branch of the load-displacement curve (PL4); vertical displacement at the stage of which the catenary action began (F_t), at which the slope of the decrease of load resistance changed significantly (PL5); and vertical displacement at the final failure stage (F_{FF}), which was defined as the point when the load resistance totally vanishes (PL6).

4.2 Test Results of the Control Specimen F3

F3 was non-seismically detailed and had a medium amount of beam transverse reinforcement (0.314 %) in the potential plastic hinge zones. Transverse reinforcement was not installed in the joint region. The longitudinal reinforcement ratio was 0.87 % for both beams. The beam span aspect ratio was 1.0.

4.2.1 General Behavior

The general behavior of the specimen was described based on the crack pattern development during the test. Under the applied load, the first cracks were observed at the beam end near the fixed support (BENF) at a load of 4.3 kN, while the first joint shear cracks were observed corresponding to a load of 21.0 kN. The flexural and shear cracks that occurred in the joint and in the BENF became more severe with increasing vertical displacement. Distinct concrete crushing was observed in the BENF when the displacement reached 120.0 mm. The failure mode of F3 is illustrated in **Fig. 4.2**. When the vertical displacement reached 257.9 mm, the vertical load resistance began to ascend again and this was attributed to the catenary action developing in the beams. The load resistance at a deflection of 456.2 mm was 11.9 kN, but it was suddenly reduced to 0.0 kN at a deflection of 461.3 mm due to fracture of the top beam longitudinal rebar occurring in the BENFs.

4.2.2 Load-Displacement Relationship

The load-displacement relationship of F3 is presented in **Fig. 4.3**. It can be seen that initially, there was a slightly linear relationship between the vertical displacement and the applied vertical load. However, at 4.3 kN (PL1), the slope of the curve became milder although the relationship was still remain linear. When the steel began to yield at a load of 22.5 kN (PL2), the displacement increased significantly with a slight increase in load resistance. When the vertical displacement reached 44.0 mm, F3 achieved the ultimate capacity (25.8 kN), which was about 138.7 % of the design axial load in the corner column based on DoD [D1]. The ultimate resistant capacity dropped by 25 % when the vertical displacement reached 102.3 mm (PL4). The measured maximum axial compressive and tensile forces for horizontal load cells are tabulated in **Table 4.1**. It should be noted that the tensile phase was found after the beam reached 296.2 mm and 346.6 mm (PL5) of vertical displacement for longitudinal and transverse beam, respectively. The load resistance was increasing gradually with increasing vertical displacement until the displacement reached 456.2 mm due to catenary action.

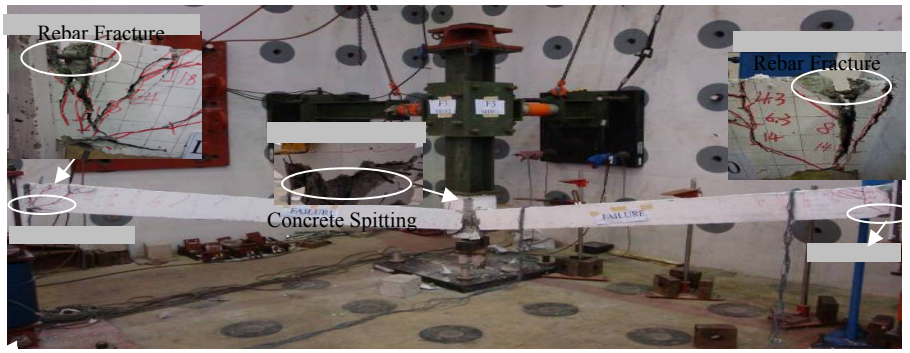

Fig. 4.2: Cracking patterns of F3 at failure

Table 4.1: Beam Measured Axial Force Results

Test	THR Fixed Support		THR Corner Constraint		LHR Fixed Support		LHR Corner Constraint	
	MC(kN)	MT(kN)	MC(kN)	MT(kN)	MC(kN)	MT(kN)	MC(kN)	MT(kN)
F1	-18.3	4.7	-18.5	3.5	-18.6	8.8	-19.5	5.9
F2	-27.2	6.2	-27.7	5.8	-27.8	11.6	-28.0	10.6
F3	-18.8	7.9	-20.6	4.5	-19.8	7.5	-19.8	6.6
F4	-20.0	3.3	-20.4	3.8	-20.3	7.7	-21.1	7.3
F5	-20.5	4.6	-20.8	4.0	-20.2	3.5	-20.6	3.2
F6	-19.1	5.4	-19.5	4.4	-20.6	1.9	-21.2	0.8
F7	-19.5	1.9	-20.0	1.5	-18.6	1.6	-18.2	1.0

Note: THR, LHR =Transverse horizontal reaction and longitudinal horizontal reaction force, respectively.
MC, MT=Maximum compressive force and maximum tensile force, respectively.

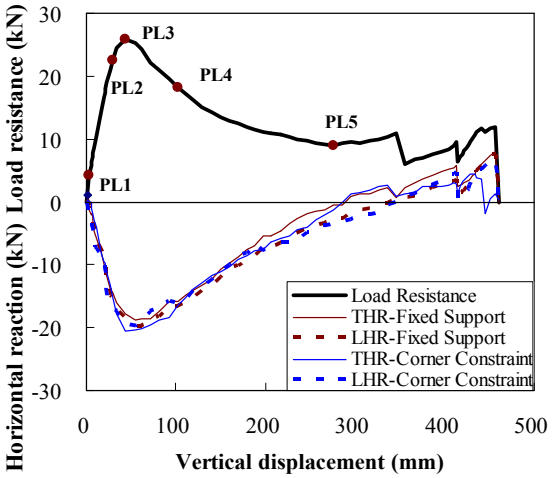

Fig. 4.3: Vertical and axial loads of F3

4.2.3 Strain Results

4.2.3.1 Strains in the Beam Reinforcing Bars

Fig. 4.4 gives the strain profile of the beam longitudinal reinforcement of F3 corresponding to different performance levels. As shown in the figure, the strains of top longitudinal reinforcement at the BENF significantly increase while the strains of top longitudinal reinforcement at the BENC started to decrease after PL3. Moreover, the inflection point (zero strain point) of both top and bottom longitudinal reinforcement was moving towards the corner joint after PL3 and this indicates that the resistance mechanism of the specimen was changing to cantilever beams after

severe failure occurred in the corner joint. The strain of bottom longitudinal reinforcement at the BENF yielded at PL4 while the strain of bottom longitudinal reinforcement at the BENC did not yield during the test.

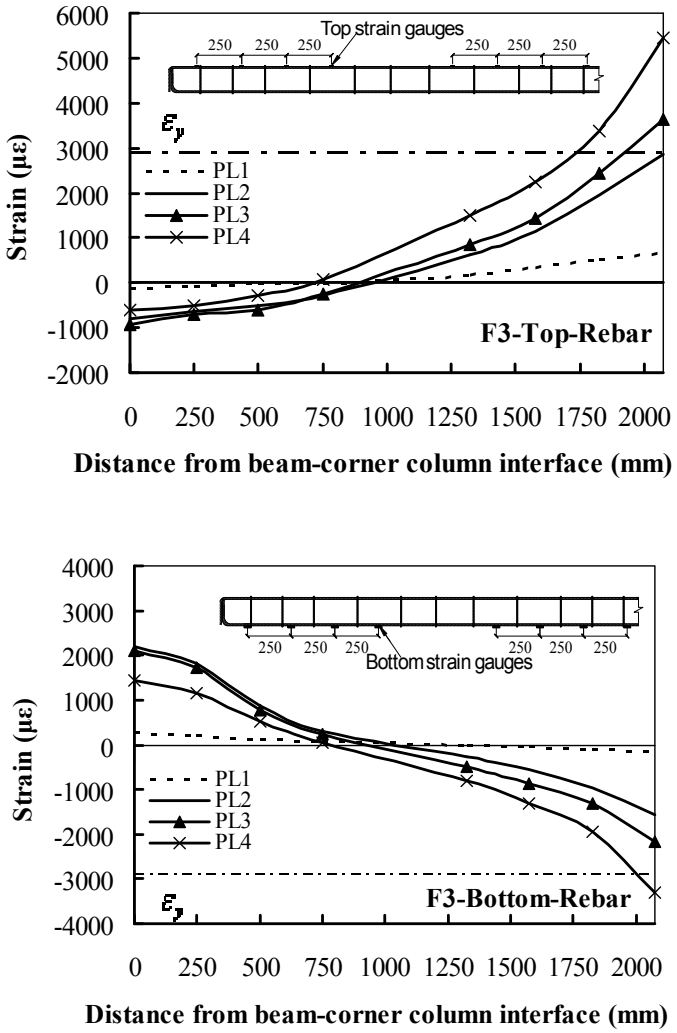

Fig. 4.4: Strain profile of the beam longitudinal reinforcement of F3

4.2.4 Rotation Results

Fig. 4.5 illustrates the comparison of the rotation at the BENC (θ_2) with the rotation in the BENF (θ_1) of F3. The rotation results were measured through pairs of LVDTs installed along the beam as described in **Chapter 3**. As presented in the figure, the rotations at both ends were limited before signs of cracks were observed in the beam

(PL1). After PL1, the rotations at both ends were increased significantly. However, the slope of θ_1 was much larger than θ_2. Moreover, θ_2 kept almost constant after PL3 while θ_1 was increasing with the increase of the vertical displacement. The values of θ_1 and θ_2 at PL2 were 0.005 rad and 0.0033 rad, respectively. Moreover, the values of θ_1 and θ_2 at PL3 were 0.0215 rad and 0.0138 rad, respectively. The constraint effective factor ξ was defined as the ratio of θ_2 to θ_1. The value of ξ was 0.66 and 0.64 corresponding to the PL2 and PL3, respectively. There were two effect factors resulted in the value of θ_1 less than θ_2 and ξ less than 1. The first factor was the designed steel assembly allowed the corner joint to rotate and released the rotation of the BENC. The second factor was the severe damage occurring in the corner joint loosened the effectiveness of the rotation constraints. As shown in **Eq. 3-7**, the steel assembly was designed based on the required rotation of the corner joint equals to 0.0089 rad, when the vertical displacement of corner joint reached 180 mm. If assuming the development of the rotation was linear, the released rotation of the corner joint due to the designed steel assembly could be determined. For example, the vertical displacement of F3 at PL3 was 44 mm. Thus, the released rotation due to the design steel assembly was $\frac{44}{180} \times 0.0089 = 0.0021$ rad. **Table 4.2** illustrates the contribution of the factors resulting in the value of θ_2 significantly less than θ_1. In general, the contribution of factor 1 decreased and the contribution of factor 2 increased when the displacement increased from PL2 to PL3. This is due to more severe damage occurred at the BENC when the displacement increased from PL2 to PL3.

Table 4.2: Decomposition of the contribution of the factors resulting in the value of θ_2 significantly less than θ_1

Test	PL2		PL3		PL2		PL3	
	θ_1	θ_2	θ_1	θ_2	Factor 1*	Factor 2*	Factor 1	Factor 2
F1-Tran.	0.0085	0.0062	0.0105	0.0071	63.0 %	37.0 %	57.8 %	42.2 %
F2-Tran.	0.0101	0.0070	0.0155	0.0098	59.0 %	41.0 %	45.9 %	54.1 %
F3-Tran.	0.0050	0.0033	0.0215	0.0138	64.7 %	35.3 %	27.2 %	72.8%
F4-Tran.	0.0106	0.0075	0.0129	0.0082	44.8 %	56.3 %	48.0 %	52.0 %
F6-Tran.	0.0115	0.0079	0.0166	0.0108	37.9 %	62.1 %	33.9 %	66.1 %
F7-Tran.	0.0091	0.0061	0.0145	0.0093	49.2 %	50.8 %	37.0 %	63.0 %

Note: Factor 1*= released rotation at the BENC due to the designed steel assembly;
Factor 2*= released rotation due to severe damaged occurring at the corner joint loosening the rotation constraints;

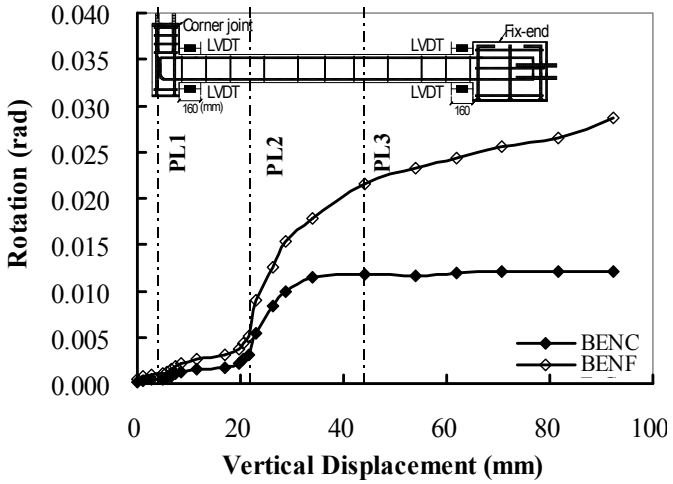

Fig. 4.5: The comparison of the rotation in the BENC with the rotation in the BENF of F3

4.2.5 Bending Moment-Displacement Relationship

Two double action load cells (Item 10 in **Fig. 3.15a**) were installed vertically in each fixed support to determine the bending moment response during the test. **Fig. 4.6** illustrates the beam bending moments at fixed supports versus vertical displacement of F3. It can be seen from the figure that initially, the bending moment in both fixed supports was increasing with an increase in the vertical displacement. When the displacement reached 28.9 mm, the bending moment in both fixed supports kept almost constant with increasing vertical displacement. The bending moment measured in the transverse and longitudinal fixed supports began to decrease at a displacement

of 130.0 mm and 140.0 mm, respectively. This was possibly due to concrete crushing occurring in the BENF. However, when the displacement was further increased, the degradation of the bending moment in both fixed supports was relatively gradual. Significant decreases in the bending moment happened in the transverse fixed support and longitudinal fixed support when the displacement reached 346.0 mm and 412.0 mm, respectively. It should be noted that the maximum bending moment of 15.9 kN.m was obtained at a deflection of 54.0 mm in the longitudinal fixed support while the maximum bending moment of 15.7 kN.m was obtained at a deflection of 61.9 mm in the transverse fixed support. The calculated ultimate moment capacity of the beam by including the material over-strength factors as provided in ASCE 41-06 [A4], which were adopted by DoD [D1], was 16.6 kN.m.

Both nonlinear static procedure (NS) and nonlinear dynamic procedure (ND) need to properly define the plastic hinge properties. The current version of DoD [D1] has adopted the modeling parameters of plastic hinges for the frame element from ASCE 41-06 [A4]. The measured plastic hinge's modeling parameters of this specimen were compared with the recommended parameters of DoD [D1] in **Table 4.3** and further discussion was shown in the following section.

Table 4.3: Comparison the Measured Plastic Hinge's Parameters with the Modeling Parameters Provided in DoD [D1]

Test	a in Beam-T (rad)	a in Beam-L (rad))	a in DoD* (rad)	b in Beam-T (rad)	b in Beam-L (rad)	b in DoD* (rad)	c in Beam-T	c in Beam-L	c in DoD*
F1	0.031	0.035	0.05	0.181	0.189	0.06	0.56	0.55	0.2
F2	0.058	0.063	0.063	0.198	0.198	0.10	0.58	0.55	0.2
F3	0.046	0.046	0.05	0.146	0.177	0.06	0.74	0.75	0.2
F4	0.052	0.052	0.05	0.143	0.161	0.06	0.72	0.75	0.2
F5	0.042	0.042	0.05	0.134	0.134	0.06	0.50	0.50	0.2
F6	0.040	0.038	0.05	0.137	0.140	0.06	0.66	0.49	0.2
F7	0.043	0.037	0.05	0.143	0.136	0.06	0.59	0.51	0.2

Note: DoD*= DoD [D1]; Beam-T=Transverse Beam; Beam-L=Longitudinal Beam

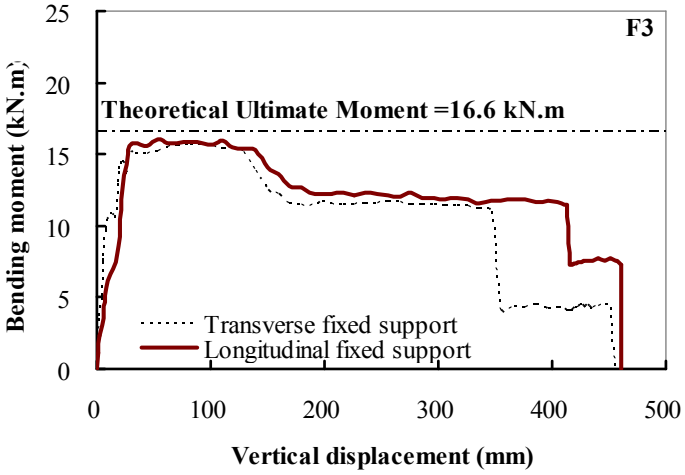

Fig. 4.6: Bending moment response in the fixed supports of F3

4.3 Test Results of the Seismically Detailed Specimen F2

F2 was seismically detailed according to the ACI 318-08 [A3]. It was designed to investigate the influence of seismic detailing on the overall performance of the substructure against progressive collapse. The dimensions and reinforcement details are given in **Table 3.3**.

4.3.1 General Behavior

Under the applied load, the first crack was observed at the BENF at a load of 5.0 kN while the first crack occurred in BENC was at a load of 10.0 kN. Following the first crack, joint shear cracks were observed at a load of 25.3 kN. The crack width of the flexural cracks in the BENF increased significantly with an increase in the vertical displacement. Simultaneously, the joint shear cracks became more severe and concrete splitting was observed at a displacement of 280.0 mm. Compared to F3, limited concrete crushing was observed in the BENF of F2. Slight crushing of concrete cover was observed only after a deflection of 250.0 mm. Upon further increasing the vertical deflection, the top rebar at the BENF fractured when the vertical displacement reached 462.0 mm and the test was terminated. The final failure mode of F2 is illustrated in **Fig. 4.7**. As shown in the figure, severe flexural cracks not

only occurred in the BENF but also were observed in the BENC. Different from F3, no obvious shear cracks were formed in the beams during the test because of seismic detailing with much higher transverse reinforcement ratio in the potential plastic hinge zones. However, more severe flexural cracks occurred in BENC of F2 compared to F3. As explained below, additional shear strength provided by the joint transverse reinforcement of F2 delayed the shear failure in the corner joint and ensured that the plastic hinges were formed in the BENC.

4.3.2 Load-Displacement Relationship

The load-displacement relationship of F2 is presented in **Fig. 4.8**. Similar to F3, initially, there was a slightly linear relationship between the vertical displacement of corner column and the applied vertical load. However, at 5.0 kN (PL1), the slope of the curve became gentler although the relationship remained linear. When the steel began to yield at a load of 29.1 kN (PL2), there was a great increase in displacement with a slight increase in load resistance. When the relative displacement reached 53.0 mm, F2 obtained the ultimate capacity (36.5 kN), which was about 196 % of the design axial load in the corner column based on DoD [D1]. The ultimate capacity dropped by 25 % when the displacement reached 127.7 mm (PL4). The measured maximum axial compressive and tensile forces of the horizontal load cell are tabulated in **Table 4.1**. It should be noted that the tensile phase was found after the beams reached 361.0 mm and 351.0 mm (PL5) of vertical displacement for longitudinal and transverse beam, respectively. The load resistance was increased gradually with increasing vertical displacement until the displacement reached 462.0 mm.

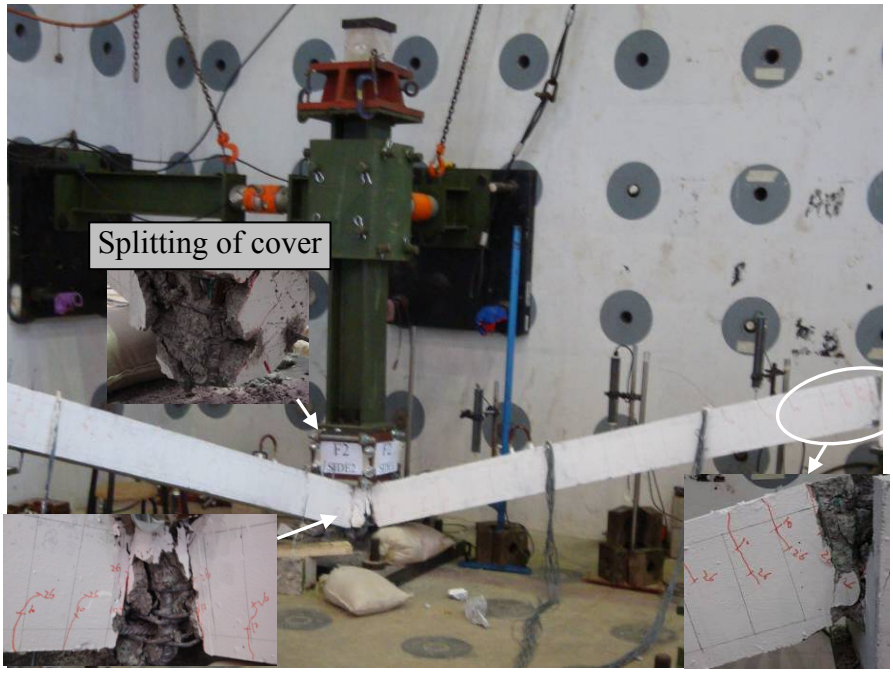

Fig. 4.7: Cracking patterns of F2 at failure

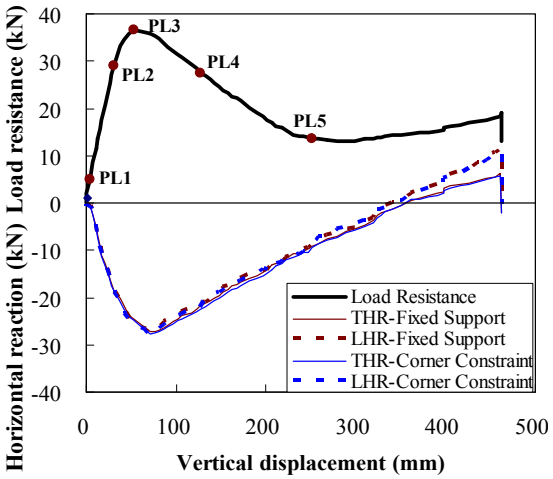

Fig. 4.8: Vertical and axial loads of F2

4.3.3 Strain Results

4.3.3.1 Strains in the Beam Reinforcing Bars

Fig. 4.9 illustrates the strain profile of the beam longitudinal reinforcement of F2 corresponding to different performance levels respectively. In general, the strain profile of F2 was similar to F3. The difference between these two specimens was that the beam bottom longitudinal reinforcement yielded at BENC at PL3 for F2 while it did not yield during the test of F3.

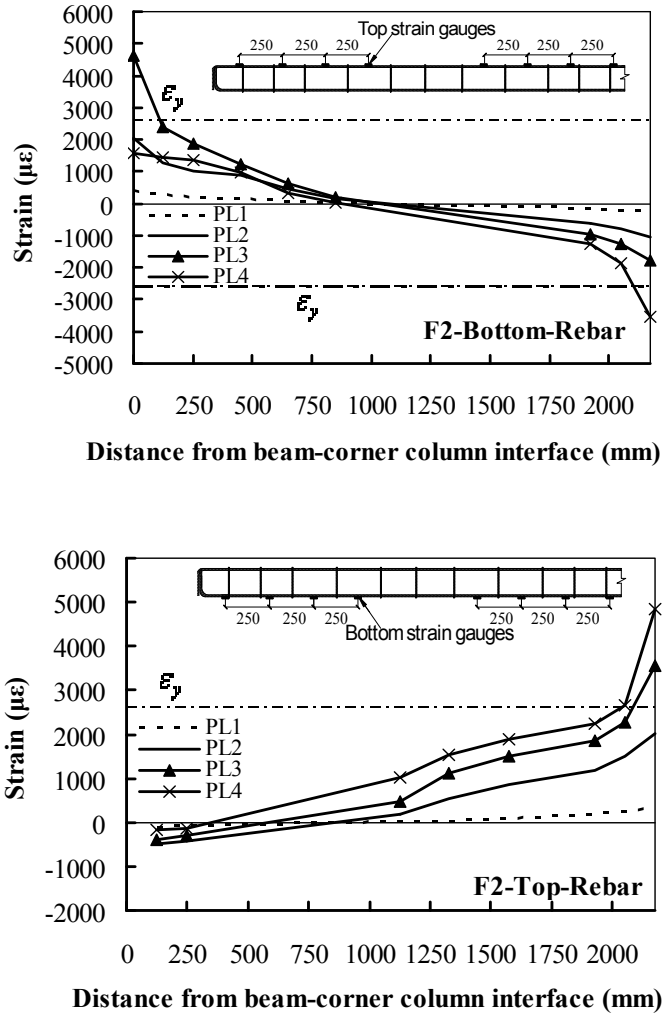

Fig. 4.9: Strain profile of the beam longitudinal reinforcement of F2

4.3.3.2 Strains in the Column Reinforcing Bars

Fig. 4.10 illustrates the strain gauge results of the column longitudinal reinforcement as well as joint shear reinforcement versus vertical displacement of F2. It should be

noted that three-dimensional (3D) beam-column substructures were designed and tested in this study. If we consider only the 2D longitudinal frame, rebar C2 (as illustrated in **Fig. 4.10**) was a compressive rebar. However, if we see only the 2D transverse frame, rebar C2 was tensile. Thus, it resulted in the net strain of rebar C2 being limited in tensile at the initial part of the test. Due to C1 and C4 were tensile and compressive rebar in both longitudinal and transverse 2D frame respectively, the maximum tensile strain and compressive strain were recorded in C1 and C4, respectively. It was found that the corner column was in elastic range during the test. The strains in the joint transverse reinforcements were also measured in F2. The strains in the joint transverse reinforcements were limited initially. The strains increased rapidly after the first diagonal shear crack occurred in the corner joint. One consequence of the shear was the expansion of the core concrete. Joint transverse reinforcement partially restrained the expansion and appeared to increase the strain. Finally, the strain of joint transverse reinforcement kept constant with increasing displacement. The maximum strain of joint transverse reinforcement was 2380 $\mu\varepsilon$. This indicated that the joint transverse reinforcements had not yielded.

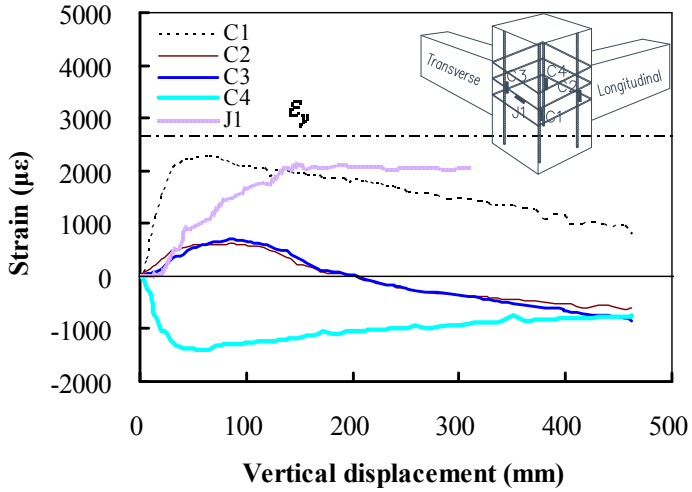

Fig. 4.10: Local strain in the column reinforcing bars of F2

4.3.4 Rotation Results

Fig. 4.11 illustrates the comparison of θ_1 with θ_2 of F2. In general, the trends of the rotation results of F2 are similar to that of F3. However, θ_2 in F2 kept increasing until

PL3 while θ_2 in F3 kept almost constant after PL2. This is consistent with the strain gauge results (strain in BSBL1 kept increasing until PL3). The constraint effective factor ξ was 0.68 and 0.63 at PL2 and PL3, respectively. The contribution of each factor resulting in the value of ξ less than 1 was shown in **Table 4.2.**

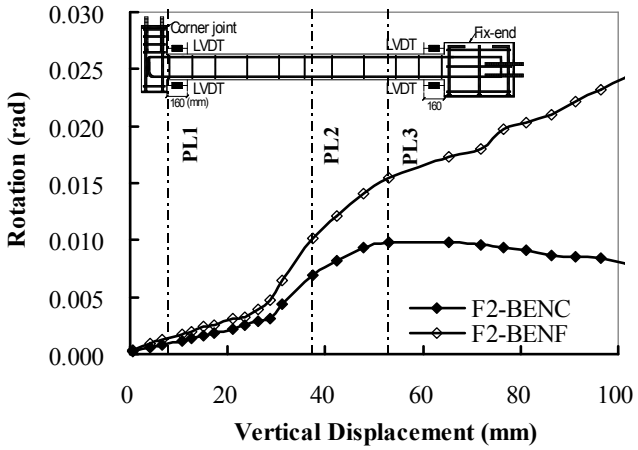

Fig. 4.11: The comparison of the rotation in the BENC with the rotation in the BENF of F2

4.3.5 Bending Moment-Displacement Relationship

Fig. 4.12 illustrates the bending moments in the beam fixed supports versus vertical displacement of F2. It can be seen from the figure that the maximum bending moment of 25.0 kN.m was obtained at a deflection of 91.4 mm in the longitudinal fixed support while the maximum bending moment of 24.9 kN.m was obtained at a deflection of 76.4 mm in the transverse beam. The bending moments measured in the transverse and longitudinal fixed supports began to decrease at the displacements of 167.6 mm and 157.4 mm, respectively. The calculated ultimate moment capacity of beam by including the material over-strength factors as provided in ASCE 41-06 [A4], was 24.4 kN.m. The measured plastic hinge's modeling parameters of this specimen were compared with the recommended parameters of DoD [D1] in **Table 4.3**.

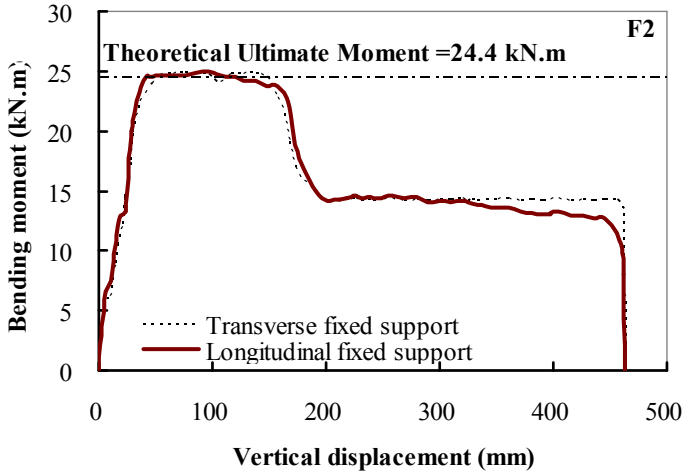

Fig. 4.12: Bending moment response in the fixed supports of F2

4.4 Test Results of the Modified Detailed Specimen F1

F1 was non-seismically detailed and had a small amount of transverse reinforcement ratio (0.23 %) in the potential plastic hinge zones of the beams. It was designed to investigate the influence of the transverse reinforcement ratio on the overall performance of the substructure against progressive collapse. The dimensions and reinforcement details are given in **Table 3.3**.

4.4.1 General Behavior

Under the applied load, the first crack was observed in the BENF at a load of 4.4 kN while the first crack occurred in the BENC at a load of 10.0 kN. At a load of 18.7 kN, first diagonal shear crack in the corner joint was observed. The flexural and shear cracks occurred in the joint and BENF became more severe with increasing vertical displacement. When the displacement reached 120.0 mm, concrete crushing was observed at the BENF while the concrete splitting occurred at the corner joint at a displacement of 220.0 mm. Further increasing the displacement, concrete crushing became more severe. Top rebar at the BENF fractured when the vertical displacement reached 438.0 mm and the test was terminated. **Fig. 4.13** shows the final crack pattern of the specimen after test. As shown in the figure, the dominating diagonal shear

cracking was observed in the BENFs. Simultaneously, severe diagonal shear cracks were also formed in the corner joint. Moreover, severe buckling of the compressive rebar was also observed at the bottom of BENFs.

4.4.2 Load-Displacement Relationship

The vertical load-displacement relationship of F1 is presented in **Fig. 4.14.** Similar to F3, initially, there was a linear relationship between the vertical displacement and the applied vertical load. However, at a load of 4.4 kN (PL1), the slope of the curve became milder although the relationship was still linear due to first crack forming in the BENFs. When the vertical displacement reached 29.4 mm (PL2), plastic hinges were formed in the BENFs. Further increasing the vertical displacement to 45.0 mm (PL3), the ultimate capacity of the specimen (23.7 kN) was achieved. The ultimate capacity dropped by 25 % when the displacement reached 81.4 mm (PL4). The axial forces in the longitudinal and transverse beams were monitored during the test. The measured maximum axial compressive and tensile forces in each load cell are given in **Table 4.1**. It should be noted that the tensile phase was found after the beam reached 251.0 mm and 321.0 mm (PL5) of the vertical displacement for the longitudinal and transverse beam, respectively. The load resistance rose gradually with increasing vertical displacement until the displacement reached 440.0 mm due to catenary action.

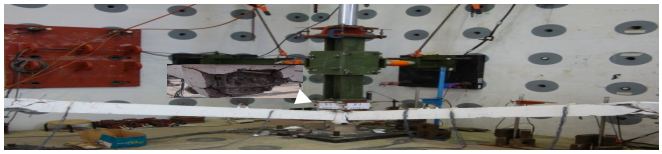

Fig. 4.13: Cracking patterns of F1 at failure

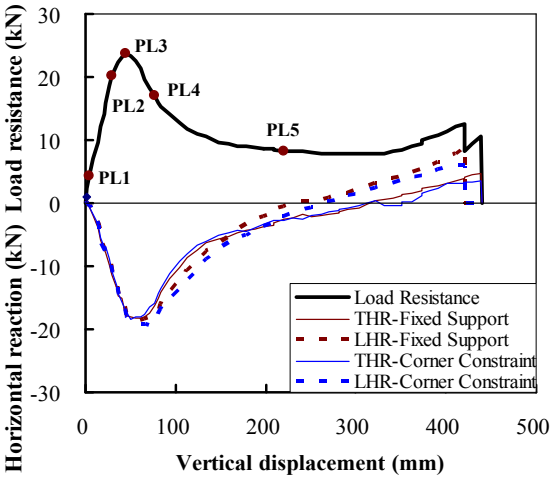

Fig. 4.14: Vertical and axial loads of F1

4.4.3 Strain Results

4.4.3.1 Strains in the Beam Reinforcing Bars

Fig. 4.15 presents the strain profile of the beam longitudinal reinforcement of F1 corresponding to different performance levels respectively. Similar to F3, the strains in the top longitudinal reinforcement at the BENF increased significantly while the strains in the top longitudinal reinforcement at the BENC started to decrease after PL3. Moreover, the inflection point (zero strain point) of both top and bottom longitudinal reinforcement was moving towards the corner joint after PL3 and this indicates that the resistance mechanism of specimen was changing to cantilever beam after severe failure occurred in the corner joint. The strain of bottom longitudinal reinforcement at the BENF yielded at PL4 while the strain of bottom longitudinal reinforcement at the BENC never yielded during the test.

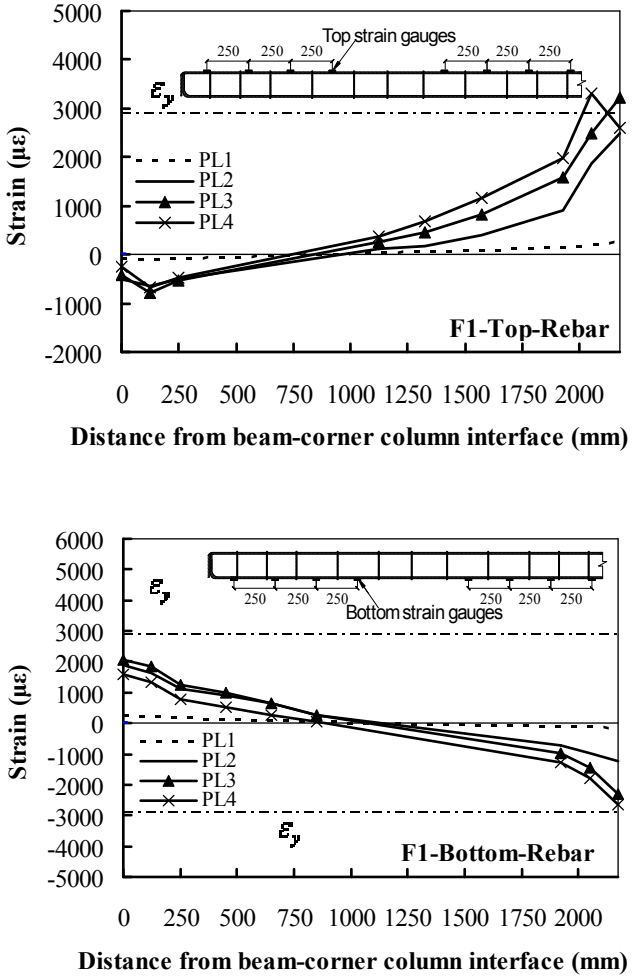

Fig. 4.15: Strain profile of beam longitudinal reinforcement of F1

4.4.3.2 Strains in the Column Reinforcing Bars

Fig. 4.16 illustrates the strain gauge results of the column longitudinal reinforcement of F1. Similar to F2, the strain results indicated that the corner column was elastic during the test. The maximum tensile strain in the column longitudinal reinforcement (1560 με) was measured by C1. However, the maximum compressive strain (-985με) was recorded in C4.

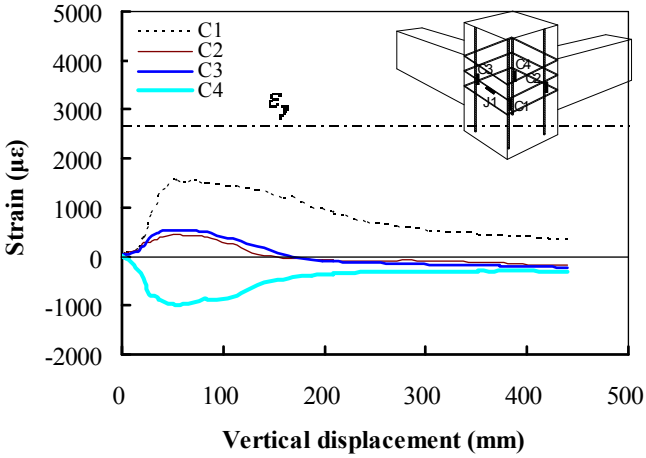

Fig. 4.16: Local strain in the column reinforcing bars of F1

4.4.4 Rotation Results

Fig. 4.17 illustrates the comparison of θ_2 with θ_1 of F1. Similar to F3, the rotations at both ends were limited before signs of cracks were observed in the beam (PL1). After PL1, the rotations at both ends increased significantly. However, the slope of θ_1 was much steeper than for θ_2. Moreover, θ_2 kept almost constant after PL3 while θ_1 increased with increasing vertical displacement. The constraint effective factor ξ was 0.73 and 0.68 at PL2 and PL3, respectively. The contribution of each factor resulting in the value of ξ less than 1 was shown in **Table 4.2.**

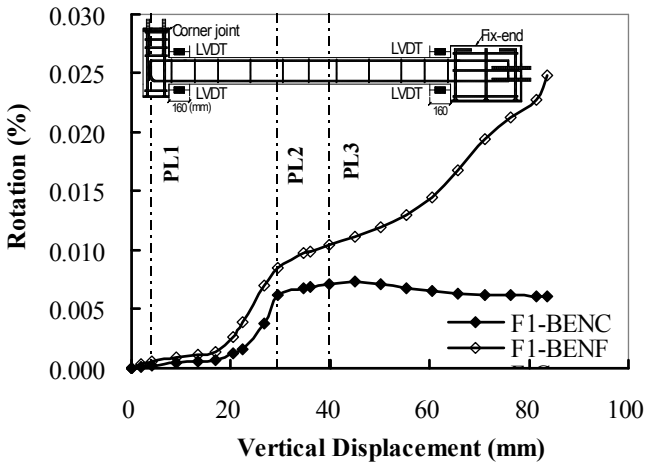

Fig. 4.17: The comparison of the rotation in the BENC with the rotation in the BENF of F1

4.4.5 Bending Moment-Displacement Relationship

Fig. 4.18 illustrates the bending moments in the beam fixed supports versus vertical displacement of F1. It can be seen from the figure that initially, the bending moments in both fixed supports were increasing with an increase in the vertical displacement. When the displacement reached 26.7 mm, the increase became gradual with increasing vertical displacement. The bending moments measured in the transverse and longitudinal fixed supports began to decrease at a displacement of 103.8 mm. This was possibly due to concrete crushing occurring in the BENF. However, when the displacement was further increased, the degradation of the bending moment in both fixed supports was relatively gradual. Significant decrease in the bending moment happened in the transverse and longitudinal fixed support when the displacement reached 421.0 mm and 438.4 mm, respectively. It should be noted that the maximum bending moment of 15.3 kN.m and 15.2 kN.m were obtained in the longitudinal and transverse fixed support at a deflection of 60.6 mm. Similar to F3, the displacement in accordance with the ultimate bending moment did not coincide with the displacement corresponding to the ultimate capacity of the specimen. Moreover, the theoretical ultimate bending moment capacity of the beam by including the material over-strength factors as suggested in ASCE 41-06 [A4] was 16.6 kN.m. The modeling parameters measured for each beam of the tested specimens were compared with the recommended parameters in DoD [D1] (**Table 4.3**). Further discussion for this comparison is presented in the **Section 4.9**.

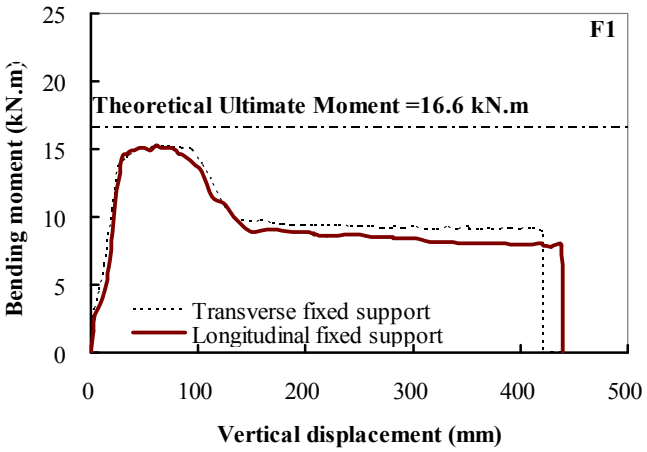

Fig. 4.18: Bending moment response in the fixed supports of F1

4.5 Test Results of Modified Detailed Specimen F4

F4 was non-seismically detailed and had a high amount of beam transverse reinforcement (0.72 %) at the beam potential plastic hinge zone. Similar to F1, F4 was designed to investigate the effect of transverse reinforcement ratio in the beam potential plastic hinge zone on the overall performance of RC frame against progressive collapse.

4.5.1 General Behavior

The general behavior of the specimen was based on the crack pattern development observed during the test. Under the applied load, the first crack was observed at the BENF at a load of 6.0 kN while the first crack occurred in the BENC at a load of 14.0 kN. Following the first crack, joint shear cracks were observed at a load of 18.0 kN while the plastic hinges formed at the BENFs at a load of 23.2 kN. Compared to F3, limited shear cracks were formed in the beam of F4. When the displacement reached 140.0 mm, concrete crushing was observed in the BENF while concrete splitting occurred in the corner joint at a displacement of 200.0 mm. With further increase in displacement, the concrete crushing became more severe. Top rebar at the BENF fractured when the vertical displacement reached 406.5 mm and the test was terminated. **Fig. 4.19** shows the failure mode of F4. As displayed in the figure, extremely wide cracks occurred in the BENFs. However, the beam shear cracks and buckling of the compressive reinforcing bars in the BENFs were limited compared to F3.

4.5.2 Load-Displacement Relationship

The load-displacement relationship of F4 is presented in **Fig. 4.20**. It can be seen that initially, when the specimen reached its yield strength of 23.2 kN (PL2), a large increase in displacement occurred with a limited rise in loading. Moreover, the strength of the specimen began to decrease after reaching its ultimate capacity of 27.5 kN due to severe damage occurring in the corner joint panel and compression

crushing occurring at the BENF. When the displacement reached 347.0 mm, the load resistance suddenly dropped with the rupture of one of the longitudinal reinforcements at the BENF. Then, the resistant capacity kept further increasing until both top reinforcements were ruptured. The measured maximum axial compressive and tensile forces by horizontal load cells are given in **Table 4.1**. It should be noted that the tensile phase was found after the specimen reached the vertical displacement of 317.1 mm and 327.8 mm (PL5) in the longitudinal and transverse beam, respectively.

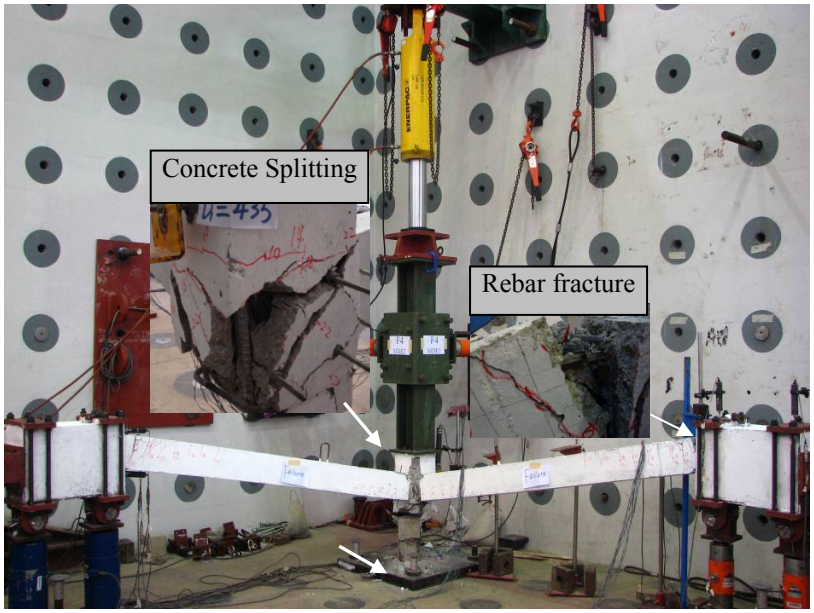

Fig. 4.19: Cracking patterns of F4 at failure

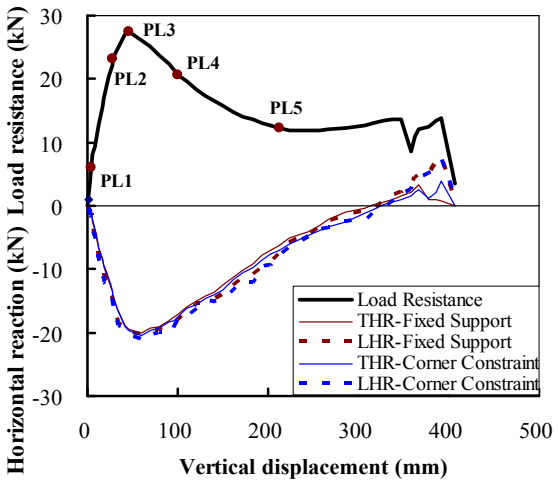

Fig. 4.20: Vertical and axial loads of F4

4.5.3 Strain Results

4.5.3.1 Strains in the Beam Reinforcing Bars

Fig. 4.21 illustrates the strain profile of the beam longitudinal reinforcement of F4 corresponding to different performance levels respectively. Similar to F3, the strains of the top longitudinal reinforcement at the BENF significantly increased while the strains of the top longitudinal reinforcement at the BENC started to decrease after PL3. Moreover, the inflection point (zero strain point) of both top and bottom longitudinal reinforcement was moving towards the corner joint after PL3 and this indicated that the resistance mechanism of specimen was changing to cantilever beam after severe failure occurred in the corner joint. The strain of bottom longitudinal reinforcement at the BENF yielded at PL4 while the strain of bottom longitudinal reinforcement at the BENC never yielded during the test.

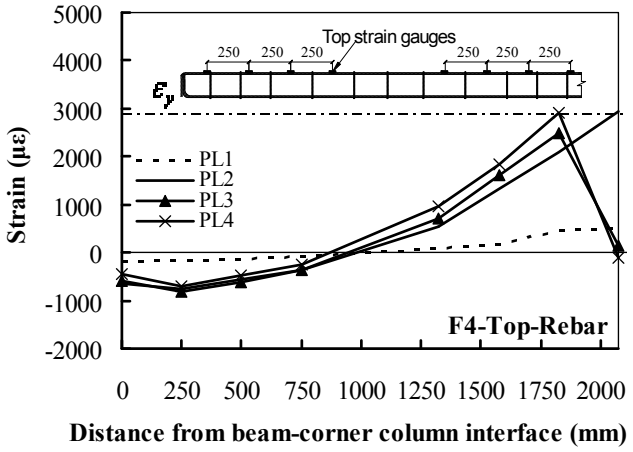

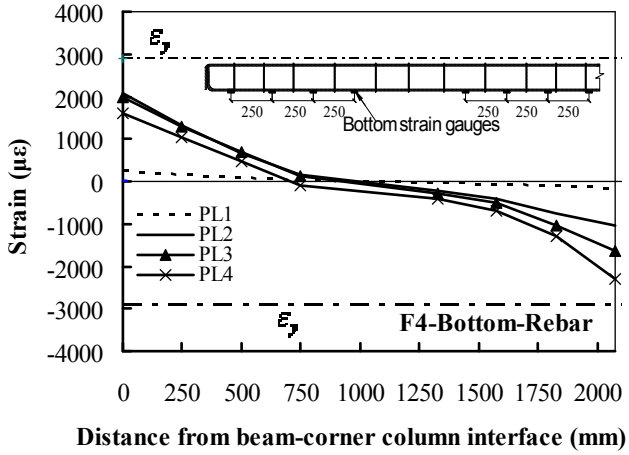

Fig. 4.21: Strain profile of the beam longitudinal reinforcement of F4

4.5.4 Rotation Results

Fig. 4.22 illustrates the comparison of the rotation at the BENC with the rotation in the BENF of F4. Similar to F3, limited rotation was observed for both θ_1 and θ_2 before PL1. However, the rotations in both ends obviously increased after PL2. The constraint effective factor ξ was about 0.70 and 0.64 at PL2 and PL3, respectively. The contribution of each factor resulting in the value of ξ less than 1 was shown in **Table 4.2.**

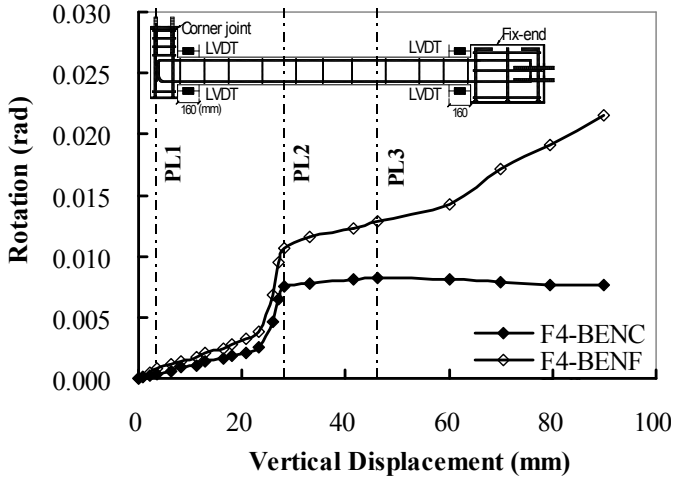

Fig. 4.22: The comparison of the rotation in the BENC with the rotation in the BENF of F4

4.5.5 Bending Moment-Displacement Relationship

Fig. 4.23 illustrates the beam bending moments in the beam fixed supports versus vertical displacement of F4. It can be seen from the figure that the transverse beam yielded and lost its resistant capacity earlier than the longitudinal beam. However, both beams kept increasing the deflections until they reached their ultimate moment capacities. The ultimate moment capacity in the longitudinal and transverse support was 16.5 kN.m and 17.1 kN.m, respectively. The calculated ultimate moment capacity of beam by including the material over-strength factors as provided in ASCE 41-06 [A4] was 16.6 kN.m. The measured plastic hinge's modeling parameters of this specimen were compared with the ones provided in DoD [D1] in **Table 4.3**.

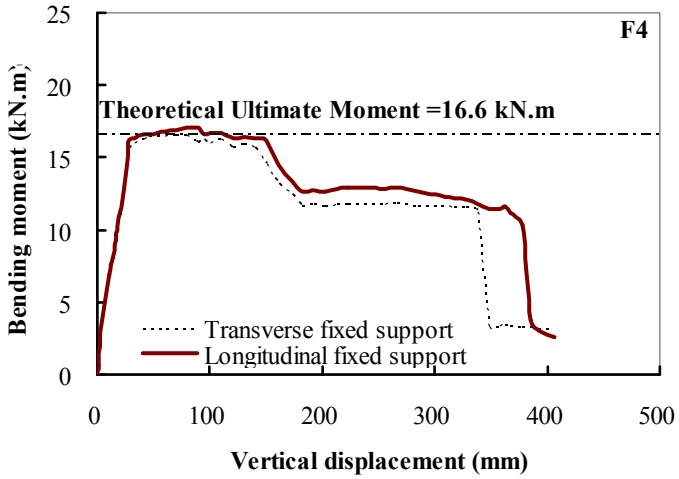

Fig. 4.23: Bending moment response in the fixed supports of F4

4.6 Test Results of the Long Span Specimen F5

F5 was a non-seismically detailed specimen. It had a longer design span length than that of F3. The dimensions and reinforcement details are given in **Table 3.3**. This specimen was designed and tested to investigate the influence of the span length on the performance of RC frame to resist progressive collapse.

4.6.1 General Behavior

Under the applied load, the first crack was observed at the BENF at a load of 6.3 kN (PL1) while the first crack occurred in the BENC at a load of 10.0 kN. At a load of 14.3 kN, diagonal shear cracks formed in the corner joint. The plastic hinges occurred in the BENFs at a load of 25.2 kN. The flexural cracks became wider and inclined with an increase in the vertical displacement. When the displacement reached 100.0 mm, concrete splitting was observed in the corner joint. Concrete cover began to crush at a displacement of 180.0 mm. However, crushing was limited compared with F3 and the core concrete was almost intact during the test. Top rebar at the transverse BENF fractured when the vertical displacement reached 403.0 mm and subsequently, the top rebar at the longitudinal BENF was fractured and the test was terminated.

Fig. 4.24 presents the failure mode of F5 after the test. As illustrated in **Fig. 4.24**, severe flexural cracks were observed in the BENFs. Although diagonal shear cracks were formed in the final load stages, they were limited compared to F3. Another notable difference in the failure mode between F5 and F3 was that relatively limited concrete crushing observed in the BENFs of F5.

4.6.2 Load-Displacement Relationship

The load-displacement relationship of F5 is presented in **Fig. 4.25**. It can be seen that initially, there was a slightly linear relationship between the vertical displacement of corner column and the applied vertical load. However, at a load of 6.3 kN (PL1), the slope of the curve became milder although the relationship was still linear. When the steel began to yield at a loading of 25.2 kN (PL2), a large increase in displacement in accordance with a limited increase in loading. After reaching ultimate capacity of this specimen (26.8 kN), the strength began to decrease rapidly due to severe damage occurring in the corner joint panel and compression crushing occurring in the BENFs. When the displacement reached 403.0 mm, the strength of the system was significantly decreased due to longitudinal reinforcement fracturing in the transverse BENF. The resistant capacity was lost completely and the test was terminated at a displacement of 438.9 mm due to the rebar in both BENFs being fractured. The

measured maximum axial compressive and tensile forces by horizontal load cells are given in **Table 4.1**. It should be noted that the tensile phase was found after the beam reached the vertical displacement of 342.9 mm.

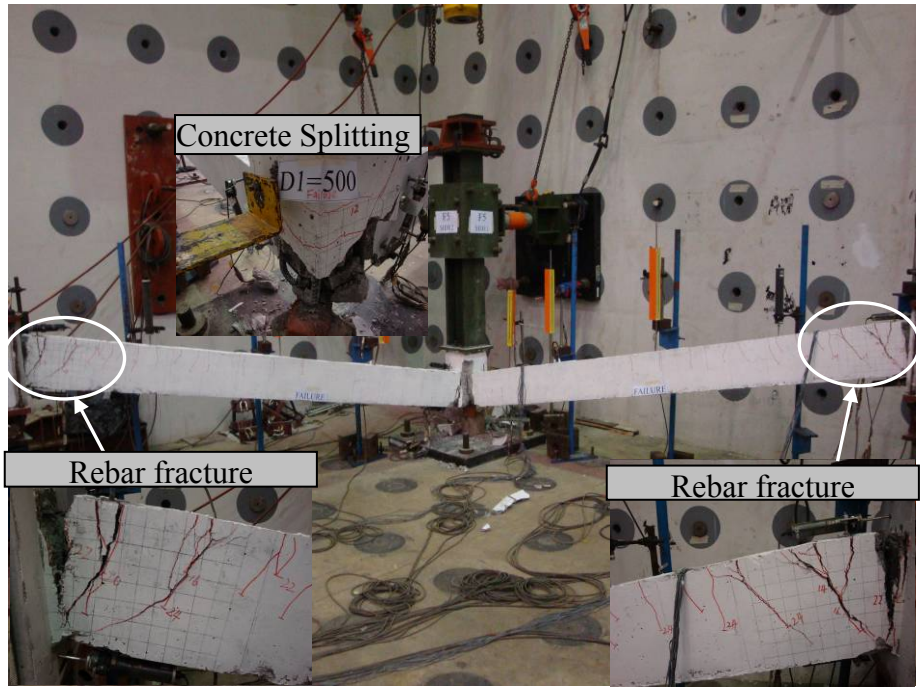

Fig. 4.24: Cracking patterns of F5 at failure

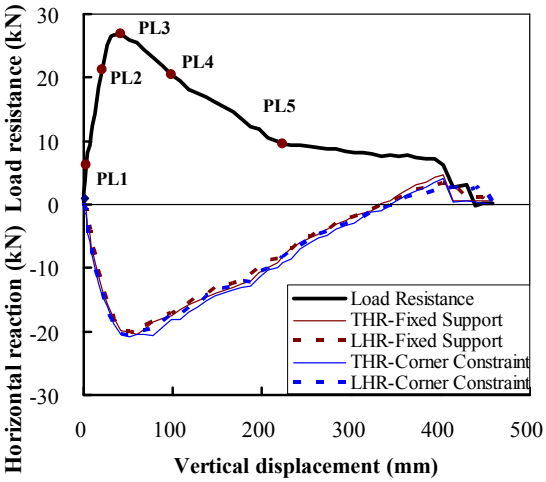

Fig. 4.25: Vertical and axial loads of F5

4.6.3 Strain Results

4.6.3.1 Strains in the Beam Reinforcing Bars

Fig. 4.26 illustrates the strain profile of the beam longitudinal reinforcement of F5 corresponding to different performance levels respectively. Similar to F3, the strains of the top longitudinal reinforcements at the BENF significantly increased while the strains of the top longitudinal reinforcements at the BENC started to decrease after PL3. Similarly, the inflection point (zero strain point) in the longitudinal reinforcement moved towards the corner joint after PL3 and this indicates that the resistance mechanism of the specimen was changing to that of a cantilever beam after severe failure occurred in the corner joint. The bottom longitudinal reinforcement at the BENF yielded at PL4 while the strain of bottom longitudinal reinforcement at the BENC never yielded during the test.

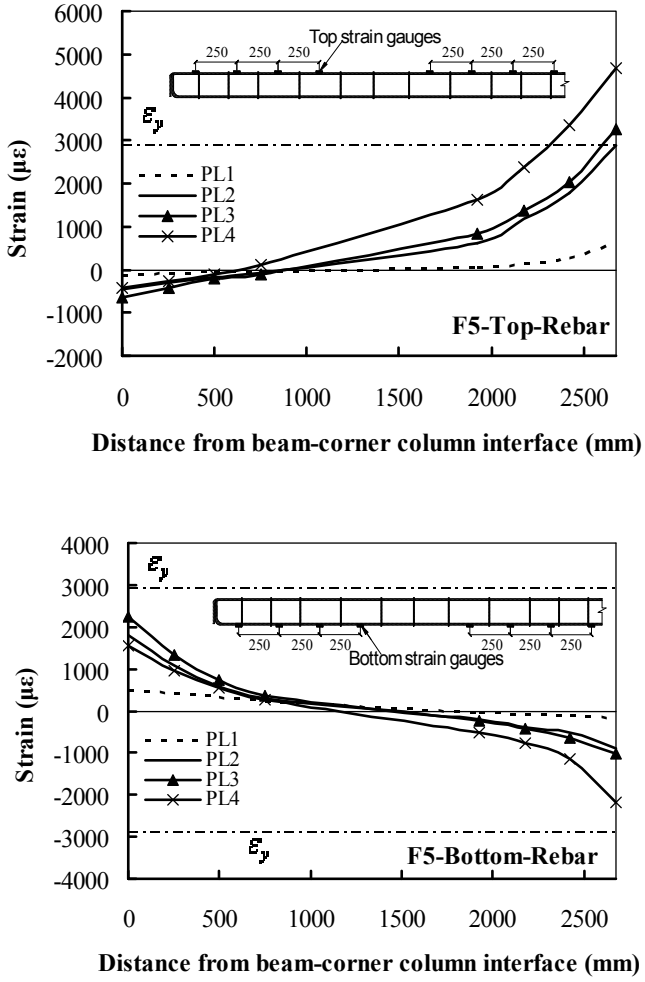

Fig. 4.26: Strain profile of the beam longitudinal reinforcement of F5

4.6.4 Rotation Results

Fig. 4.27 illustrates the comparison of θ_1 with θ_2 of F5. In general, the rotation response was similar to that of F3. The constraint effective factor ξ was about 0.69 and 0.66 at PL2 and PL3, respectively. As the rotation of the plastic hinges at BENC and BENF were not measured completely, no decomposition of the contribution of each factor affecting the value of ξ less than 1 was analyzed.

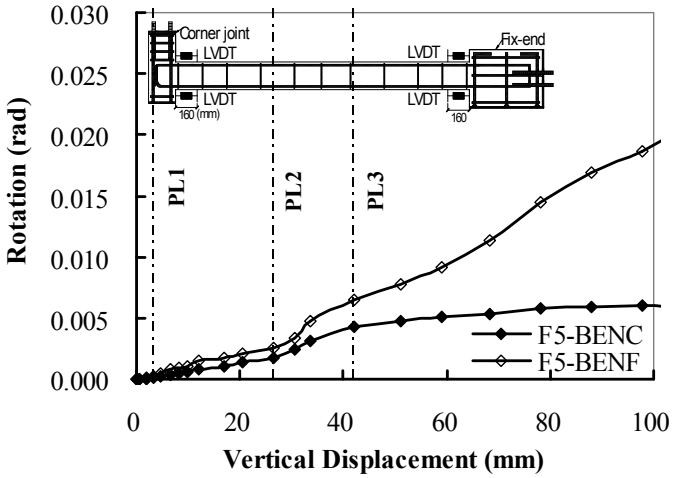

Fig. 4.27: The comparison of the rotation in the BENC with the rotation in the BENF of F5

4.6.5 Bending Moment-Displacement Relationship

Fig. 4.28 illustrates the beam bending moments in the beam fixed support versus vertical displacement of F5. As can be seen from the figure, the bending moment response measured in the longitudinal support was similar to that measured in the transverse support. The ultimate moment capacities measured in the longitudinal and transverse beams were 21.6 kN.m and 20.8 kN.m, respectively. The theoretical ultimate moment capacity of the beam by including the material over-strength factors as provided in ASCE 41-06 [A4] was 23.4 kN.m. Furthermore, the measured plastic hinge's modeling parameters of this specimen were compared with the ones provided in DoD [D1] in **Table 4.3**.

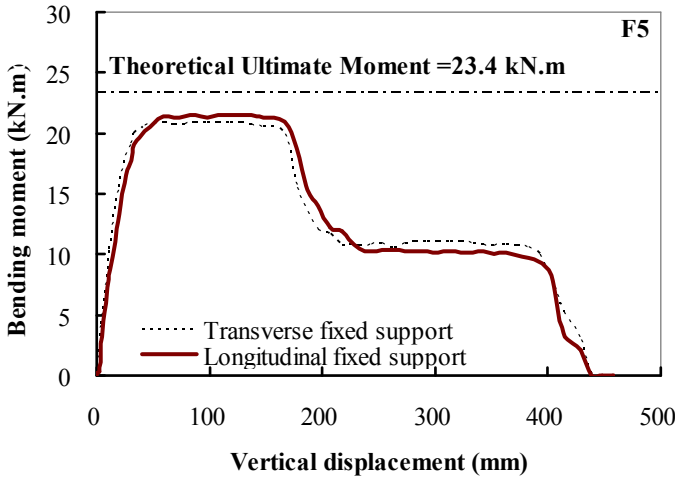

Fig. 4.28: Bending moment response in the fixed support of F5

4.7 Test Results of the Unequal Span Specimen F6

F6 was a non-seismically detailed specimen. It had unequal spans in the longitudinal and transverse directions. The dimensions and reinforcement details are given in **Table 3.3**. This specimen was designed and tested to investigate the effect of span aspect ratio on the performance of RC frame to resist progressive collapse.

4.7.1 General Behavior

For F6, the crack developments in the longitudinal and transverse beams were distinctly different and need to be described separately. The first cracks were observed in the transverse and longitudinal beams at the loads of 5.9 kN and 10.0 kN, respectively. Moreover, the first flexural cracks occurred in the transverse and longitudinal BENC at the loads of 10.0 kN and 20.0 kN, respectively. Asymmetrical joint shear cracks were observed. First joint shear cracks occurred in the joint face along the transverse direction at a load of 17.8 kN while the shear cracks occurring in the joint face along the longitudinal direction were at a load of 19.6 kN. Though the cracks in the joint along the longitudinal direction occurred later than the ones along the transverse direction, the development of the cracks in the longitudinal direction was faster. The ultimate capacity of F6 was at a load of 26.0 kN. With a further

increase in the vertical displacement by 120.0 mm, concrete crushing was observed in the transverse BENF while the bottom compression region of the longitudinal beam was intact. Concrete crushing was first observed in the longitudinal beam at a deflection of 200.0 mm. The failure mode of F6 is presented in **Fig. 4.29.**

4.7.2 Load-Displacement Relationship

The load-displacement relationship of F6 is presented in **Fig. 4.30**. It can be seen that initially, there was a slightly linear relationship between the vertical displacement and the applied vertical load. However, at a load of 5.9 kN (PL1), the slope of the curve reduced slightly although the relationship was still linear. When the steel began to yield at a loading of 21.5 kN (PL2), a large increase in displacement occurred with a limited further increase in loading. When the loading reached 26.0 kN, the strength of the system began to decrease more rapidly due to severe damage happening in the corner joint panel. Similar to F5, no secondary ascending stage was observed in the curve. However, the slope of the decreasing resistance became much milder after the displacement exceeded 205.0 mm. The measured maximum axial compressive and tensile forces by horizontal load cells are given in **Table 4.1**. It should be noted that the tensile phase was found after the beam reached the vertical displacement of 355.2 mm and 314.6 mm for the longitudinal and transverse beam, respectively.

Fig. 4.29: Cracking patterns of F6 at failure

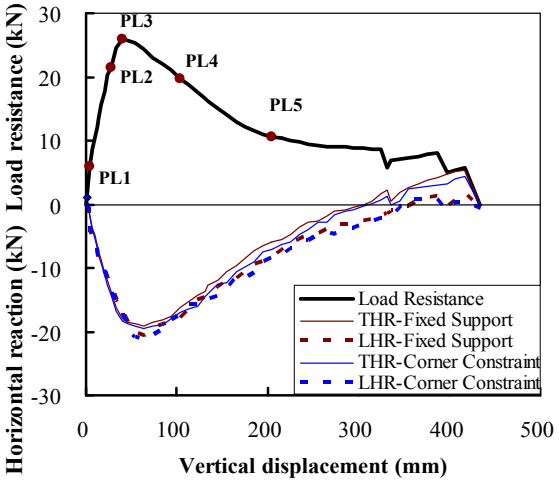

Fig. 4.30: Vertical and axial loads of F6

4.7.3 Strain Results

4.7.3.1 Strains in the Beam Reinforcing Bars

Fig. 4.31 illustrates the strain profile of the beam reinforcement of F6 corresponding to different performance levels respectively. As illustrated in the figure, the first yield of the reinforcement was observed in the transverse BENF. It can be explained that the same vertical displacement in the corner joint will result in larger rotation happened in the transverse BENC due to shorter span in this beam. For the same reason, the damage accumulated in the transverse beam was more rapidly than that in the longitudinal beam. As seen from the figure, it can be found that the force resistant mechanism in the transverse beam mainly relied on the cantilever beam mechanism after PL4 while Vierendeel action still dominated in longitudinal beam after that performance level. Furthermore, the reinforcement in the longitudinal BENF began to yield until PL4, which was after severe damage had occurred in the transverse beam.

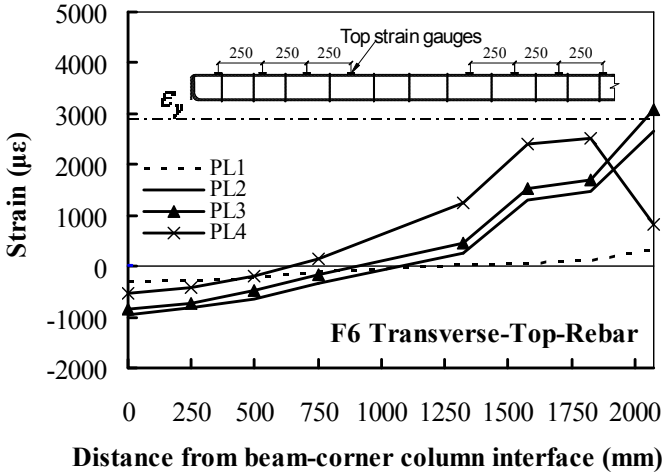
Top strain gauges
250 250 250 250 250 250
ε_y
PL1
PL2
PL3
PL4
Strain (με)
F6 Transverse-Top-Rebar
5000
4000
3000
2000
1000
0
-1000
-2000
0 250 500 750 1000 1250 1500 1750 2000
Distance from beam-corner column interface (mm)

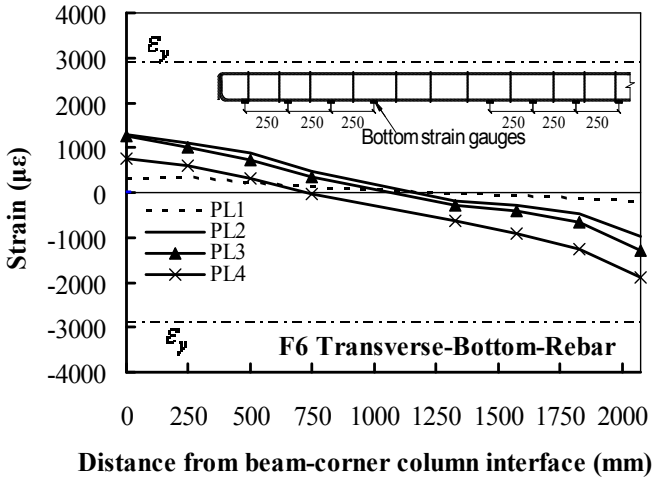
ε_y
250 250 250 250 250 250
Bottom strain gauges
PL1
PL2
PL3
PL4
Strain (με)
F6 Transverse-Bottom-Rebar
4000
3000
2000
1000
0
-1000
-2000
-3000
-4000
0 250 500 750 1000 1250 1500 1750 2000
Distance from beam-corner column interface (mm)

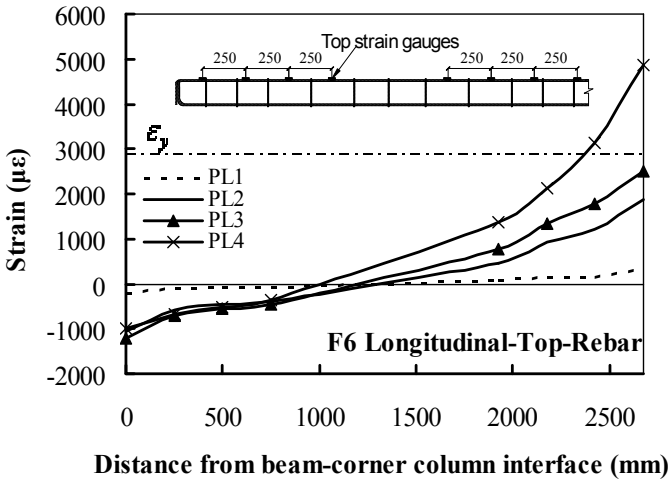
Top strain gauges
250 250 250 250 250 250
ε_y
PL1
PL2
PL3
PL4
Strain (με)
F6 Longitudinal-Top-Rebar
6000
5000
4000
3000
2000
1000
0
-1000
-2000
0 500 1000 1500 2000 2500
Distance from beam-corner column interface (mm)

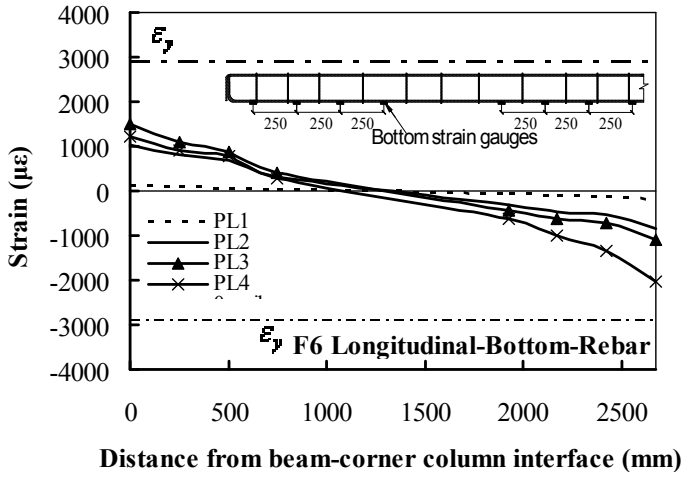

Fig. 4.31: Strain profile of the beam longitudinal reinforcement of F6

4.7.4 Rotation Results

Due to unequal span in the longitudinal and transverse directions in F6, the rotation results of both beams were presented in **Fig. 4.32**. As illustrated in the figure that the rotation in the transverse BENC (θ_1) and BENF (θ_2) of F6 significantly increased after PL2 while the rotation in the longitudinal BENC (θ_1) and BENF (θ_2) considerably increased after PL4. This was consistent with the strain gauge results. For the transverse beam, the value of ξ was about 0.69 and 0.65 at PL2 and PL3, respectively. However, for the longitudinal beam, ξ was about 0.66 and 0.63 at PL2 and PL3, respectively. Moreover, when the displacement reached 39.9 mm, which corresponded to the ultimate capacity of F6, the rotation of the transverse BENC and BENF was 0.0115 rad and 0.0166 rad, respectively. However, the rotation of the longitudinal BENC and BENF was only 0.0044 rad and 0.0073 rad, respectively. The rotation in the longitudinal beam was much less than the rotation in the transverse beam because of longer span in the longitudinal beam and the measuring of the rotations in the BENC and BENF were not completely in longitudinal beam.

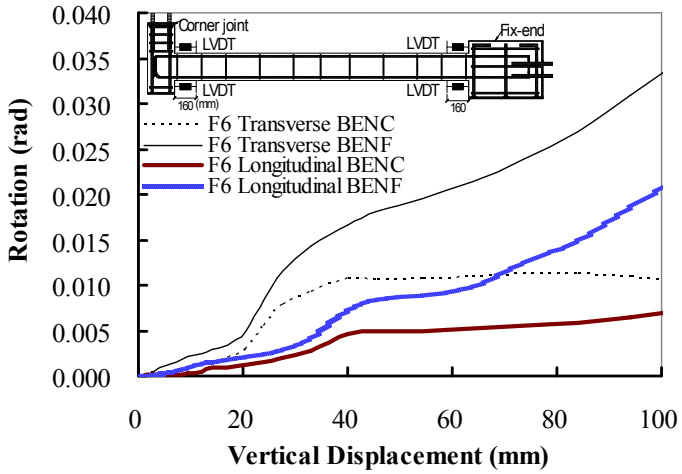

Fig. 4.32: The comparison of the rotation in the BENC with the rotation in the BENF of F6

4.7.5 Bending Moment-Displacement Relationship

Fig. 4.33 illustrates the beam bending moments of the fixed supports versus vertical displacement of F6. The moment-displacement curves in the transverse and longitudinal fixed support were different from F6. The measured ultimate moment capacities in the longitudinal and transverse BENF were 16.4 kN.m and 23.6 kN.m, respectively. However, the theoretical ultimate moment capacity of the beams by including the material over-strength factors as provided in ASCE 41-06 [A4] were 16.6 kN.m and 23.4 kN.m, respectively. The measured plastic hinge's parameters of this specimen were compared with the recommended modeling parameters of DoD [D1] in **Table 4.3**.

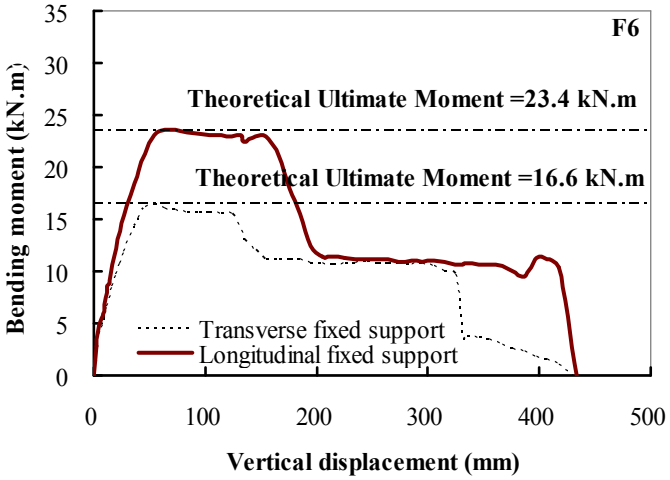

Fig. 4.33: Bending moment response in the fixed supports of F6

4.8 Test Results of Unequal Span Specimen F7

F7 was similar to F6 except for the beam depth of the longitudinal beam. The depth in the longitudinal beam of F6 was 240.0 mm while it was 210.0 mm in F7. The dimensions and reinforcement details are given in **Table 3.3**. This specimen was designed and tested to investigate the effect of stiffness ratio of the longitudinal beam to the transverse beam on the force redistribution of the substructures for progressive collapse.

4.8.1 General Behavior

Under the applied load, the first crack was observed at the longitudinal BENF at a load of 3.9 kN (PL1) while the first crack occurred at the transverse BENC at a load of 10.0 kN. At the same time, the joint shear cracks and flexural cracks in the BENCs also formed. The crack patterns development and strain gauge results recorded in F6 indicated that the transverse beam was damaged before the longitudinal beam. However, the performance of F7 was different and the crack patterns indicated that these two beams worked simultaneously. Concrete crushing was observed in the longitudinal and transverse BENF at the displacements of 130.0 mm and 160.0 mm, respectively. It should be emphasized that the concrete crushing in the stiffer transverse beam deteriorated more rapidly than that in the longitudinal beam. The top

rebar in the transverse and longitudinal BENF began to fracture at the displacements of 340.0 mm and 436.0 mm, respectively. **Fig. 4.34** presents the failure mode of F7.

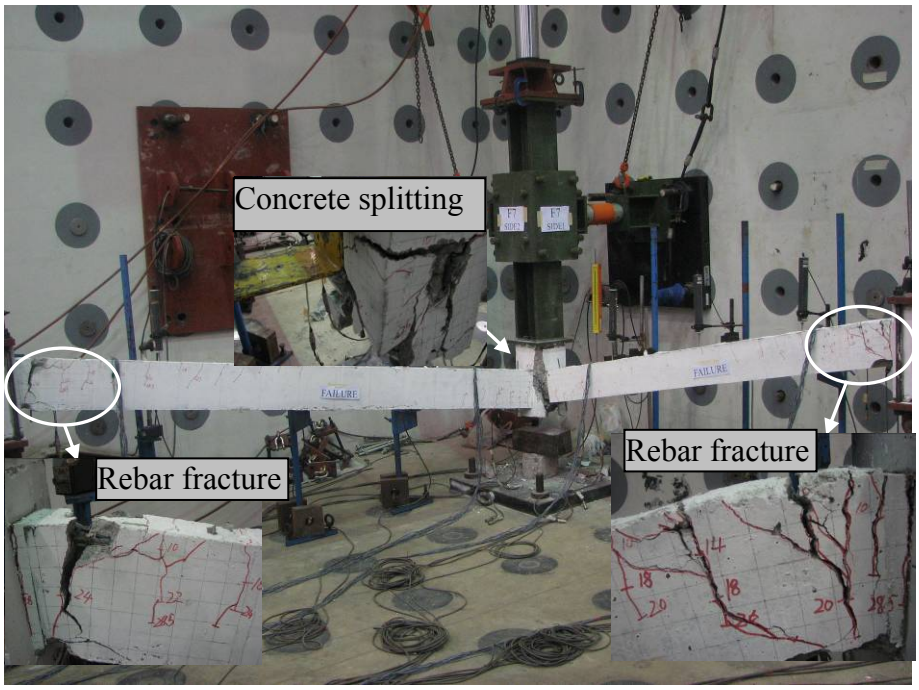

Fig. 4.34: Cracking patterns of F7 at failure

4.8.2 Load-Displacement Relationship

The vertical load-displacement relationship of F7 is presented in **Fig. 4.35**. It can be seen that initially, there was a slightly linear relationship between the vertical displacement of corner column and the applied vertical load. However, at a load of 3.9 kN (PL1), the slope of the curve reduced although the relationship was still linear. When the steel began to yield at a load of 21.0 kN (PL2), a large increase in the displacement occurred with a limited increase in the load. After reaching the ultimate capacity of the specimen (23.0 kN), the resistance of the specimen began to decrease. However, the slope of the decrease of the resistance became much milder when the displacement reached 208.0 mm although no re-ascending branch was observed in the load-displacement curve.

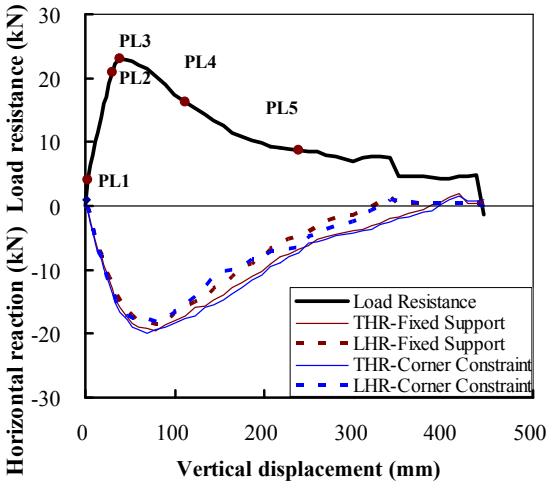

Fig. 4.35: Vertical and axial loads of F7

4.8.3 Strain Results

4.8.3.1 Strains in the Beam Reinforcing Bars

Fig. 4.36 illustrates the strain profile of the beam longitudinal reinforcement of F7 corresponding to the different performance levels. In contrast to F6, the first yield of the beam longitudinal reinforcement was observed in the longitudinal BENF of F7. In PL4, Vierendeel action still provided significant contribution to the load resistance of both beams.

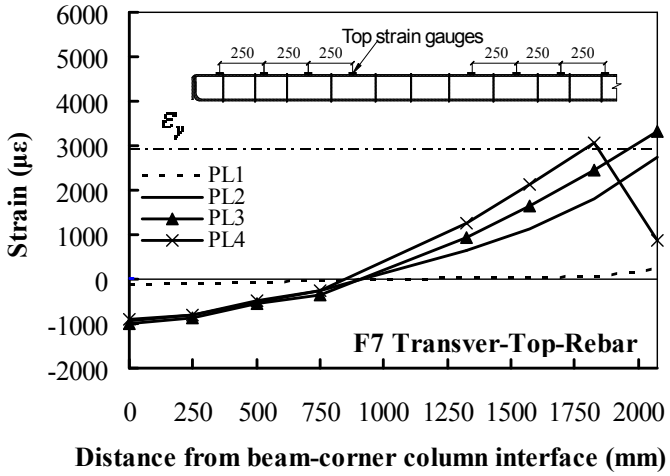

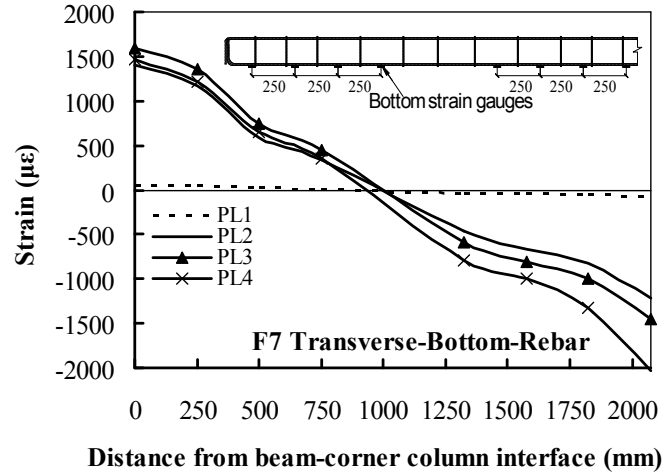

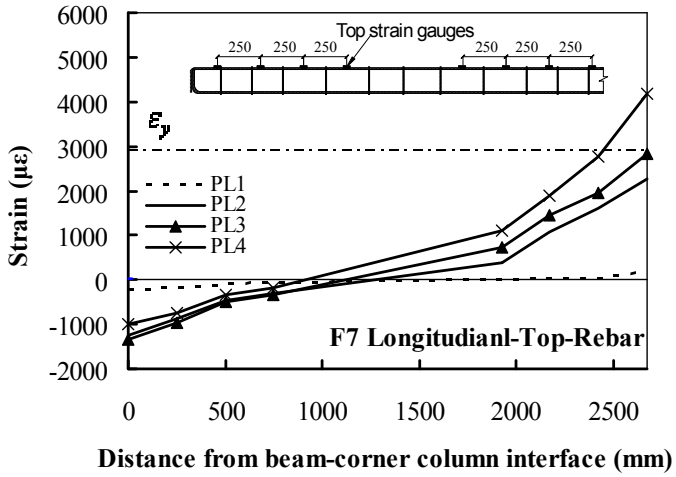

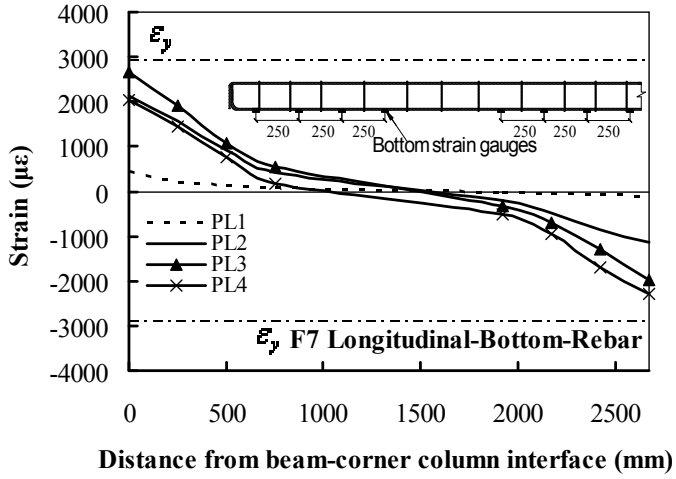

Fig. 4.36: Strain profile of the beam longitudinal reinforcement of F7

4.8.4 Rotation Results

Fig. 4.37 illustrates the comparison of θ_1 with θ_2 of F7. In general, the rotation result of F7 was similar to F6. For transverse beam, the value of ξ was about 0.67 and 0.64 at PL2 and PL3, respectively. For longitudinal beam, ξ was about 0.70 and 0.64 at PL2 and PL3, respectively. The value of θ_1 and θ_2 in the transverse beam at a vertical displacement of 38.9 mm (PL3) were 0.0093 rad and 0.0145 rad. However, the value of θ_1 and θ_2 in the longitudinal beam were 0.0035 rad and 0.0055 rad, respectively. As explained for F6, a smaller value of θ_1 was measured in the longitudinal beam compared with that in the transverse beam due to incomplete plastic hinge rotation was measured and longer span in the longitudinal beam of F7.

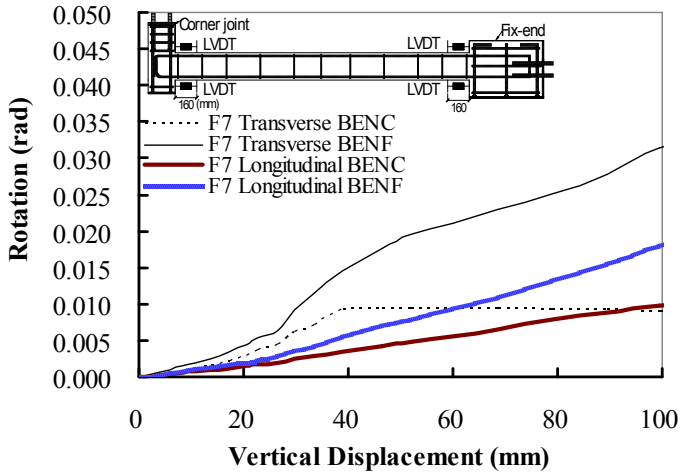

Fig. 4.37: The comparison of the rotation in the BENC with the rotation in the BENF of F7

4.8.5 Bending Moment-Displacement Relationship

Fig. 4.38 illustrates the beam bending moments of the beam fixed supports versus vertical displacement of F7. The moment-displacement curve in the transverse and longitudinal fixed support was different due to the beams had different cross-sections. The measured ultimate moment capacities of the longitudinal and transverse beam were 16.7 kN.m and 18.7 kN.m, respectively. However, the theoretical ultimate moment capacity of the beam by including the material over-strength factors as provided in ASCE 41-06 [A4] were 16.6 kN.m and 20.0 kN.m, respectively. The measured plastic hinge parameters of this specimen were compared with the recommended modeling parameters of DoD [D1] in **Table 4.3**.

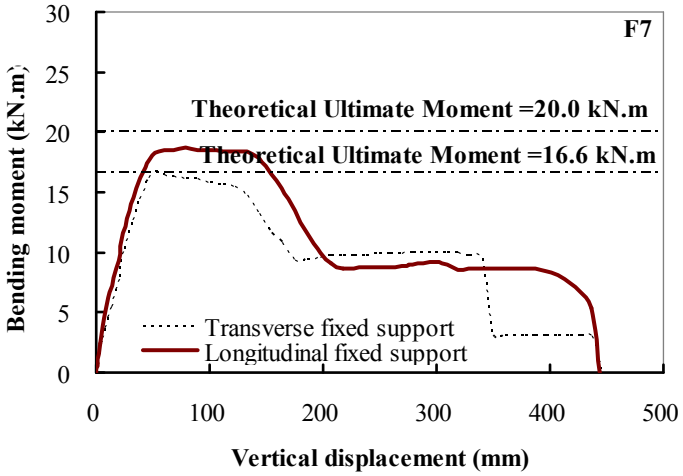

Fig. 4.38: Bending moment response in the fixed supports of F7

4.9 Discussion

4.9.1 Tie Strength Method Proposed in DoD [D1]

The design guideline DoD [D1] was just updated recently by implementing a number of significant improvements. One of the significant modifications in the updated DoD [D1] was that horizontal tie forces (internal and peripheral) are no longer permitted to be concentrated in the beams, girders and spandrels unless the designer can show that these members are capable of carrying the tensile loads while undergoing large rotations (0.2 rad). As shown in the **Table 4.4**, the final rotation for the majority of the beams in the test specimens was close to 0.2 rad. Thus, the beams can be utilized (instead of the floor system) to carry the required peripheral tie strength. The required peripheral tie strength F_p (kN) is:

$$F_p = 6 w_F L_1 L_p \qquad (5\text{-}1)$$

As shown in **Table 4.5**, the top rebar in the beam section could provide enough tie force to satisfy the required peripheral tie strength in accordance with DoD [D1]. However, the measured maximum tie force was significantly less than the required peripheral tie strength due to partial rotation constraint in the corner joint and the limited horizontal constraint provided in the corner joint. Thus, using the tie strength

method to resist progressive collapse for RC frames caused by losing a corner column is extremely unsafe, especially for precast structures with inadequate beam-slab connections.

Table 4.4: Summary of the Test Results

Test	First yield load (kN)	Ultimate load Pcu, (kN)	MCHR in Beam-T (kN)	MCHR in Beam-L (kN)	MBM in Beam-T (kN.m)	TMBM in Beam-T (kN.m)	MBM in Beam-L (kN.m)	TMBM in Beam-L (kN.m)	Measured Rotation of Beam-T at FF (rad)	Measured Rotation of Beam-L at FF (rad)
F1	20.1	23.7	18.3	18.6	15.2	16.6	15.3	16.6	0.199	0.194
F2	29.1	36.5	27.3	27.9	24.8	25.6	25.0	25.6	0.209	0.201
F3	22.5	25.8	19.6	19.8	15.7	16.6	15.9	16.6	0.208	0.199
F4	23.2	27.5	20.2	20.7	16.5	16.6	17.1	16.6	0.187	0.180
F5	25.2	26.8	20.5	20.3	20.8	23.5	21.6	23.5	0.164	0.173
F6	21.5	26.0	19.3	20.9	16.4	16.6	23.6	23.5	0.197	0.155
F7	21.0	23.0	19.6	18.4	16.7	16.6	18.7	20.0	0.201	0.159

Note: MCHR= Maximum Compressive Horizontal Reaction; MBM=Maximum Bending Moment
MBM, TMBM=Maximum Bending Moment and Theoretical Maximum Bending Moment, respectively
Beam-T=Transverse Beam; Beam-L=Longitudinal Beam
NF= Normal Failure stage defined as the resistance decreased to 75% of the ultimate capacity
FF= Final Failure stage defined as totally lose the resistance capacity

Table 4.5: Comparison of the Measured Tie Force with the Requirement Tie Force Determined Based on DoD [D1]

Test	RTTB (kN)	RTLB (kN)	ATTB (kN)	ATLB (kN)	MTTB (kN)	MTLB (kN)
F1	55.7	55.7	72.2	72.2	8.3	8.8
F2	55.7	55.7	122.1	122.1	11.1	11.3
F3	55.7	55.7	72.2	72.2	7.9	7.5
F4	55.7	55.7	72.2	72.2	7.5	7.5
F5	69.7	69.7	72.2	72.2	4.3	3.1
F6	55.7	69.7	72.2	72.2	6.9	1.1
F7	55.7	69.7	72.2	72.2	1.7	1.3

Note: RTTB, RTLB= Required Tie Force in the Transverse Beam and Longitudinal Beam, respectively
ATTB, ATLB= Allowable Tie Force in the Transverse Beam and Longitudinal Beam, respectively
MTTB, MTLB= Measured Tie Force in the Transverse Beam and Longitudinal Beam, respectively

4.9.2 Modeling Parameters of the Plastic Hinge Provided in DoD [D1]

The current version of DoD [D1] adopts the modeling parameters for beam plastic hinges from ASCE 41-06 [A4]. The modeling parameters measured from each beam of the tested specimens were compared with the recommended parameters in DoD [D1]. As illustrated in **Table 4.3,** the measured value of parameter "a" was close to the value provided in DoD [D1]. However, the provided values of parameters "b" and

"c" in DoD [D1] were extremely conservative. This was possibly due to the recommended parameters in ASCE 41-06 [A4] being based on seismic tests where the measured parameters were through quasi-static test in the current study. The definitions of the parameters of "a", "b" and "c" are shown in **Fig. 4.39**.

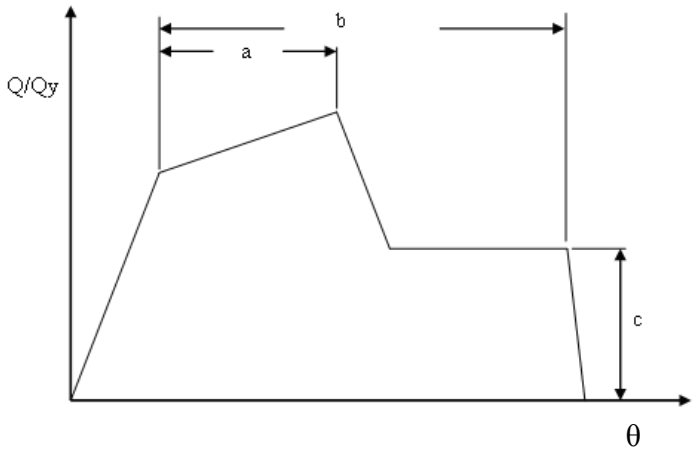

Fig. 4.39: Generalized plastic hinge model

4.10 Summary

This chapter compared the experimental results obtained from the quasi-static tests in terms of cracking patterns, load-displacement curves and local strain results. The measured tie force and plastic hinge parameters were compared with the recommended parameters recommended in DoD [D1]. Based on the above comparisons as well as the test results reported in **Chapter 4**, the following conclusions can be drawn:

1. Specimens with seismic detailing (F2) saw a 41.5% increase in ultimate resistant capacity compared to those with non-seismically detailed (F3). The behavior improved mainly due to higher longitudinal reinforcement ratio in the beam, which increased the flexural capacity of the beam section. Moreover, medium amount of transverse reinforcement placed in the corner joint region allowed plastic hinges to develop in the beam end adjacent to the corner joint.

2. As the transverse beam reinforcement ratio in the potential plastic hinge zone

was increased from 0.23 % (F1) to 0.31 % (F3), the load capacity was enhanced by about 8.9 %. This is due to shear failure that occurred in the plastic hinge zone which reduced the effectiveness of compressive arch action and resulted in a lower ultimate resistant capacity. However, when the transverse reinforcement ratio was increased from 0.31 % (F3) to 0.72 % (F4), the vertical load resistance of the tested specimen was only enhanced by a further 6.5 %. This indicated that the effect of the transverse reinforcement ratio in the potential plastic hinge zone for ultimate capacity is limited as long as the shear failure is not severe in the plastic hinge zone.

3. F5 reached an ultimate capacity of 26.8 kN while the design axial force of the corner column is 29.1 kN. Thus, F5 will totally collapse even if the dynamic increase factor is 1.0. This confirmed that specimens with longer design spans are more vulnerable than specimens with shorter design span when they under similar distributed load.

4. The plastic hinge properties of RC elements suggested in DoD [D1] are adoption of the modeling parameters presented in ASCE 41-06 [A4]. The accuracy of these parameters was evaluated by comparing them with the parameters obtained from the current tests. In general, the recommended value for parameter “a” in DoD [D1] is reasonable if the beam section is controlled by flexural failure while it is too conservative if the beam section is controlled by the composite flexural and shear failure. However, the recommended values for parameters “b” and “c” in DoD [D1] are extremely conservative. Further studies are needed to evaluate the accuracy of these modeling parameters.

5. Although DoD [D1] has implemented significant modifications for tie strength design, no difference was proposed between the peripheral tie nearby the corner column and the tie nearby the exterior column in DoD [D1]. As illustrated in the test results, the allowable tie strength determined based on the reinforcement details was larger than the required tie strength based on DoD [D1]. However, the measured horizontal tensile force (tie force) was

significantly less than the allowable DoD [D1] tie strength due to insufficient of the horizontal constraint provided by the corner joint. Thus, it is suggested that catenary effect (tie strength method) is not considered in practical design for building to resist progressive collapse caused by losing one of the ground corner columns especially for precast structures with inadequate beam-slab connections.

6. Test results indicated that there are two ways to improve the performance of RC frames against progressive collapse caused by loss corner columns: firstly, by increasing the flexural capacity of the beam section by amplifying the beam longitudinal reinforcement ratio for new buildings or by externally bonded composite materials (such as fiber-reinforced polymer) along the beam length for existing buildings. Secondly, upgrade the shear strength of the corner joint by installing more joint transverse reinforcement for new buildings or by externally wrapping composite materials (such as fiber-reinforced polymer) to confine the corner joint for existing buildings. It should be emphasized that failure due to rebar anchorage and splicing is beyond the scope of this study.

CHAPTER 5

ANALYTICAL PREDICTION OF THE LOAD DISPLACEMENT CURVES OF THE SPECIMENS UNDER QUASI-STATIC TESTS

5.1 Introduction

Few experimental research studies have been carried out on RC frames in resisting progressive collapse. These studies have been reviewed in **Chapter 2**. The quasi-static performance of seven RC substructures under the loss of a corner column is reported in **Chapter 4**.

This chapter is devoted towards developing a simple model to predict the load-displacement curves of the test substructures. This chapter comprises two parts. In the first part, the proposed analytical method was validated by comparing its results with the measured load-displacement curves. In the second part, a parametric study was conducted to improve the understanding of the effects of the various critical parameters on the load-displacement curve.

5.2 Proposed Method to Establish Load-Displacement Curve of RC Substructure to Resist Progressive Collapse

Fig. 5.1 presents a typical load-displacement curve of a special RC substructure. There are five control points (A, B, C, D and E in **Fig. 5.1**) and 10 key values ($F_y, \Delta_y, F_u, \Delta_u, F_{NF}, \Delta_{NF}, F_t, \Delta_t, F_{FF}, \Delta_{FF}$), where F_y and Δ_y are the yield strength and yield displacement, respectively; F_u and Δ_u are the ultimate strength and corresponding displacement, respectively; F_{NF} and Δ_{NF} are the load resistance and displacement at normal failure stage, which corresponds to a 25 % reduction in the

ultimate capacity on the descending branch of the load-displacement curve; F_t and Δ_t are the load resistance and displacement at the stage of which the catenary action began; F_{FF} and Δ_{FF} are the load resistance and displacement at the final failure stage, which is defined as the point when the load resistance totally vanishes. In the following sections, the analytical prediction of each key value is individually presented.

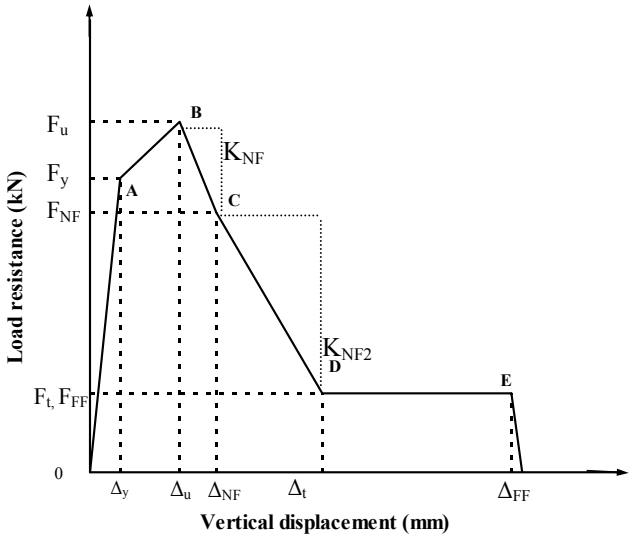

Fig. 5.1: Typical load-displacement curve

5.2.1 Ultimate Capacity F_u

The load-displacement curve of test specimens indicated that catenary action was negligible for substructures to resist progressive collapse caused by losing a ground corner column. Therefore, the first ultimate capacity of the structure became extremely important for the structure in resisting progressive collapse. Some of the previous researchers (Tan *et al*. [T1]) have predicted the capacity of the substructures by assuming the beam as a cantilever beam while others (Sun and Xu [S6]) assumed full rotational constraint at the beam end near the corner joint (BENC). The results of Sasani *et al*. [S1] and Mohamed [M2] indicated that significant positive moment exists in the BENC and thus, assuming the beam as a cantilever beam can prove to be overly conservative. On the other hand, if full rotational constraint was applied to the corner joint, the resistance mechanism was similar to the structures subjected to the

loss of an interior column and resulted in overestimation of the ultimate capacity. The extent of the rotational constraints in the corner joint is related to the ratio of the rotation in the BENC to the rotation in the BENF (ξ) (see **Chapter 4**). ξ is named as the rotational constraint effectiveness factor. The mean values of the measured ξ in each beam of the test specimens in PL2 and PL3 were about 0.70 and 0.65, respectively (please refer to **Chapter 4**). In order to accurately predict the ultimate capacity of the substructures, a design strategy is proposed in the current analytical study.

The main steps are clarified as follows:

Step 1: A plastic hinge formed in the BENF when the substructures reached ultimate capacity. The material over-strength factors as provided in ASCE 41-06 [A4] (1.25 for reinforcing bars and 1.5 for concrete) were used to determine the ultimate bending moment at the BENF M_u.

Step 2: The interaction of the joint shear strength with the bending moment capacity of the beam determined whether the bottom longitudinal reinforcement in the BENC would yield. A solution strategy was proposed to calculate the allowable bending moment capacity in the BENC. The detailed derivation of the solution strategy is illustrated in the next section.

Step 3: The ultimate capacity of the specimen can be determined by Eq. (5-1), which was derived based on the virtual work method by assuming that the rotation at the BENC was ξ times of the rotation in the BENF.

$$F_u^{predicted} = \frac{\xi M_a + M_u}{l_n} \qquad (5\text{-}1)$$

where $F_u^{predicted}$ is the predicted ultimate strength of the substructures; M_a is the allowable moment in the BENC; M_u is the ultimate bending moment in the BENF; and l_n is the clear span of the beam

The value of ξ was selected as 0.65 based on the test results. The predicted results were compared to the experimental results in **Table 5.1.** As indicated in **Table 5.1**, the cantilever model ($\xi = 0.0$) noticeably underestimated the ultimate capacity while the full constraint model ($\xi = 1.0$) consistently overestimated the ultimate capacity. Although the proposed partial constraint model ($\xi = 0.65$) still gave a slight underestimation of the ultimate capacity, especially for F4, the proposed model generally predicted the capacity of substructures to a greater degree of accuracy compared to the other two models. The differences between the measured and predicted results were possibly due to the compressive arch action which was not considered in the theoretical model. As presented in **Chapter 4**, significant compressive beam axial force was observed in the results of the horizontal reaction forces. This indicated that compressive arch action was developed in the beams to resist the vertical load. However, the analytical analysis proposed above did not include the effects of the compressive arch action for conservative consideration.

Table 5.1: Comparison of the Predicted Ultimate Capacity with the Experimental Results

Specimen	F1	F2	F3	F4	F5	F6	F7	Mean	COV (%)
$F_u^{measured}$ (kN)	23.7	36.5	25.8	27.5	26.8	26.0	23.0		
$F_u^{cantilever}$ (kN)	15.3	23.0	15.3	15.3	16.9	16.1	14.8		
$F_u^{partial}$ (kN)	22.6	35.1	22.6	22.6	24.0	23.2	21.7		
F_u^{full} (kN)	30.5	46.0	30.5	30.5	33.7	32.2	29.7		
$F_u^{cantilever} / F_u^{measured}$	0.64	0.63	0.59	0.56	0.63	0.62	0.65	0.62	5.3
$F_u^{partial} / F_u^{measured}$	0.95	0.96	0.87	0.82	0.89	0.89	0.95	0.91	5.6
$F_u^{full} / F_u^{measured}$	1.29	1.26	1.18	1.11	1.26	1.24	1.29	1.23	5.3

Note: $F_u^{measured}$ = Measured ultimate capacity

$F_u^{partial}$ = Predicted ultimate capacity by proposed partial constraint model ($\xi = 0.65$)

$F_u^{cantilever}$ = Predicted ultimate capacity by cantilever model ($\xi = 0.0$)

F_u^{full} = Predicted ultimate capacity by full constraint model ($\xi = 1.0$)

5.2.1.1 Joint Shear Strength

As mentioned in the above section, the allowable bending moment in the BENC, M_a is dependent on the interaction between the shear strength of the corner joint and the

bending moment capacity of the beam. Thus, the shear strength of the corner joint should be clarified before one tries to predict the ultimate capacity of the specimen.

In the present study, a three-dimensional (3D) corner joint was subjected to special load conditions after losing a ground corner column. The performance and load path of the corner joint was similar to a 3D inverted knee joint in closing action. Normal shear strength predictions, such as Bakir and Boduroglu [B1], were not suitable for this study and as such, a strut-and-tie model was utilized to predict the shear strength of the joint. A 2D model was established instead of a 3D model due to the analytical complexity of the 3D model and 2D planes were utilized in practice. The 2D joint in the transverse direction was presented for symmetrical specimens F1, F2, F3, F4 and F5 while the 2D joint in both longitudinal and transverse directions was presented for asymmetrical specimens F6 and F7.

As shown in the **Fig. 5.2**, a positive bending moment was observed in the BENC due to Vierendeel action. The crack pattern indicated that a diagonal strut formed to resist the joint shear force for non-seismically detailed specimens. For seismically detailed specimen F2, joint transverse reinforcement was installed in the joint region and was able to provide additional shear resistance. **Fig. 5.3** illustrates the external force applied on the joint and internal force flow of the typical non-seismically detailed corner joint.

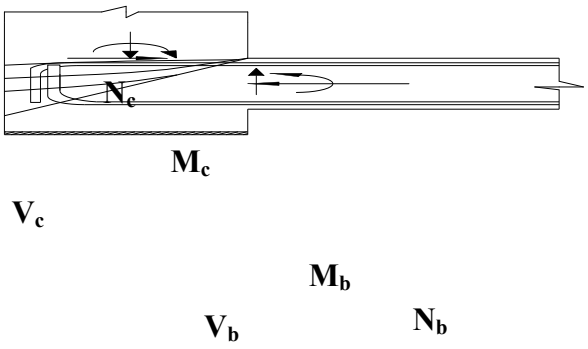

Fig. 5.2: The external forces applied on the corner joint

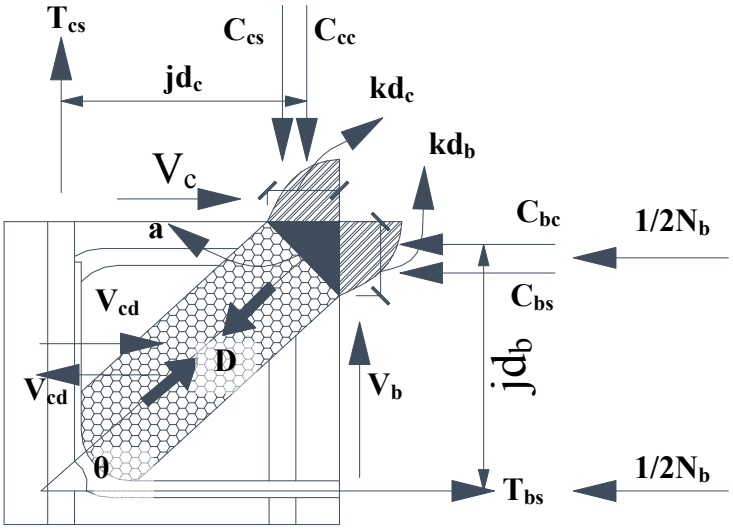

Fig. 5.3: The strut-and-tie model utilized to display the resistant mechanism of the corner joint

The equations to determine the joint shear strength capacity of non-seismically detailed specimens were derived as follows:

$$V_{jd} = V_{cd} = C_{bc} + C_{bs} + \frac{1}{2}N_b - V_c = T_{bs} - \frac{1}{2}N_b \qquad (5\text{-}2)$$

where V_{jd} is the total joint shear strength; V_{cd} is the design shear force resistance of concrete in a joint; C_{bc} is the compression force of beam concrete; C_{bs} is the compression force of beam reinforcement; V_c is the shear force in the upper column, T_{bs} is the tensile force in the beam longitudinal reinforcement; N_b is the beam axial force.

$$N_b = V_c \qquad (5\text{-}3)$$

$$T_{bs} = D \times \cos\theta \qquad (5\text{-}4)$$

where D is the compression force of the joint diagonal strut; θ is the angle between the beam axial and the strut center line.

$$\cos\theta = \frac{jd_c}{\sqrt{jd_c^{\,2} + jd_b^{\,2}}} \qquad (5\text{-}5)$$

where jd_c is the distance from the centroid of compressive forces in the steel and concrete to the centroid of tension of column section; jd_b is the distance from the centroid of compressive forces in the steel and concrete to the centroid of tension of beam section.

$$D = \nu f_c' b_{eff} a \qquad (5\text{-}6)$$

where ν is the compressive effectiveness strength factor that is less than unity, 0.34 was suggested in Schlaich *et al.* [S7]; b_{eff} is the average of the beam and column width; a is the strut width.

$$a = \sqrt{(kd_c)^2 + (kd_b)^2} \qquad (5\text{-}7)$$

where kd_b is the neutral axial depth of beam section; kd_c is the neutral axial depth of column section.

For seismically detailed specimens, joint transverse reinforcements were installed in the joint region. Thus, the joint shear strength consisted of two components: shear strength provided by joint transverse reinforcement V_{sd}, and shear strength provided by concrete strut V_{cd}. The transverse reinforcement within the corner joint was assumed to serve a dual role in resisting the shear force and maintaining the strength of the diagonal compressive strut by passively confining the joint core concrete. The shear force resisted by the joint transverse reinforcement was taken as Bakir and Boduroglu [B1].

$$V_{jd} = V_{cd} + V_{sd} \qquad (5\text{-}8)$$

where V_{sd} is the shear force resistance provided by joint transverse reinforcement.

$$V_{sd} = 0.664 A_{js} f_{yv} \qquad (5\text{-}9)$$

where A_{js} is the total area of the horizontal transverse reinforcement crossing the diagonal plane from corner to corner of the joint between the beam compression and tension reinforcement; f_{yv} is the tensile strength of the transverse reinforcement.

As shown in Eqs. 5-5 and 5-7, the shear strength of the joint was related to jd_c, jd_b, kd_c and kd_c. However, jd_c, jd_b, kd_c and kd_c were also dependent on the allowable bending moment in the BENC (M_a). As shown in **Fig. 5.4**, a solution strategy (trial and error method) was proposed to predict the shear strength of the corner joint and to determine M_a. **Table 5.2** shows the predicted and measured shear strength of each specimen. For symmetrical Specimens F1, F2, F3, F4 and F5, only the joint in 2D transverse frame was presented. For asymmetrical Specimens F6 and F7, the joint in both 2D frames were given. The ratio of $V_j^{measured} / V_j^{predicted}$ in **Table 5.2** indicated that the proposed equations can accurately predict the shear strength of the corner joint after losing one of the corner columns, especially for the specimens with symmetric beams (F1, F2, F3, F4, and F5). For the specimens with asymmetric beams, especially for F6, the agreement was not very well. This was possibly due to the interaction of the compressive struts along the deep beam and flat beam affected their shear resistances. For F2, due to the joint shear transverse reinforcement that could provide additional shear resistance, failure occurred only after the formation of plastic hinges in the BENC.

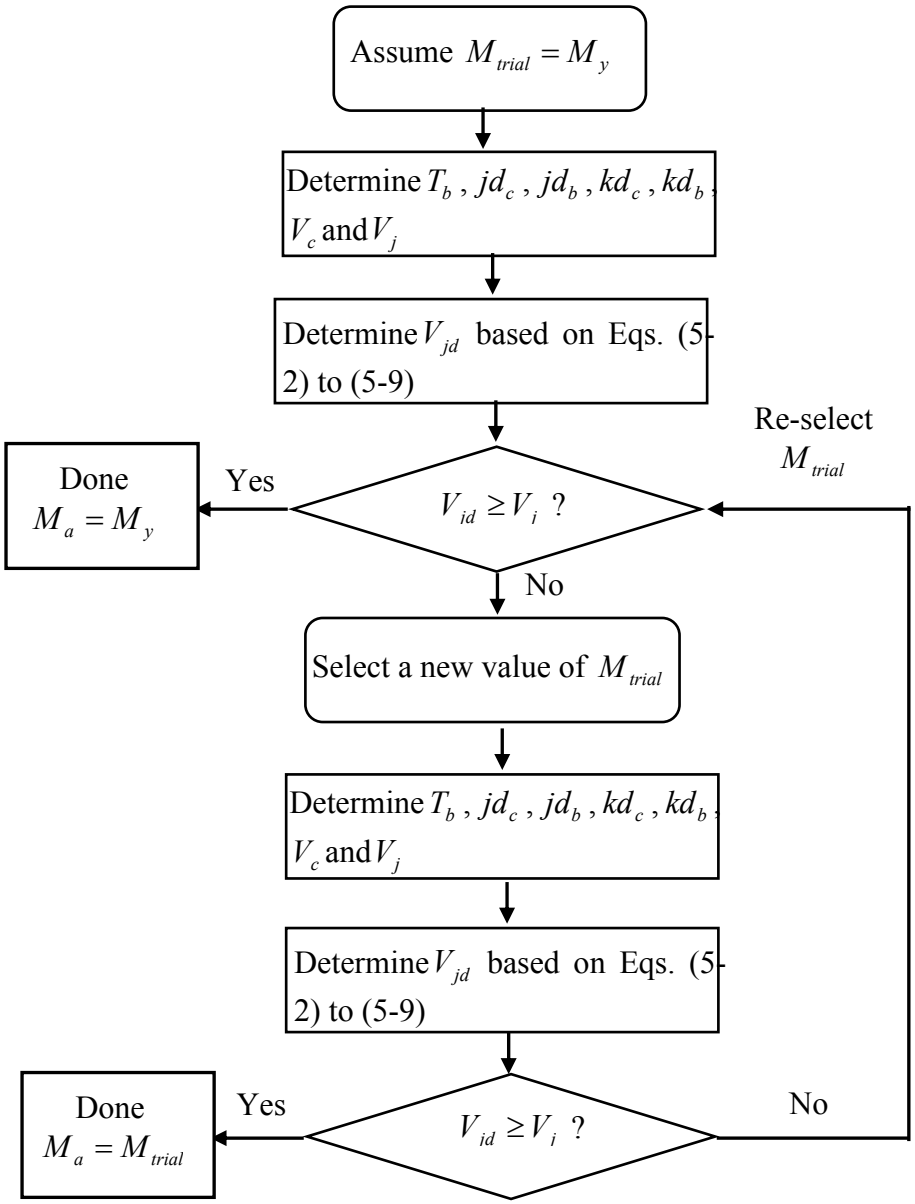

Fig. 5.4: The solution strategy to predict the joint shear strength and allowable bending moment in the BENC

Table 5.2: Comparison of the Predicted Joint Shear Strength with the Experimental Results

Specimen	F1-T	F2-T	F3-T	F4-T	F5-T	F6-T	F6-L	F7-T	F7-L
$V_j^{measured}$ (kN)	68.9	134.6	73.6	64.7	62.9	32.7	38.2	41.8	75.4
$V_j^{predicted}$ (kN)	76.5	135.9	76.5	76.5	64.9	76.5	64.9	76.5	71.3
$\frac{V_j^{measured}}{V_j^{predicted}}$	0.90	0.99	0.96	0.85	0.97	0.43	0.59	0.55	1.06

Note: $V_j^{measured}$ = Measured joint shear strength;

$V_j^{predicted}$ = Predicted joint shear strength

$$V_j^{measured} = A_l \varepsilon_s^m E_s - \frac{1}{2} N_b^m \qquad (5\text{-}10)$$

where A_l is the total area of bottom longitudinal reinforcement at the BENC; ε_s^m is the measured tensile strain of the bottom longitudinal reinforcement at the BENV at PL3; N_b^m is the measured axial force applied on the beam at PL3.

5.2.2 Yield Strength (F_y)

Similar to determine the ultimate capacity of specimens, the yield strength of the test specimen was derived based on the virtual work method by assuming the rotation at the BENC was ξ times of the rotation at the BENF. The value of ξ was 0.70 in the yield strength prediction based on the test results (introduced in **Chapter 4**).

$$F_y^{predicted} = \frac{\xi M_a + M_y}{l_n} \qquad (5\text{-}11)$$

where $F_y^{predicted}$ is the predicted yield strength.

Table 5.3 presents the comparison of the analytical results with the test results. Similar to the prediction of ultimate capacity, the cantilever model significantly underestimated the yield strength. However, both models managed to predict the yield strength very well. The proposed partial constraint model was utilized in this analytical study as the full constraint model ($\xi = 1.0$) slightly overestimate the test results.

Table 5.3: Comparison of the Predicted Yield Strength with the Experimental Results

Specimen	F1	F2	F3	F4	F5	F6	F7	Mean	COV (%)
$F_y^{measured}$ (kN)	20.1	29.1	22.5	23.2	25.2	21.5	21.0		
$F_y^{cantilever}$ (kN)	12.2	18.6	12.2	12.2	13.5	12.9	11.9		
$F_y^{partial}$ (kN)	20.1	31.6	20.1	20.1	21.1	20.6	19.3		
F_y^{full} (kN)	24.5	37.1	24.5	24.5	27.0	25.7	23.8		
$F_y^{cantilever} / F_y^{measured}$	0.61	0.64	0.54	0.53	0.53	0.60	0.57	0.57	7.3
$F_y^{partial} / F_y^{measured}$	1.00	1.09	0.89	0.87	0.84	0.96	0.92	0.94	9.1
$F_y^{full} / F_y^{measured}$	1.22	1.28	1.09	1.05	1.07	1.20	1.13	1.15	7.3

Note: $F_y^{measured}$ = Measured yield strength

$F_y^{partial}$ = Predicted yield strength by proposed partial constraint model ($\xi = 0.70$)

$F_y^{cantilever}$ = Predicted yield strength by cantilever model ($\xi = 0.0$)

F_y^{full} = Predicted yield strength by full constraint model ($\xi = 1.0$)

5.2.3 Yield Displacement (Δ_y)

5.2.3.1 Introduction

The boundary and load conditions of RC frames changed after the removal of one of corner columns on the ground floor. The first yield strength and ultimate capacity could be attained by the proposed analytical models introduced in the above sections. However, the first yield displacement is as important as the yield strength as it is related to the stiffness of the specimen. However, there is no existing model that can predict the yield displacement of a RC substructure after losing a corner column.

This section is devoted to develop a simple model to estimate the yield displacements of the RC frames, with different detailing, after the removal of the corner column. The applicability and accuracy of the proposed model is verified by comparisons with the test results.

5.2.3.2 Typical Failure Mode of the Test Specimens

As observed in the crack pattern development, flexural cracks initially occurred in the BENF and BENC as the specimen was loaded to PL1. In the subsequent loading to PL2, more flexural cracks developed at both ends. No new cracks formed in the BENC while cracks in the BENF further propagated after PL3. When the specimen was loaded to PL5, the existing flexural cracks in the BENF opened up and penetrated the whole depth of the beam. A typical crack pattern of the beam in a test specimen is presented in **Fig. 5.5**. Moreover, the observed crack pattern development indicated that a positive moment (tensile strain developed in the bottom rebar) formed in the BENC after removal of the corner column. However, this positive moment began to decrease after PL2. The sketch of the varying of the bending moments in accordance with different performance levels is presented in **Fig. 5.6**.

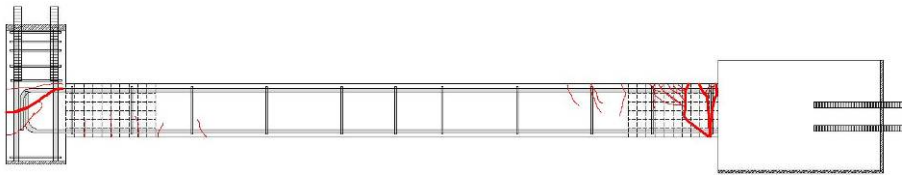

Fig. 5.5: Typical crack pattern of the tested specimen in the final of the test

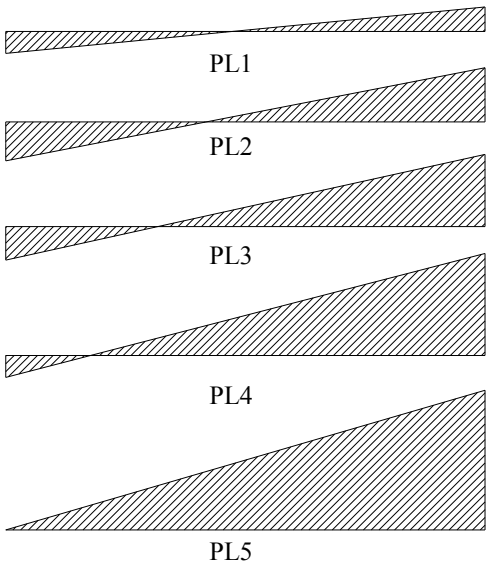

Fig. 5.6: Sketch of the bending moment diagram along the beam of specimen corresponding to different performance levels

5.2.3.3 Yield Displacement Excluded Strain Penetration

As displayed in **Fig. 5.7**, the real boundary condition of the test specimens (**Fig. 5.7c**) lay between the full (**Fig. 5.7a**) and free constraints (**Fig. 5.7b**). The yield displacement corresponding to these three different boundary conditions was evaluated individually and presented in the following section. It should be emphasized that a linear distribution of curvature along the beam was assumed in the current analytical study (Paulay and Priestley [P3]).

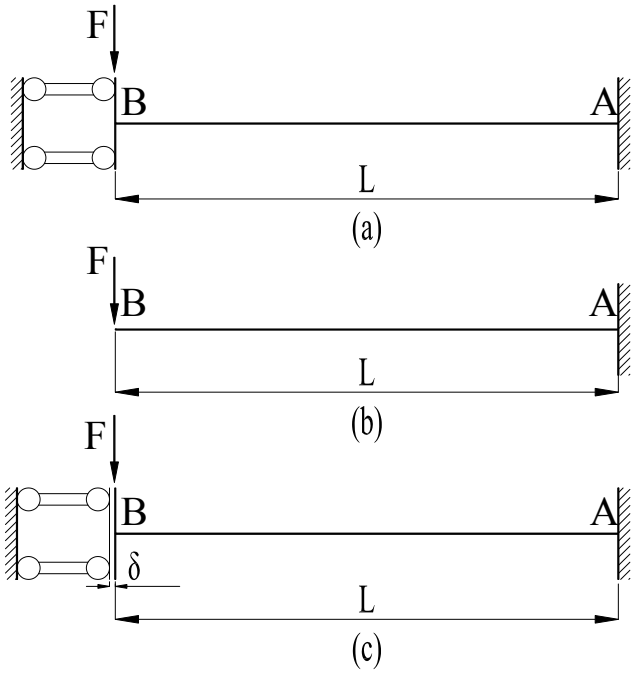

Fig. 5.7: Sketch of the boundary condition assumption for analytical analysis

For full rotational constraint mode l **(** $\xi = 1$ **):**

$$\Delta_y^{full} = \frac{\varphi_y}{6} l_n^{\,2} \qquad (5\text{-}12)$$

where Δ_y^{full} is the yield displacement excluded strain penetration by full constraint model, and φ_y is the yield curvature at point A in **Fig. 5.7** .

For free rotational constraint (cantilever beam) model **(** $\xi = 0$ **):**

$$\Delta_y^{cantilever} = \frac{\varphi_y}{3} l_n^{\,2} \qquad (5\text{-}13)$$

where $\Delta_y^{cantilever}$ is the yield displacement excluded strain penetration by cantilever model.

For partial rotational constraint model **(** $0 \le \xi \le 1$ **):**

The test results indicated that

$$\varphi_B = \xi \varphi_A = \xi \varphi_y \qquad (5\text{-}14)$$

where φ_B is the curvature at the point B, φ_A is the curvature at point A, and ξ is the constraint effective factor ($0 \le \xi \le 1$).

The vertical displacement at point B from the tangent to the axis of the member at point A due to curvature along the whole length of the member is given by:

$$\Delta_y^{partial} = \Delta_{BA} = \int_B^A x \varphi_x dx = \int_0^{l_n} -(\frac{\xi \varphi_y (z-x)}{z}) x dx = \frac{l_n^{\,2}}{6}(2-\xi)\varphi_y \qquad (5\text{-}15)$$

where z is a constant for a specific ξ, $z = \frac{L\xi}{1+\xi}$, φ_x is the curvature at point x away from B, x is the distance of element dx from B, and $\Delta_y^{partial}$ is the yield displacement excluded strain penetration by partial constraint model.

It should be noted that Eq. 5-15 becomes Eq. 5-12 when $\xi = 1$, while Eq. 5-15 becomes Eq. 5-13 when $\xi = 0$. However, the shear displacements and the strain penetration are not explicitly accounted for in Eq. 5-15.

5.2.3.4 Yield Displacement Included Strain Penetration

In order to capture the yield displacement more accurately, the strain penetration into the fixed support was included in the calculation. Hines [H1] suggested adding a term to the flexural displacement $\Delta_{y.f}$ to account for the fixed end rotation due to strain penetration:

$$\Delta_{y.f}^{partial} = \Delta_{y}^{partial} + \varphi_y L_{spy} l_n \qquad (5\text{-}16)$$

where L_{spy} is the equivalent plastic hinge length to account for strain penetration prior to yielding.

From his experiments, Hines [H1] found that L_{spy} could be approximated as 1.5 times the strain penetration length after yielding, which is often estimated as $L_{sp} = 0.022 d_l f_y$. This is because the strain penetration lengths prior to yielding are longer than the post yield lengths. Before yielding, the strain penetration into the foundation is almost linear. After yielding, the strain penetrates only slightly further into the foundation since the forces in the reinforcing bars do not increase substantially.

$$\Delta_{y.f}^{partial} = \Delta_{y}^{partial} + \varphi_y L_{spy} (\frac{2}{3} l_n) \qquad (5\text{-}17)$$

However, Eq. 5-16 was derived based on the cantilever beam ($\xi = 0$) condition. For tested specimens, $\xi = 0.70$ was measured and thus, Eq. 5-16 was modified based on present boundary conditions: the clear span l_n was replaced by the distance from the inflection point to the fixed support at PL2 (about $\frac{2}{3} l_n$). It was noted that shear deformation was limited and hence it was ignored in this analytical analysis (proven in the following section). The comparison between the theoretical and experimental results of yield displacement is given in **Table 5.4**. It should be noted that F6 and F7 had different spans in the longitudinal and transverse directions. However, vertical

load was applied on the corner stub of the substructures by the displacement control approach. Thus, the yielding of the longitudinal rebar was controlled by the beam with the shorter span (same detailing as the F3). As such, in the first yield, displacement was also controlled by the same beam. Therefore, the yield displacements of F6 and F7 were similar to F3.

Table 5.4: Comparison of the Predicted Yield Displacement with the Experimental Results

Specimen	F1	F2	F3	F4	F5	F6	F7	Mean	COV (%)
$\Delta_{y.f}^{measured}$ (mm)	29.4	31.2	28.9	28.1	26.5	27.5	29.9		
$\Delta_{y.f}^{cantilever}$ (mm)	47.7	50.3	47.7	47.7	50.3	47.7	47.7		
$\Delta_{y.f}^{partial}$ (mm)	30.2	31.9	30.2	30.2	31.9	30.2	30.2		
$\Delta_{y.f}^{full}$ (mm)	23.8	25.2	23.8	23.8	25.1	23.8	23.8		
$\Delta_{y.f}^{cantilever} / \Delta_{y.f}^{measured}$	1.62	1.61	1.65	1.70	1.90	1.73	1.60	1.69	6.2
$\Delta_{y.f}^{patial} / \Delta_{y.f}^{measured}$	1.03	1.02	1.04	1.07	1.20	1.10	1.01	1.07	6.3
$\Delta_{y.f}^{full} / \Delta_{y.f}^{measured}$	0.81	0.81	0.82	0.85	0.95	0.87	0.80	0.84	6.2

Note: $\Delta_{y.f}^{measured}$ = Measured yield displacement

$\Delta_{y.f}^{partial}$ = Predicted yield displacement by proposed partial constraint model ($\xi = 0.70$)

$\Delta_{y.f}^{cantilever}$ = Predicted yield displacement by cantilever model ($\xi = 0.0$)

$\Delta_{y.f}^{full}$ = Predicted yield displacement by full rotational constraint model ($\xi = 1.0$)

The mean value and the coefficient of variation of the ratio of the predicted to measured yield displacement for the proposed partial constraint model were 0.99 and 0.068 respectively. However, the mean value and coefficient of variation for cantilever beam model were 1.44 and 0.069, respectively. This indicated that the cantilever beam model would considerably overestimate the yield displacement. On the contrary, a full rotational constraint model would significantly underestimate the yield displacement. The mean value of the ratio of the predicted yield displacement obtained from the full constraint model to the measured one was 0.72. It should be emphasized that the proposed models are not suitable for substructures with over-reinforced and under-reinforced beams.

5.2.4 Displacement at PL4 (Δ_{NF})

5.2.4.1 Introduction

For normal seismic and monotonic tests, performance of the specimen undergoing large displacements is not of interest. Thus, the tests are normally stopped when the resistance capacity have dropped by 25% of the ultimate capacity. We define this point as the normal failure stage and the displacement corresponding to this load stage is defined as the ultimate displacement. However, for progressive collapse tests, the behavior of the structures with large deformation is of interest. Thus, it is emphasized that the ultimate displacement calculation method in normal tests corresponds to Δ_{NF} of the load-displacement curve as illustrated in **Fig. 5.1**.

5.2.4.2 Flexural Displacement at PL4 (Δ_{NF}^{f})

The lumped plasticity approach was utilized to predict displacement at the normal failure stage (Δ_{NF}). The lumped plasticity approach assumes that the inelastic deformation can be modeled as being concentrated in one flexural plastic hinge which is located near the section subjected to the largest moment demand (refer to **Fig. 5.8**). This is, of course, only an approximation of the physical behavior of RC members. However, the plastic hinge model is appealing due to its simplicity and it has been yielding good estimates of the displacement capacity of the structural member. In addition, it is widely accepted and used by the design engineering community (Such as, Park and Paulay [P2], Paulay and Priestley [P3], and Hines [H1]). As illustrated in **Fig. 5.6**, the bending moment significantly increased in the BENF while the bending moment was slightly reduced in the BENC as the load was applied up to PL4. After reaching PL2, the effectiveness of the Vierendeel action began to decrease while the effectiveness of the cantilever beam mechanism began to develop. After reaching PL4, the major force resistance mechanism had changed to the cantilever beam mechanism.

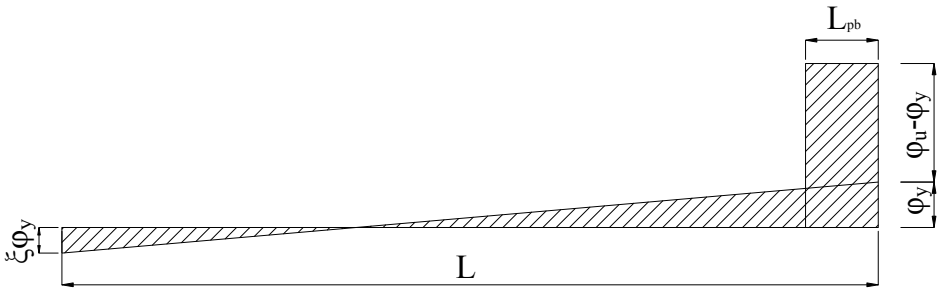

Fig. 5.8: Ideal curvature distribution along the beam at ultimate curvature status

Thus, the plastic displacement Δ_{NF}^{P} was determined by assuming the beams as cantilever beams and expressed as follows (Paulay and Priestley [P3]):

$$\Delta_{NF}^{P} = (\varphi_u - \varphi_y) \times L_{sp} \times (l_n - 0.5L_{sp}) \qquad (5\text{-}18)$$

where Δ_{NF}^{P} is the plastic displacement, φ_u is the ultimate curvature which is typically determined from strain limits, and L_{sp} is the plastic hinge length.

It is noted that in this equation, the term describing the plastic deformation is formulated as a rotation with the centre of the plastic hinge at mid-span of the plastic hinge. However, Hines [H1] noted that assuming a centre of rotation at mid-span of the plastic hinge is conservative, which might be suitable for design, but that a centre of rotation at the base is a more suitable assumption for assessment purpose and the equation is thus modified as follows:

$$\Delta_{NF}^{P} = (\varphi_u - \varphi_y) \times L_{sp} \times l_n \qquad (5\text{-}19)$$

Paulay and Priestley [P3] proposed an equation to evaluate the plastic hinge length:

$$L_{sp} = 0.08 \times l_n + 0.022 \times d_l \times f_y \qquad (5\text{-}20)$$

where l_n is the clear span of the beam, and d_l is the bar diameter of the longitudinal reinforcement.

Thus the ultimate flexural displacement can be determined as follows:

$$\Delta_{NF}^{f} = \Delta_{y.f}^{partial} + \Delta_{NF}^{P} \qquad (5\text{-}21)$$

5.2.4.3 Shear Displacement at first yield ($\Delta_{y.s}$)

The shear displacement when the beam onset of shear cracking was estimated as:

$$\Delta_{s1} = \frac{V_{cr}}{G_c A_{sb}} l_n \qquad (5\text{-}22)$$

where V_{cr} is the shear force when the beam onset of shear cracking, $G_c = 0.43E_c$ is the shear modulus, and $A_{sb} = 0.87A_g$ is the shear area, as recommended by Calvi *et al.* [C1].

The shear force V_{cr} of which the onset of shear cracking occurred is estimated as the concrete contribution to the shear capacity, as proposed by Paulay and Priestley [P3]:

$$V_{cr} = (0.07 + 10\rho_s) \times \sqrt{f_c'} \times b_w \times d \qquad (5\text{-}23)$$

If the shear force demand V_n is larger than the shear force resistant capacity of V_{cr} at first yield, the shear deformation corresponding at first yield can be determined by:

$$\Delta_{y.s} = \Delta_{s1} + \frac{V_n - V_{cr}}{K_v} l_n \qquad (5\text{-}24)$$

where K_v is the shear stiffness of the beam per unit length after cracks.

Park and Pauley [P2] derived an equation for this shear stiffness based on analogous truss as follows:

$$K_v = \frac{\rho_v \sin^4(\alpha) \times \sin^4(\beta)(\cot\alpha + \cot\beta)^2}{\sin^4(\alpha) + n\rho_v \sin^4(\beta)} \times E_s b_w d \qquad (5\text{-}25)$$

When the shear reinforcement is perpendicular to the element axis, the shear stiffness per length can be simplified as:

$$K_v = \frac{\rho_v \sin^2(\alpha) \times \cos^2(\alpha)}{\sin^4(\alpha) + n\rho_v} \times E_s b_w d \qquad (5\text{-}26)$$

where α is the inclination of the compression struts with respect to the element axis, β is the angle between the transverse reinforcement to the horizontal axis, $\rho_v = A_v/(b_w\, s \cdot \sin(\beta))$ is the transverse reinforcement ratio, $n = E_s/E_c$ is the modular ratio, b_w is the beam width, and d is the effective depth of the beam.

5.2.4.4 Flexural Displacement Included Shear Displacement at PL4 (Δ_{NF})

Hines [H1] suggested that the ratio of shear displacements to flexural displacements of structural columns is relatively constant over the entire displacement range. Thus, the ultimate displacement including the shear displacement is:

$$\Delta_{NF} = (\Delta_{y.f}^{partial} + \Delta_{NF}^{P}) \times (1 + \frac{\Delta_{y.s}}{\Delta_{y.f}^{partial}}) \qquad (5\text{-}27)$$

where $\Delta_{y.s}$ is the shear displacement at first yield (ductility equal to 1).

As illustrated in **Table 5.5**, the shear displacement was negligible compared to the flexural displacements. The mean ratios of the predicted ultimate displacement to the measured one for Paulay and Priesley's [P3] equation and Hines's [H1] equation are 0.91 and 0.96 respectively, and the coefficient of variation of the ratio is 9.8 % for both equations. Comparing the results attained from these two models with

experimental data indicated that Hines's [H1] model produced more accurate results than Paulay and Priesley's [P3] model. This was because the plastic rotation of the beam was not around the center of the plastic hinge but around the base of the plastic hinge.

Table 5.5: Comparison of the Predicted Displacement at Normal Failure Stage with the Experimental Results

Test	$\Delta_{NF}^{measured}$	Δ_{NF}^{S}	$\Delta_{NF}^{[P3]}$	$\Delta_{NF}^{[H1]}$	$\Delta_{NF}^{[P3]}/\Delta_{NF}^{measured}$	$\Delta_{NF}^{[H1]}/\Delta_{NF}^{measured}$
F1	110.0	0.59	107.3	112.8	0.98	1.03
F2	130.0	0.54	103.8	108.6	0.80	0.84
F3	120.0	0.59	107.3	112.8	0.89	0.94
F4	120.0	0.59	107.3	112.8	0.89	0.94
F5	160.0	0.54	153.6	163.5	0.96	1.02
F6-L	180.0	0.58	153.6	163.5	0.85	0.91
F6-T	120.0	0.59	107.3	112.8	0.89	0.94
F7-L	130.0	0.54	142.3	149.9	1.09	1.15
F7-T	130.0	0.59	107.3	112.8	0.83	0.87
Mean					0.91	0.96
Coefficient of Variation (%)					9.8	9.8

Note: $\Delta_{NF}^{measured}$ = Measured displacement at normal failure stage (PL4);

Δ_{NF}^{S} = Predicted shear displacement at normal failure stage (PL4);

$\Delta_{NF}^{[P3]}$ = Predicted displacement at normal failure stage exclusive the shear displacement based on Paulay and Priestley [P3] and Eq. 5-18;

$\Delta_{NF}^{[H1]}$ = Predicted displacement at normal failure stage exclusive the shear displacement based on Hines [H1] and Eq. 5-19;

5.2.5 Displacement at PL3 (Δ_u)

The displacement at the ultimate capacity stage (Δ_u), was related to the strain hardening stiffness of the load-displacement curve. The strain hardening stiffness beyond the yield stage was assumed to be 0.2 of the elastic stiffness (Calvi *et al*. [C1]). However, the measured mean value of the ratio of the strain hardening stiffness to the elastic stiffness for the test specimens was 0.31 (tabulated in **Table 5.6**). This difference was possibly because monotonic tests were conducted in the current study while the value provided by Calvi *et al*. [C1] was based on seismic tests. Therefore, the strain hardening stiffness was taken to be 0.31 of the elastic stiffness in the current analytical study.

Table 5.6: Illustrates the Stiffness Ratio of the Hardening Stiffness to the Initial Stiffness

Test	Measured stiffness ratio	Recommended in [C1]	Measured K_{NF2}/K_{NF1}
F1	0.34	0.20	0.49
F2	0.36	0.20	0.93
F3	0.28	0.20	0.71
F4	0.29	0.20	0.59
F5	0.10	0.20	0.77
F6	0.47	0.20	0.97
F7	0.31	0.20	0.93
Mean	0.31	0.20	0.77

Note: K_{NF} = The slope of the descending branch between PL3 to PL4;
K_{NF2} =The slope of the descending branch between PL4 to PL5;

5.2.6 Displacement and Strength at PL5 (Δ_t, F_t)

Based on the test results, the displacement at PL5 was about one tenth of the clear span of the beam. As given in **Table 5.6**, the mean ratio of K_{NF2} to K_{NF} was 0.77. K_{NF1} and K_{NF2} are defined as the slope of the descending branch of the load-displacement curve before and after PL4, respectively (refer to **Fig. 5.1**). Thus, the residual strength at the stage when catenary action began to develop can be determined.

5.2.7 Final Displacement and Strength at PL6 (Δ_{FF}, F_{FF})

As observed in the test results of the tested specimens (refer to **Chapter 4**), no obvious re-ascending of the force resistant was measured when catenary action had developed in the specimen with large deformation. Thus, the residual strength of the specimen at the final of the test (F_{FF}) was assumed to be equal to the strength at PL5 (F_t). Furthermore, the final displacement was assumed to be 20 % of the clear span. For specimens with unequal spans in the longitudinal and transverse directions, the final displacement was assumed to be 20 % of the clear span of the shorter beam. It should be emphasized that the above assumption was based on test observations. Further experimental and analytical studies are needed to predict the final

displacement and strength of the substructures under the scenario of loss of a corner column.

5.3 Comparison of the Theoretical Load-Displacement Curves with the Experimental Results

Fig. 5.9 presents the comparison of the analytical load-displacement curves with the curves obtained from the tests. In general, the analytical curves captured the measured curves very well (initial stiffness, first peak load, general decrease trends and final displacement). The theoretical key values were compared with the experimental ones in **Tables 5.2-5.6**. The above comparisons indicated that the proposed analytical model might be suitable as an assessment tool to predict the load-displacement curve of substructures for progressive collapse caused by the loss of a corner column.

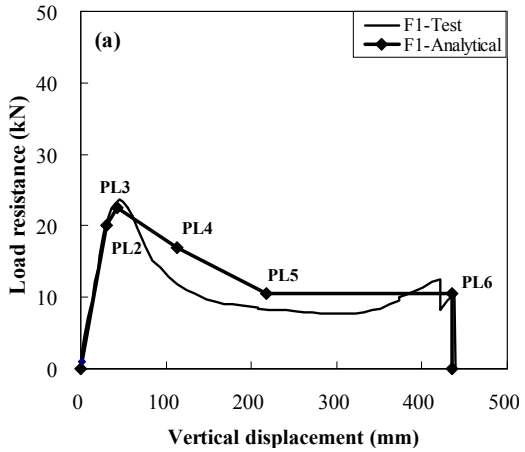

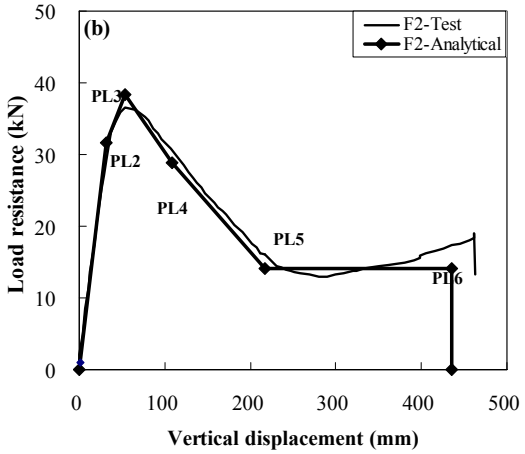

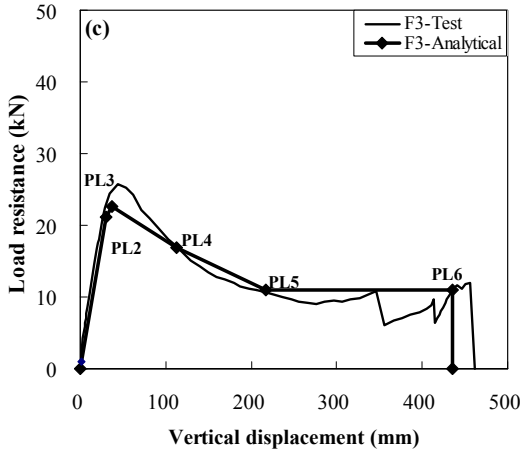
(c)
F3-Test
F3-Analytical
Load resistance (kN)
Vertical displacement (mm)
PL2
PL3
PL4
PL5
PL6
0
10
20
30
40
50
0
100
200
300
400
500

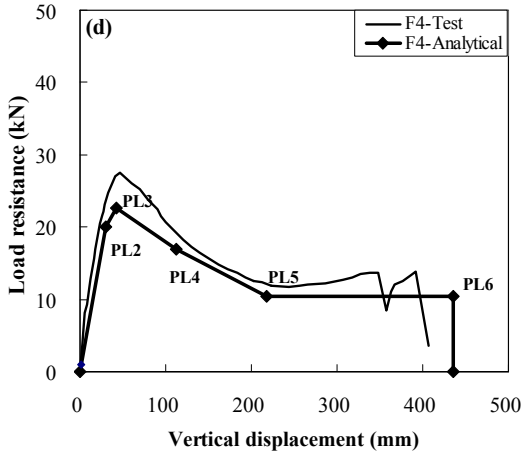
(d)
F4-Test
F4-Analytical
Load resistance (kN)
Vertical displacement (mm)
PL2
PL3
PL4
PL5
PL6
0
10
20
30
40
50
0
100
200
300
400
500

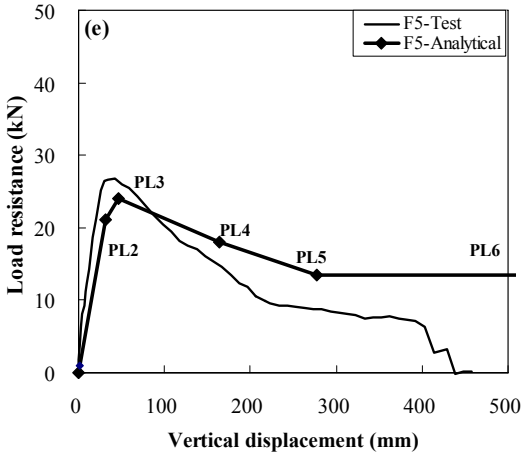
(e)
F5-Test
F5-Analytical
Load resistance (kN)
Vertical displacement (mm)
PL2
PL3
PL4
PL5
PL6
0
10
20
30
40
50
0
100
200
300
400
500

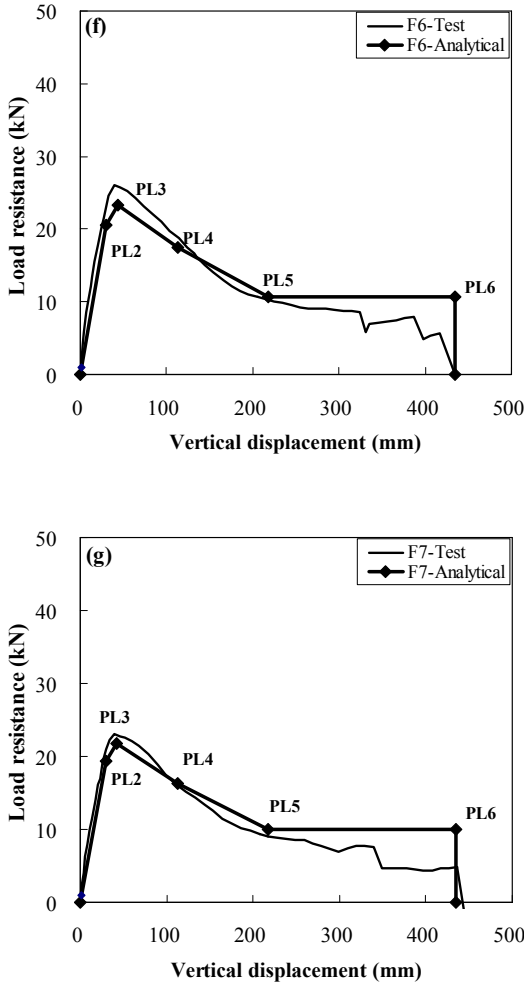

Fig. 5.9: Comparison of the analytical load-displacement curves with the curves obtained from the tests

5.4 Parametric Studies

In order to further understand the performance of RC substructures against progressive collapse caused by the loss of a corner column, using the analytical models developed above, an extensive parametric study of RC substructures was carried out with the following cases being considered for each parameter: the size of beam longitudinal reinforcement F3-4T8, F3-4T10, F3-4T13, and F3-4T16; the clear span of the beam $l_n = 1775mm$, $l_n = 1975mm$, $l_n = 2175mm$, $l_n = 2375mm$, $l_n = 2575mm$, and $l_n = 2775mm$; the depth of the beam $d_B = 180mm$, $d_B = 210mm$, $d_B = 240mm$, and $d_B = 270mm$; the width of the beam $w_B = 100mm$, $w_B = 120mm$, $w_B = 140mm$, $w_B = 160mm$, and $w_B = 180mm$; the

dimensions of the corner column $150\times150mm$, $175\times175mm$, $200\times200mm$, $225\times225mm$, and $250\times250mm$; and the joint transverse reinforcement ratio $\rho_J=0\%$, $\rho_J=0.25\%$, $\rho_J=0.50\%$, and $\rho_J=0.75\%$.

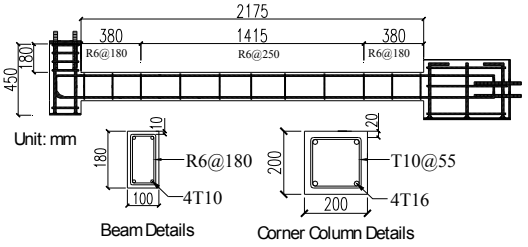

F3

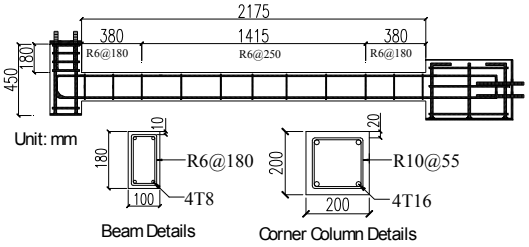

F3-4T8

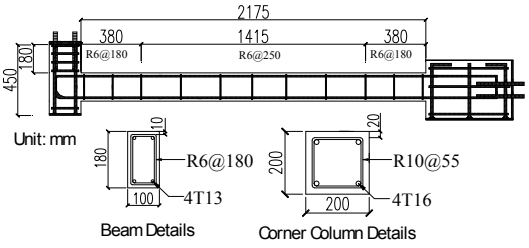

F3-4T13

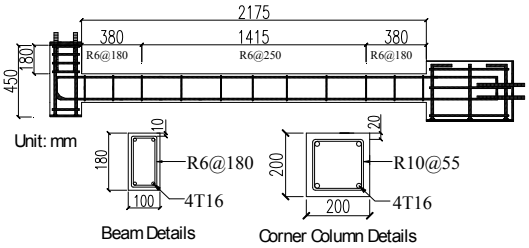

F3-4T16

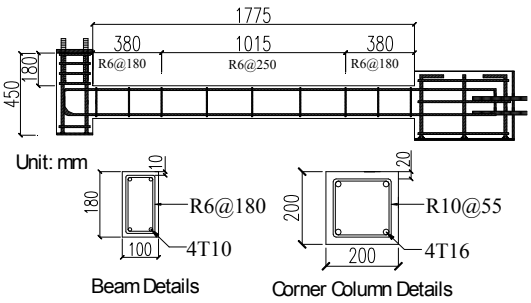

F3-1775

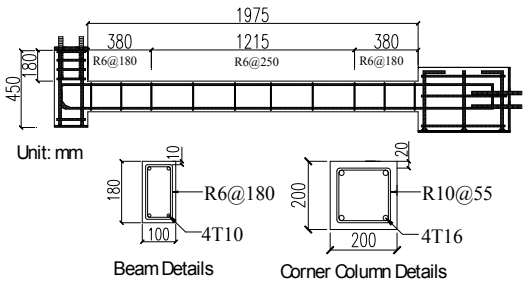

F3-1975

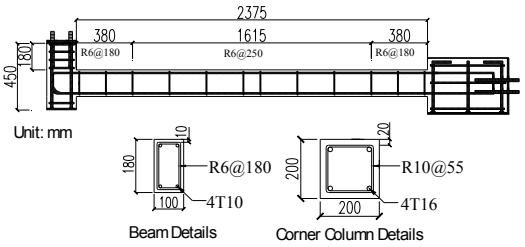

F3-2375

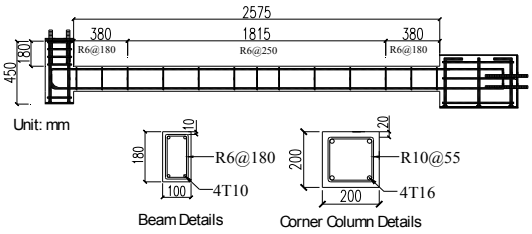

F3-2575

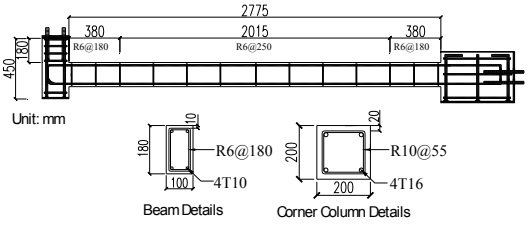

F3-2775

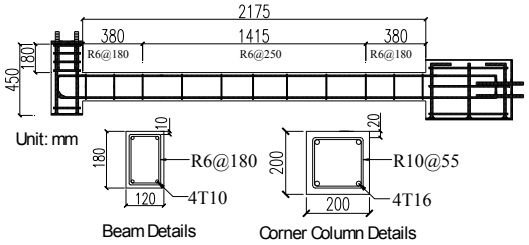

F3-w-120

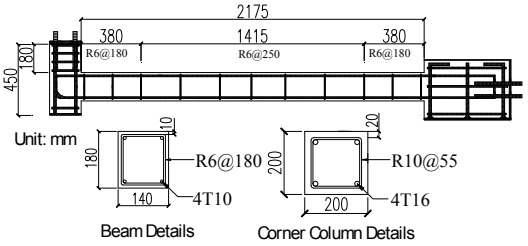

F3-w-140

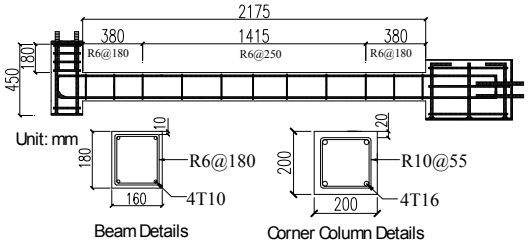

F3-w-160

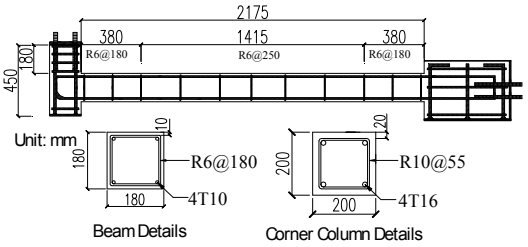

F3-w-180

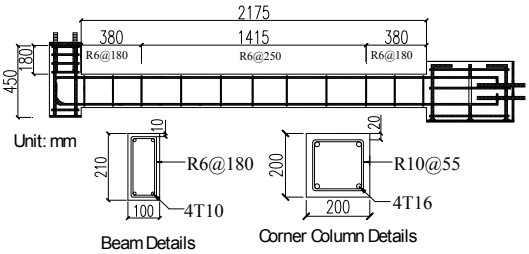

F3-d-210

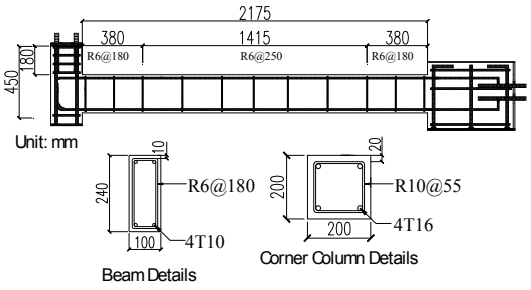

F3-d-240

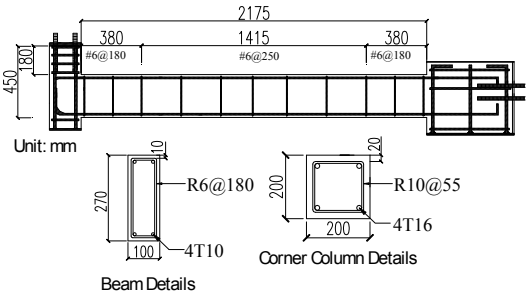

F3-d-270

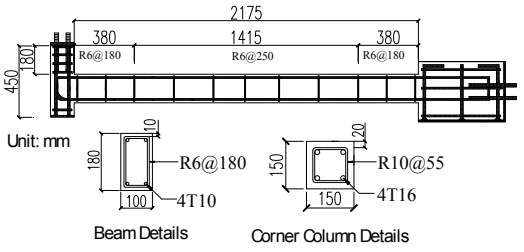

F3-C-150

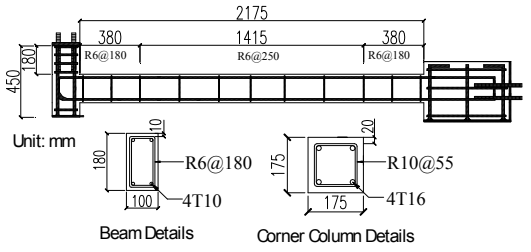

F3-C-175

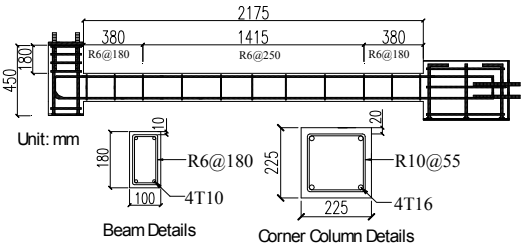

F3-C-225

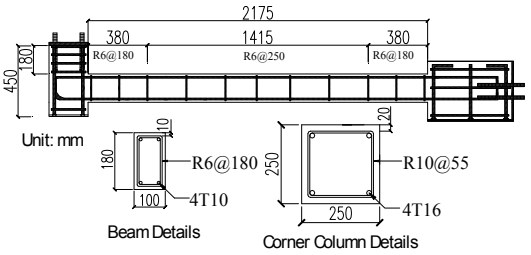

F3-C-250

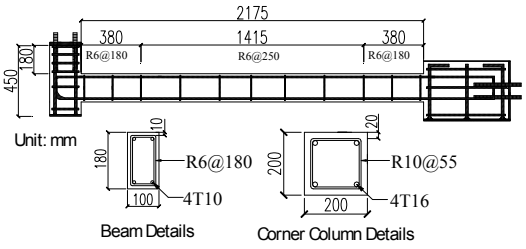

F3-J-0.25 %

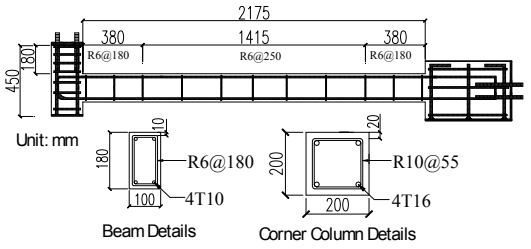

F3-J-0.50 %

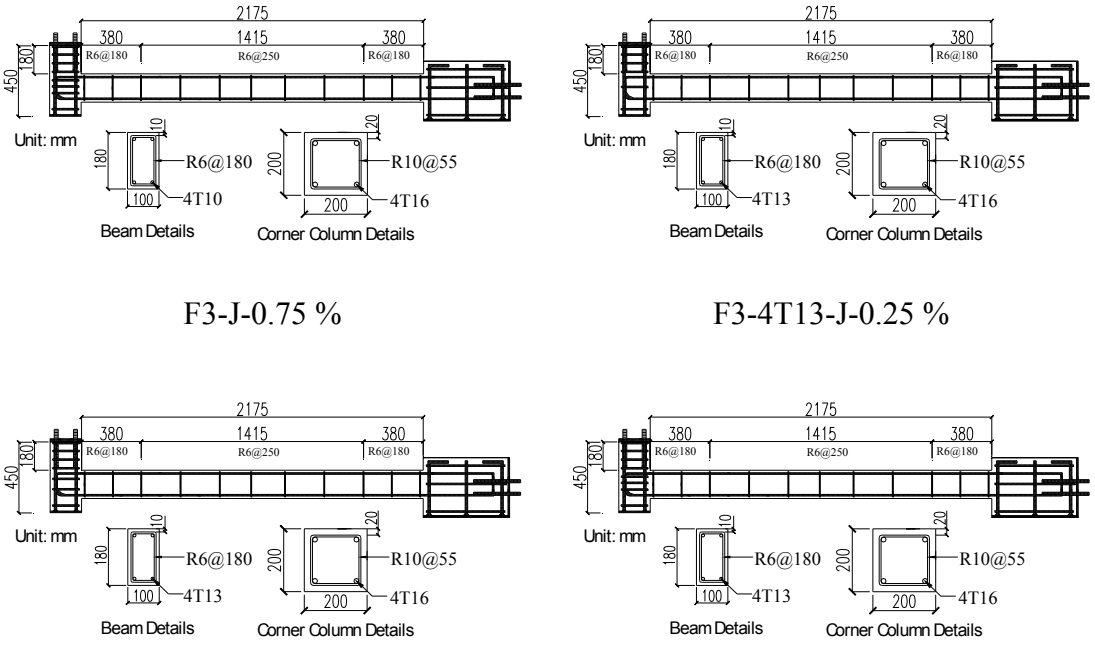

Fig. 5.10: Matrix of the geometry and reinforcement details of the parametric studied substructures

Fig. 5.10 presents the details of the geometry and reinforcement of the substructures studied parametrically. Specimen F3 which had non-seismic detailing is considered the reference specimen in the parametric study. The name of the specimen was designated to emphasize the difference between the specimen and the reference specimen F3. For example, Specimen F3-2375 had similar beam and column cross-section as F3, but it had a longer clear span (2375 mm) compared to that of F3.

5.4.1 Influence of the Beam Longitudinal Reinforcement Ratio

The influence of the beam longitudinal reinforcement ratio is presented in **Fig. 5.11**. Four types of beam longitudinal reinforcement ratio, 4-T8, 4-T10, 4-T13 and 4-T16 respectively corresponding to beam longitudinal reinforcement ratios ρ_{Bl} of 0.56 %, 0.78 %, 1.47 % , and 2.23 %, were considered. As shown in the figure, the initial stiffness, yield strength and ultimate strength of the specimen were significantly increased with an increase in the longitudinal rebar size. However, the displacement

ductility, defined as the ratio of displacement at PL4 to the displacement at PL2, was decreased with an increase in the longitudinal reinforcement ratio. Moreover, the residual strength (due to catenary action) increased slightly when the rebar size increased from T8 to T10 but it began to decrease when the rebar size increased from T10 to T13 and T16. This was due to the significant increase of the beam longitudinal reinforcement ratio, resulted in the concrete crushing at the BENF to occur faster and earlier. Moreover, the substructures with larger beam longitudinal reinforcement ratio suffered more severe damage in the corner joint.

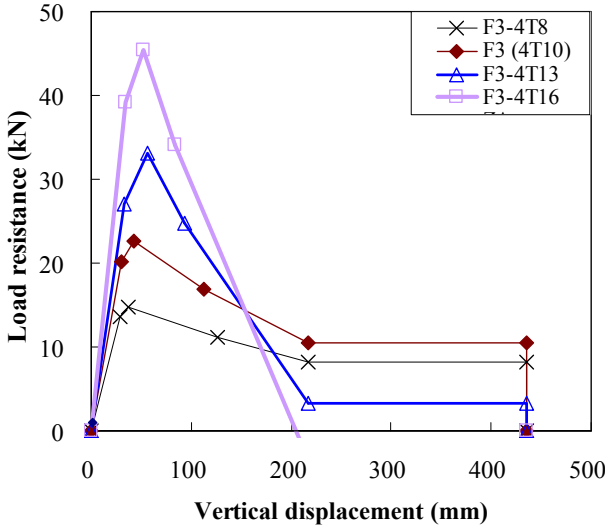

Fig. 5.11: Influence of the beam longitudinal reinforcement ratio on the load-displacement curve

5.4.2 Influence of the Clear Span of the Beam

Six types of clear span of the beam–1775 mm, 1975mm, 2175mm, 2375mm, 2575 mm, and 2775 mm–were chosen to investigate the influence of this variable on the load-displacement curve. As shown in **Fig. 5.12**, with an increase in the clear span of the beam from 1775 mm to 1975 mm, 2175 mm, 2375 mm, 2575 mm, and 2775 mm, the ultimate strength decreased by approximately 9.9 %, 18.4 %, 25.0 %, 31.1 % and 36.0 %, respectively. Similarly, the initial stiffness and yield capacity also decreased with an increase in the span length. It was understandable that increasing the clear span of the beam, the yield strength and initial stiffness would decrease significantly.

However, the slope of the decrease became gentler as substructures with longer span leaned to failure by flexural while substructures with shorter span leaned to failure by shear. Thus, although the substructures with longer span had less ultimate strength, it still had similar residual strength as the substructures with shorter span.

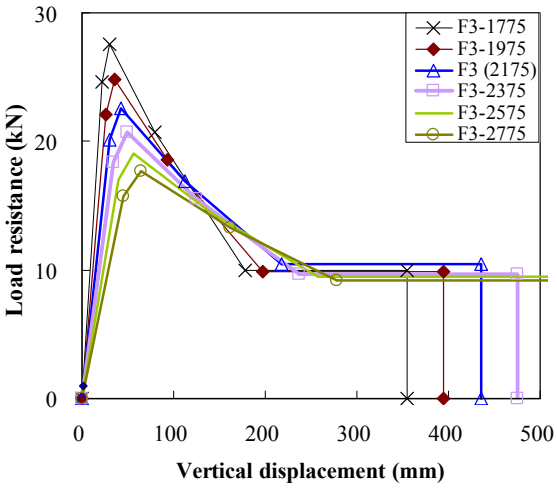

Fig. 5.12: Influence of the clear span of the beam on the load-displacement curve

5.4.3 Influence of the Depth of the Beam

Fig. 5.13 illustrates the influence of the depth of the beam on the load-displacement curve. The depths of the beam investigated were 180 mm, 210 mm, 240 mm, and 270 mm, respectively. As seen from the figure, with an increase in the depth of the beam from 180 mm to 210 mm, 240 mm and 270 mm, the ultimate strength of the specimens rose by approximately 16.9 %, 35.1 %, and 52.8 %, respectively. Similar trends were observed for the initial stiffness and yield strength. It was predictable that the ultimate strength and initial stiffness of the substructures would increase with increasing beam depth due to significant increase of bending moment in the beam section. However, the failure mode of the substructures with deeper beam leaned to be controlled by shear. Fortunately, increasing the depth of the beam increased the shear strength of the substructures. Thus, the substructures with deeper beams had higher ultimate strength, almost same slope of decreasing branch, and had slightly larger residual strength.

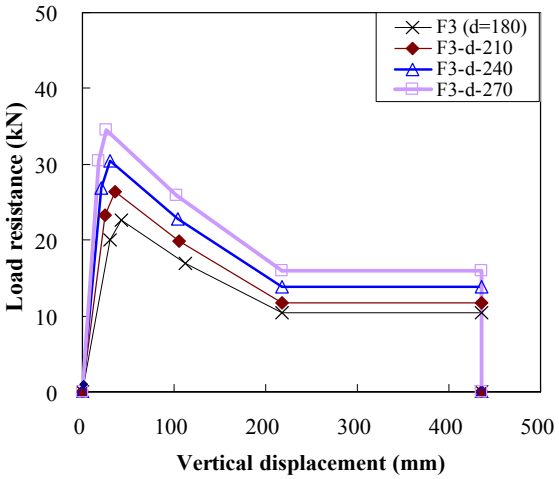

Fig. 5.13: Influence of the depth of the beam on the load-displacement curve

5.4.4 Influence of the Width of the Beam

Fig. 5.14 shows the influence of the width of the beam on the load-displacement curve of substructures. Five widths of the beam–100 mm, 120mm, 140 mm, 160 mm, and 180 mm–were investigated. In general, with an increase in the width of the beam, no significantly changes in the initial stiffness, yield and ultimate strength were observed. However, the residual strength of the substructures rose slightly with an increase of the beam width. This is due to increasing the width of the beam delayed the occurrence of the concrete crushing at the BENF.

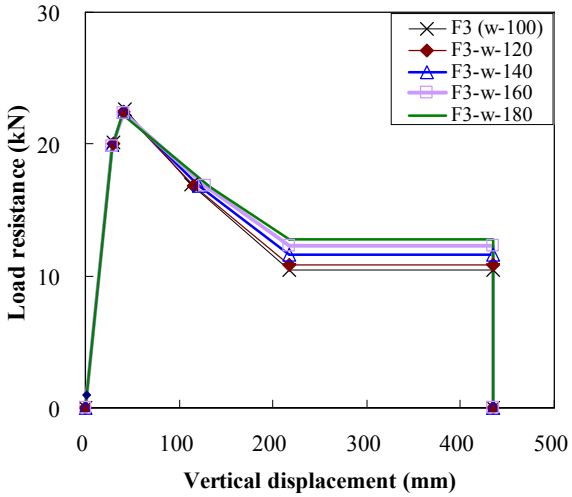

Fig. 5.14: Influence of the width of the beam on the load-displacement curve

5.4.5 Influence of the Dimension of the Corner Column

It is generally recognized that increasing the dimension of the corner column can effectively increase the shear strength of the corner joint. Due to the interaction in between the shear strength of the corner joint and the allowable bending moment in the BENC, increasing the shear strength of the corner joint might increase the yield and the ultimate strength of substructures. The dimension of the corner column was varied from 150 mm square to 250 mm square.

As illustrated in **Fig. 5.15,** with an increase in column size from $150 \times 150 mm$ to $225 \times 225 mm$, the ultimate strength rose by approximately 12.4 %. However, the load-displacement curve remained unchanged when the column size increased from $225 \times 225 mm$ to $250 \times 250 mm$. This was because the corner column with the size of $225 \times 225 mm$ had enough shear strength capacity to ensure that the plastic hinges of the beams could form in the BENC.

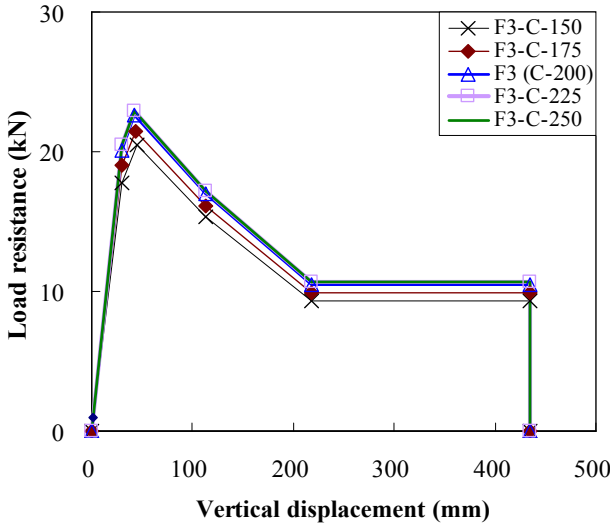

Fig. 5.15: Influence of the dimension of the corner column on the load-displacement curve

5.4.6 Influence of the Joint Transverse Reinforcement Ratio

Fig. 5.16 shows the influence of the joint transverse reinforcement ratio on the load-displacement curve for two different beam longitudinal reinforcement ratios. The joint

transverse reinforcement ratios investigated were 0.0 %, 0.25 %, 0.50 % and 0.75 %. For specimens with a beam longitudinal reinforcement ratio of 0.87 % (4-T10), no significant changes in the load-displacement curves were observed. However, for specimens with a beam longitudinal reinforcement ratio of 1.47 %, the general performance was improved with an increase in joint transverse reinforcement ratio. As can be seen from **Fig. 5.16b**, with an increase in the joint transverse reinforcement ratio from 0.0 % to 0.25 %, 0.50 % and 0.75 %; the ultimate strength of the specimens rose by approximately 5.3 %, 10.7 % and 15.1 %, respectively.

Figs. 5.16a and **5.16b** indicate that increasing the joint transverse reinforcement could not guarantee the improvement in the performance of the substructures. Rather, it was dependent on whether the original corner column had enough shear capacity to develop the plastic hinges in the beam end near the corner joint.

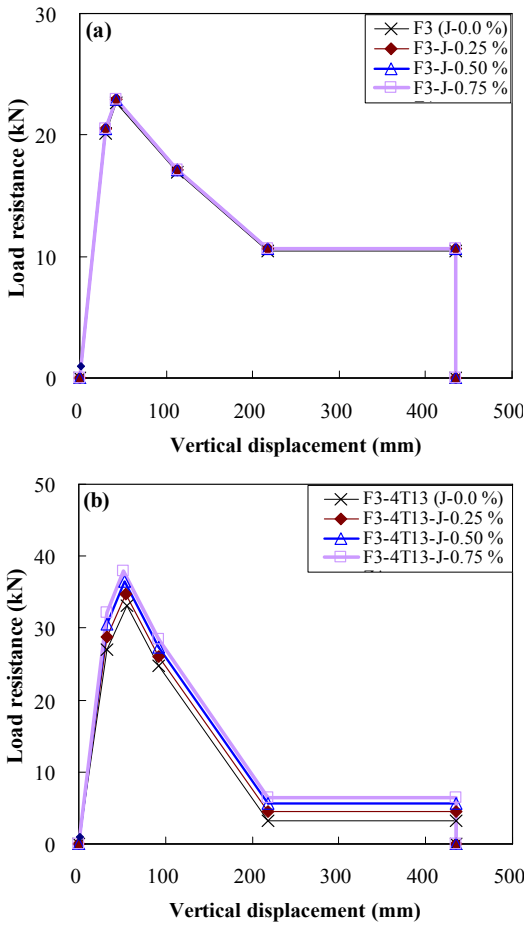

Fig. 5.16: Influence of the joint transverse reinforcement ratio on the load-displacement curve

5.5 Summary

This chapter presents the analytical models to estimate the load-displacement curves of RC substructures after losing a corner column. A comprehensive parametric study was carried out based on the proposed models to investigate the influence of several critical parameters. The following provides specific findings of the chapter:

1. Comparisons made between the analytical and experimental results have shown good agreement. This demonstrates the applicability and accuracy of the proposed method to estimate the load-displacement curves of RC substructures for progressive collapse caused by losing a corner column.

2. The parametric study based on the proposed method showed that the initial stiffness, yield strength and ultimate strength increased with a rise in the longitudinal reinforcement ratio. However, the residual strength decreased with an increase in the longitudinal reinforcement ratio.

3. The effect of the beam width on the initial stiffness, yield strength and ultimate strength of the substructures was limited. However, the residual strength increased with an increase in the width of the beam. It should be noted that increasing the beam depth significantly improved the overall performance of the substructures.

4. Increasing the clear span of the beam significantly decreased the initial stiffness, yield strength and ultimate strength of the specimen, but had no effect on the residual strength.

5. If the existing dimension of the column could not provide enough shear strength to allow the plastic hinge form in the BENC, increasing the size of the corner column could improve the overall performance of the substructures. However, increasing the dimension of the corner column would cause no change in the performance of the substructures if the existing size of the

column had enough strength to allow the plastic hinge to form in the BENC. Similar trends were observed for the influence of the joint transverse reinforcement ratio.

CHAPTER 6

DYNAMIC TESTS FOR BEAM-COLUMN SUBSTRUCTURES WITHOUT RC SLAB

6.1 Introduction

The experimental and analytical results of RC beam-column substructures subjected to quasi-static load regime were reported in **Chapters 4** and **5**, respectively. The results obtained from the quasi-static tests formed a useful database to assess the vulnerability of the RC substructures for progressive collapse.

However, it should be admitted that the nature of progressive collapse is a dynamic phenomenon. It is necessary to conduct enough dynamic tests to further understand the response of RC substructures in resisting progressive collapse. Moreover, the data pool between the performance of the substructures subjected to quasi-static and dynamic load regimes (dynamic increase factor) must be built up. Then, nonlinear static analysis (NP) can be effectively used to replace conducting relative complicated nonlinear dynamic analysis (DP) in the future. Thus, a series of dynamic tests with similar dimensions and reinforcement details as the specimens tested in the quasi-static load regime were also conducted in this study.

The experimental procedure and results of the dynamic series of tests are reported in this chapter.

6.2 Test Specimens

Similar specimens as described in the **Chapter 3** were constructed and tested for dynamic tests. Thus, the details of construction process are not repeated. The compressive strength of concrete at 28 days and the day of testing are given in **Table 6.1**. The tensile property of steel bars is the same as the quasi-static series specimens. Moreover, only the differences of experiment setup, test procedure and instrumentation between these two series of tests are presented.

Table 6.1: Compressive Strength of Concrete

Test	Compressive strength at 28 days f_c' (MPa)	Compressive strength on the day of testing f_c' (MPa)
DF1	32.2	32.8
DF2	29.9	31.4
DF3	31.5	31.8
DF4	31.9	33.1
DF5	32.1	33.8
DF6	32.1	33.1

Six one-third scale RC beam-column substructures designated as DF1, DF2, DF3, DF4, DF5 and DF6 were cast and tested to investigate the dynamic load redistribution performance of the RC moment resisting frames following predefined initial damage. The initial damage was caused by the sudden removal of the corner support. As mentioned in the above, DF1 and DF3 have similar dimensions and reinforcement details as F3 while DF2, DF4, DF5 and DF6 have similar details as F2, F4, F5 and F6, respectively. **Table 6.2** gives the dimensions and reinforcement details of each specimen. The reinforcement detailing of the test specimens was similar to the specimens tested in the quasi-static series tests and is presented in **Fig. 3.16**.

Table 6.2: Specimen Properties (Dynamic Tests)

Test	Elements		Longitudinal rebar		Transverse rebar			Load case	Design Axial load (kN) (kN)	Recorded Axial load (kN)
	Beam-T	Beam-L	Beam-T	Beam-L	Joint	Beam-T	Beam-L			
DF1	Type a*	Type a*	4 - T10	4 - T10	None	R6@180	R6@180	0.9	16.8	16.9
DF2	Type a*	Type a*	4 - T13	4 - T13	R6@55	R6@60	R6@60	0.9	16.8	16.9
DF3	Type a*	Type a*	4 - T10	4 - T10	None	R6@180	R6@180	1.0	18.6	18.7
DF4	Type a*	Type a*	4 - T10	4 - T10	None	R6@80	R6@80	1.0	18.6	18.8
DF5	Type b*	Type b*	4 - T10	4 - T10	None	R6@160	R6@160	0.8	23.3	23.5
DF6	Type a*	Type*	4 - T10	4 - T10	None	R6@180	R6@160	1.0	23.2	23.2

Note: Type a*: Clear span=2175, cross-section=180 x 100; Type b*: Clear span=2775, cross-section=240 x 100

Beam-T: Transverse beam; Beam-L: Longitudinal beam; DoD*: Gravity load combination as guideline DoD [D1]

6.3 Experimental Setup

A schematic of the test setup is shown in **Fig. 6.1**. The setup in this dynamic series tests is similar to the setup used for the quasi-static series tests, which is described in **Chapter 3**. The only difference between these two series of tests is that a column removal apparatus (Item 6 in **Fig. 6.1**) was utilized to simulate sudden removal of a corner column under extreme loading. The detailing of the column removal apparatus is shown in **Fig. 6.2**. As shown in the figure, the column removal apparatus comprised of a specially designed steel column, a pin support and a load cell. In order to reduce the friction between the steel column and the bottom surface of the corner stub and ensure the steel support can be removed as fast as possible, the tip of the steel column was welded to a hemispherical steel ball.

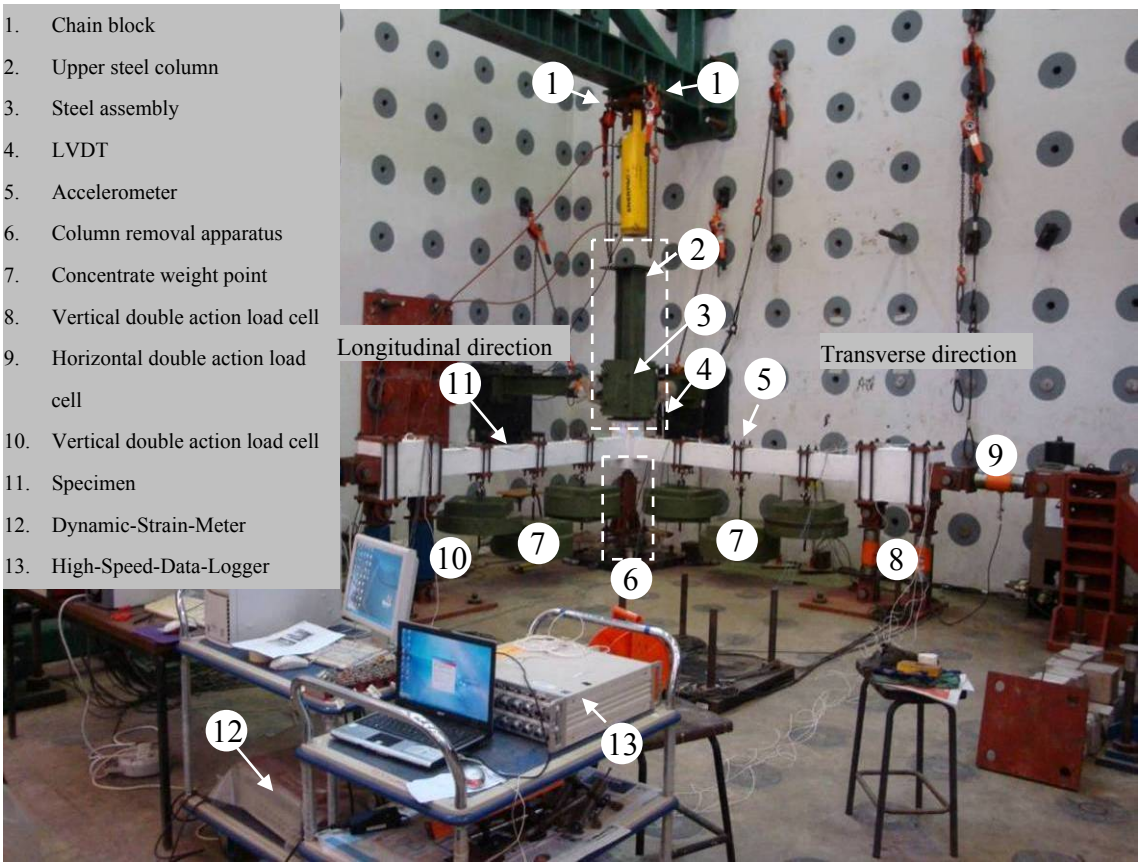

Fig. 6.1: An overview of a specimen in position ready for testing (dynamic tests)

6.4 Test Procedure

Before the commencement of any loading sequence, the test specimen was painted with a thin coat of white-wash to permit better crack observation. All instrumentation (as introduced in the **Chapter 3**) was calibrated in positions and initialized. The test process is described as follows:

Step 1: Two chain blocks (Item 1 in **Fig. 6.1**) were used to hang the upper steel column (Item 2 in **Fig. 6.1**) to prevent the corner stub moving downward during the process of adding the simulated gravity weights.

Step 2: The six specific concentrated weight assemblies (Item 7 in **Fig. 6.1**) were

slowly applied to the beams in a symmetrical sequence. It should be noted that the weight of the concentrated weight assembly is designed according to the service load condition of each specimen (the detailed design process can be found in **Appendix A**).

Step 3: The special steel column (Item 2 in **Fig. 6.2**) was elevated and the height of the pin support (Item 3 in **Fig. 6.2**) was adjusted until the tip of the hemispherical steel ball (Item 1 in **Fig. 6.2**) made contact with the bottom surface of the corner stub.

Step 4: The chain blocks (Item 1 in **Fig. 6.1**) were then loosened to allow for slight adjustment of the height of the pin support (Item 3 in **Fig. 6.2**) until the reaction force in the corner column reached the design axial force, as given in **Table 6.2**.

Step 5: A Static Data Logger was used to record the reinforcement strain, axial load, and vertical reaction force during the static load process.

Step 6: The crack development in the beams and corner joint were also monitored during this static process.

Step 7: After all the specific concentrated weight assemblies had been applied, several selected cables initially connected with the Static Data Logger were switched onto Dynamic Strain Meter by special Bridge Heads (Item 12 in **Fig. 6.1**). Only 10 cables could be connected with the Dynamic Strain Meter due to channel limitations. In order to obtain more data, different channel distribution strategies were assigned for different specimens. **Table 6.3** gives the channel distribution strategy of each specimen. Moreover, the several accelerometers

were connected with the High Speed Data Logger (Item 13 in **Fig. 6.1**)

Step 8: Finally, the corner support was suddenly knocked over by a heavy hammer to simulate sudden removal of a corner column by extreme loading.

Table 6.3: Dynamic Strain Meter Channel Label of Each Specimen

CH. NO.	DF1& DF2	DF3, DF4 & DF5	DF6
1	RF –C*	D1	D1
2	D1	BSTL1	BSTL1
3	D2	BSBL1	BSBL1
4	D3	BSTL8	BSTL8
5	D4	BSBL8	VR1-T
6	BSTL1	VR1-T*	VR2-T
7	BSBL1	VR2-T*	HR1-T
8	BSTL8	HR1-T*	VR1-L
9	BSBL8	VR1-L	VR2-L
10	BST4	VR1-T	HR1-L

Note: RF-C*=Reaction force in the corner column;
VR1-T* and VR2-T* were used to measure the vertical reaction and moment of the support in transverse beam;
HR1-T* was utilized to measure the horizontal reaction in the fixed support of transverse beam;

6.5 Instrumentation

To monitor the response of the test specimens, extensive measuring devices were installed both internally and externally. In the static load process, a total of 25 data channels were active in the Static Data Logger. However, in the dynamic load process, only 10 data channels were active. Several accelerometers were connected to the Digital High Speed Data Logger to monitor the acceleration distribution along the beams following the initial damage. The sampling frequencies of the Dynamic Strain Meter and High Speed Data Logger were 2000 Hz and 1000 Hz, respectively. A load cell (Item 4 in **Fig. 6.2**) was positioned beneath the pin support to monitor the increase

in axial force in the corner column during the static process and to record the axial force variation during the dynamic process. Four LVDTs were placed along the beams to monitor the dynamic displacement distribution in Specimens DF1 and DF2. For the remaining specimens, only one LVDT with 300 mm travel was installed to measure the response of vertical displacement in the corner column. Two compression/tension load cells were installed vertically to measure the vertical reaction force and to determine the moment on the fixed support. One compression/tension load cell was mounted horizontally to measure the horizontal reaction force at the fixed support. In total, 12 electrical resistance strain gauges were mounted on the reinforcement at strategic locations before casting. However, only the strain gauges listed in **Table 6.3** were monitored during the dynamic test. The locations of the accelerometers, LVDTs and strain gauges are illustrated in **Fig. 6.3**.

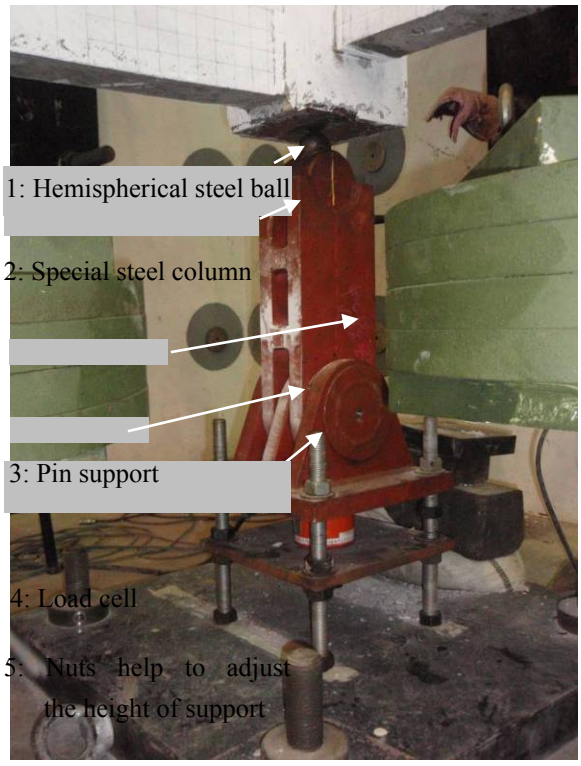

Fig. 6.2: Schematic of the column removal apparatus

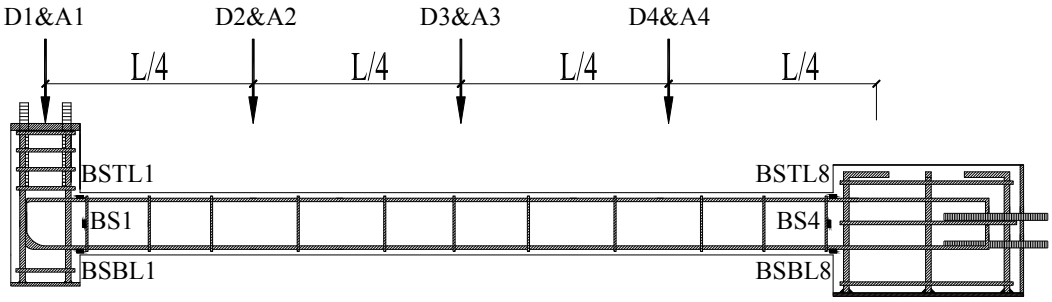

Fig. 6.3: Typical locations of strain gauges, LVDTs and accelerometers

6.6 Evaluation of the Efficiency of the Designed Column Removal Apparatus

The column removal apparatus designed in the current study involved impacting the corner support with a heavy hammer to simulate the sudden removal of a corner column in the frame by extreme loading. As the duration of corner support removal will significantly affect the accuracy of the dynamic response of the substructures, the effectiveness of the designed apparatus must be ensured. The history of the axial force in the corner column was monitored by a load cell (Item 4 in **Fig. 6.2**). As illustrated in **Fig. 6.4**, initially, the corner column of DF1 and DF2 was subjected to an axial force of -16.9 kN (negative represents compressive force). The axial force started to release (compressive force begin to reduce) at a time of 0.2 s. The column axial force in DF1 and DF2 was totally released (reduced to zero) by 0.2035 s and 0.2030 s, respectively. Thus, the duration of the force release was 0.0035 s and 0.0030 s for DF1 and DF2, respectively. This provided proof that the designed column removal apparatus satisfied the requirement of DoD [D1], which requires that the duration of the column removal to be less than one-tenth of the natural period of the vertical motion of the structure after losing the column (the measured nature period of the vibration is about 0.15 s for DF1 and DF2).

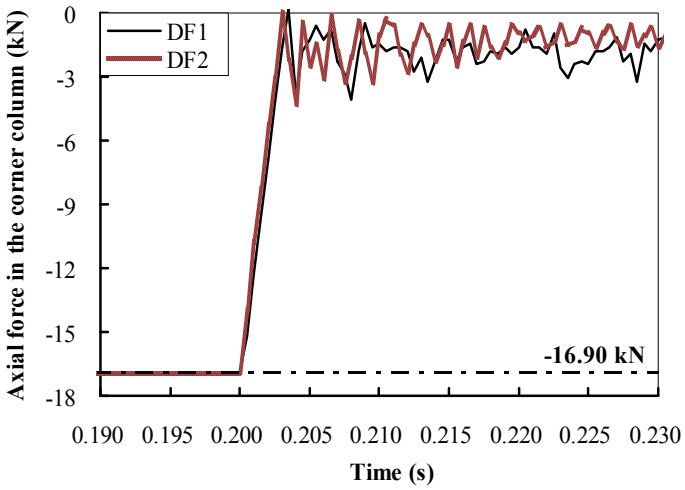

Fig. 6.4: The history of the axial force variation with time in corner support of DF1 and DF2

6.7 Test Results of DF1

As given in **Table 6.2**, the Control Specimen DF1 had similar details as DF3, but suffered reduced service load of 0.9(1.2DL+0.5LL). It was designed to investigate the influence of service load on the dynamic response of the substructures for progressive collapse.

6.7.1 General Behavior

Fig. 6.5 presents the crack patterns of this specimen after sudden removal of the corner support. As seen from the figure, severe diagonal shear cracks and slight concrete spalling occurred in the transverse BENF. However, narrow diagonal shear cracks occurred in the longitudinal BENF while symmetric hairline shear cracks were also observed in the corner joint region after removal of the corner support. Moreover, hairline flexural cracks were observed in the BENC. This indicated that the direction of the bending moment in the BENC, which was initially negative (tension at the top) under gravity loading, changed after removal of the corner support.

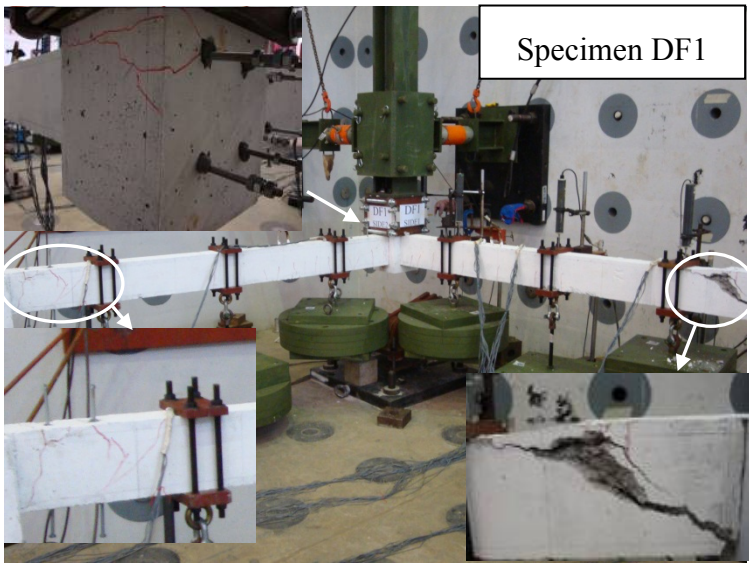

Fig. 6.5: Observed crack pattern of DF1 after test

6.7.2 Displacement Responses

Fig. 6.6 shows the vertical displacement distribution along the transverse beam of DF1. As illustrated in the figure, the displacement at the corner column suddenly increased to the maximum value (-83.9 mm) after the removal of the corner support. The displacement of the corner column reached the peak vertical displacement in only 0.176 s. After that, the whole system vibrated freely with damping. However, the rebounded displacement only reached about 5.5 % of the first peak displacement. The permanent displacement was -81.3 mm. As can be seen in **Fig. 6.6**, the maximum displacements of D1, D2, D3 and D4 were -83.9, -73.4, -46.8, and -20.0 mm, respectively. As mentioned in the above section, the column was removed at a time of 0.2 s. However, the movement at the third-quarter of the span only commences at 0.235 s. From this it can be reasoned that the dynamic force took at least 0.035 s to propagate to that point.

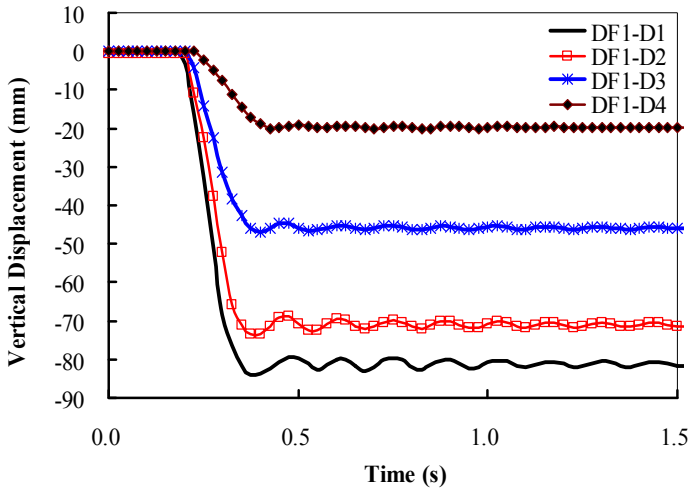

Fig. 6.6: Recorded vertical displacement distribution of DF1

6.7.3 Acceleration Results

In progressive collapse analysis, it is prudent to understand that it is a dynamic event, and that the sudden removal of a load-bearing element in a structure causes an immediate geometric change, resulting in the release of potential energy and rapid alternation of internal equilibrium. Hence, it is important to record the acceleration history at varying locations on the specimens. As mentioned in the instrumentation section, several accelerometers were placed in designated locations prior to removal of the corner support. **Fig. 6.7** presents the recorded acceleration histories of DF1. The maximum acceleration of A1, A2, A3 and A4 were -2.91g, -1.81g, -1.90g, and -0.43g respectively. All of the accelerations diminished rapidly after the peak, and was negligible by 0.003 s. As shown in the history of A1, A1 started to go in the positive phase at a time of 0.293 s. The vibration was along the zero value after a time of 0.515 s. The remaining points (A2, A3, and A4) exhibited similar behavior as A1.

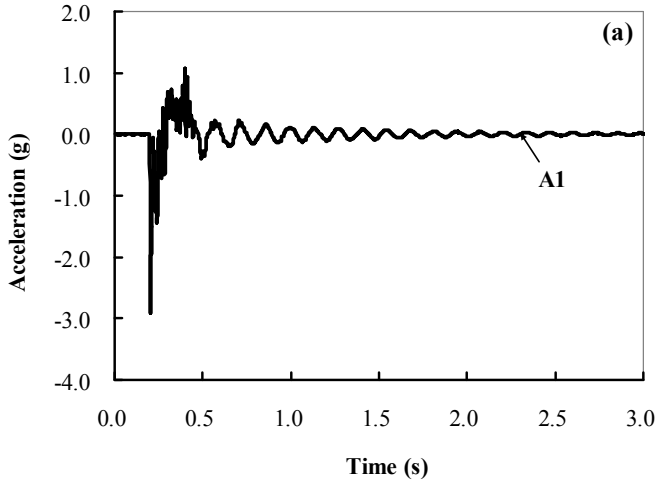
(a)
A1
Acceleration (g)
Time (s)
2.0
1.0
0.0
-1.0
-2.0
-3.0
-4.0
0.0
0.5
1.0
1.5
2.0
2.5
3.0

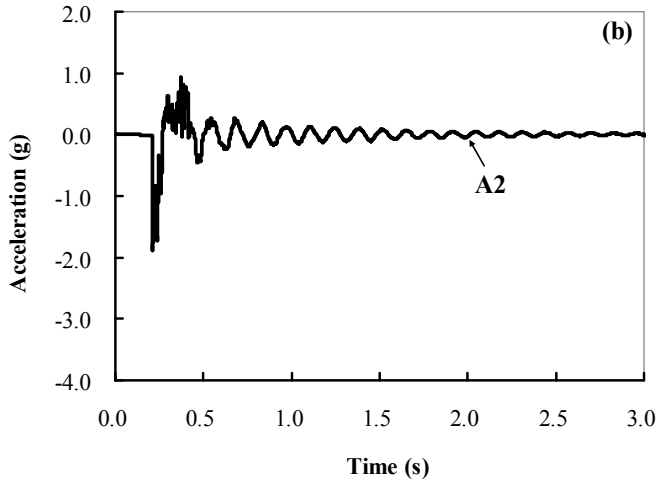
(b)
A2
Acceleration (g)
Time (s)
2.0
1.0
0.0
-1.0
-2.0
-3.0
-4.0
0.0
0.5
1.0
1.5
2.0
2.5
3.0

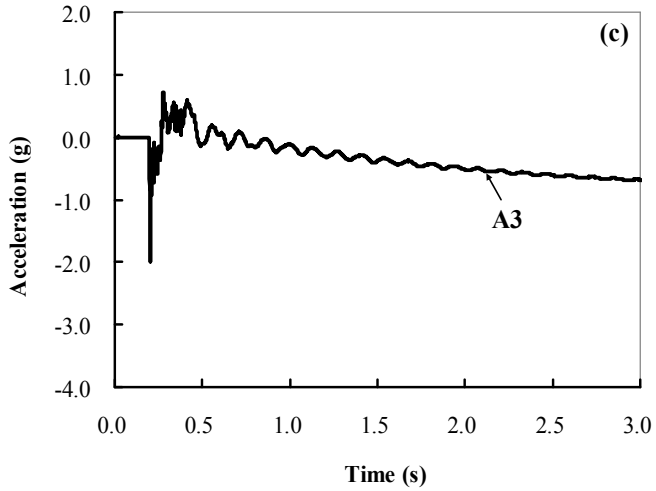
(c)
A3
Acceleration (g)
Time (s)
2.0
1.0
0.0
-1.0
-2.0
-3.0
-4.0
0.0
0.5
1.0
1.5
2.0
2.5
3.0

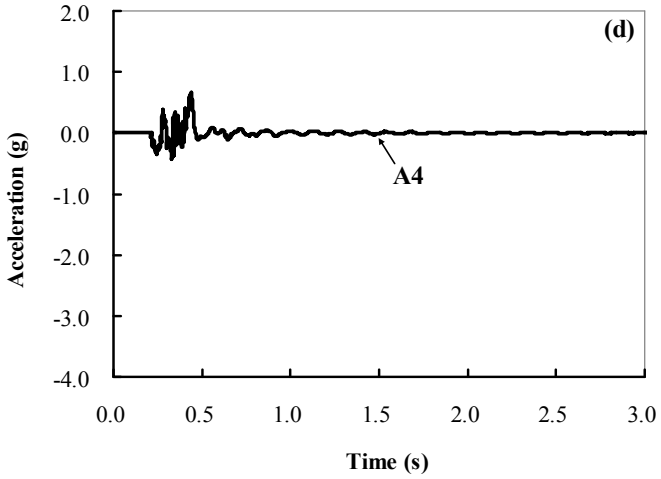

Fig. 6.7: Recorded history of the acceleration at specified locations of DF1

6.7.4 Integral Velocity Responses

No measured velocity response could be presented as no velocity sensor was installed on the specimens. However, by assuming zero initial conditions, it is possible to acquire the velocity and displacement response by direct conducting an integral transform based on the measured acceleration data:

$$\dot{u}(t) = \int_0^t \ddot{u}(\tau) d\tau \qquad (6\text{-}1)$$

$$u(t) = \int_0^t \dot{u}(\tau) d\tau \qquad (6\text{-}2)$$

Eqs. (6-1) and (6-2) can be conveniently expressed in the discrete form as:

$$\dot{u}(t) = \sum_{i=0}^{N} \frac{1}{2} (\ddot{u}(i-1) + \ddot{u}(i)) \Delta\tau \qquad (6\text{-}3)$$

$$u(t) = \sum_{i=0}^{N} \frac{1}{2}(\dot{u}(i-1) + \dot{u}(i))\Delta\tau \qquad (6\text{-}4)$$

where $u(t)$ is the displacement time series; $\dot{u}(t)$ is the velocity time series; $\ddot{u}(t)$ is the recorded acceleration time series; N is the number of sampling points in the acceleration time series; $\Delta\tau$ is the integral time step and is required to be sufficiently short to satisfy the condition of convergence.

However, the direct integration of the acceleration data often causes unrealistic drifts in the velocity and displacement, as presented in **Fig. 6.8a**, where the integral velocity response based on the recorded acceleration data of A1 in DF1 is given as an example. The integral velocity without any baseline correction has significant drifts with periodic oscillations. The drifts in velocities and displacements can be attributed to many potential factors. For example, it is generally agreed that the mechanical or electrical hysteresis in the sensor can cause an offset to occur in the acceleration records. Even a small offset in acceleration can produce significant drifts in velocities and displacements. Another main source of unrealistic drift in velocities and displacements might come from the accumulation of the random noise in accelerations resulting from the integrations. Thus, for the graph tail, polynomial curve fitting was performed and the graph was subsequently corrected to the zero-velocity baseline as shown in **Fig. 6.8a**.

In order to evaluate the accuracy of this integral method to obtain the velocity response, the displacement responses obtained by integral transform from the recorded acceleration data were compared with the measured displacement histories. As presented in **Fig. 6.9**, the integral displacement matched well with the measured displacement, although the integral displacement had a slight time lag. Thus, the accuracy of the proposed integral method was proven. In addition, the reliability of

the velocity response obtained from the integral transform can be ascertained. **Fig. 6.8** illustrates the velocity responses at prescribed locations of DF1. As shown in the figure, the peak velocities of V1, V2, V3 and V4 in DF1 were -0.61 m/s, -0.60 m/s, -0.32 m/s and -0.14 m/s, respectively. Similar to the displacement and acceleration response distribution along the transverse beam, the velocity response distribution was also non-linear. The velocities of V1, V2, V3, and V4 were reduced to zero at 0.425 s, 0.406 s, 0.437 s and 0.439 s, respectively.

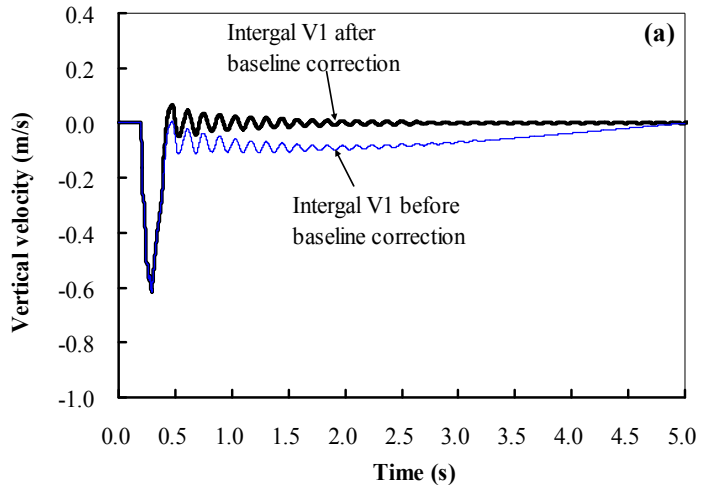

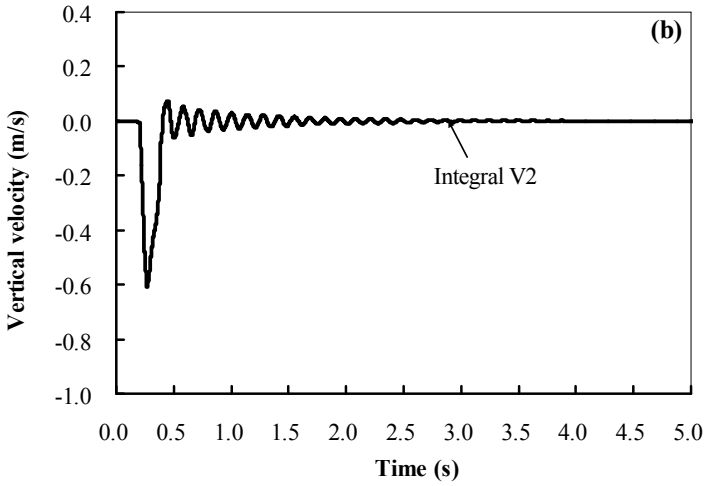

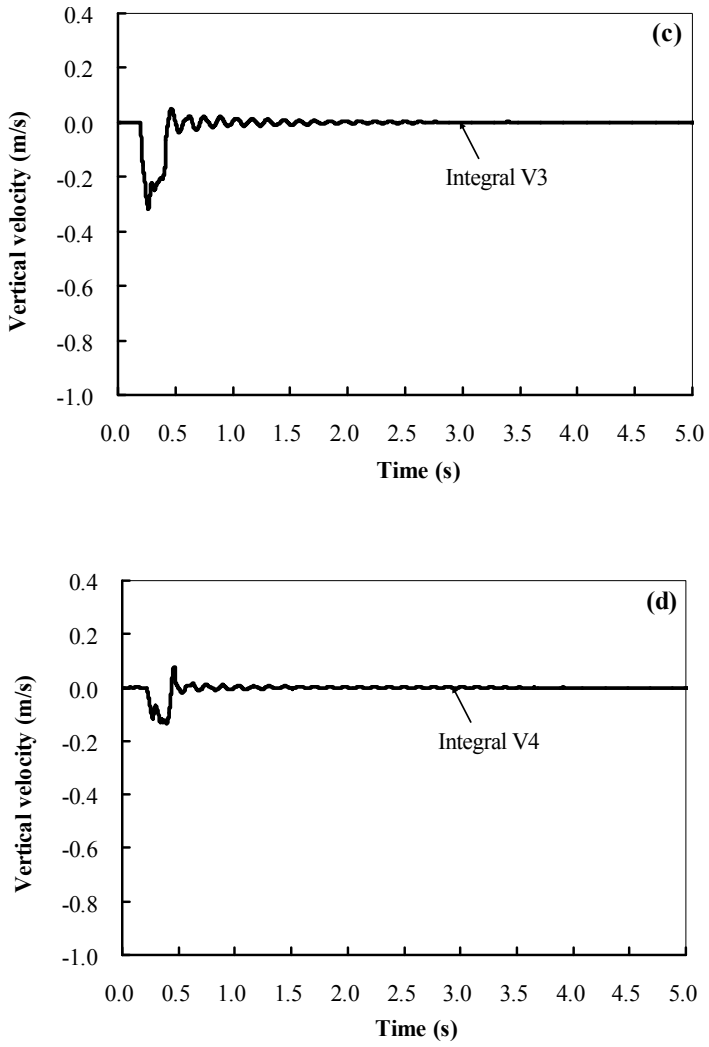

Fig. 6.8: Integral history of the velocity at specified locations of DF1

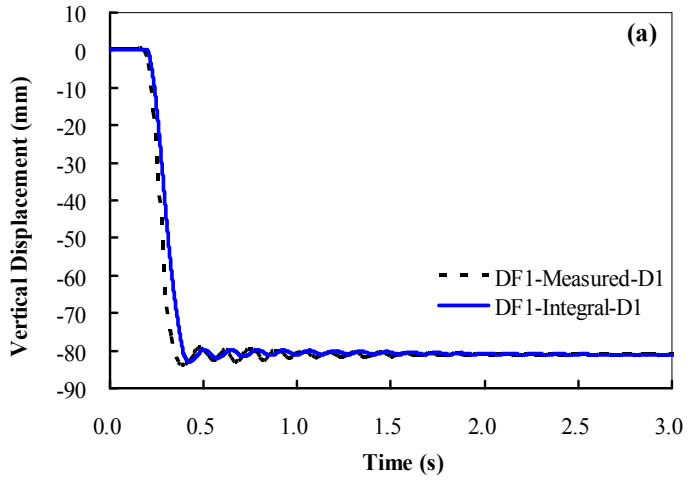

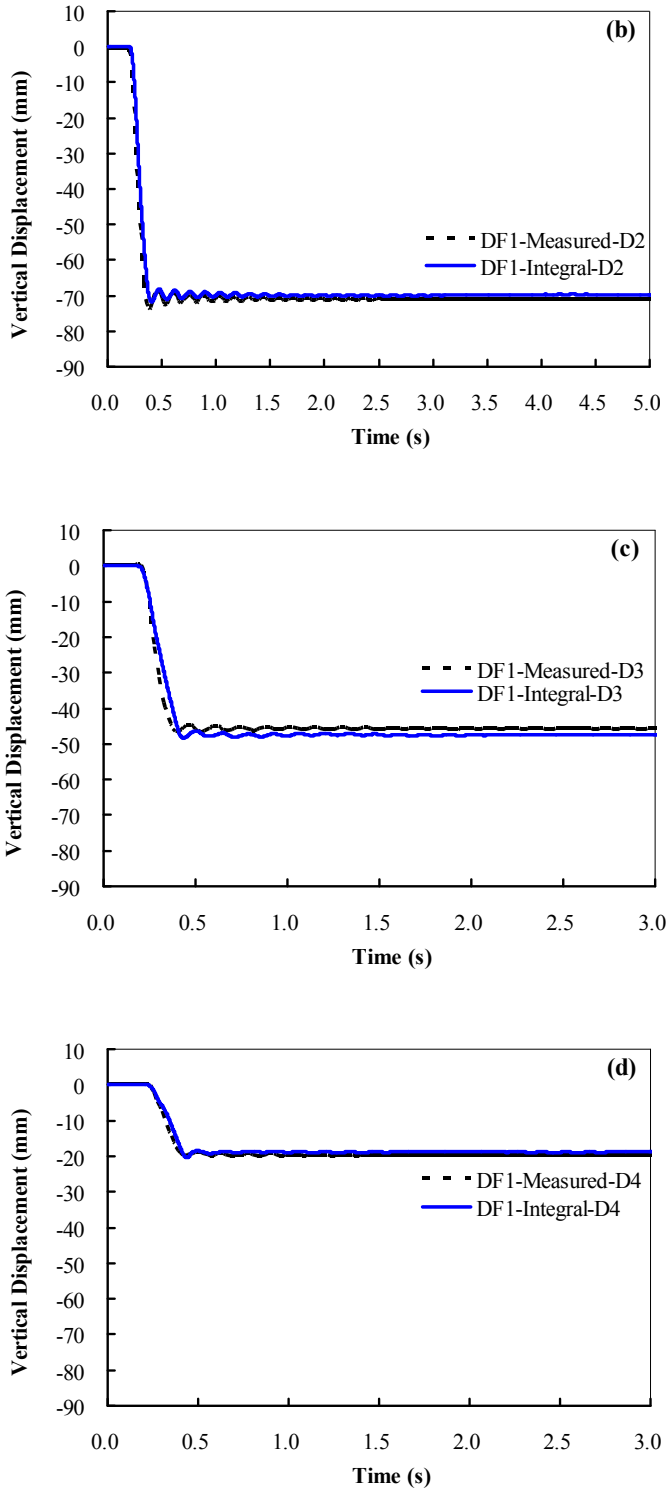

Fig. 6.9: Comparison of the measured displacement history with the corresponding integral displacement history of DF1

6.7.5 Strain Gauge Results

Figs. 6.10 and **6.11** present the strain gauge recordings of flexural and transverse reinforcement of DF1, respectively. As exhibited in **Fig. 6.10**, the strain in the top of BENC (BSTL1) was 360 με (positive represents tensile strain) before removal of the corner support. However, this tensile strain decreased and ultimately reached the maximum compressive strain of -1001 με at a time of 0.41 s. On the other hand, the strain of BSBL1 initially had compressive strain -163 με. After removal of the corner support, the compressive strain in BSBL1 suddenly decreased to zero and ultimately attained the maximum tensile strain of 2488 με at a time of 0.42 s. Both results verified that the direction of bending moment in the BENC changed after removal of the corner support. It can also be seen that the strain reading diminished after 0.5 s. The permanent strain of BSTL1 and BSBL1 at the end of vibration was about -723 με and 1731 με, respectively. The initial strain reading of BSTL8 and BSBL8 were 578 με and -205 με, respectively. After removal of the corner support, the reading of BSTL8 and BSBL8 rose to 4487 με and -1817 με at the times of 0.41 s and 0.42 s, respectively. This demonstrated that bending moment increased considerably in the BENF. As the yield strain for T10 was 2895 με, top longitudinal reinforcement in the BENF yielded after removal of the corner support.

Fig. 6.11 illustrates the strain gauge reading in the beam transverse reinforcements of DF1. As presented in the figure, the strain in BST4 was initially 430 με and suddenly increased to 1764 με after removal of the corner support. It indicated that significant shear force was transferred into the BENF after sudden removal of the corner support. However, the main failure of DF1 was still controlled by flexural failure as the peak value of the strain in BST4 was less than the yield strain (2650με). The permanent tensile strain of BST4 is 1425 με.

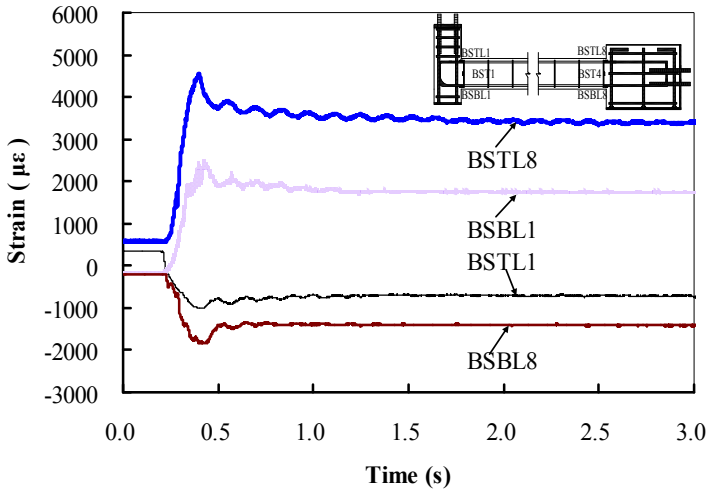

Fig. 6.10: Strain gauge recording in the flexural reinforcement of Specimen DF1

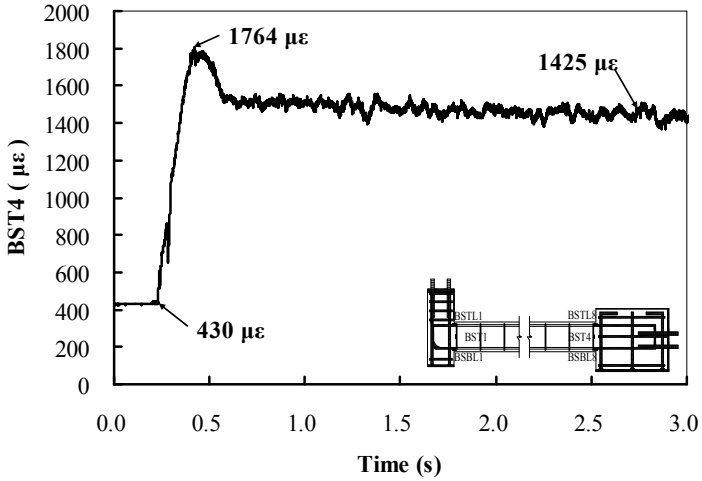

Fig. 6.11: Strain gauge recording in the transverse reinforcement of DF1

6.8 Test Results of DF2

Specimen DF2 was seismically designed and detailed. The dimensions and reinforcement details are given in **Table 6.2.** Similar to DF1, DF2 was subjected to a reduced service load of 0.9(1.2 DL+0.5 LL) before removal of the corner support. This specimen was designed to study the influence of seismic detailing on the dynamic response of substructures for progressive collapse.

6.8.1 General Behavior

Fig. 6.12 shows the final crack pattern of DF2 after test. As shown in the figure, only several flexural cracks were observed in the BENFs. Similar to DF1, the direction of the bending moment changed in the BENC. Another distinguished difference between the crack patterns of these two specimens (DF1 and DF2) was that no cracks occurred in the corner joint of DF2 due to the fact that installed joint transverse reinforcement well confined the core concrete and provided additional shear strength of the corner joint.

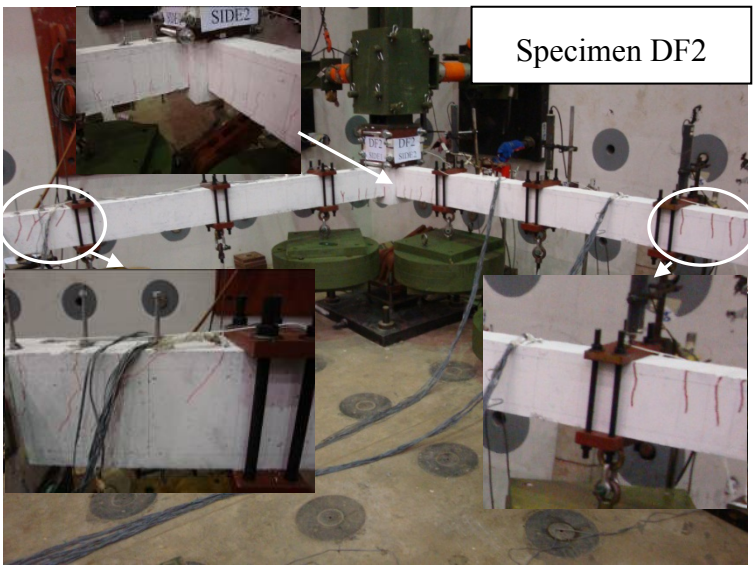

Fig. 6.12: Observed crack pattern of DF2 after test

6.8.2 Displacement Responses

Fig. 6.13 shows the vertical displacement distribution along the transverse beam of DF2. As can be seen from the figure, the maximum displacements at D1, D2, D3, and D4 of Specimen DF2 were –29.0 mm, -26.0 mm, -17.0 mm, and -4.9 mm, respectively. Similar to DF1, it indicated that the distribution of the deformation was

non-linear and the deformation of the beam occurred in a manner different from that in a cantilever beam due to partial rotational constraint applied to the corner joint. Comparing the peak vertical displacements of DF2 with that of DF1, it can be seen that the peak vertical displacement of DF2 was only 34.6 % of that of DF1. As mentioned in the above section, the column was removed at a time of 0.2 s. However, the movement at the three-quarter of the beam span only commenced at 0.237 s. Thus, it can be reasoned that the dynamic force took at least 0.037 s to propagate to that point.

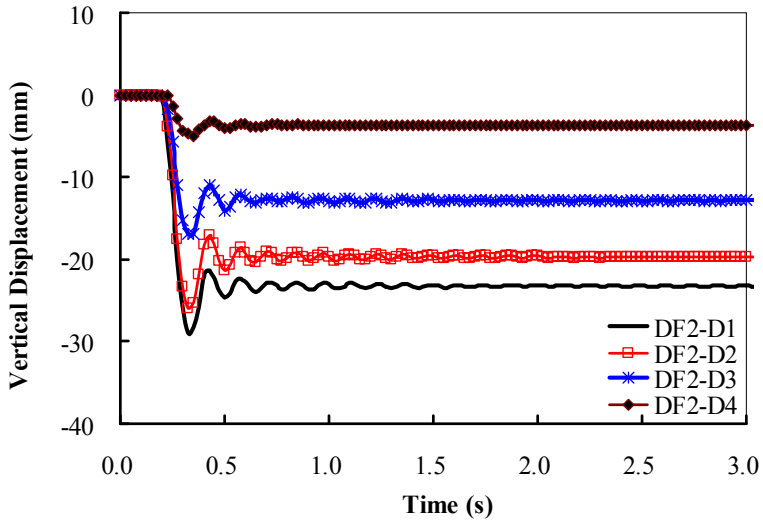

Fig. 6.13: Recorded vertical displacement distribution of DF2

6.8.3 Acceleration Results

Fig. 6.14 presents the recorded acceleration histories of DF2. The maximum acceleration of A1, A2, A3 and A4 were -2.66g, -1.85g, -1.57g and -0.49g, respectively. Similar to DF1, the acceleration diminished rapidly after the peak, and was negligible by 0.003 s. The vibration was along the axis with zero value except A1, which vibrated along an inclined line.

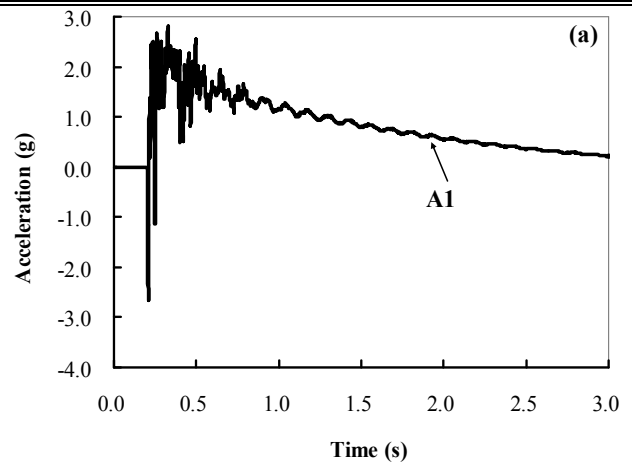
(a)
A1
Acceleration (g)
Time (s)
3.0
2.0
1.0
0.0
-1.0
-2.0
-3.0
-4.0
0.0
0.5
1.0
1.5
2.0
2.5
3.0

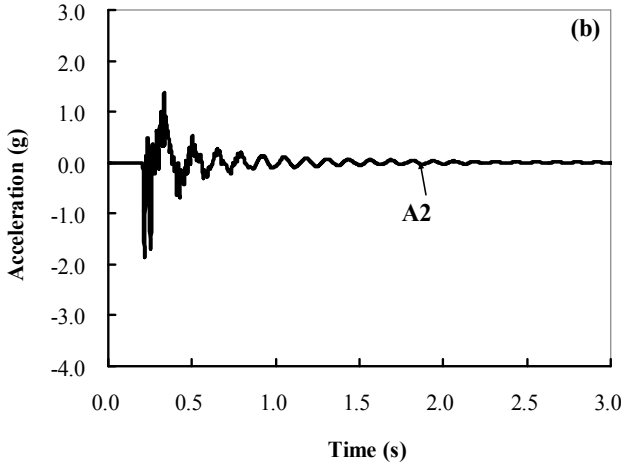
(b)
A2
Acceleration (g)
Time (s)
3.0
2.0
1.0
0.0
-1.0
-2.0
-3.0
-4.0
0.0
0.5
1.0
1.5
2.0
2.5
3.0

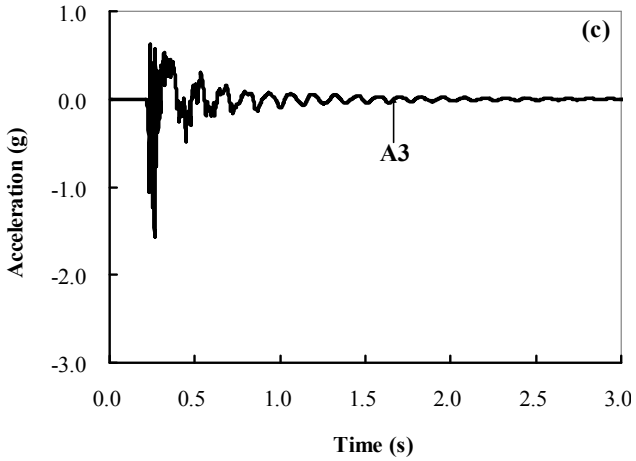
(c)
A3
Acceleration (g)
Time (s)
1.0
0.0
-1.0
-2.0
-3.0
0.0
0.5
1.0
1.5
2.0
2.5
3.0

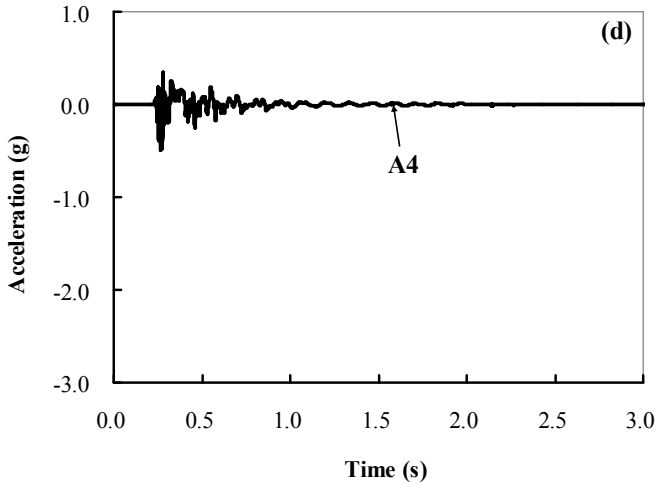

Fig. 6.14: Recorded history of the acceleration at specified locations of DF2

6.8.4 Integral Velocity Responses

Fig. 6.15 illustrates the velocity responses at prescribed locations of DF2. As shown in the figure, the peak velocities of V1, V2, V3 and V4 in DF2 were -0.25 m/s, -0.34 m/s, -0.21 m/s, and -0.07 m/s, respectively. It should be emphasized that the measured data of A1 involved considerable noise, which meant the result of V1 might not be so accurate.

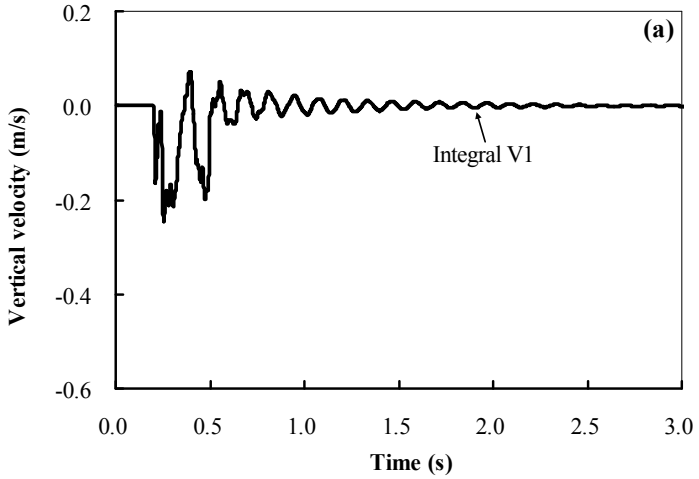

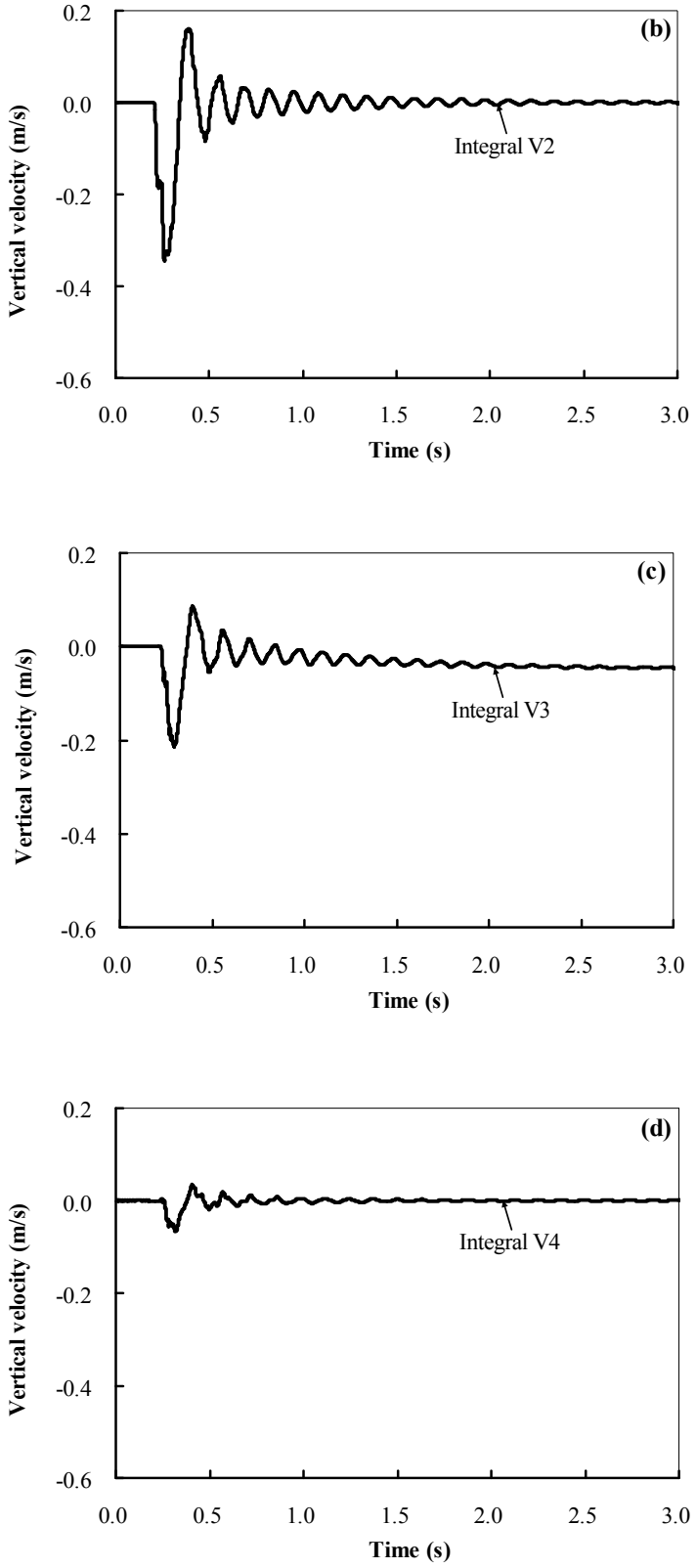

Fig. 6.15: Integral history of the velocity at specified locations of DF2

6.8.5 Strain Gauge Results

Figs. 6.16 to 6.17 present the strain gauge recording of the flexural and transverse reinforcement of DF2, respectively. As presented in **Fig. 6.16**, the strain in the top of the BENC (BSTL1) was 251 με before removal of the corner support. However, this tensile strain decreased and ultimately reached the maximum compressive strain of -502 με at a time of 0.35 s. On the other hand, the strain of BSBL1 initially had compressive strain of -199 με. After removal of the corner support, the compressive strain in BSBL1 suddenly decreased to zero and ultimately attained the maximum tensile strain of 1838 με at a time of 0.33 s. Both results verified that the direction of bending moment in the BENC changed after the corner support was removed. The permanent strains of BSTL1 and BSBL1 at the end of vibration were -243 με and 1150 με, respectively. The initial strain readings of BSTL8 and BSBL8 were 388 με and -181 με, respectively. After removal of the corner support, the readings of BSTL8 and BSBL8 rose to 3751 με and -1440 με at the times of 0.34 s and 0.35 s, respectively. The permanent strain in BSTL8 was 2385 με after vibration. It should be noted that the yield strain of T13 was 2595 με. Thus, the top rebar near the fixed supports suddenly yielded after removal of the corner support. However, after finish completing the force redistribution, DF2 rebounded back to elastic stage.

As presented in **Fig. 6.17**, the strain in BST4 was initially 390 με and suddenly increased to 1441 με after sudden removal of the corner support. The permanent tensile strain of BST4 was 1083 με. Similar to DF1, transverse reinforcement near the fixed supports did not yield although significant shear force was transferred into the fixed support due to force redistribution.

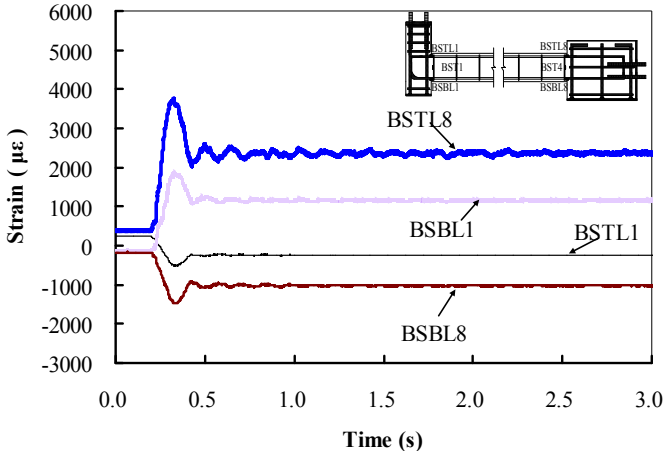

Fig. 6.16: Strain gauge recording in the flexural reinforcement of Specimen DF2

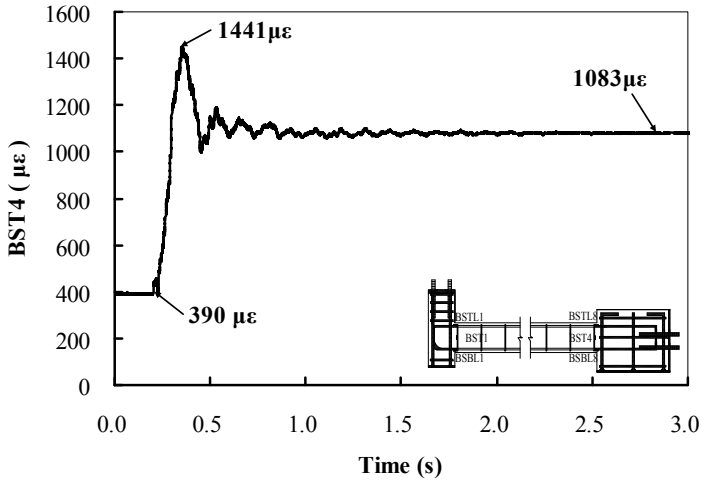

Fig. 6.17: Strain gauge recording in the transverse reinforcement of Specimen DF2

6.9 Test Results of DF3

DF3 had similar dimensions and reinforcement details as DF1. As given in **Table 6.2**, DF3 was subjected to full service load as provided in guideline DoD [D1]. This specimen was designed to investigate the influence of the magnitude of the service load on the dynamic response of the substructures. **Table 6.2** gives the dimensions and reinforcement details of this specimen.

6.9.1 General Behavior

As presented in **Fig. 6.18**, severe flexural and shear cracks were observed in the BENFs. Slight concrete crushing occurred in the bottom of the BENF. More flexural cracks developed in the BENCs and more severe diagonal shear cracks were observed in the corner joint compared to DF1. Although more severe damages took place in DF3 due to higher service load, both specimens (DF1 and DF3) managed to survive the tests.

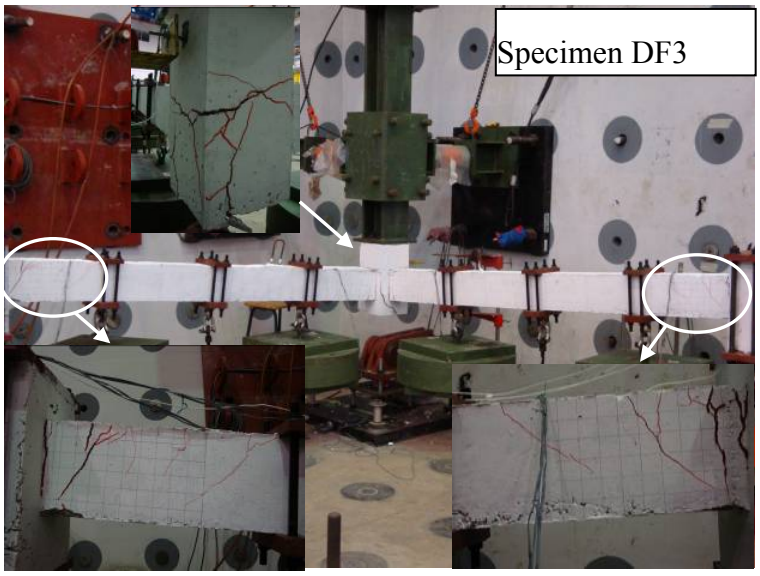

Fig. 6.18: Observed crack pattern of DF3 after test

6.9.2 Displacement Responses

As given in **Table 6.3**, only one LVDT with 300 mm travel was installed in the corner joint to monitor the vertical displacement variation with time for DF3. As illustrated in **Fig. 6.19**, DF3 reached the peak displacement 146.6 mm at a time of 0.45 s, and then rebounded to 143.2 mm at 0.50 s. The permanent displacement at the end of vibration was 143.9 mm. Thus, for DF3, the displacement rebounding was limited and

negligible compared to DF2. It can be seen in the figure, first peak displacement of DF3 was 74.7 % higher than that of DF1.

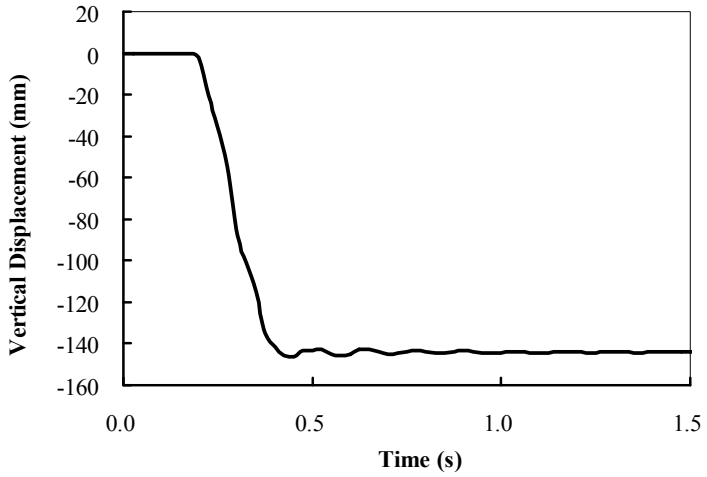

Fig. 6.19: Recorded vertical displacement in the corner joint of DF3

6.9.3 Acceleration Results

Fig. 6.20 presents the recorded acceleration histories of DF3. The maximum accelerations of A1, A2, A3 and A4 were -3.44g, -3.19g, -3.11g and -1.41g, respectively. Similar to DF1, all of the accelerations diminished rapidly after the peak, and was negligible by 0.005 s. A1 and A2 vibrated along the inclined line while A3 and A4 vibrated along the axis with zero value.

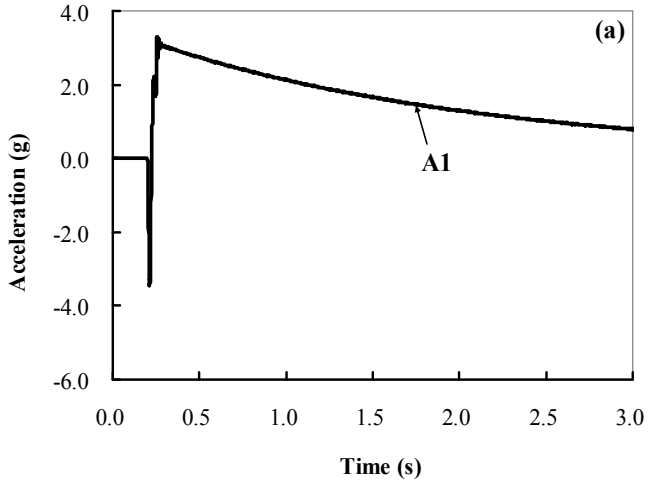

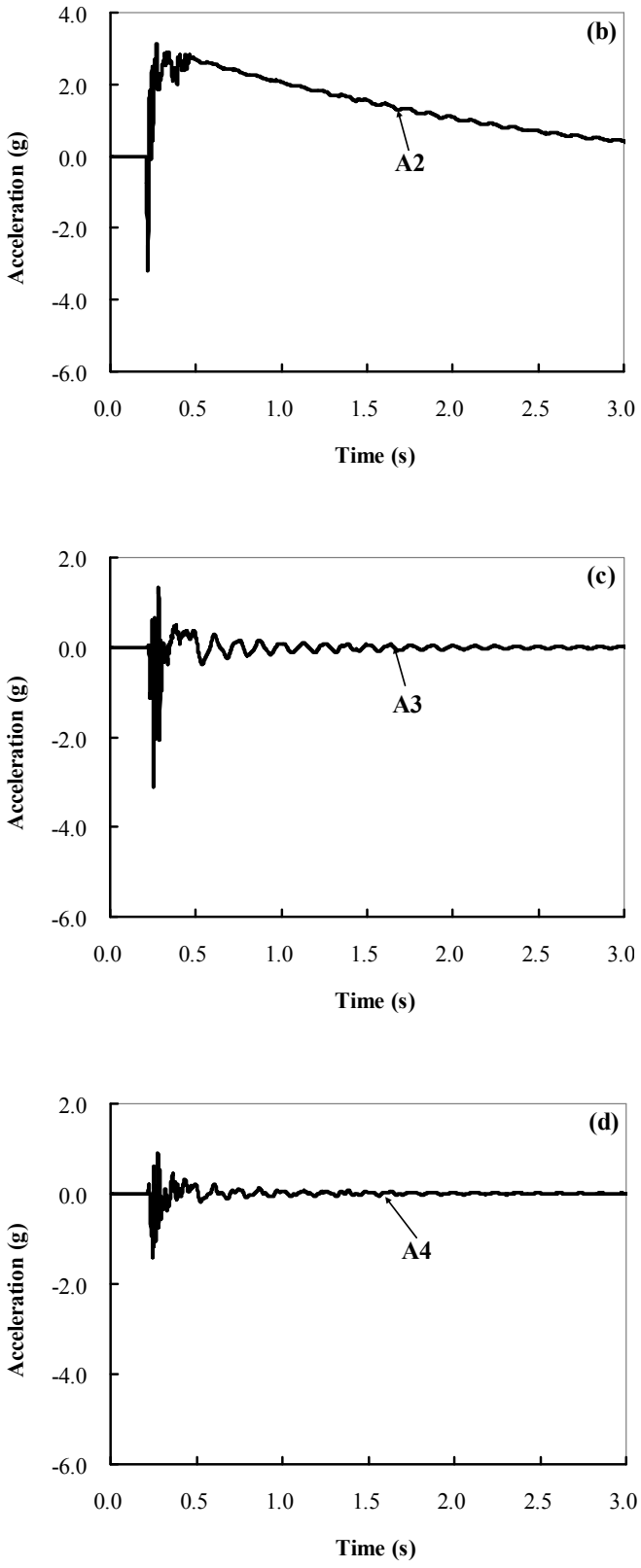

Fig. 6.20: Recorded history of the acceleration at specified locations of DF3

6.9.4 Integral Velocity Responses

Fig. 6.21 illustrates the velocity responses at prescribed locations of DF3. As shown in the figure, the peak velocities of V1, V2, V3 and V4 in DF3 were -0.63 m/s, -0.66 m/s, -0.56 m/s and -0.27 m/s, respectively. Moreover, the response of V1 and V2 was not as good as that of V3 and V4 due to large noise in the readings of A1 and A2.

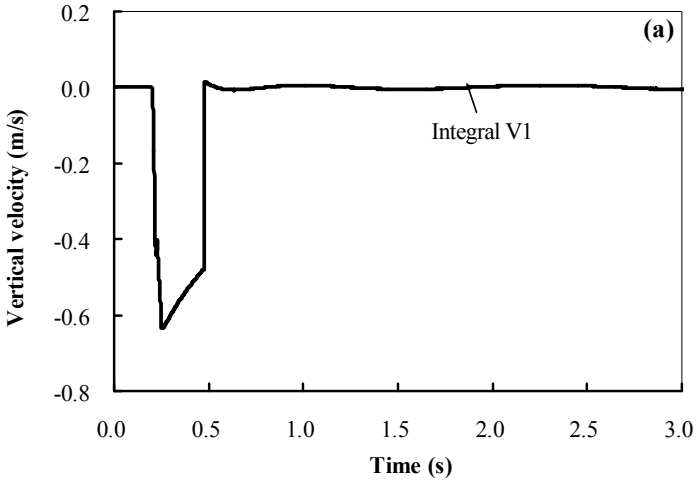

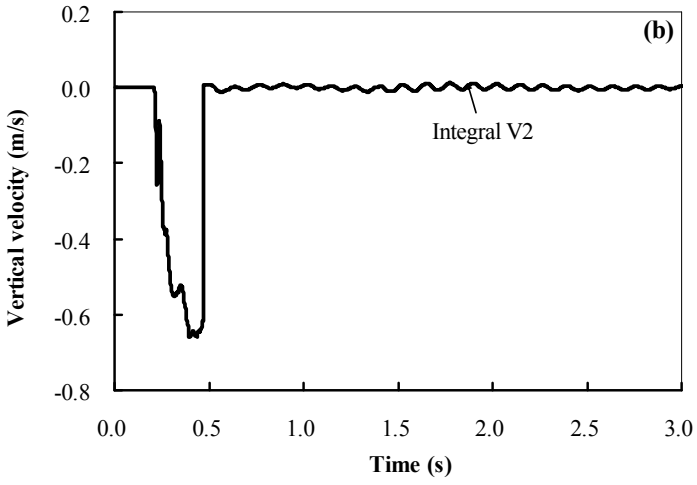

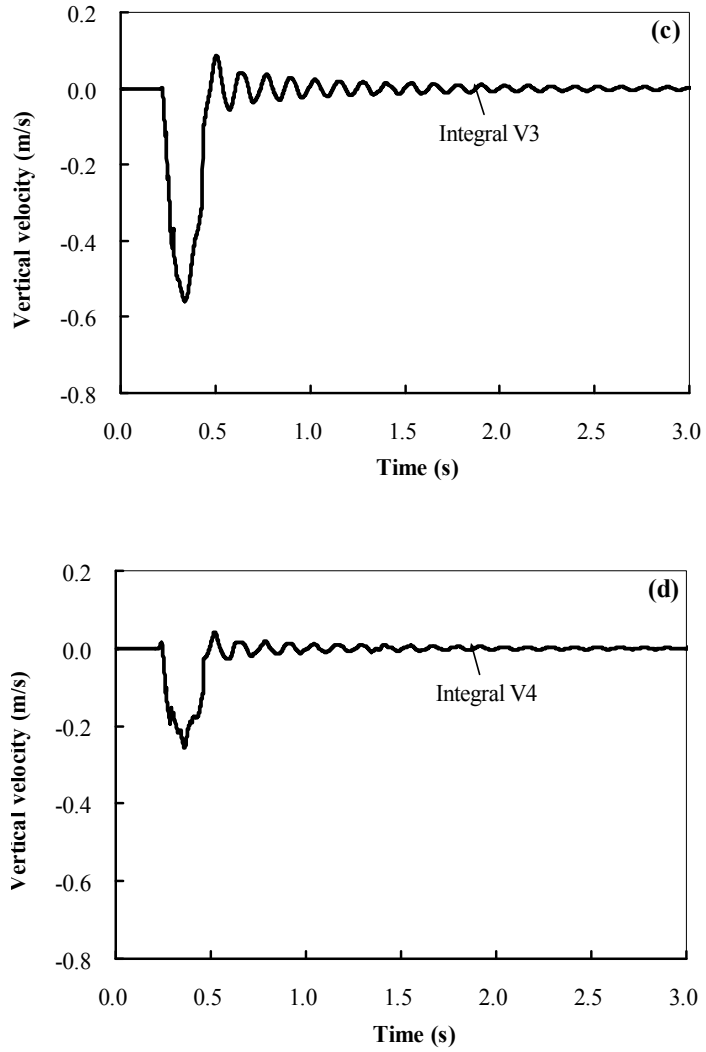

Fig. 6.21: Integral history of the velocity at specified locations of DF3

6.9.5 Strain Gauge Results

Fig. 6.21 presents the strain gauge recording of flexural reinforcement of DF3. As presented in **Fig. 6.21**, the strain of BSTL1 was initially 515 με. However, this tensile strain diminished and ultimately reached a maximum compressive strain of -1147 με at a time of 0.35 s. On the other hand, the strain of BSBL1 was initially -190 με. It suddenly decreased to zero and ultimately attained the maximum tensile strain of 2707 με at a time of 0.37 s. Both results indicated that the direction of the bending

moment reversed at the BENC after removal of the corner support. The permanent strain of BSTL1 and BSBL1 was -778 με and 2295 με, respectively. The initial strain readings of BSTL8 and BSBL8 were 670 με and -238 με, respectively. After removal of the corner support, the readings of BSTL8 and BSBL8 rose to 4500 με and -1615 με at the times of 0.38 s and 0.31 s, respectively. As the permanent strain of BSTL8 (3691 με) was significantly larger than the yield strain (2895 με), DF3 yielded and could not rebound back to elastic stage after force redistribution.

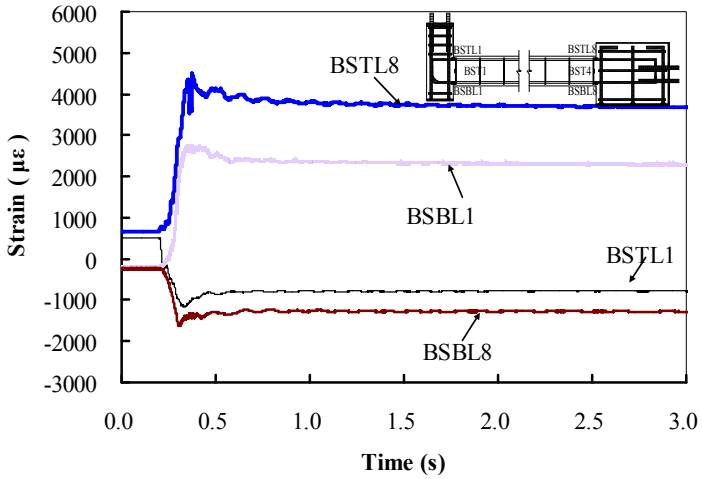

Fig. 6.21: Strain gauge recording in the transverse reinforcement of DF3

6.9.6 Vertical Reaction Force Responses

Fig. 6.22 illustrates the recorded history of the total vertical reaction force of DF3. As displayed in the figure, the initial total vertical reaction force measured from the longitudinal and transverse fixed supports was -20.4 kN. The vertical reaction force suddenly increased to -44.5 kN at 0.29 s. After 0.70 s, the vertical reaction force vibrated along the line with the value of -39.1 kN.

As listed in **Table 6.2**, the axial force in the corner support of DF3 before it was lost was -18.7 kN. However, the maximum increased reaction force in the fixed supports

of DF3 was -24.1 kN. In other words, the maximum increased reaction force was larger than the initial axial force in the corner support. The dynamic increase factor for the released column axial forces in DF3 was 1.29.

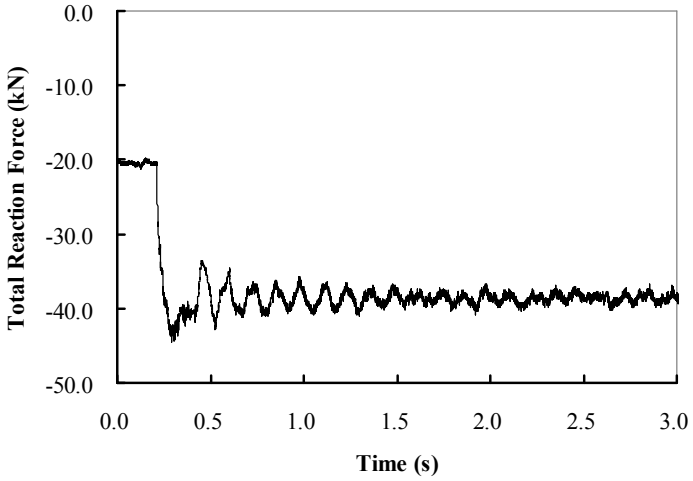

Fig. 6.22: Recorded history of the total vertical reaction force of DF3

6.9.7 Horizontal Reaction Force Responses

Fig. 6.23 presents the history of the horizontal reaction force measured in the fixed supports of the transverse beams of DF3. Horizontal tensile force (4.1 kN) was measured before removal of the corner support. After sudden removal of the corner support, the horizontal reaction force plunged to its peak value of -20.4 kN at a time of 0.37 s. The permanent compressive reaction force (-14.7 kN) was measured after vibration. Thus, it can be concluded that arching action was developed and helped to redistribute the initial axial force in the corner support. However, there was no horizontal tensile force measured during the dynamic process. Therefore, no catenary action was developed to resist progressive collapse for DF3 during the test. As significantly compression force was measured, compressive arch action was possibly developed to resist the collapse.

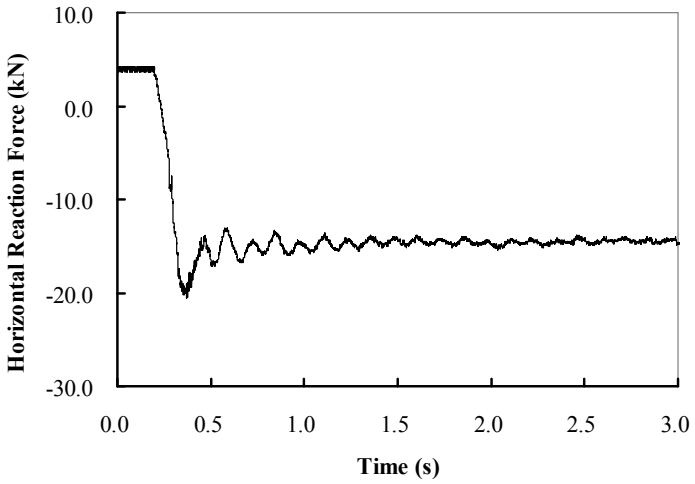

Fig. 6.23: Recorded history of the horizontal reaction force in the transverse beam of DF3

6.9.8 Bending Moment Responses

The history of the bending moment at the longitudinal and transverse fixed supports of DF3 was presented in **Fig. 6.24**. As can be seen from the figure, the initial bending moments at the longitudinal and transverse supports were 2.66 kN.m and 2.45 kN.m, respectively. The bending moment in the longitudinal and transverse fixed supports suddenly increased to 20.8 kN.m and 20.1 kN.m, respectively after removal of the corner support. After free vibration, the permanent moments in the longitudinal and transverse fixed supports were 16.6 kN.m and 16.3 kN.m, respectively. Thus, the beams yielded after sudden removal of the corner support. Moreover, it can be seen that the bending moment suddenly increased by 682.0 % and 720.5 % respectively in the longitudinal and transverse BENFs after removal of the corner support. This demonstrated that the most possibly failure mode was flexural failure at the BENFs, which agreed well with the test observation of F3.

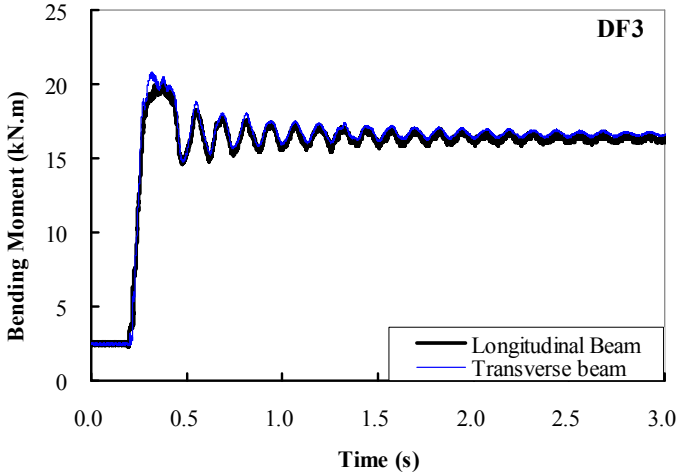

Fig. 6.24: Calculated histories of the bending moments in the fixed supports of DF3

6.10 Test Results of DF4

Specimen DF4 was non-seismically detailed but had a higher transverse reinforcement ratio in the beam potential plastic hinge zones compared to that of DF3. Similar to DF3, it was subjected to full service load as recommended in DoD [D1]. This specimen was designed and tested to investigate the influence of the proposed improved details on the dynamic performance of the substructures for progressive collapse.

6.10.1 General Behavior

Fig. 6.25 illustrates the final crack pattern of the DF4 after test. As illustrated in the figure, severe flexural cracks and hairline shear cracks were observed in the BENFs. However, only flexural cracks were observed in the BENC while hairline diagonal shear cracks were observed in the corner joint.

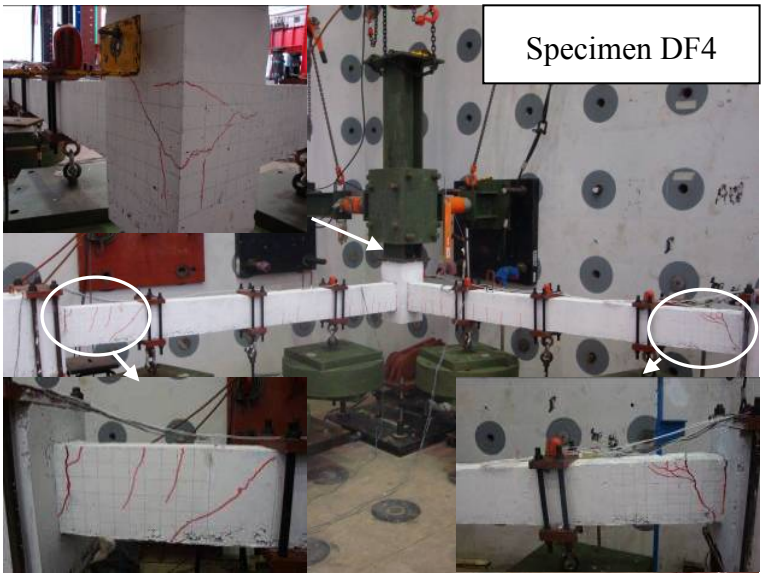

Fig. 6.25: Observed crack pattern of DF4 after test

6.10.2 Displacement Responses

Fig. 6.26 shows the vertical displacement history of the corner joint of DF4. As shown in the figure, DF4 reached the peak displacement of 98.6 mm at a time of 0.38 s. Then, the vertical displacement rebounded to 93.4 mm at a time of 0.45 s, which was about 94.7 % of the first peak displacement. The permanent displacement at the end of vibration was 96.1 mm, which was 97.4 % of the first peak displacement.

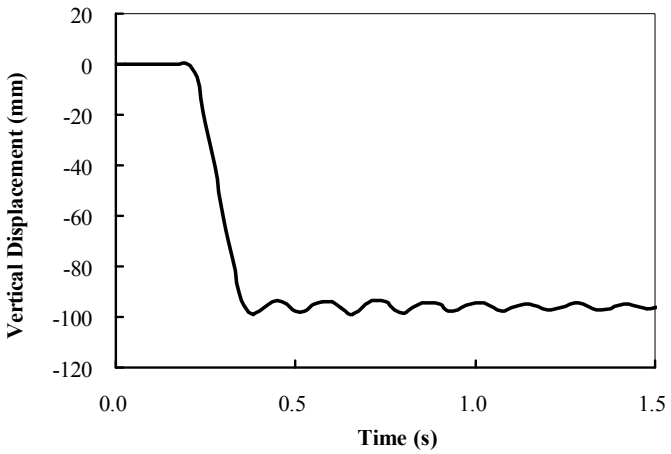

Fig. 6.26: Recorded vertical displacement in the corner joint of DF4

6.10.3 Acceleration Results

Fig. 6.27 presents the recorded acceleration histories of DF4. Only the responses of A2 and A4 were presented as no reliable data was recorded for A1 and A3. The maximum accelerations of A2 and A4 were -2.38g, and -2.44g, respectively. The response of A4 was not similar to A2. Large negative acceleration was observed again after the time of 0.38 s possibly due to a small amount of rigid body vibration occurring in the fixed support of this specimen.

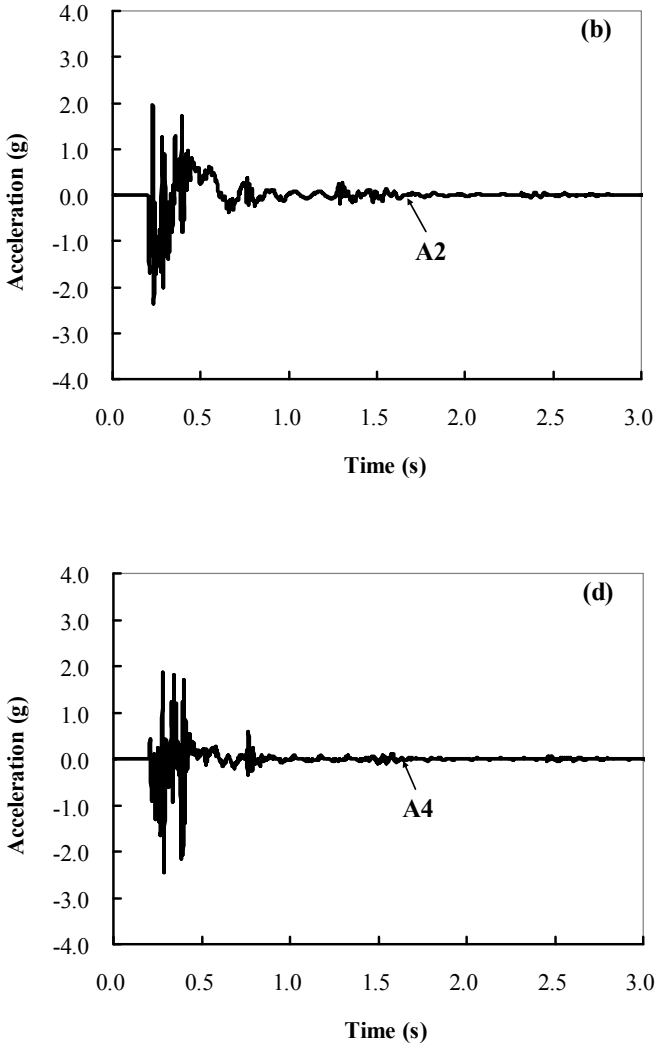

Fig. 6.27: Recorded history of the acceleration at specified locations of DF4

6.10.4 Integral Velocity Responses

Fig. 6.28 illustrates the velocity responses at prescribed locations of DF4. As shown in the figure, the peak velocities of V2 and V4 in DF4 were -0.75 m/s and -0.19 m/s, respectively. The responses of V1 and V3 were not provided as no reliable acceleration readings were recorded for A1 and A3.

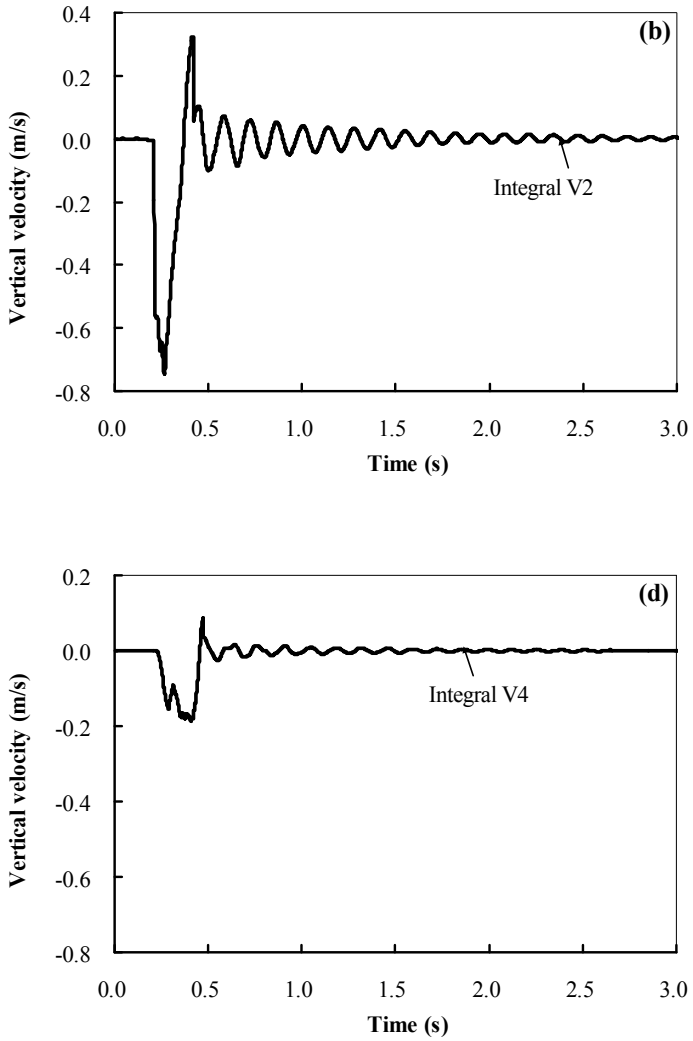

Fig. 6.28: Integral history of the velocity at specified locations of DF4

6.10.5 Strain Gauge Results

Fig. 6.29 presents the strain gauge recording in the flexural reinforcement of DF4. As presented in the figure, the strain of BSTL1 was initially 406 με. However, this tensile strain diminished and ultimately reached the maximum compressive strain of -986 με at a time of 0.47 s. On the other hand, the strain of BSBL1 was initially -165 με. It was suddenly decreased to zero and ultimately attained the maximum tensile strain of 2448 με at a time of 0.40 s. The permanent strains of BSTL1 and BSBL1 were -527 με and 1538 με, respectively. The initial strain readings of BSTL8 and BSBL8 were 584 με and -224 με, respectively. After removal of the corner support, the readings of BSTL8 and BSBL8 rose to 4380 με and -1872 με at the times of 0.47 s and 0.50 s, respectively. This indicates that additional bending moment increased considerably in the BENF.

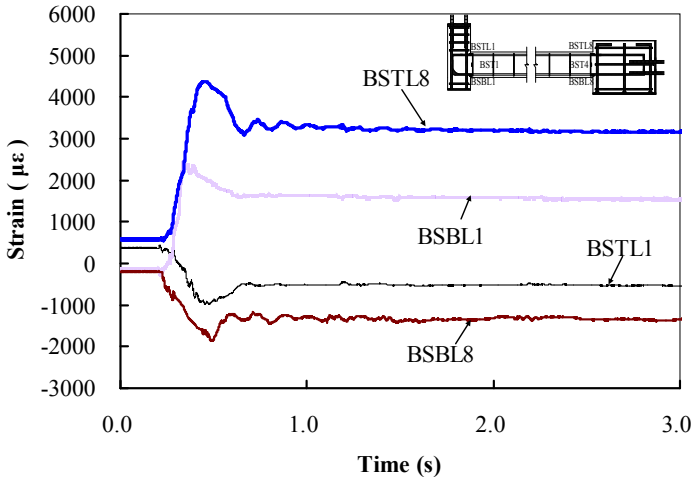

Fig. 6.29: Strain gauge recording in the transverse reinforcement of DF4

6.10.6 Vertical Reaction Force Responses

Fig. 6.30 illustrates the recorded history of the total vertical reaction force of DF4. As displayed in the figure, the total vertical reaction force of DF4 initial was -20.8 kN. The vertical reaction force suddenly increased to -46.6 kN at a time of 0.24 s. After 1.0 s, the total reaction force vibrated along the line with a value of -40.2 kN.

As given in **Table 6.2**, the axial force in the corner support of DF4 before it was lost was -18.8 kN. However, the maximum increased reaction force in the fixed supports of DF4 was -25.8 kN. Thus, the dynamic increase factor for the released column axial forces in DF4 was 1.37.

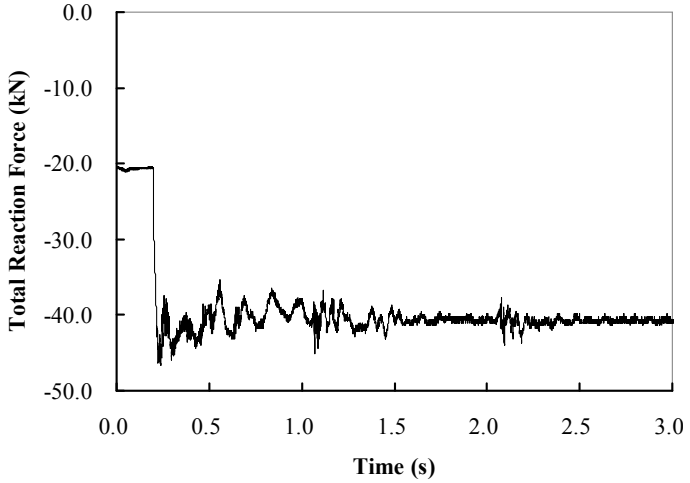

Fig. 6.30: Recorded history of the total vertical reaction force of DF4

6.10.7 Horizontal Reaction Force Responses

Fig. 6.31 presents the history of the horizontal reaction force measured in the fixed supports of the transverse beams of DF4. The horizontal reaction force was 3.8 kN before removal of the corner support. After the sudden removal of corner support, the horizontal reaction force plunged to its peak value of -24.0 kN at a time of 0.33 s. The permanent compressive reaction force of -16.6 kN was measured after vibration. Thus, similar to DF3, no horizontal tensile force was measured during the dynamic process. Thus, no catenary action was developed to resist progressive collapse for DF4 during the test.

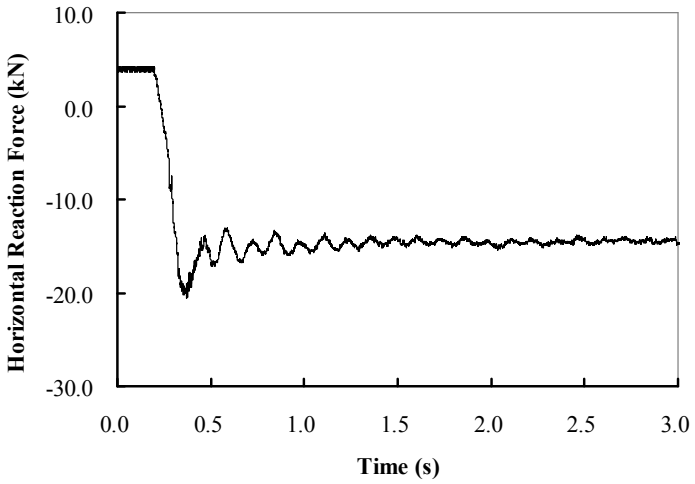

Fig. 6.31: Recorded history of the horizontal reaction force in the transverse beam of DF4

6.10.8 Bending Moment Responses

The histories of the bending moments at the longitudinal and transverse fixed supports of DF4 were presented in **Fig. 6.32**. As can be seen from the figure, the initial bending moments at the longitudinal and transverse supports were 2.79 kN.m and 2.51 kN.m, respectively. The bending moments in the longitudinal and transverse fixed supports suddenly rose to 20.1 kN.m and 19.5 kN.m, respectively after removing the corner support. After free vibration, the permanent moments recorded in the longitudinal and transverse fixed supports were 14.0 kN.m and 14.8 kN.m , respectively. It can be seen that the bending moment suddenly rose by 620.0 % and 676.9 %, respectively in the longitudinal and transverse fixed supports, respectively.

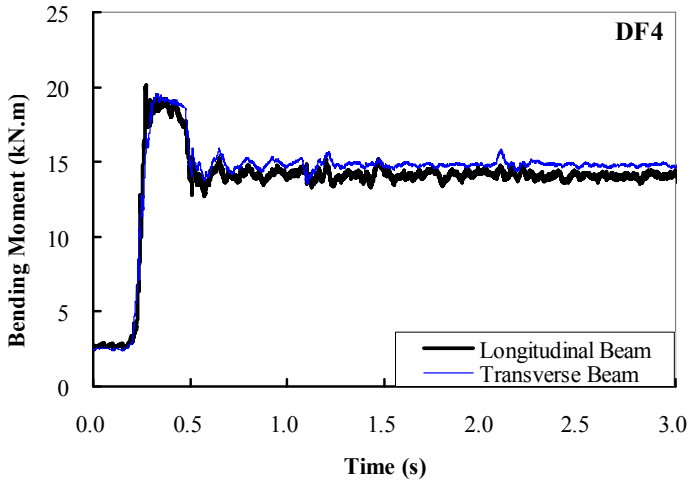

Fig. 6.32: Calculated histories of the bending moments in the fixed supports of DF4

6.11 Test Results of DF5

Specimen DF5 had a longer design span length (2775 mm) than that of DF3 (2175 mm). The dimensions and reinforcement details are given in **Table 6.2**. This specimen was designed to investigate the influence of span length on the dynamic response of substructures for progressive collapse. The quasi-static results had indicated that the ultimate capacity of F5 was 26.8 kN. However, the design axial force in the corner column of DF5 was 29.1 kN, if it was subjected to the full service load condition. Thus, it was predictable that DF5 will collapse when subjected to the full service load. Therefore, a reduced service load 0.8(1.2 DL+0.5 LL) was applied to the specimen before removal of the corner support. As shown in **Table 6.2**, the measured axial force in the corner support before removed was 23.5 kN, which was about 87.6 % of the measured static ultimate capacity of F5 (26.8 kN).

6.11.1 General Behavior

As displayed in **Fig. 6.33**, DF5 suffered severe damage after removal of the corner support. Extremely wide shear cracks and flexural cracks were observed in the BENFs while significant spalling was observed in the corner joint. The damage in the BENCs was negligible compared with that in the BENFs. It should be pointed out that the collapse of DF5 was stopped by the pin support of the column removal apparatus when the maximum displacement exceeded the allowed displacement of about 360.0 mm. It was concluded that in the absence of the pin support, DF5 would have totally collapsed.

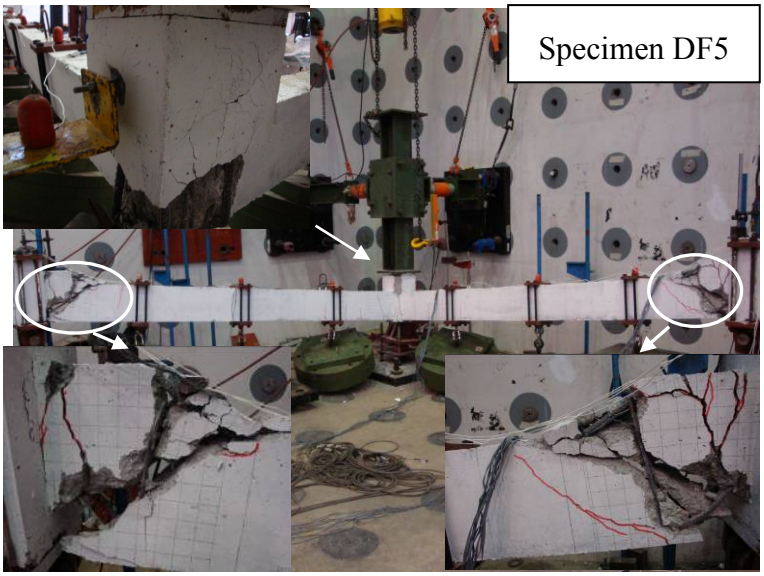

Fig. 6.33: Observed crack pattern of DF5 after test

6.11.2 Displacement Responses

Fig. 6.34 shows the vertical displacement history of the corner joint of DF5. As shown in the figure, the vertical displacement suddenly increased and exceeded 280.0 mm, which was the measurement capacity of the LVDT placed in the corner column. As described in the above, the permanent vertical displacement exceeded 360.0 mm, which was the distance from the bottom surface of the corner column to the top of the pin support. No reliable data was recorded for this specimen as its collapse was

stopped by the pin support of the column removal apparatus, causing about large random noises in the acceleration readings.

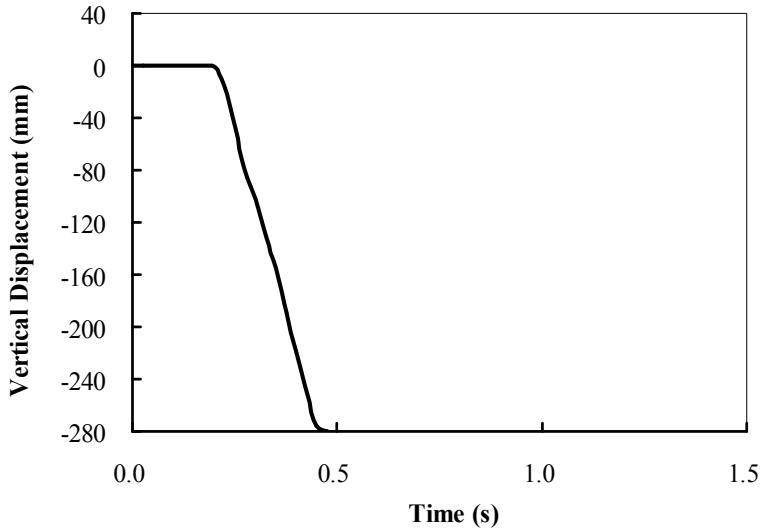

Fig. 6.34: Recorded vertical displacement in the corner joint of DF5

6.12 Test Results of DF6

Specimen DF6 had unequal spans in the longitudinal and transverse directions in order to investigate the influence of the unequal span on the dynamic response of substructures for progressive collapse. The dimensions and reinforcement details are given in **Table 6.2**. Full service load (1.2 DL+0.5 LL) was applied on this specimen before removal of the corner support. As shown in **Table 6.2**, the measured axial force in the corner support before removed was 23.2 kN, which was about 89.2 % of the measured static ultimate capacity of F6 (26.0 kN).

6.12.1 General Behavior

Fig. 6.35 presents the failure mode of DF6 at the final stage of the test. Similar to DF5, DF6 collapsed following removal of the corner support. However, asymmetrical

damages were observed in the longitudinal and transverse beams. Similar to DF5, extreme damage concentrated in the transverse BENF. However, the damages occurring in the longitudinal BENF of DF6 were much milder compared to that of DF5.

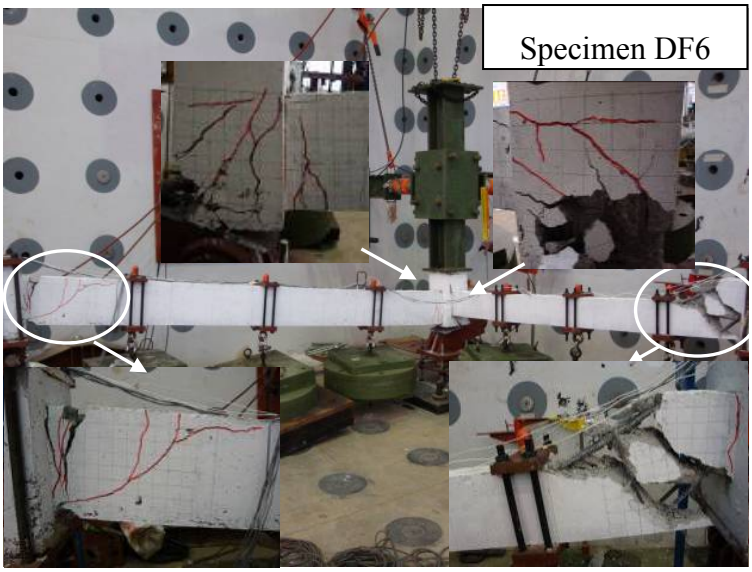

Fig. 6.35: Observed crack pattern of DF6 after test

6.12.2 Displacement Responses

Fig. 6.36 presents the vertical displacement history of the corner column of DF6. As shown in the figure, the vertical displacement suddenly increased and exceeded 260.0 mm, which was the measurement capacity of the LVDT placed in the corner column. Similar to DF5, it would have completely collapsed in the absence of the pin support of the column removal apparatus or should there be sufficient space to allow the gravity weights to drop freely.

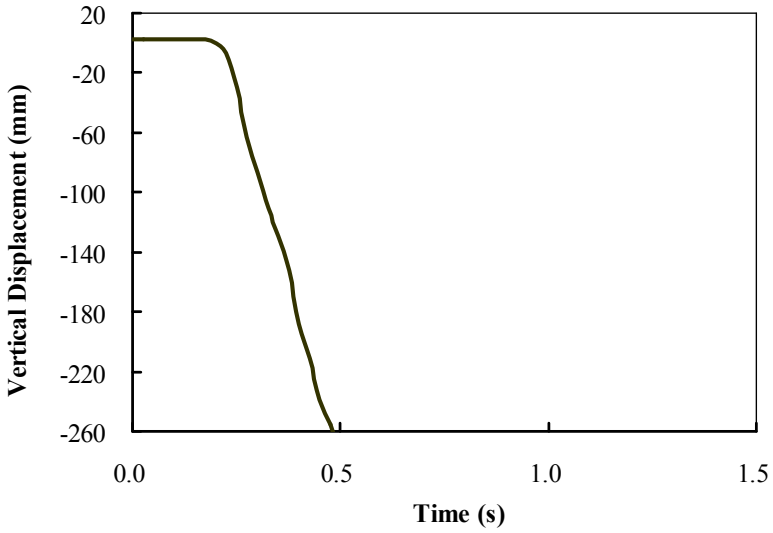

Fig. 6.36: Recorded vertical displacement in the corner joint of DF6

6.13 Discussion of the Influence of Each Variable

6.13.1 The Effect of Seismic Detailing

The non-seismically detailed specimen DF1 had severe flexural and shear cracks in the BENFs, while only limited flexural cracks in the BENFs were observed in the seismically detailed specimen DF2. Moreover, no cracks were observed in the corner joint of DF2, while several hairline diagonal cracks were observed in the corner joint of DF1. Comparing with the peak vertical displacements of these two specimens, it can be seen that the peak vertical displacement of DF2 was only 34.6 % of that of DF1. Similar trends were observed for the acceleration and velocity results.

6.13.2 The Effect of Different Service Load Condition

As listed in **Table 6.2**, DF3 was subjected to a full service load (1.2DL+0.5LL) while DF1 was subjected to a reduced service load of 0.9(1.2DL+0.5 LL) before removal of the corner support. Comparing the crack patterns of DF3 with that of DF1, more severe cracks were observed in the corner joint and longitudinal BENF in DF3. However, the shear cracks occurring in the transverse BENF of DF1 were more severe than those of DF3. This was an unexpected phenomenon and was possibly due to inherent drawbacks existing in DF1. Comparing the displacement response of DF3 with that of DF1 indicated that the measured vertical displacement response of DF3 was larger than that of DF1 by 74.7 %.

6.13.3 The Effect of Modified Detailing

DF4 had a much higher transverse reinforcement ratio in the beam potential plastic hinge zone compared to that of DF3. Similar to DF3, DF4 was subjected to a full service load (1.2DL+0.5LL) before removal of the corner support. Comparing the crack pattern of DF4 with that of DF3, it can be seen that a slight reduction of cracks were observed in the BENFs and corner joint in DF4 although, in general, similar crack patterns were observed in both specimens. By comparing the displacement response of DF4 to that of DF3, it can be found that DF4 sustained a decrease in the peak vertical displacement by 32.2 %.

6.13.4 The Effect of Design Span Length

As illustrated in **Table 6.2**, DF5 had 2775 mm clear span and was subjected to a factored service load of 0.8 (1.2DL+0.5LL). DF5 failed with extensive damage in the BENFs and corner joint. The peak vertical displacement exceeded 360 mm. In fact, without the pin support of the column removal apparatus or should there be sufficient

space to allow the gravity weights to drop freely, the specimen would be expected to fail completely because the dynamic ultimate strength of F5 obtained from the analytical analysis (SDOF), which was presented in **Chapter 7**, was significantly less than the initial axial force in the corner support (23.5 kN).

6.13.5 The Effect of Span Aspect Ratio

DF6 had different span lengths in the longitudinal and transverse directions, and it was subjected to the full service load of (1.2DL+0.5LL). It can be seen from **Fig. 6.35** that extensive damage occurred in the transverse BENF. Although severe cracking also occurred in the longitudinal BENF, it was much milder compared with that in the transverse beam. Compared with DF3, DF6 collapsed because of the longer span in the longitudinal beam, which resulted in a larger initial axial force in the corner support of DF6 (refer to **Table 6.2**). The axial force, previously resisted by the corner support, tried to redistribute into both fixed supports after the corner support was removed. However, almost half of the axial force will redistribute into the transverse fixed support as the stiffness in the longitudinal and transverse beams were similar. Therefore, more axial force was distributed into the transverse fixed support of DF6 compared to that of DF3. This resulted in the total collapse of the transverse beam of DF6 while less damage was observed in that of DF3.

6.14 Discussion of the Dynamic Load Increase Factor

As described in the introduction section, during a collapse event after one of the members has failed, the structure will redistribute its applied loads and come to rest in a new equilibrium position. The movement during this change produces inertial forces. Previous researchers, such as Pretlover *et al.* [P8], concluded that a static analysis predicting a damaged structure to be safe from progressive failure may not be

conservative if inertial effects are taken into consideration. Thus, it is important to evaluate the dynamic effects. Unfortunately, little research regarding progressive collapse has considered dynamic effects especially for the experimental tests. The dynamic load increase factors (DLIF), which is defined as the static ultimate strength divided by the dynamic ultimate strength of the tested substructures, can be evaluated in this study due to similar specimens were both subjected to quasi-static and dynamic tests.

The quasi-statically tests, which were described in **Chapter 4**, indicated that the static ultimate strength of F2, F3, F4, F5, and F6 were 36.5 kN, 25.8 kN, 27.5 kN, 26.8 kN, and 26.0 kN, respectively. As shown in **Table 6.2**, the dimensions and reinforcement details of the specimen tested in the dynamic tests were similar to the corresponding specimen tested in the quasi-static tests. The axial force in the corner support of DF1, DF2, DF3, DF4, DF5, and DF6 initially were 16.9 kN, 16.9 kN, 18.7 kN, 18.8 kN, 23.5 kN and 23.2 kN, respectively. Because DF1, DF2, DF3, and DF4 survived after removal of the corner support, it can be concluded that the DLIF of Specimens F2, F3, and F4 were less than 2.16, 1.38, and 1.46, respectively. Conversely, DF5 and DF6 totally collapsed after removal of the corner support. Thus, it can be concluded that the DLIF of Specimens F5 and F6 were larger than 1.14 and 1.12, respectively. As the exact value of the dynamic ultimate strength of each specimen can not be obtained by a single dynamic test, the exact value of the DLIF for each specimen could not be specified. Therefore, a series of analytical analyses were implemented to predict the dynamic ultimate strength of each specimen, which will be introduced in **Chapter 7**. After that, the values of DLIF obtained from the analytical results were compared with that suggested in the DoD [D1] to evaluate the accuracy of the dynamic increase factor (DIF) recommended in the existing design guideline.

6.15 Summary

Considering of the lack of related experimental tests to validate numerical tools and analytical models and the fact that in-situ tests are extremely costly and time consuming, a series of beam-column substructures with suitable boundary conditions were tested dynamically at NTU, Singapore. A column removal apparatus was designed to simulate the sudden removal of the ground corner column under extreme loading. Extensive instrumentations were installed to monitor the dynamic performance of the substructures following the column removal. Based on the above comparisons as well as the test results reported in **Chapter 6**, the following conclusions can be drawn:

1. The column removal apparatus proved to be effective in dynamic tests as the measured release time did not exceed 0.0035 s, which was much less than 10% of the natural period of the substructures.

2. Peak acceleration measured in the corner column could reach up to 3.5 g in Specimen DF3 but the peak acceleration decreased with distance away from the corner column.

3. Integration method could be utilized to determine the velocity and displacement responses when only the acceleration results were available. However, the baseline correction must be conducted before integration.

4. The peak value of the total vertical reaction force measured in the fixed supports was larger than the axial force of the corner column before its subsequent removal. This was due to the inertial force which was developed after the sudden removal of the corner support.

5. No tensile force was observed in the horizontal reaction force in the fixed supports of DF3 and DF4. This indicated that catenary action did not develop to resist the progressive collapse during the tests of DF3 and DF4.

6. The crack patterns and strain gauge results indicated that the direction of the bending moment changed in the BENC after the sudden removal of the corner support.

7. The bending moment results calculated in the fixed supports and strain gauge results verified that significant bending moment developed in the BENF after the sudden removal of the corner support.

8. The test results confirmed that seismic detailing succeeded in increasing the resistant capacity of the structures against progressive collapse. Structures with longer design span lengths exhibited a higher vulnerability for progressive collapse compared with the structures with shorter span lengths. Furthermore, more attention should be paid to structures subjected to a higher service load.

9. The dynamic performance of the test specimen together with the quasi-static behavior of the corresponding specimens indicated that the values of DLIF ranged from 1.14 to 1.38 for the test specimens.

CHAPTER 7

ANALYTICAL PREDICTION OF THE DYNAMIC BEHAVIOR OF RC SUBSTRUCTURES FOR PROGRESSIVE COLLAPSE

7.1 Introduction

The dynamic test results of the six RC beam-column substructures under the loss of a corner column scenario are presented in **Chapter 6**. In this chapter, analytical analysis will be carried out to establish a deeper understanding of the dynamic performance of RC substructures for progressive collapse. A single degree of freedom (SDOF) model was utilized to predict the exact value of the dynamic ultimate strength of the dynamically tested specimens. In addition, the values of the dynamic load increase factor (DLIF) of the test specimens can be determined by comparing the static ultimate strength values attained in **Chapter 4** with the dynamic ultimate strength obtained via the SDOF model. The test results obtained in the experimental study in **Chapter 6** were used for validation of the SDOF method. Moreover, the values of DLIF obtained from the SDOF analysis were compared with the values suggested by the existing design guideline DoD [D1]. Another simplified analytical model–the capacity curve model, was also conducted to predict the dynamic ultimate strength of the dynamically tested specimens as well as the values of DLIF.

7.2 SDOF Representing of RC Substructures Subject to a Step Force

The essential physical properties of any linearly elastic structural or mechanical system subjected to an external source of excitation or dynamic loading include its mass, elastic properties (flexibility or stiffness), and energy-loss mechanism or damping. In the simplest model of a SDOF system, each of these properties is assumed to be concentrated in a single physical element. A sketch of such a system is shown in **Fig. 7.1.** The equation of the motion for this system is given as:

$$m_e\ddot{x} + c_e\dot{x} + k_e x = P(t) - R(t) \qquad (7\text{-}1)$$

where m_e is the equivalent mass, c_e is the equivalent viscous damping, k_e is the effective stiffness, $P(t)$ and $R(t)$ are the applied force and reaction force respectively, and x , $\dot{x}$ and $\ddot{x}$ are the displacement, velocity and acceleration of the mass, respectively.

Rigorous or exact analysis of structural elements subjected to a dynamic loading condition is only possible for relatively simple structures, and only when the loading function is a convenient mathematical function. Fortunately, when a building is subjected to sudden column loss, its dynamic response may be simulated by imposing a step load on the remaining parts of the structure (Izzuddin *et al*. [I2]; Kim and Park [K2] and Ruth *et al*. [R1]). Moreover, since the structural behavior under sudden column loss is usually dominated by a single deformation mode, an inelastic SDOF model may be used to simulate the sustained loading and the displacement of the removed column point (Sasani and Sagiroglu [S3]). However, there are several difficulties in using SDOF model to predict the progressive collapse performance of RC substructures:

- The beam equivalent mass m_e is difficult to calculate as it constantly changes

during the loading process.

- The beams do not remain elastic until the point of failure; in fact, their load-displacement behavior is nonlinear, thus rendering their effective stiffness k_e nonlinear as well.

- The equivalent viscous damping c_e varies along with the stiffness if the damping ratio is assumed to be constant.

In the following sections, the parameters m_e, k_e, and c_e are individually determined.

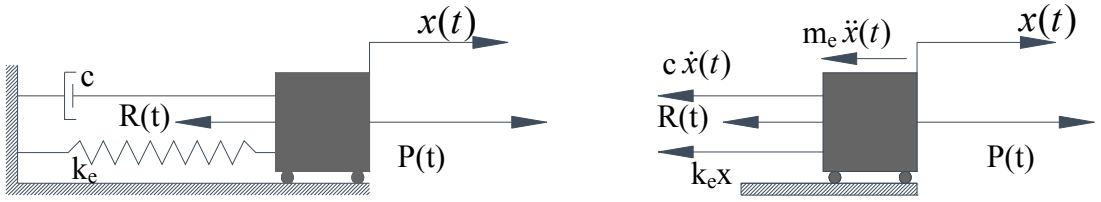

(a) Idealized SDOF system (b) Free body diagram

Fig. 7.1: Equivalent single degree of freedom system

7.2.1 Equivalent Mass m_e

As presented in **Fig. 7.2**, gravity weights were applied on the beams before removal of the corner support. The equivalent mass can be mathematically expressed as follows:

$$m_e = \int m(z)[\psi(z)]^2 d_z + \sum_k m_k[\psi(z_k)]^2 \qquad (7\text{-}2)$$

where $m(z)$ is the distributed mass function, $\psi(z)$ is the shape function, m_k is the concentrated mass k at location of z_k, and $\psi(z_k)$ is the shape function value at location of z_k.

Based on the test results, the deformation shape function of the beam was assumed to be that of a cantilever beam in this analysis. The equivalent masses of DF1, DF2, DF3, DF5 and DF6 were determined based on Eq. 7-2 as 1256 kg, 1256 kg, 1361 kg, 1361 kg, 1602 kg and 1532 kg, respectively.

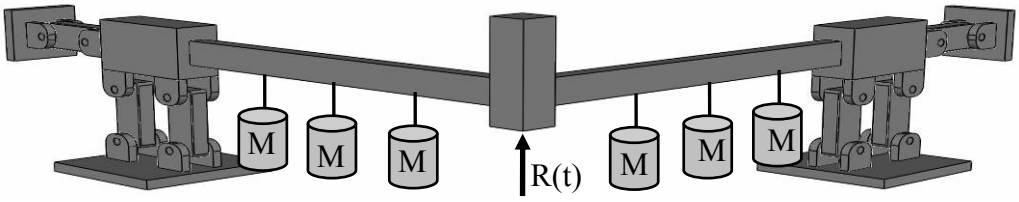

Fig. 7.2: The weight distribution along the beams of the substructures

7.2.2 Effective Stiffness k_e

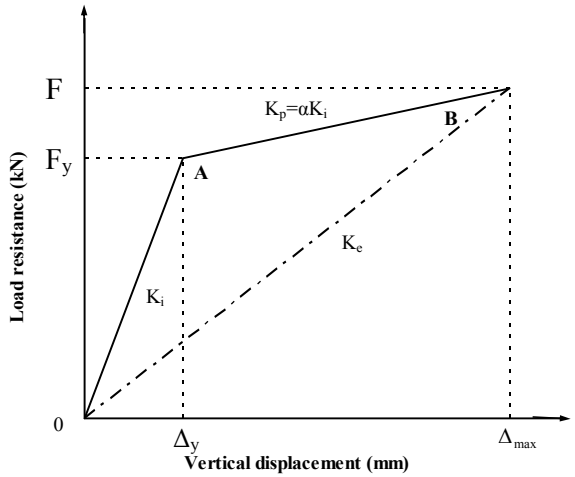

Fig. 7.3: The approaches for determining the post-yield stiffness of substructures in Tsai [T2] and Calvi *et al.* [C1]

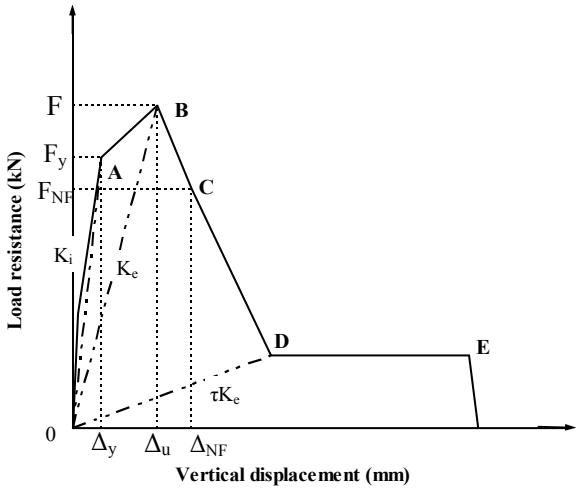

Fig. 7.4: The proposed approach for determining the post-yield stiffness of the substructures

As mentioned above, another challenge in this analytical study was the need to properly determine the effective stiffness k_e. As large deformations are acceptable for structures against progressive collapse, the effective stiffness of a structure with large deformation should be well qualified. There are two common approaches to consider the post-yield stiffness of the structures:

- Tsai [T2] and Sasani and Sagiroglu [S3] assume the resistant function of a frame after losing an interior column as a bilinear load-displacement relationship. The strain hardening stiffness of the structure was determined by a strain hardening ratio α. As shown in **Fig. 7.3**, the bilinear resistant function assumes the resistance of the structure slowly increases with a rise in the displacement until the maximum displacement Δ_{max} is reached. The maximum displacement can be defined in a number of ways, including displacement at peak strength, displacement corresponding to 20 % or 50 % degradation from the peak (nominal strength), and displacement at initial fracture of transverse reinforcement

(Priestley [P5]).

- Calvi *et al.* [C1] characterizes the post-yield performance of the structures via defining the secant stiffness k_e at the maximum displacement Δ_{max} (refer to **Fig. 7.3**).

The two approaches above are frequently used due to the simplicity of the methods and the ease in interpreting the results of the SDOF analysis. However, in order to reproduce the displacement-time response of each specimen well, a more rigorous definition of effective stiffness is needed.

As shown in **Fig. 7.4**, the initial stiffness (segment 0-A) was taken as the secant stiffness of the structure at the first yield (Paulay and Priestley [P3]); the post-yield stiffness at point "B" was equated to the secant stiffness of the structure at that point. The interpolation method was used to determine the effective stiffness of the point in between the points A to B. The post-yield stiffness at point "D" was set equal to the secant stiffness at that point multiplied by a stiffness reduction factor τ=0.5, and the interpolation method was also used to determine the effective stiffness of the points in between the points B to D. The reduction factor τ was introduced here for considering the structural softening of substructures after yield. The influence of the stiffness reduction factor τ on the response of the substructures was investigated in the following parametric study.

7.2.3 Equivalent Viscous Damping c_e

The damping coefficient and damping force depend on the stiffness value adopted. In most inelastic analysis, this is taken as the initial stiffness. This, however, results in

large and spurious damping forces when the response is inelastic. Priestley and Grant [P6] have claimed that this is inappropriate, and that secant stiffness should be used instead as the basis for elastic damping calculations. Thus, the equivalent viscous damping used in the current study was based on the secant stiffness. It should be emphasized that the damping coefficient varied along with the secant stiffness. A large damping ratio (ζ=20%) was used in the current SDOF analysis because of large damping was observed in the test results. The influence of the damping ratio on the response of the substructures was also investigated as a parameter in the following parametric study.

7.2.4 Applied Force $p(t)$

As shown in **Fig. 7.2**, the gravity weights were applied on the substructures, generating a reaction force in the corner support equivalent to P. As illustrated in **Fig. 7.5**, at a time of t_0, the reaction force began to decrease, reaching zero at a time of $t_0+\Delta t$. The duration of the column removal (Δt) is 0.003 s based on the test results.

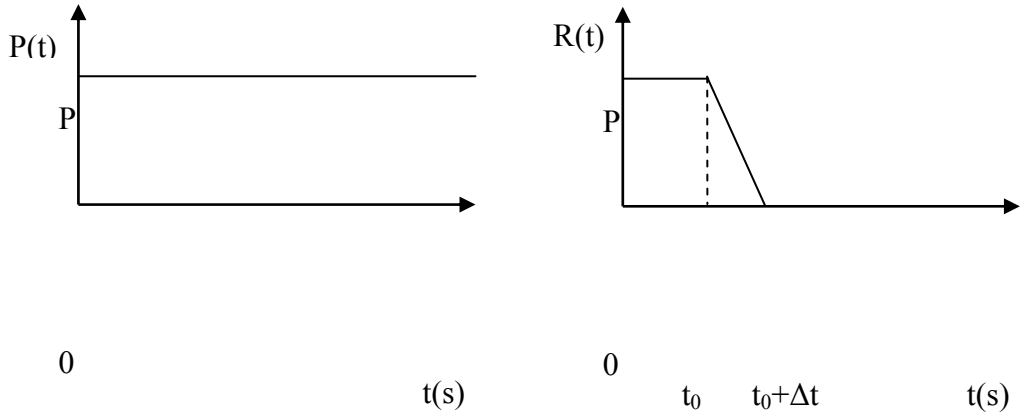

(a) Applied load-time relationship (b) Reaction force-time relationship

Fig. 7.5: The applied load and reaction force-time relationship

7.3 Validating the Proposed SDOF Model

Fig. 7.6 presents the comparison of the analytical displacement response of each specimen with the response obtained from the test. In general, the analytical model captured the first peak displacement very well, especially for DF2. DF2 had the best match as its performance remained in the elastic region during the test. Moreover, the analytical method successfully predicted the total collapse of DF5 and DF6 after removal of the corner support. However, it should be pointed out that the analytical model prediction of the free vibration of the specimens (natural damping period) was mediocre, except DF2. Furthermore, the first peak displacement of each specimen obtained in the SDOF model occurred after the one measured in the test. As shown in **Fig. 7.6a**, the rate of increase of the displacement was significantly reduced after the displacement reached about 40 mm. This was due to the significant decrease of effective stiffness after the specimens exceeded the static ultimate strength (refer to **Fig. 7.4**). Fortunately, the extent of damage of the structure for progressive collapse was mainly controlled by the first peak displacement. Thus, the proposed SDOF model was able to provide adequate projections to conduct the parametric studies and predict the dynamic ultimate strength of each specimen as illustrated in the following sections.

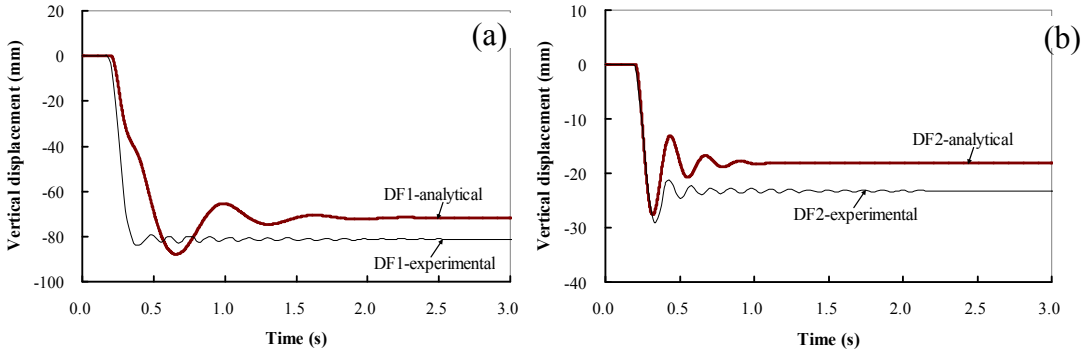

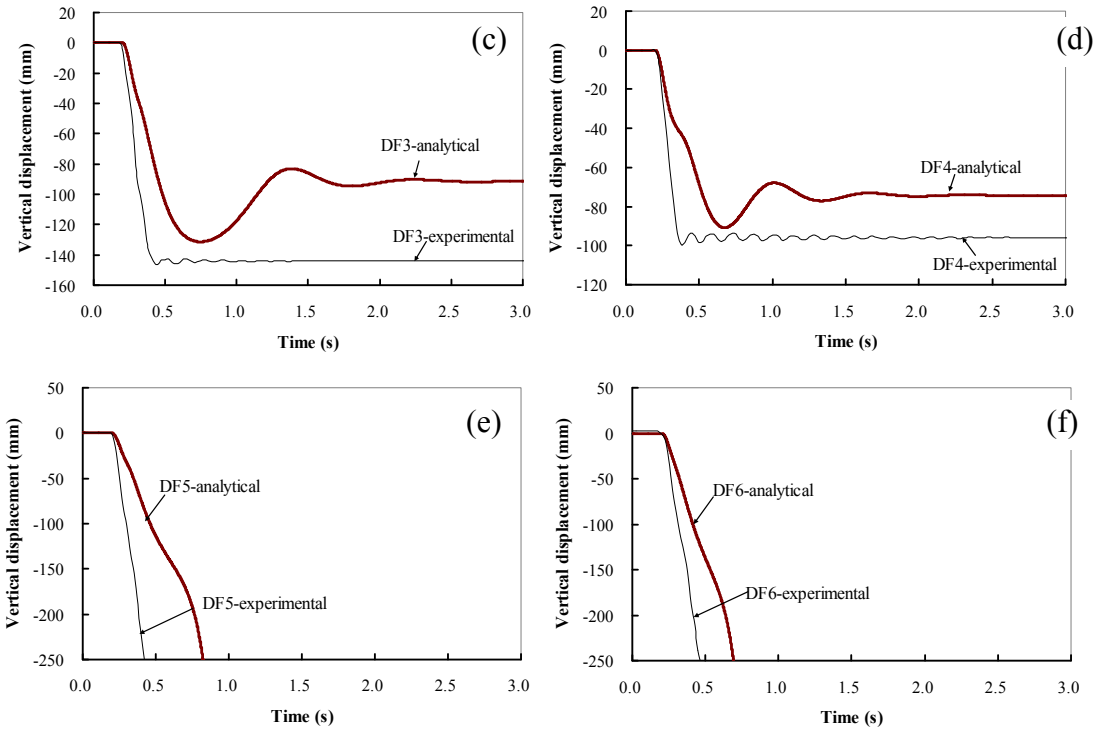

Fig. 7.6: Comparison of the experimental and analytical vertical displacement response of each specimen

7.4 Parametric Studies

Using the SDOF models developed above, a parametric study of RC substructures was carried out with the following cases being considered for each parameter: stiffness reduction factors τ=0.0, τ=0.3, τ=0.5, τ=0.6, τ=0.7, τ=0.8, and τ=1.0, respectively; and damping ratios ζ=5%, ζ=10%, ζ=15%, ζ=20%, and ζ=25%, respectively.

7.4.1 Influence of the Stiffness Reduction Factor τ

The influence of the stiffness reduction factor τ in the descending branch of the load-displacement curve is presented in **Fig. 7.7**. As shown in the figure, DF1 will collapse

totally if τ equals to 0.0. It should be emphasized that τ=0.0 represented the residual strength in the descending branch of the load-displacement curve which was not included in the analytical analysis. The peak and permanent vertical displacement of the specimen decreased significantly with an increase in the stiffness reduction factor. However, the effect of the stiffness reduction factor on the response of the specimen became negligible when the factor was larger than 0.7. This was due to the displacement response being controlled by the ascending part of the load-displacement curve. In previous research, such as Sasani and Sagiroglu [S3], the effective stiffness and resistance of the specimen in the descending branch was excluded in their SDOF models. However, both the experimental and analytical results indicated that this simplification was rather conservative. In the current analytical study, τ=0.5 was utilized and the comparison of the experimental with the analytical results proved that it was a reasonable assumption. However, more dynamic progressive collapse tests should be conducted to further verify it.

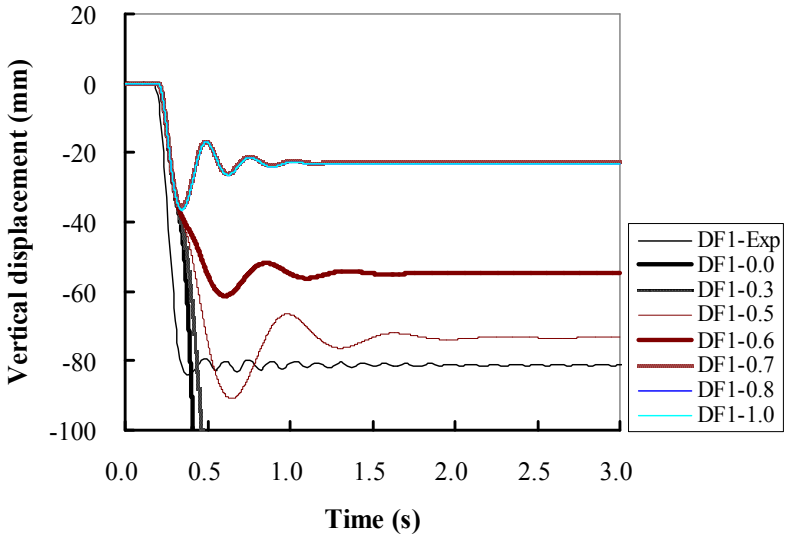

Fig. 7.7: Influence of the stiffness reduction factor on the displacement-time response

7.4.2 Influence of the Damping Ratio

Five damping ratio values, ζ=5%, ζ=10%, ζ=15%, ζ=20%, and ζ=25% were chosen to investigate the influence of this variable on the displacement response. As shown in **Fig. 7.8**, with the damping ratio increasing from 5% to 10%, 15%, 20%, and 25%; the peak displacement decreased by approximately 17.2 %, 26.9 %, 33 %, and 47.0 %, respectively. Similarly, the permanent displacements also decreased with an increasing damping ratio. Similar results were obtained in Sasani and Sagiroglu [S3] where the peak displacement ductility decreased by 42 % as the damping ratio in the SDOF system was increased from 5% to 20%. The damping ratio of ζ=20% was utilized in the current analytical study as the closest analytical results was achieved. The large damping observed in the experimental results was perhaps in part due to the dynamic friction between the steel column and the steel pin in the rotational constraint assembly mechanism. The large plastic deformations of the reinforcing bars and the associated dissipation of energy may be considered as an additional source of damping in the system, according to Sasani *et al*. [S1].

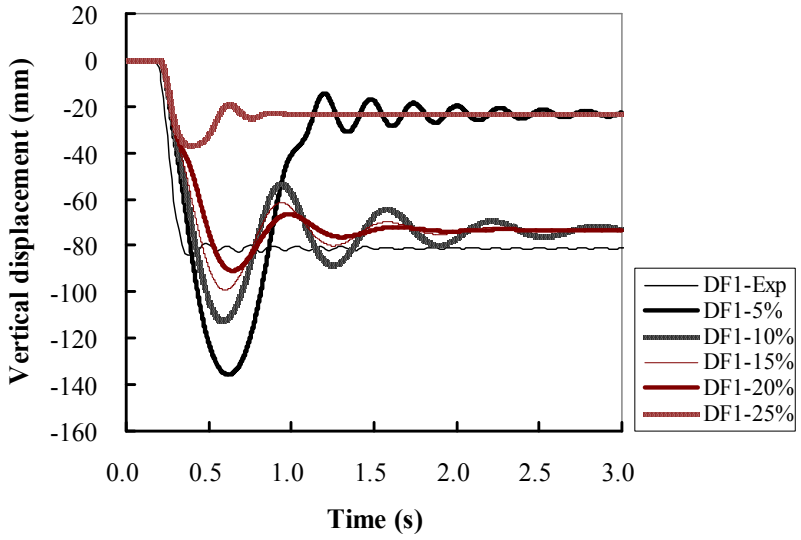

Fig. 7.8: Influence of the damping ratio on the displacement-time response

7.5 Dynamic Ultimate Strength of the Tested Specimens

The dynamic ultimate strength of each specimen could be determined by conducting a series of incremental dynamic analyses for each specimen. **Fig. 7.9** presents the displacement response of each specimen with increasing initial axial force in the corner support. As illustrated in **Fig. 7.9a**, the peak displacement increased by 2.7 % when the axial force in the corner support increased from 16.1 kN to 16.2 kN. However, when the initial axial force increased from 16.2 kN to 16.3 kN, the peak displacement increased by 116.9 %. Moreover, the first peak displacement was 138.2 mm when the initial axial force in the corner support before removal was 18.8 kN. However, the peak displacement exceeded 1000 mm when the initial axial force in the corner support was 18.9 kN. Therefore, the dynamic ultimate strength of DF1 was 18.8 kN. As obtained in the quasi-static test, the static strength of this specimen was 25.8 kN (F3 in **Chapter 4**). Thus, we found that the dynamic load increase factor (DLIF), defined as the ratio of the static ultimate strength (SUS) to the dynamic ultimate strength (DUS), was 1.37 for this specimen.

If we excluded the contribution of the residual strength of the specimen (assume τ=0.0), the DUS of DF1 was only 16.2 kN. Thus, the value of DLIF was 1.59. For the remaining specimen, similar behavior was observed and the comparison of the static and dynamic ultimate strength is given in **Table 7.1**.

Table 7.1: Comparison of the Analytical Values of DLIF with the Values of DIF Suggested in DoD (2009)

Test	DUS (τ=0.0) (kN)	DUS (τ=0.5) (kN)	SUS (kN)	DLIF (τ=0.0)	DLIF (τ=0.5)	DIF (DoD[D1])
DF1	16.2	18.8	25.8	1.59	1.37	2
DF2	23.5	25.6	36.5	1.55	1.43	2
DF4	18.3	20.8	27.5	1.50	1.32	2
DF5	19.0	21.3	26.8	1.41	1.26	2
DF6	16.4	21.5	26.0	1.59	1.21	2

Note: DUS , SUS = Dynamic Ultimate Strength, Static Ultimate Strength, respectively

$DLIF$=Dynamic Load Increase Factor ($\frac{SUS}{DUS}$); DIF=Dynamic Increase Factor

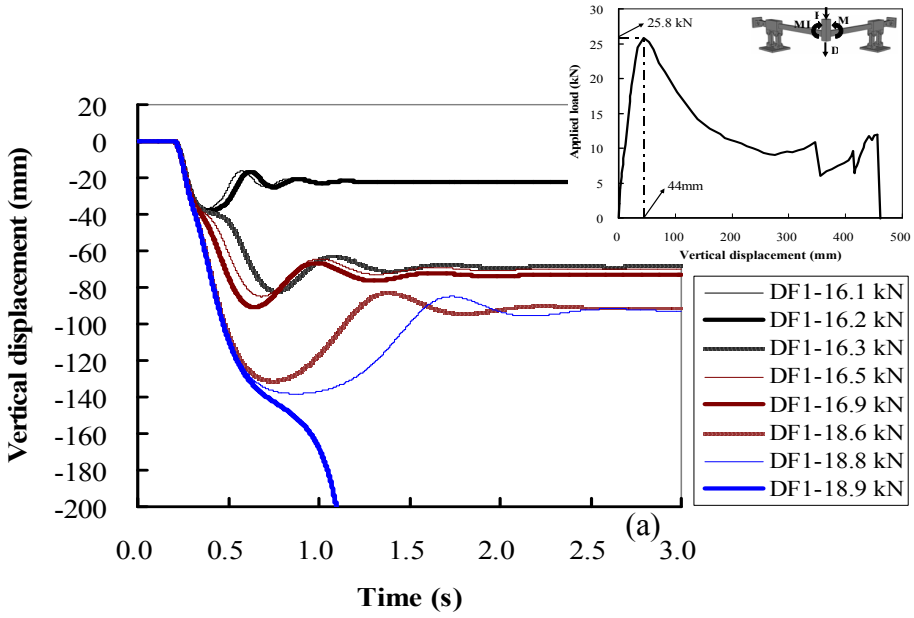

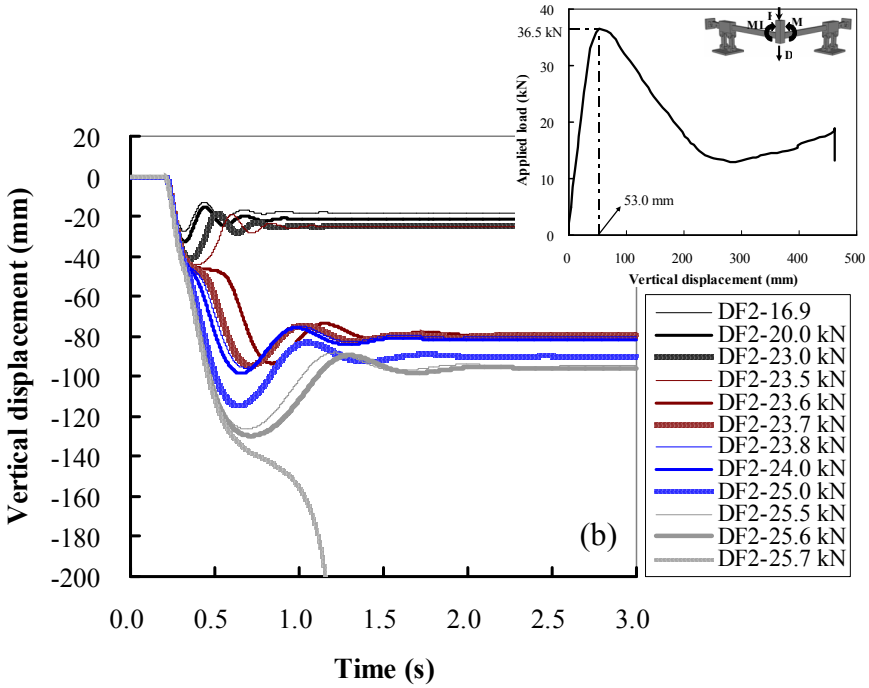
Vertical displacement (mm)
Time (s)
Applied load (kN)
Vertical displacement (mm)
36.5 kN
53.0 mm
(b)
DF2-16.9
DF2-20.0 kN
DF2-23.0 kN
DF2-23.5 kN
DF2-23.6 kN
DF2-23.7 kN
DF2-23.8 kN
DF2-24.0 kN
DF2-25.0 kN
DF2-25.5 kN
DF2-25.6 kN
DF2-25.7 kN

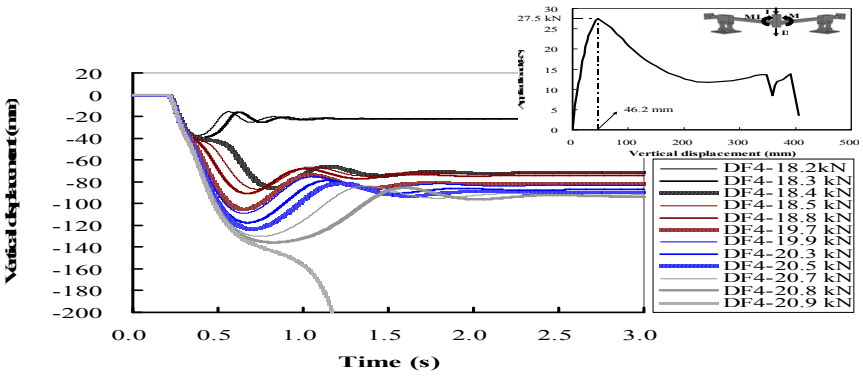
Time (s)
27.5 kN
46.2 mm
DF4-18.2kN
DF4-18.3 kN
DF4-18.4 kN
DF4-18.5 kN
DF4-18.8 kN
DF4-19.7 kN
DF4-19.9 kN
DF4-20.3 kN
DF4-20.5 kN
DF4-20.7 kN
DF4-20.8 kN
DF4-20.9 kN

(c)

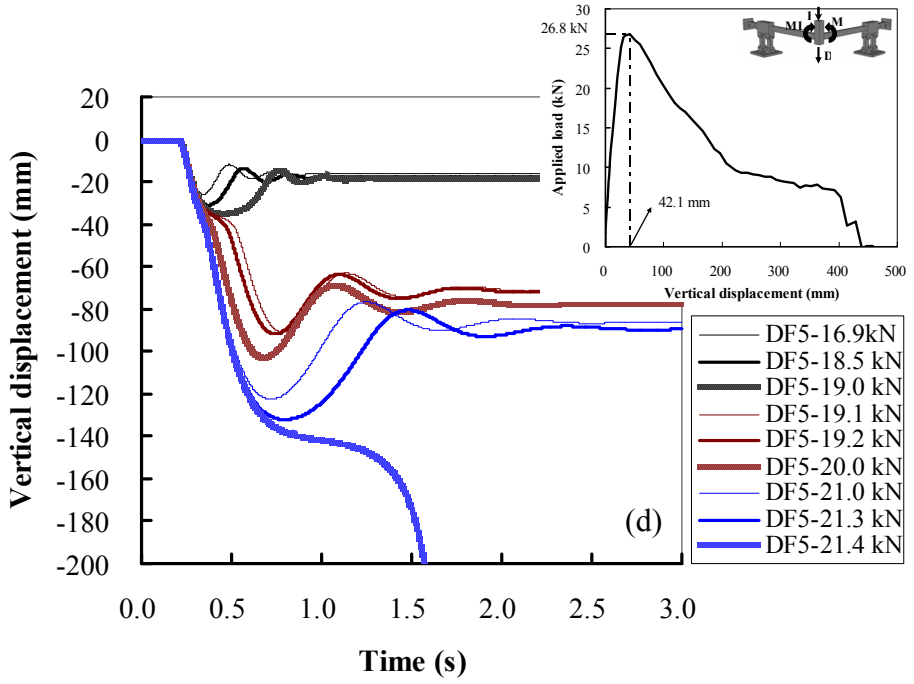

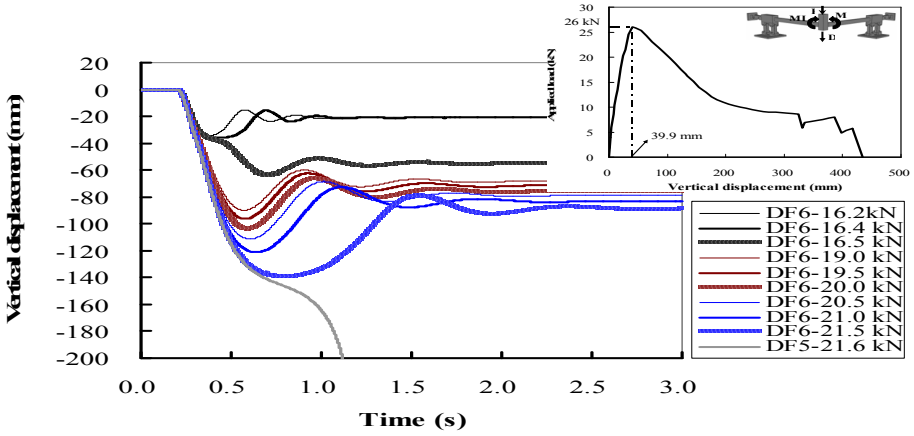

(e)

Fig. 7.9: The effects of the axial force in the corner support on the displacement-time response of test specimens

7.6 Evaluation of the Accuracy of the Recommended DIF in DoD [D1]

A number of improvements have been incorporated in the recently updated design guideline DoD [D1]. One of the significant improvement points is the decoupling of the load increase factor (LIF) and the dynamic increase factor (DIF) to be considered for linear static analysis (LS) and nonlinear static analysis (NS), respectively. For structural components with deformation controlled action, DoD [D1] proposed an equation (Eq. 7-3) to specify the value of DIF. For structural components with force controlled action, DoD [D1] suggested the value of DIF equals to 2.0. The proposed equation for calculating the DIF for RC structures in DoD [D1] and Marchand *et al*. [M3] is:

$$DIF = 1.04 + 0.45/(\theta_p / \theta_y + 0.48) \qquad (7\text{-}3)$$

where θ_P is the allowable plastic rotation, and θ_y is the member yield rotation.

However, this method demands the development of a LIF and DIF data pool which is currently reliant on numerical simulations. In order to evaluate the accuracy of the proposed DIF values in DoD [D1], the values of DLIF obtained in the current analytical study was compared with the suggested value of DIF in DoD [D1], as shown in **Table 7.1**.

DoD [D1] defines a structural component action as deformation-controlled if it has a Type 1 curve (as shown in **Fig. 7.10**) and $e \geq 2g$ or if it has a Type 2 curve (as shown in **Fig. 7.10**) and $e \geq 2g$. Otherwise it was force-controlled.

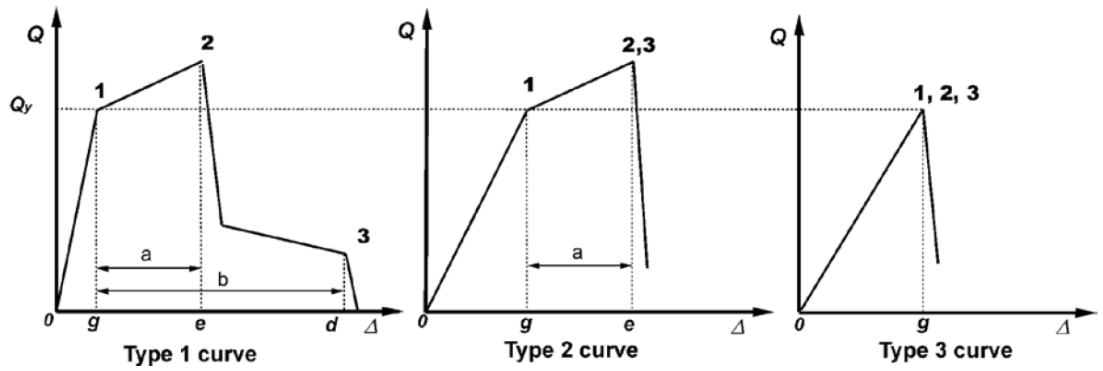

Fig. 7.10: Definition of force-controlled and deformation-controlled actions, from ASCE 41-06 [A4]

As illustrated in **Chapter 5**, the load-displacement curve of each specimen belongs to Type 1 with $e < 2g$ (force controlled action) in DoD [D1]. As mentioned above, the value of DIF for force controlled action in DoD [D1] was 2.0. Thus, based on the load-displacement curves introduced in **Chapter 4**, the DLIF of each specimen was determined and given in **Table 7.1**. As shown in **Table 7.1**, the value of DLIF for the test specimens ranged from 1.41 to 1.59, if the residual strength was not included. However, the value of DLIF only ranged from 1.21 to 1.43, if the residual strength was considered. By comparing the values of DLIF obtained in the analytical analysis with the value of DIF suggested in DoD [D1], we found that the proposed value of DIF in DoD [D1] was over-conservative for the test specimens, especially when the residual strength of the specimen after yielding was included. It should be noted that the definition of the DIF in DoD [D1] was not exactly same as DLIF in this study. However, they are naturally similar.

7.7 Determining the DUS by the Capacity Curve Method

The capacity curve method proposed by Abruzzo *et al*. [A1] and Tsai and Lin [T3] is based on the conservation of energy. After conducting nonlinear quasi-static analysis, the load-displacement curve of the structure can be obtained where the area under this curve represents the strain energy in the structure. At the moment where the system achieves a balanced condition, this internal energy will be equal to the external work. The external work is defined as the product of the constant applied load (column axial force before damage) and the resulting displacement. If the system does not have adequate ductility to dissipate the required energy, the internal and external work will never balance each other and a collapse will ensue. Thus, a capacity curve may be constructed by dividing the accumulated stored energy by its corresponding displacement. It is mathematically expressed as:

$$P_{CC}(u_d) = \frac{1}{u_d}\int_0^{u_d} P_{NS}(u)du \qquad (7\text{-}4)$$

where $P_{CC}(u)$ and $P_{NS}(u)$ are the capacity function and the nonlinear static loading estimated at the displacement demand u_d, respectively.

Fig. 7.11 presents the load-displacement curve, capacity curve and load curve of each specimen. As can be seen from **Fig. 7.11a**, the load curves intersect the capacity curves at displacements of 44.9 mm and 55.4 mm for Specimens DF1 and DF3, respectively. Thus, both of the specimens will not collapse as energy balance can be achieved. Moreover, as shown in the figure, the maximum capacity was attained at a displacement of 90.8 mm, which was larger than the displacement corresponding to the static ultimate strength (44.0 mm). Thus, ignoring the contribution of the residual strength of the specimen would prove too conservative (consistent with the SDOF method). Similar behavior was observed for the remaining specimens. It should be

noted that the load curves in DF5 and DF6 were larger than the peak value of the capacity curve of the corresponding specimen. Thus, both DF5 and DF6 would totally collapse if the corner support was removed. This is consistent with the experimental and SDOF results.

By comparing the dynamic ultimate strength obtained from SDOF model with that obtained from capacity curve method (refer to **Table 7.2)**, it was found that the capacity curve method was able to accurately predict the dynamic ultimate strength of the test specimens with the resistance of the residual strength excluded. However, it would be unsafe if the residual strength were taken into consideration. This could be attributed to the fact that the residual strength of the specimen was fully considered in the capacity curve method but only a portion of the residual strength (τ=0.5) was included in the SDOF analysis.

Table 7.2: Comparison of the Dynamic Ultimate Strength Obtained from SDOF with the Results Obtained by Capacity Curve Method

Test	$DUS_{SDOF}^{\tau=0.0}$ (kN)	$DUS_{SDOF}^{\tau=0.5}$ (kN)	$DUS_{CC}^{\tau=0.0}$ (kN)	$DUS_{CC}^{\tau=1.0}$ (kN)	$\frac{DUS_{SDOF}^{\tau=0.0}}{DUS_{CC}^{\tau=0.0}}$	$\frac{DUS_{SDOF}^{\tau=0.5}}{DUS_{CC}^{\tau=1.0}}$
DF1	16.2	18.8	16.7	20.0	0.97	0.94
DF2	23.5	25.6	23.4	29.0	1.00	0.88
DF4	18.3	20.8	18.3	21.7	1.00	0.96
DF5	19.0	21.3	19.2	22.0	0.99	0.97
DF6	16.4	21.5	16.4	20.7	1.00	1.04

Note: $DUS_{SDOF}^{\tau=0.0}$, $DUS_{SDOF}^{\tau=0.5}$ = Dynamic Ultimate Strength of the test specimens obtained from SDOF method excluded or partially included the residual strength, respectively.

$DUS_{cc}^{\tau=0.0}$, $DUS_{cc}^{\tau=1.0}$ = Dynamic Ultimate Strength of the test specimens obtained from capacity curve method excluded or included the residual strength, respectively.

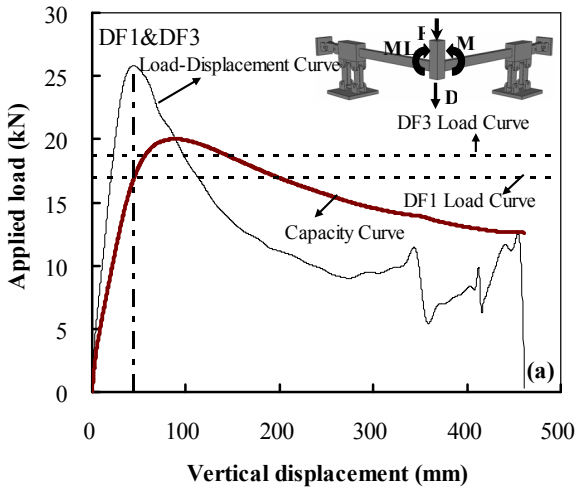
DF1&DF3
Load-Displacement Curve
I
ML
M
D
DF3 Load Curve
DF1 Load Curve
Capacity Curve
(a)
Applied load (kN)
Vertical displacement (mm)
0
5
10
15
20
25
30
0
100
200
300
400
500

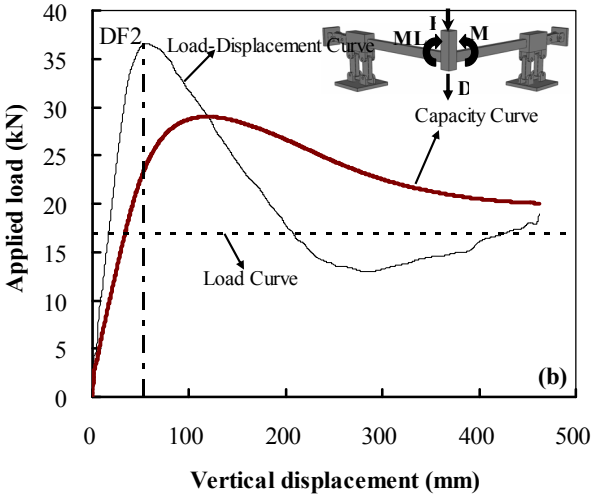
DF2
Load-Displacement Curve
I
ML
M
D
Capacity Curve
Load Curve
(b)
Applied load (kN)
Vertical displacement (mm)
0
5
10
15
20
25
30
35
40
0
100
200
300
400
500

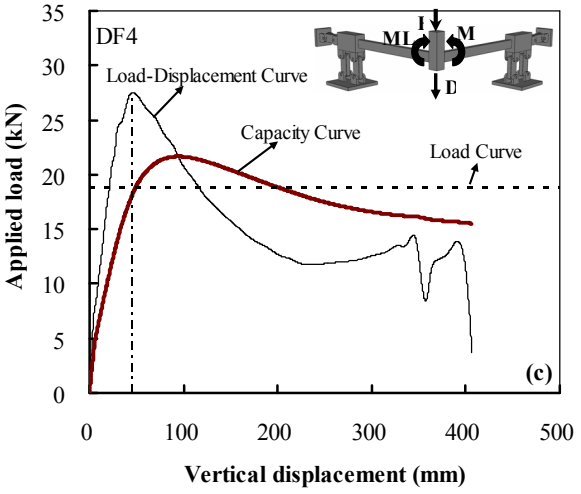
DF4
Load-Displacement Curve
I
ML
M
D
Capacity Curve
Load Curve
(c)
Applied load (kN)
Vertical displacement (mm)
0
5
10
15
20
25
30
35
0
100
200
300
400
500

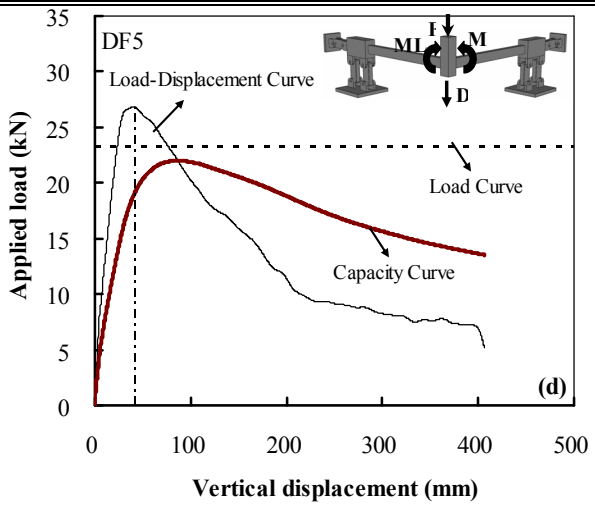

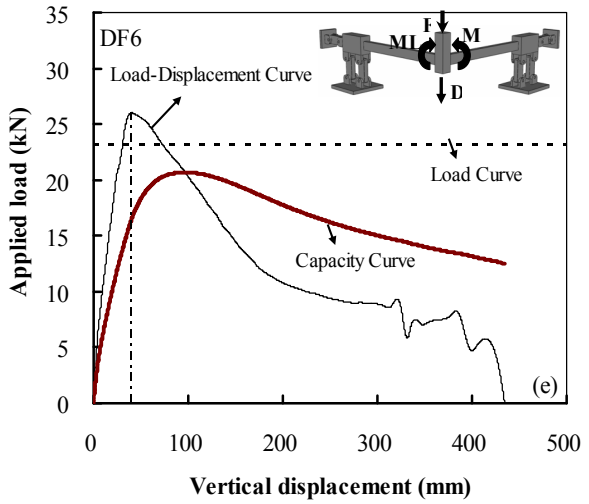

Fig. 7.11: Illustrates the load-displacement curve, capacity curve and load curve of each specimen

7.8 Summary

This chapter presents the SDOF method to estimate the displacement-time responses of RC substructures after the sudden removal of a corner support. In addition, the accuracy of the capacity curve method to judge the vulnerability of RC substructures for progressive collapse was evaluated. The followings provide specific findings of the chapter:

1. The SDOF method can accurately predict the displacement response of substructures in progressive collapse, as validated by the comparison between the analytical results and experimental data.

2. The residual strength of the substructure beyond the static ultimate strength should be considered in the SDOF models.

3. The damping ratio significantly influences the displacement response of the specimens. Large damping ratios (ζ=20%) were used in the current SDOF analysis because of the large damping observed in the experimental tests.

4. Comparing the value of the dynamic load increase factor (DLIF) obtained from SDOF with that suggested in DoD [D1], it was found that the proposed DIF values in DoD [D1] were over-conservative.

5. The capacity curve method can predict whether the test specimens will totally collapse, as well as predict the dynamic ultimate strength of the substructures without residual strength. However, it does not produce conservative results if the residual strength of the substructures is considered.

CHAPTER 8

QUASI-STATIC TESTS FOR BEAM-COLUMN SUBSTRUCTURES WITH RC SLAB

8.1 Introduction

In typical cast-in-situ construction, beams, columns and slabs are cast simultaneously and therefore act as a single structural unit. Ignoring the effect of the slab on the stiffness and strength of the beams will most likely result in a significant underestimation of the vertical force resistance capacity. Therefore, another series of tests (S-series specimens) were conducted in this study to investigate the quasi-static performance of RC substructures incorporated RC slabs for progressive collapse. By comparing the failure mechanisms and load-displacement response of S-series specimens with corresponding F-series specimens (introduced in **Chapter 4**), the effect of the slabs on the performance of the RC substructures can be determined.

In this chapter, firstly, the dimensions and reinforcement details of the S-series specimens are presented. Then, the experimental setup of the S-series of tests is shown. After that, the experimental results of the S-series specimens are displayed. Finally, a simplified analytical model was proposed to predict the ultimate capacity and the tensile membrane action of the S-series specimens.

8.2 Test Specimens

Three substructures (S1, S2 and S3) incorporating a RC slab were designed to evaluate the influence of RC slabs on the performance substructures under the loss of

a corner column scenario. **Fig. 8.1** demonstrates the typical beam and column dimensions and reinforcement details of Specimens S1 and S2 while **Fig. 8.2** illustrates the slab reinforcement details of S1 and S2. The concrete cover of the beam, column and slab were 10 mm, 20 mm and 7 mm, respectively. As shown in **Fig. 8.1**, for S-series specimens, there is one corner column stub, three adjacent enlarged columns and four RC beams cast monolithically. The corner column stub representing the removed column was a 200.0 mm square for all specimens while the adjacent enlarged columns were 250.0 mm squares to ensure failure would not occur in these adjacent enlarged columns. The dimensions and reinforcement details of each specimen are given in **Table 8.1**. As shown in **Table 8.1**, S1 and S3 are non-seismically designed and detailed. Thus, 4 T10 was doubly longitudinal reinforced in the beams and transverse reinforcements were hoop stirrups with 90° bends. Moreover, no transverse reinforcement was provided in the joint region. However, S2 was seismically designed and detailed. Thus, 4 T13 was doubly longitudinal reinforced in the beams. Transverse reinforcements were hoop stirrups with 135° bends and transverse reinforcements were provided in the joint region. It should be noted that S1 and S2 had equal span in the longitudinal and transverse directions, while S3 had 2775 mm and 2175 mm clear span in the longitudinal direction and the transverse direction, respectively. In general, Specimens S1, S2, S3 corresponded to F3, F2 and F7, respectively. As shown in **Table 8.1**, similar details were provided in the beams and columns of the S-series specimens as the corresponding F-series specimens while a RC slab was incorporated. The concrete properties of S-series specimens are shown in **Table 8.2** while the properties of reinforcing steel are similar to the F-series specimens and shown in **Table 3.3**.

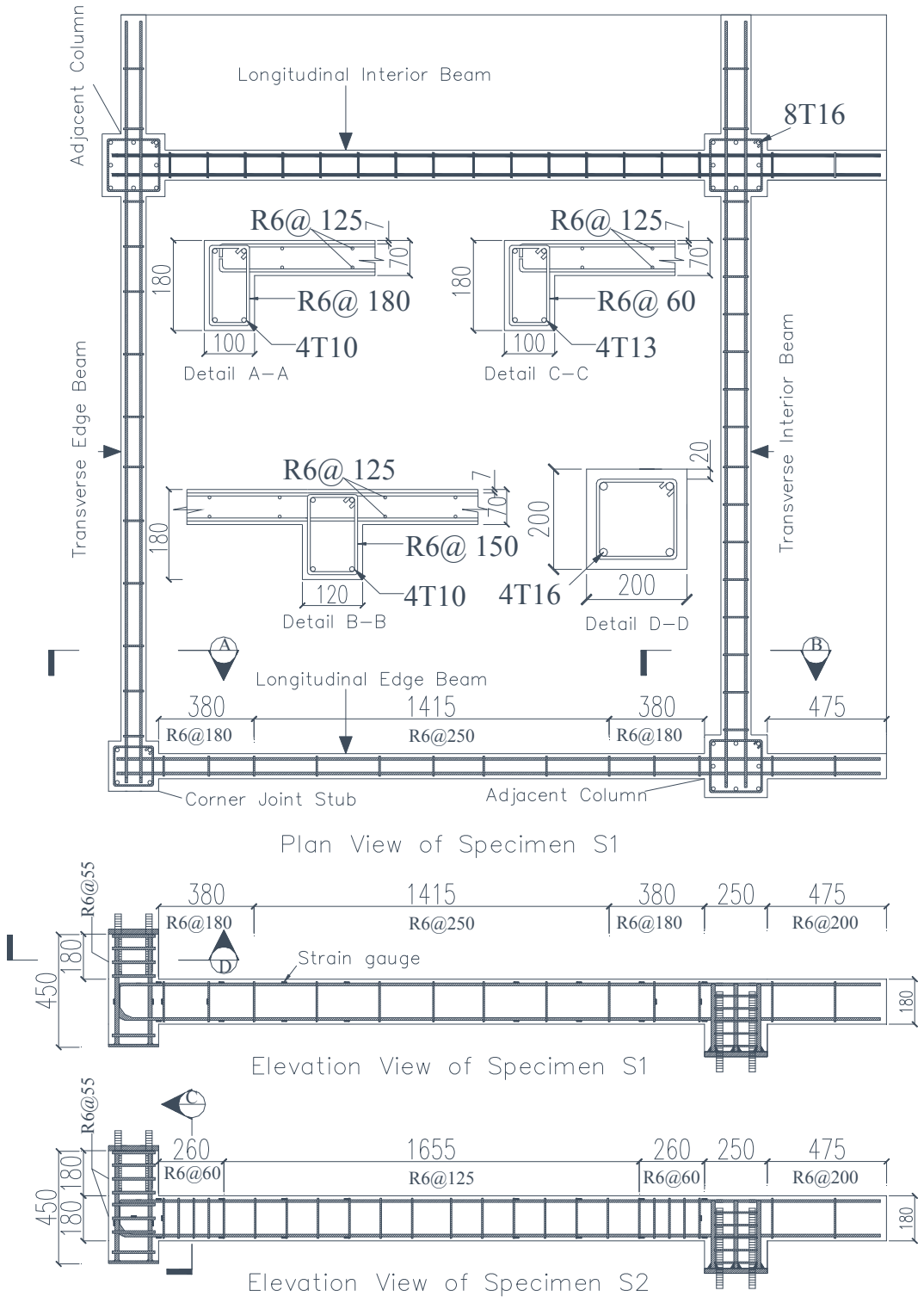

Fig. 8.1: Typical detailing of the beam and column in the non-seismically detailed specimens

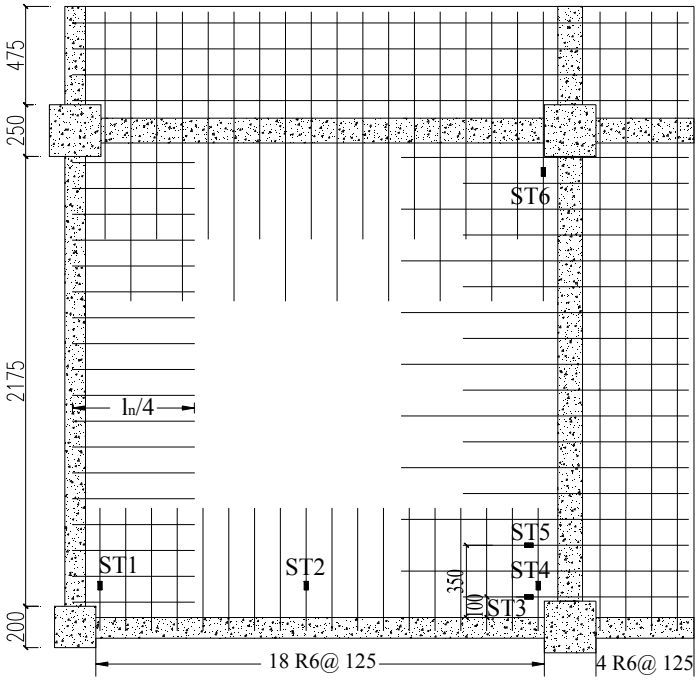

Top Slab Reinforcement

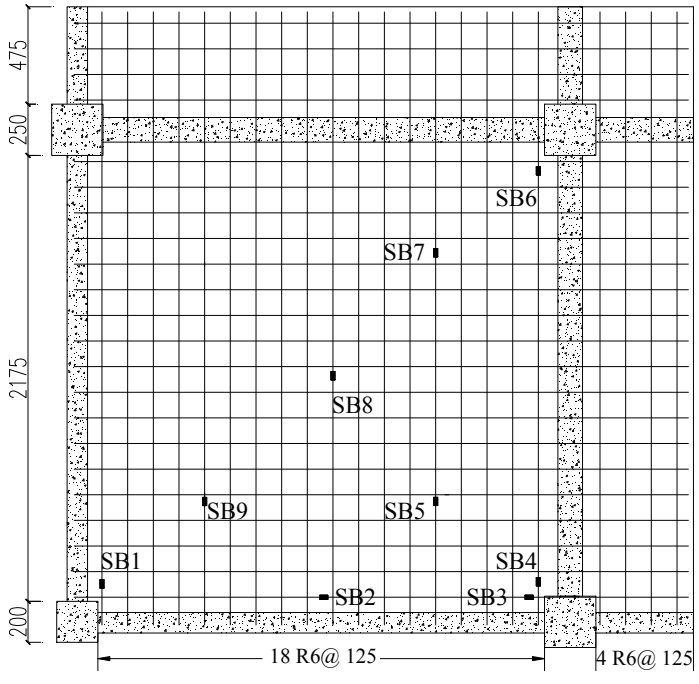

Bottom Slab Reinforcement

Fig. 8.2: Typical detailing of slab for non-seismically detailed specimen

Table 8.1: Specimens Properties (Slab Specimens)

Test	Elements		Beam-T		Beam-L			Design axial load (kN)	Slab thickness (mm)	Slab rebar
	Beam-T	Beam-L	Beam-T	Beam-L	Joint	Beam-T	Beam-L			
F3	Type a*	Type a*	0.87 %	0.87 %	None	0.31 %	0.31 %	18.6	N/A	None
F2	Type a*	Type a*	1.47 %	1.47 %	0.49 %	0.95 %	0.95 %	18.6	N/A	None
F7	Type a*	Type b*	0.87 %	0.75 %	None	0.31 %	0.36 %	23.2	N/A	None
S1	Type a*	Type a*	0.87 %	0.87 %	None	0.31 %	0.31 %	18.6	70	0.4 %
S2	Type a*	Type a*	1.47 %	1.47 %	0.49 %	0.95 %	0.95 %	18.6	70	0.4 %
S3	Type a*	Type b*	0.87 %	0.75 %	None	0.31 %	0.36 %	23.2	70	0.4 %

Note: Beam-T, Beam-L= Transverse beam and longitudinal beam respectively

Type a*: Clear span=2175 mm cross-section=180 x 100 mm.

Type b*: Clear span=2775 mm cross-section=210 x 100 mm.

Table 8.2: Compressive Strength of Concrete

Specimen ID	Compressive strength at 28 days f_c' (MPa)	Compressive strength on the day of testing f_c' (MPa)
F3	30.4	31.9
F2	30.6	32.1
F7	30.9	33.3
S1	30.5	31.6
S2	30.6	31.5
S3	30.8	32.1

8.3 Experimental Setup

A schematic of the test setup of S-series specimens is shown in **Fig. 8.3**. In general, the experimental setup of the three S-series specimens was similar to the F-series specimens (introduced in **Chapter 3**). The existing axial load in the corner column before it was lost was simulated by applying downward displacements at the corner stub through a hydraulic jack with 600.0 mm stroke. A steel assembly was utilized to provide the prescribed partial rotational and horizontal constraints on the corner joint. The differences between the setup of S-series specimens and F-series specimens were: three steel legs were utilized to apply equivalent fixed supports for the slab, each steel leg was connected with a 75 mm thick strong plate through $4\,\phi\,27$ bolts and these steel plates were fastened to the strong floor using pre-tensioned steel rods; seven

steel weight assemblies are applied on the extended part of the slab to simulate the influence of continuity of the surrounding slab on the response of the S-series specimens.

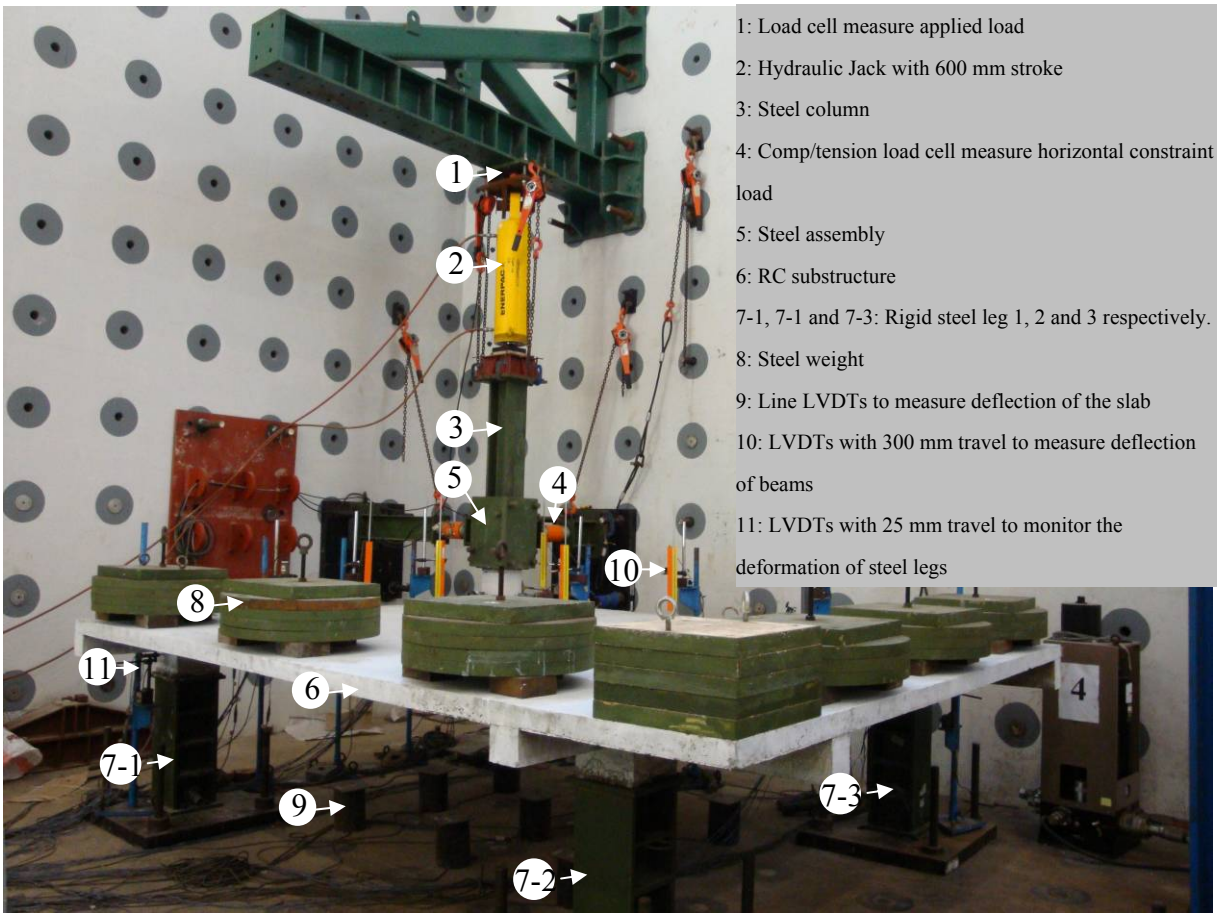

Fig. 8.3: Experimental setup of the substructures with slab (quasi-static test)

8.4 Instrumentation

Extensive measurement devices were installed both internally and externally in order to monitor the response of the test specimens. A total of 130 data channels were active during the testing process of S-series specimens. Similar to the F-series specimens, a load cell was used to measure the applied force on the corner stub. Two tensile and compressive load cells were connected horizontally with the steel box and were used

to measure the horizontal reaction of the box in each direction. A series of LVDTs and Linear Potentiometers were also placed at various locations of the substructure to measure the different types of internal deformation, such as fixed end rotation, curvature and diagonal deformations. For details of the instrumentation please refer to section 3.5 in **Chapter 3**. For S-series specimens, 15 LVDTs (items 9 and 10 in **Fig. 8.3**) were placed vertically to monitor the deflection of the slab and beams. One LVDT was installed horizontally to measure the horizontal movement of the corner column stub with increasing vertical displacement. Moreover, for S-series specimens, strain gauges were not only installed in the beam and column but were also installed in the slab reinforcement. **Fig. 8.2** shows the locations of the strain gauges placed in the slab of the S-series specimens.

8.5 Test Results of S1

8.5.1 General Behavior

The general behavior of the specimen was based on the crack pattern development observed during the test. **Fig. 8.4** presents the load displacement curve of S1 and the crack pattern of this specimen corresponding to the different performance level. Similar to the F-series tests, five performance levels at significant parts of the test were identified. PL1, PL2, PL3, PL4 and PL5 represent first flexural cracks in the beam or slab, first yield of the beam top longitudinal reinforcement, the resistance capacity drops more than 25 % of ultimate capacity and begins to develop tensile catenary/membrane action, respectively.

At a load of 18.0 kN (PL1), flexural cracks were initiated in the slab. No cracks were observed within the beam and corner joint regions at this load. At a load of 22.0 kN, a

few flexural cracks were observed in the beam end near the adjacent column (BENAC), and the first diagonal crack in the slab formed and passed through the center of the slab. At a load of 24.0 kN, the first diagonal shear cracks occurred in the corner joint. When the applied load was increased further, more diagonal cracks formed in the slab. When the vertical displacement reached 43.0 mm, which was equivalent to 2.0 % of tip displacement ratio (TDR), the specimen reached the maximum horizontal compressive load of 21.0 kN. It should be noted that the TDR was defined as the ratio of the vertical displacement to the clear span of the beam. When the vertical displacement reached 56.0 mm, which was equivalent to 2.6 % of TDR, the specimen reached the ultimate capacity of 39.1 kN (PL3) and corresponded to 210.2 % of the design axial load in the corner column specified by DoD [D1]. With a further increase in the vertical displacement, the major diagonal crack in the slab and corner joint diagonal cracks became wider and considerable torsion deformation was observed at the edge beams. When the vertical displacement reached 90 mm, concrete crushing occurred in the BENAC and concrete splitting occurred in the corner joint were observed at a deflection of 120.0 mm. When the displacement reached 200.0 mm, which is equivalent to 9.2 % TDR, a diagonal crack in the slab penetrated through the depth of the slab and the load-displacement curve began to ascend again (attribution to tensile membrane action). **Fig. 8.5** illustrates the crack pattern development at different performance levels of the slab of S1. As can be seen from the figure, severe diagonal cracks were observed in the slab. Concrete crushing and compressive reinforcement buckling were observed in the longitudinal and transverse BENAC. Slight flexural cracks happened in the corner column just above the lost one. Severe shear cracks were observed in the corner joint and splitting of the concrete occurred in the corner joint at the end of the test.

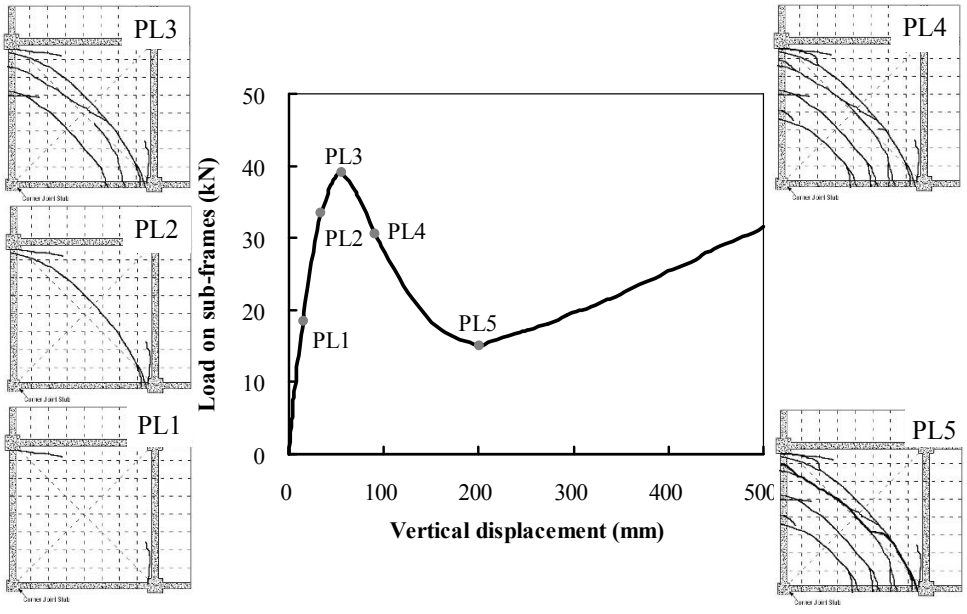

Fig. 8.4: Load-displacement curve of S1 corresponding to different performance levels

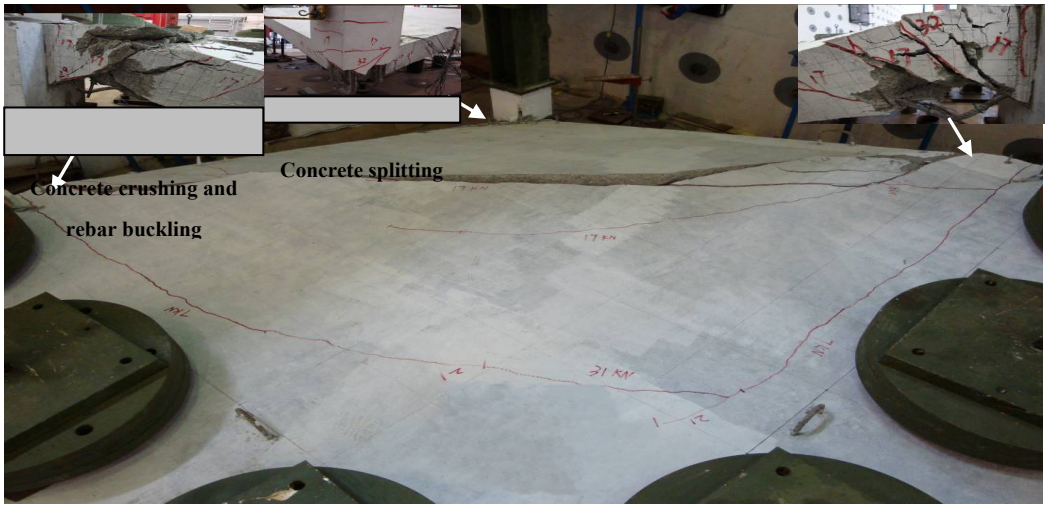

Fig. 8.5: Final failure mode of S1

8.5.2 Horizontal Load-Displacement Relationship

Fig. 8.6 illustrates the horizontal reaction versus displacement relationship of S1. The compressive load developed when increasing the vertical displacement from the beginning of the test. This indicated that compressive arching action was developed during the test. However, the compressive force decreased when the strength of the system decreased. This was due to severe damage cumulated in the corner joint and resulted in loose beam horizontal axial constraint. The compressive axial force changed to tension in the longitudinal and transverse beams when the corner column had the displacements of 248.1 mm and 263.2 mm, respectively. It indicated that catenary action was developed with relatively large deflection. When the displacement reached 500.0 mm, which was equivalent to 22.9 % of TDR, the measured tensile force in longitudinal and transverse beam was 22.8 kN and 17.0 kN, respectively. This large tensile force resulted in the notable secondary ascend part, as observed in the load-displacement curve. Compared with F3, this obvious secondary ascend can only be explained by the tensile membrane action developed in the RC slab.

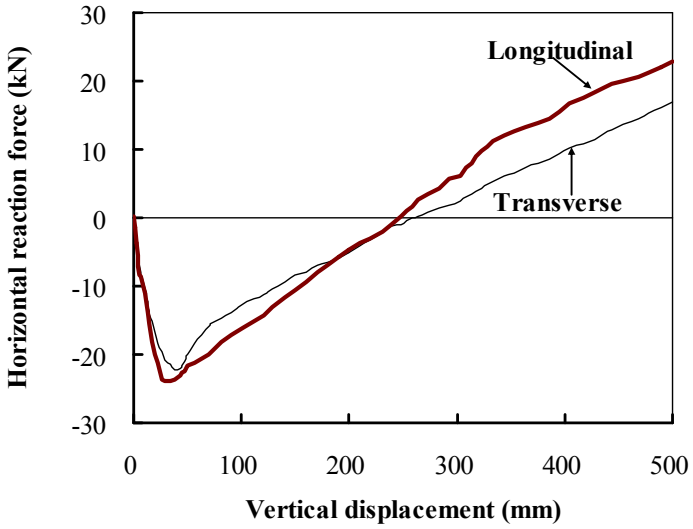

Fig. 8.6: Horizontal reaction force-displacement relationship of S1

8.5.3 Strain Profile along the Beam

Fig. 8.7 illustrates the strain profile of beam longitudinal reinforcement of S1 corresponding to different performance levels respectively. In general, the strain distribution profile of S1 was similar to that of F3. As illustrated in **Fig. 8.7**, the distinguishing point between these two specimens was that the maximum compressive strain of the bottom longitudinal reinforcement in the BENAC of S1 was much larger than that of F3. This might be due to the slab had invoked a flange effect on the beam section in Specimen S1.

8.5.4 Strain Gauge Results in the Slab Reinforcement

Fig. 8.8 illustrates the relationship of strain in the slab reinforcement versus vertical displacement of S1. The locations of strain gauges are illustrated in **Fig. 8.2**. As shown in **Fig. 8.8a**, the ST1 was compressive initially. However, it started to decrease when the vertical displacement reached 22.4 mm. At this vertical displacement, diagonal shear cracks were observed in the corner joint. ST1 converted into tension after the vertical displacement exceeded 200.0 mm. The tensile membrane action was developed at this displacement stage. The strain of ST3 suddenly increased and passed its maximum limit when the displacement reached 90.0 mm. However, the strain of ST6 was close to zero during the test and this proved that the majority of the force initially resisted by the damaged corner column was transferred to the adjacent columns and only negligible force was transferred to the interior column.

Fig. 8.8b depicts the relationship of the strain in the slab bottom reinforcement versus vertical displacement. The strain in all bottom reinforcements except SB1 and SB2 were tensile during the test regime. The strains observed in SB3, SB5 and SB8 were

much larger than the rest of the strain points due to the fact that major deformation was concentrated at the diagonal crack. When the slab developed a tensile membrane action, the strain distribution in SB5, SB8, SB9 and SB1 indicated that the strain in the slab reinforcement decreased with increasing distance away from the adjacent column. This is one of the major differences between the membrane action developed in the present slabs and that developed in the slabs tested by previous researchers (Park [P4]). In their tests, all bottom reinforcements in the center slab were assumed yielded after tensile membrane action was developed. Moreover, the strains of SB6 and SB7 were extremely small and this was confirmed by the observed failure mode, with limited damage occurred in the interior half triangle of the slab during the test.

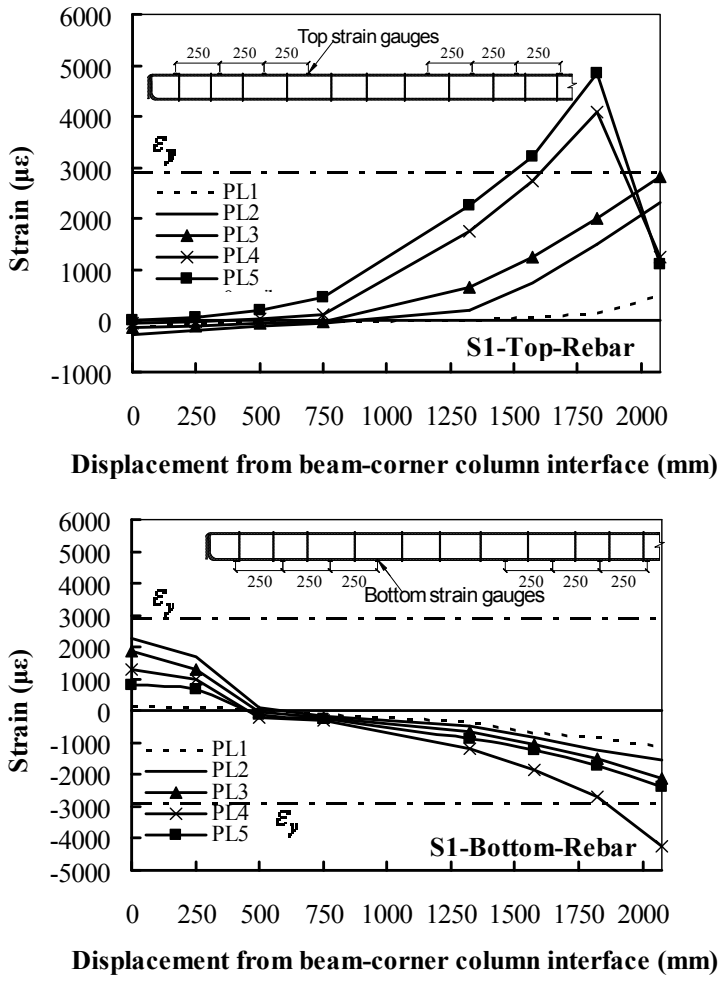

Fig. 8.7: Strain profile of beam longitudinal reinforcement of S1

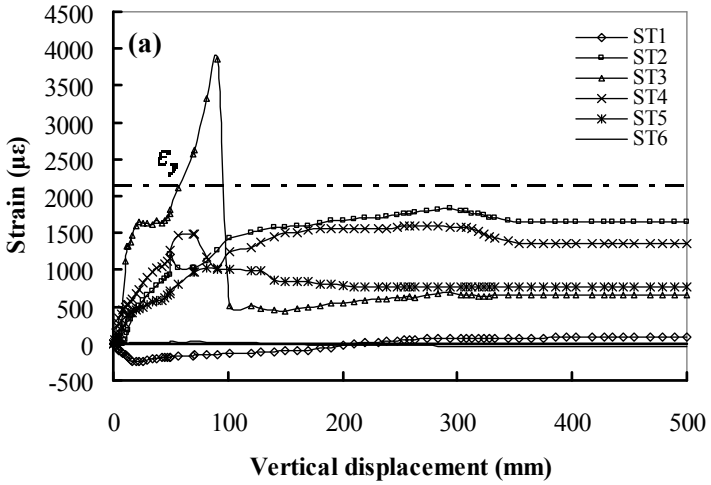

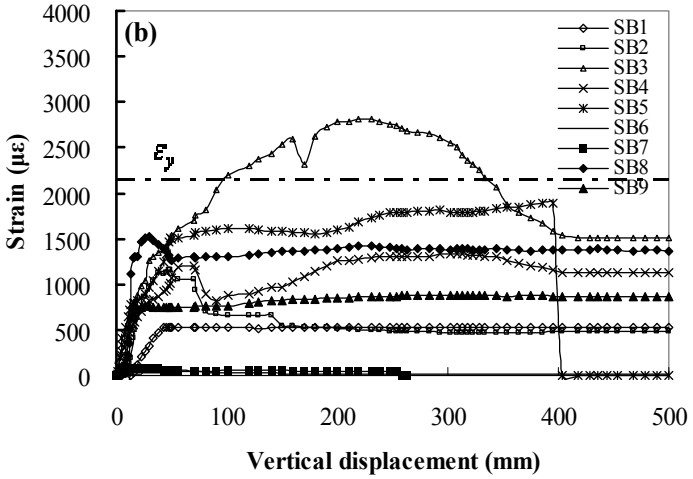

Fig. 8.8: Strain results in slab reinforcement of S1

8.6 Test Results of S2

Seismically detailed specimen S2 was designed and tested to study the seismic effect on the global performance of RC substructures incorporating a RC slab for progressive collapse. The dimensions and reinforcement details are given in **Table 8.3**.

Table 8.3: Summary of the Test Results

Test	First beam crack (kN)	First yield load (kN)	First joint shear crack (kN)	First diagonal slab crack (kN)	Ultimate load P_{cu} (kN)	MCHR in Beam-T (kN)	MCHR in Beam-L (kN)	Beam-T rotation at PL4 (rads)	Beam-L rotation at PL4 (rads)	Start to develop tensile membrane (mm)
F3	4.3	22.5	21.0	None	25.8	19.8	19.6	0.051	0.049	332.8
F2	5.0	29.1	25.3	None	36.5	27.9	27.3	0.061	0.056	275.9
F7	3.9	21.0	16.1	None	23.0	19.6	18.4	0.058	0.047	299.2
S1	22.0	33.5	24.0	22.0	39.1	22.3	21.0	0.047	0.044	200.0
S2	18.0	45.8	22.0	34.0	52.0	28.7	27.3	0.057	0.050	218.0
S3	17.0	32.8	17.0	20.0	37.5	22.0	23.3	0.054	0.049	260.0

Note: MCHR= Maximum compressive horizontal reaction

Beam-T, Beam-L= Transverse beam and longitudinal beam respectively

8.6.1 General Behavior

The measured load- displacement curve of S2 is shown in **Fig. 8.9**. In general, the crack development of S2 was similar to that of S1 and the key points of the test results are listed in **Table 8.3**. Thus, only the foremost discrepancies between these two specimens were emphasized. For S1, the first diagonal crack in the slab formed at a load of 22.0 kN. However, for S2, the diagonal crack in the slab formed and passed through the center of the slab at a load of 34.0 kN. Moreover, for S2, the splitting of the concrete of joint occurred at a displacement of 260.0 mm, which was much later than that of S1 as the joint shear reinforcement helped to maintain the strength of the diagonal compressive strut by passively confining the joint concrete core. When the vertical displacement reached 69.4 mm, which was equivalent to 3.2 % of TDR, the specimen reached the ultimate capacity of 52.0 kN and corresponded to 279.6 % of the design axial load in the corner column specified by DoD [D1]. When the vertical displacement reached 218.0 mm, tensile membrane action was observed in the load-displacement curve. **Fig. 8.10** illustrates the failure mode of S2 at final of the test.

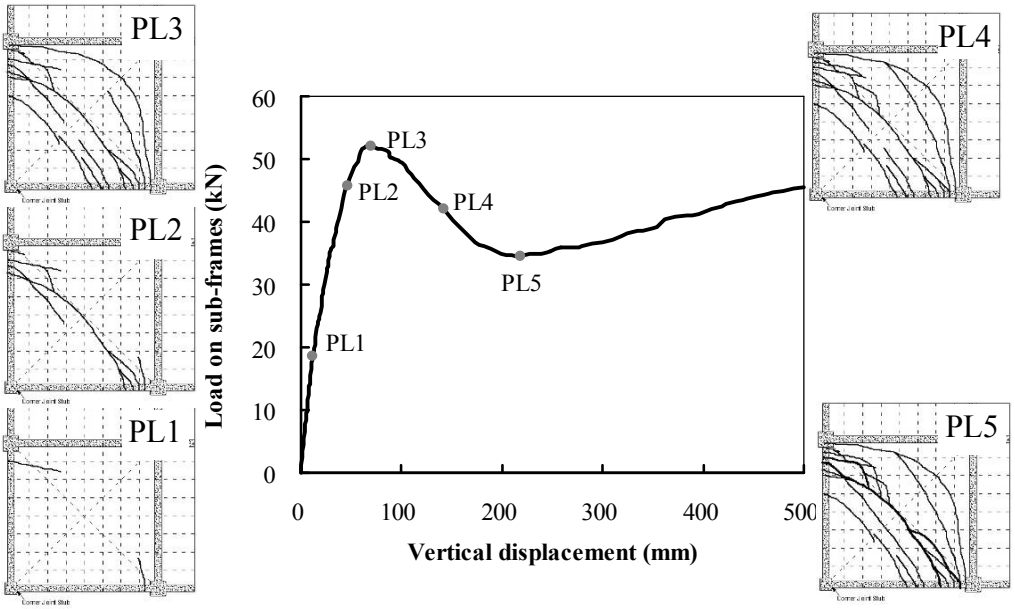

Fig. 8.9: Load-displacement curve of S2 corresponding to different performance level

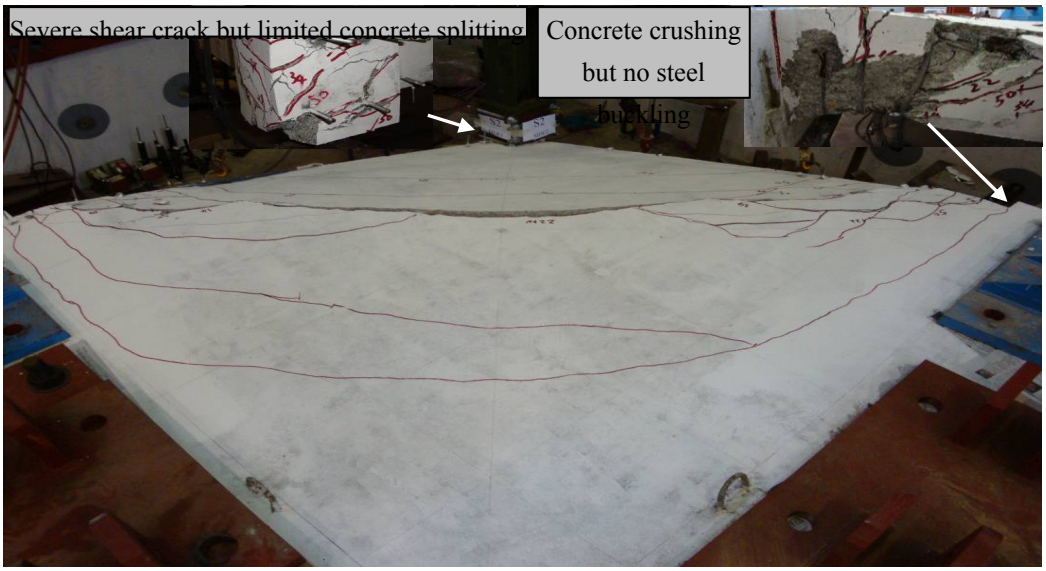

Fig. 8.10: Final failure mode of S2

8.6.2 Horizontal Load-Displacement Relationship

Fig. 8.11 illustrates the horizontal reaction versus displacement relationship of S2. Similar to S1, the compressive load was developed as the vertical displacement increased from the beginning of the test and this indicated compressive arching action was developed during the test. However, the compressive force decreased when the strength of the system decreased. This was due to severe damage cumulated in the corner joint and resulted in reduction of the beam horizontal axial constraint. For S2, the decrease of the horizontal reaction force was observed when the vertical displacement reached 69.2 mm, which was later than S1. This was possibly due to the joint transverse reinforcement had confined the corner joint and improved the integrity of the joint. For S2, the compressive axial force changed to tension in the longitudinal and transverse directions when the corner column had the displacements of 309.9 mm and 319.4 mm respectively. For S1, the compressive axial force changed to tension in the longitudinal and transverse directions when the corner column had the displacements of 249.1 mm and 263.2 mm, respectively. When the displacement reached 500.0 mm equivalent to 22.9 % of TDR, the measured tensile force in longitudinal and transverse beam was 21.0 kN and 18.1 kN, respectively.

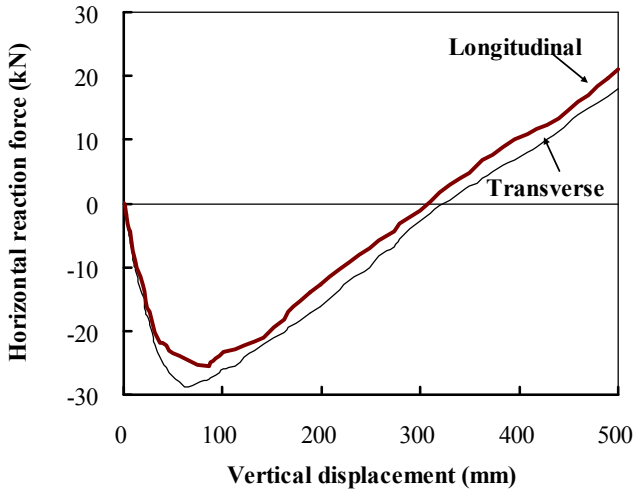

Fig. 8.11: Horizontal reaction force-displacement relationship of S2

8.6.3 Strain Profile along the Beam

Fig. 8.12 illustrates the strain profile of beam longitudinal reinforcement of S2 corresponding to different performance levels respectively. In general, the strain distribution profile of S2 was similar to that of F2. As illustrated in **Fig. 8.12**, the distinguishing point between these two specimens was that the bottom longitudinal reinforcement in the BENAC of S2 yielded at PL3 while the reinforcement in F2 did not yield until PL4. This might be due to the slab had invoked a flange effect on the beam section in Specimen S2.

8.6.4 Strain Gauge Results in the Slab Reinforcement

Fig. 8.13a illustrates the relationship of strain in the slab top reinforcement versus vertical displacement of S2. Similar to S1, the ST1 was compressive initially. However, it started to decrease when the vertical displacement reached 46.0 mm. This was slightly later than for S1 due to the joint transverse reinforcement which effectively increased the integrity of the corner joint. ST1 converted into tension after the vertical displacement exceeded 218.0 mm. The tensile membrane action was developed at this displacement stage. The strain of ST3 suddenly increased and passed its maximum limit when the displacement reached 50.4 mm. Similar to S1, the strain of ST6 was close to zero during the test and this proved that the majority of the force initially resisted by the damaged corner column was transferred to the adjacent columns and only negligible force was transferred to the interior column.

Fig. 8.13b depicts the relationship of the strain in the slab bottom reinforcement versus vertical displacement. The strain in all bottom reinforcements except SB1 and SB2 were tensile during the test regime. The strains observed in SB3 and SB5 were

much larger than the rest of the strain points due to the fact that major deformation was concentrated in the diagonal crack. Similar to S1, the strain distribution in SB5, SB8, SB9 and SB1 indicated that the strain in the slab reinforcement decreased with increasing distance away from the adjacent column when the slab developed tensile membrane action. Moreover, the strains of SB6 and SB7 were extremely small and there were confirmed by the observed failure mode, with limited damage occurred in the interior half triangle of the slab during the test.

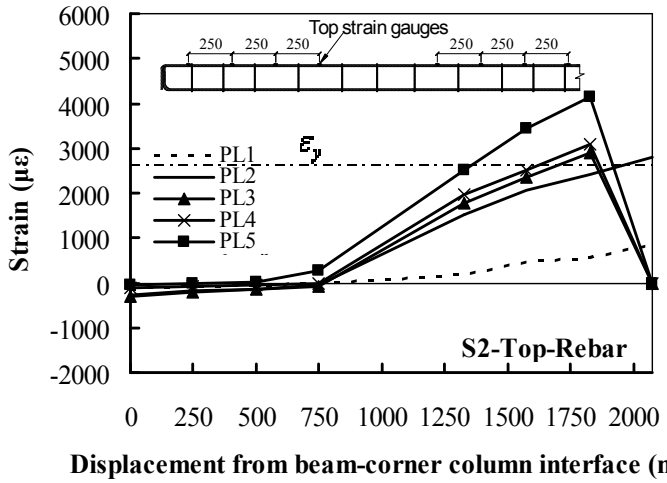

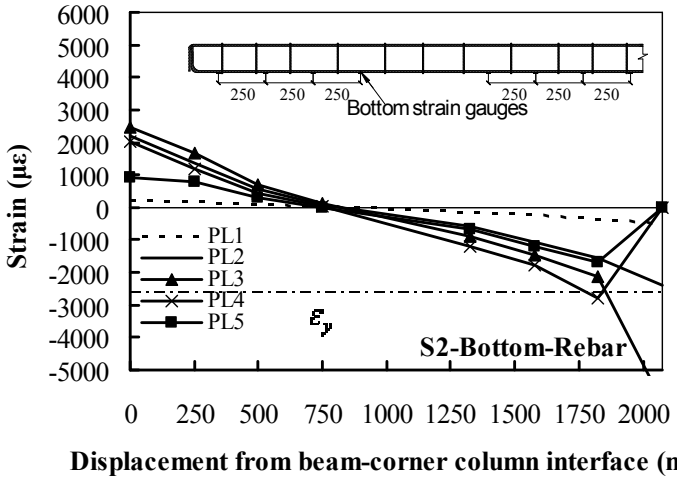

Fig. 8.12: Strain profile of beam longitudinal reinforcement of S2

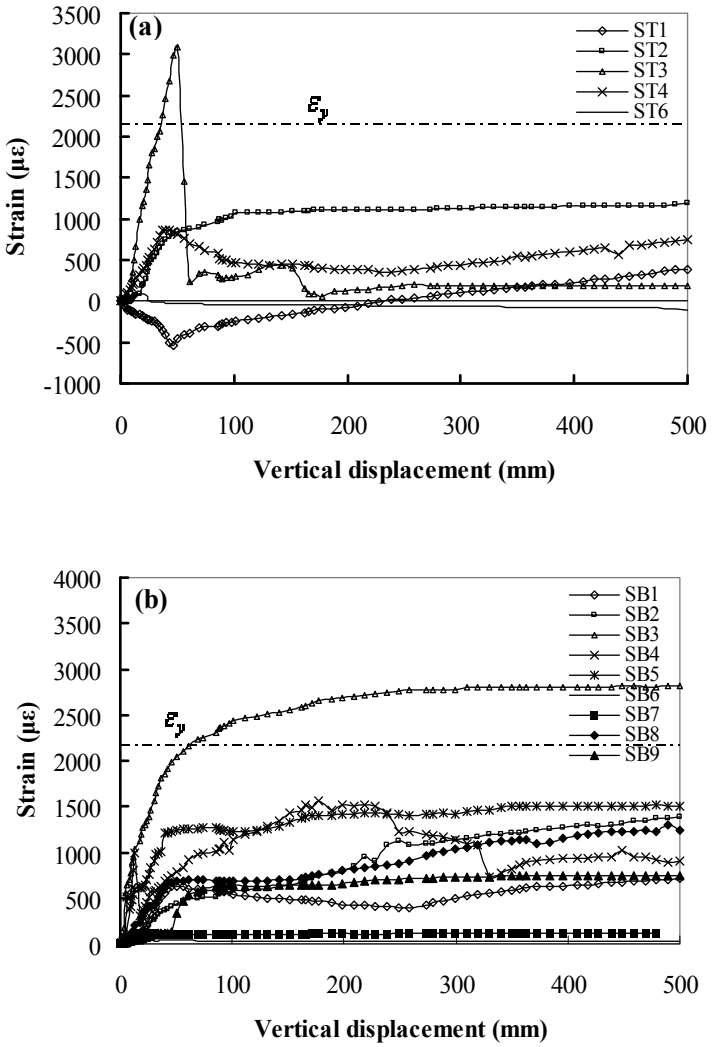

Fig. 8.13: Strain results in the slab reinforcement of S2

8.7 Test Results of S3

S3 had unequal spans in the longitudinal and transverse directions. The beam detailing of S3 was similar to F7. The dimensions and reinforcement details of S3 are given in **Table 8.1**.

8.7.1 General Behavior

The measured load-displacement curve of Specimen S3 is shown in **Fig. 8.14**. An asymmetrical crack pattern was developed in longitudinal and transverse beams due to unequal design span in the longitudinal and transverse directions. The first diagonal crack in the slab was observed at a load of 20.0 kN. However, the first diagonal crack was not connected to the two interfaces between the beam and the adjacent column. It was like an arc and the radius of the arc was the clear span of the short beam. The first flexural cracks occurred in the transverse and longitudinal beam ends near the adjacent columns at the loads of 17.0 kN and 20.0 kN respectively. However, the first flexural cracks occurred in the BENC were observed at a load of 24.0 kN for both beams. The first joint diagonal shear cracks at the face along the transverse and longitudinal directions were observed at the loads of 17.0 kN and 20.0 kN respectively. At a load of 24.0 kN, new branch cracks formed to connect the first diagonal crack to the interfaces of the longitudinal and transverse beam-adjacent columns. When the vertical displacement reached 60.2 mm, the specimen reached the ultimate capacity of 37.5 kN and corresponded to 161.6 % of the design axial load in the corner column specified by DoD [D1]. When the vertical displacement reached 70.0 mm, the joint shear cracks became severely wide and the crushing of concrete was observed in the bottom of the transverse BENAC. When the vertical displacement reached 100.0 mm, the splitting of the concrete occurred in the corner joint and the concrete crushing was observed in the bottom of the longitudinal BENAC. A further rise in the displacement resulted in the increase of the width of the major diagonal crack in slab. **Fig. 8.15** illustrates the crack pattern development at different performance levels of the slab of S3.

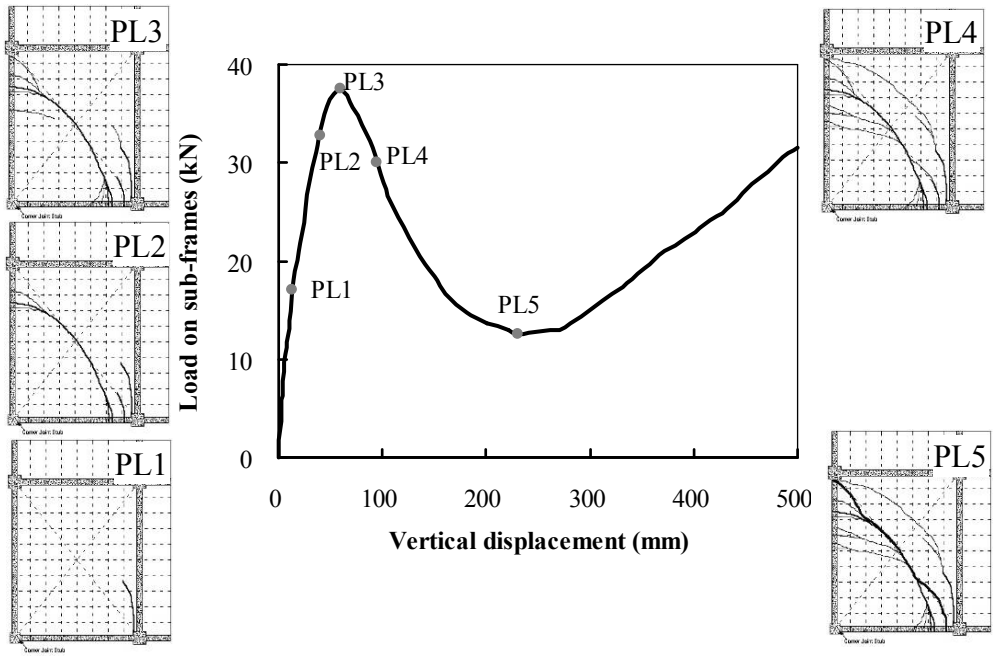

Fig. 8.14: Load-displacement curve of S3 corresponding to different performance levels

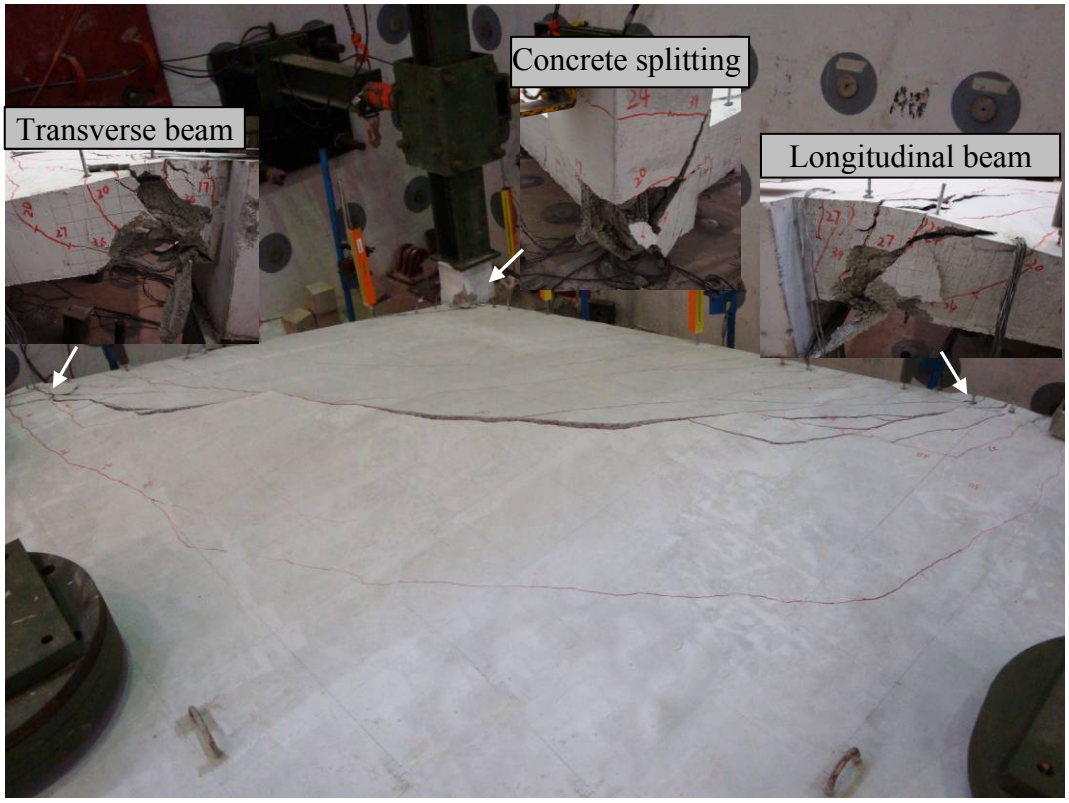

Fig. 8.15: Final failure mode of S3

8.7.2 Horizontal Load-Displacement Relationship

Fig. 8.16 illustrates the horizontal reaction versus displacement relationship of S3. As the different span length in longitudinal and transverse beam, different horizontal reaction force responses were attained in the longitudinal and transverse directions. However, the difference between these two curves was limited as shown in the figure. The maximum compressive axial forces in the longitudinal and transverse direction were 23.3 kN and 22.0 kN, respectively. However, the tensile axial forces in the longitudinal and transverse direction at final of the test (500.0 mm) were 15.1 kN and 10.0 kN, respectively.

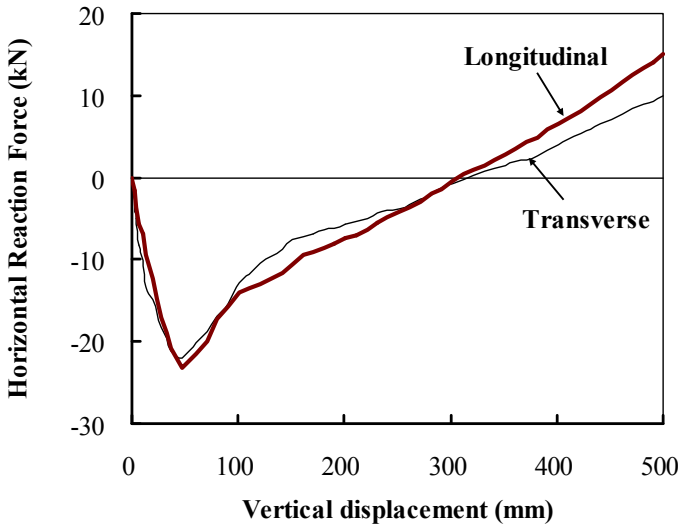

Fig. 8.16: Horizontal reaction force-displacement relationship of S3

8.7.3 Strain Profile along the Beam

Fig. 8.17 illustrates the measured strain distribution of S3 corresponding to different performance levels. The strain profiles of both beams are presented due to asymmetric dimensions and reinforcement details in the longitudinal and transverse beams. As shown in the figure, the yield of the longitudinal reinforcement was first observed in

the transverse beam. At PL5, all of the longitudinal reinforcements in the transverse beam were in tension. This was consistent with the horizontal axial force results. However, the compressive strain in the longitudinal beam near the adjacent column began to decrease at PL5 as the tensile axial force started to develop at this performance level.

8.7.4 Strain Gauge Results in the Slab Reinforcement

Fig. 8.18a illustrates the relationship of strain in the slab top reinforcement versus vertical displacement of S3. ST3 yielded at a displacement of 27.8 mm. After that, ST3 kept increasing with an increase in the vertical displacement. ST4 suddenly increased when the displacement was close to 261.8 mm. Similar to S1, the strain of ST6 was close to zero during the test and this proved that the majority of the force initially resisted by the damaged corner column was transferred to the adjacent columns and only negligible force was transferred to the interior column.

Fig. 8.18b depicts the relationship of the strain in the slab bottom reinforcement versus vertical displacement. Similar to S1, the strains in all bottom reinforcement except SB1 and SB2 were tensile during the test regime. SB1 and SB2 went into positive regime when the displacements reached 161.1 mm and 190.9 mm, respectively. The slope of the increase of SB3 significantly decreased when the displacement reached 24.1 mm although the strain of SB3 was still increasing and finally yielded. Similar to S1, the strain distribution in SB5, SB8, SB9 and SB1 indicated that the strain in the slab reinforcement decreased with increasing distance from the adjacent column when the slab developed a tensile membrane action. Moreover, the strains of SB6 and SB7 were extremely small and there were confirmed

by the observed failure mode, with limited damage occurred in the interior half triangle of the slab during the test.

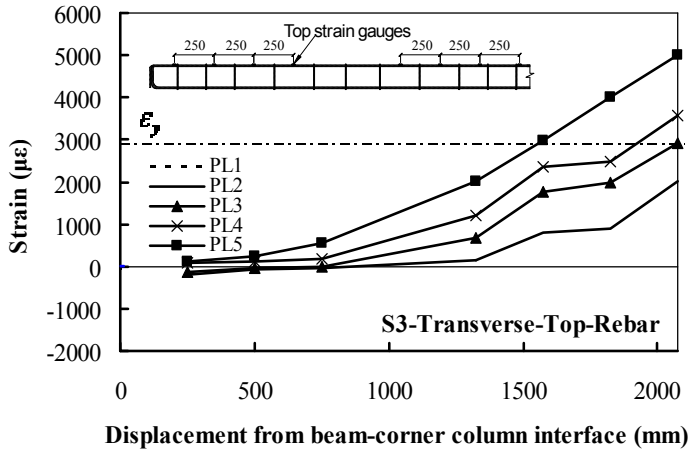

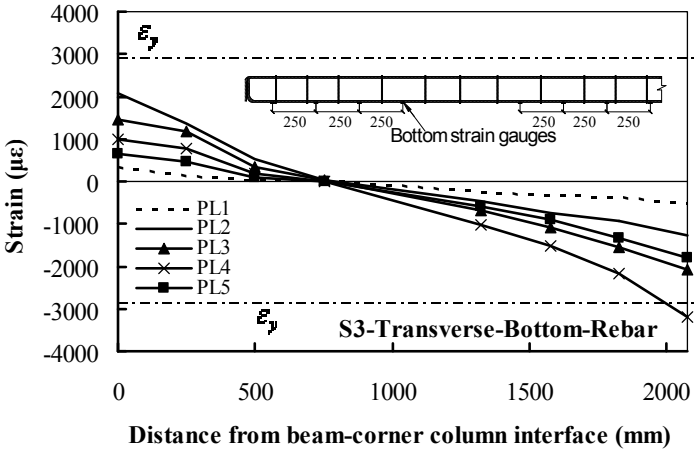

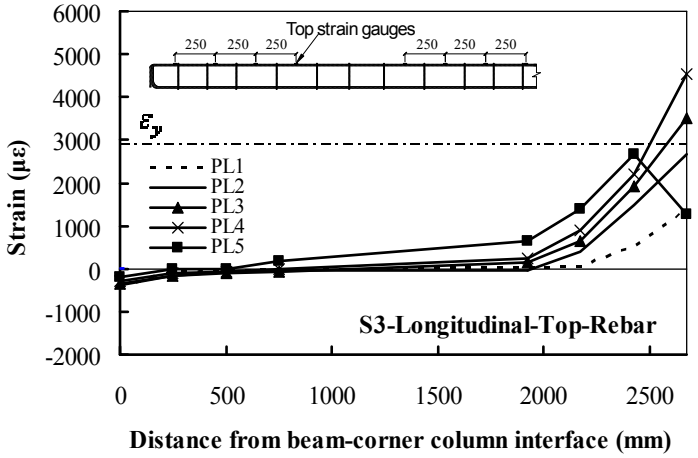

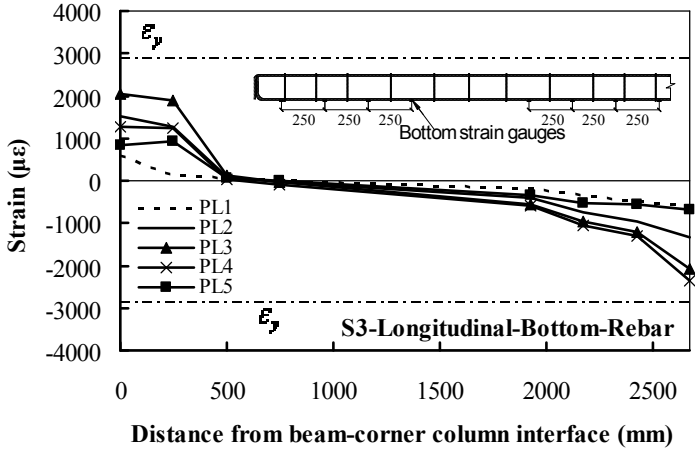

Fig. 8.17: Strain profile of beam longitudinal reinforcement of S3

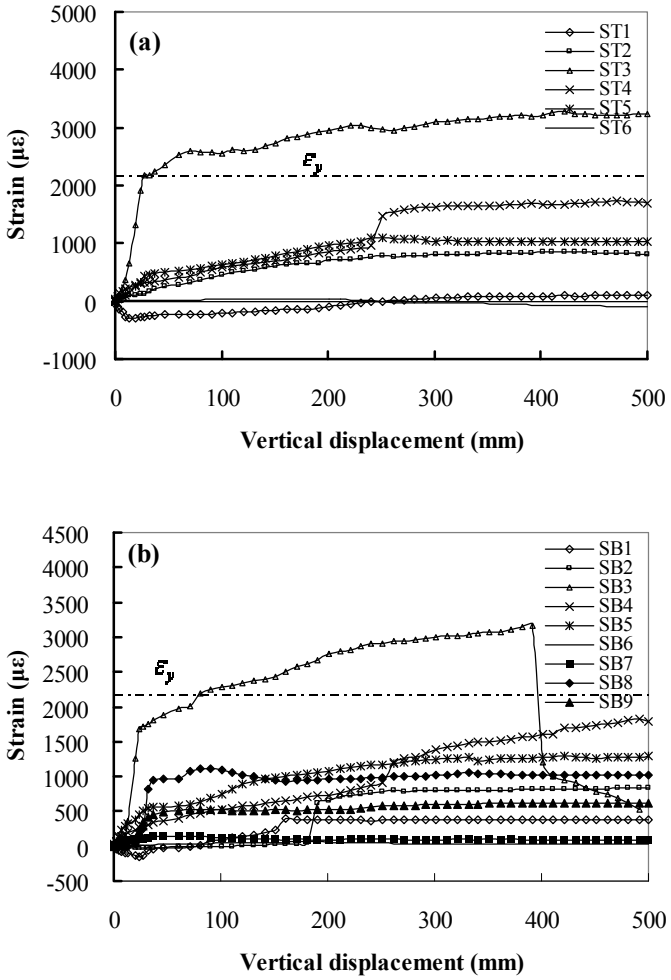

Fig. 8.18: Strain results in the slab reinforcement of S3

8.8 Discussion of the Slab Effects

As mentioned in previous chapters, in typical cast-in-situ construction, beams, columns and slabs act as a single structural unit. Ignoring the slab contribution to the strength and ductility of beams will result in a significant underestimation of the vertical force resistance. The influence of the slab on the strength of the floor system under imposed vertical deformation is significantly greater than that anticipated by the interpretation of the current provisions for effective slab widths acting as a flange in a T-beam analysis. Thus, it was important to evaluate ratio of the slab contribution on the overall resistant of the two-way slabs. In addition, as listed in the **Table 8.1,** S1, S2 and S3 were designed by just adding a RC slab based on F3, F2 and F7, respectively. Therefore, the influence of the RC slab on the resistant capacity of frame could be directly assessed by comparing the load-displacement curves of the above two series specimens.

8.8.1 Load-Displacement Relationship

The comparison of the load-displacement relationship of the S1 to F3 is shown in **Fig. 8.19**. The static ultimate strength of F3 and S1 were 25.8 kN and 39.1 kN, respectively. The ultimate capacity of S1 increased by about 51.6 % compared with F3. In addition, it should be noted that both specimens had the same design axial load, which equals to 18.6 kN using DoD [D1] suggested load combination. Thus, F3 reached only 138.7 % of the design column axial force, while S1 could reach 210.2 % of the design column axial force. Even the value of DIF was conservatively assumed to 2.0, S1 still could survive for progressive collapse. The initial stiffness of F3 and S1 obtained from the tests were 0.82 kN/mm and 1.08 kN/mm respectively.

As shown in **Fig. 8.20**, by comparing the static ultimate strength of F2 and that of S2, it can be seen that F2 and S2 could reach 196.2 % and 279.6 % of the design column axial force specified by DoD [D1], respectively. For S2 and F2, both specimens could survive even assumed the DIF equals to 2.0. It should be noted that the design column axial force for S2 and F2 was 18.6 kN while the initial stiffness of F2 and S2 obtained from the tests were 0.95 kN/mm and 1.13 kN/mm respectively.

As illustrated in **Fig. 8.21** and based on the test data, 99.1 % and 161.6 % of the loads specified by DoD [D1] that are required to resist progressive collapse could be achieved by F7 and S3, respectively. The design column axial force for S3 and F7 was 23.2 kN. Thus, F7 definitely could not survive for progressive collapse, even if the DIF was assumed to be 1.0. If the DIF was assumed to be 2.0, S3 also could not survive despite the contribution of the slab had been considered. The initial stiffness of F7 and S3 obtained from the tests were 0.75 kN/mm and 1.04 kN/mm, respectively.

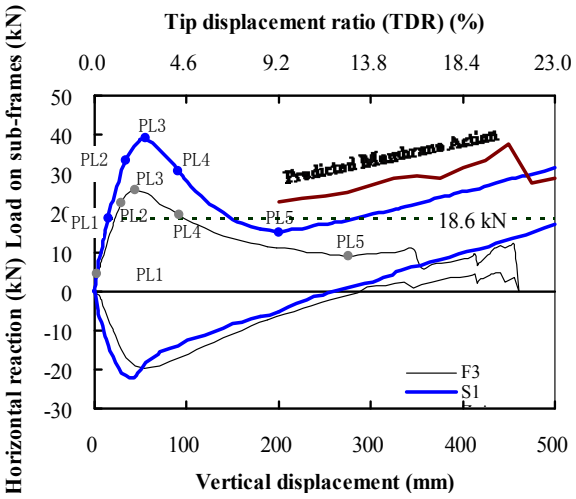

Fig. 8.19: Comparison of the load-displacement relationship of S1 to F3

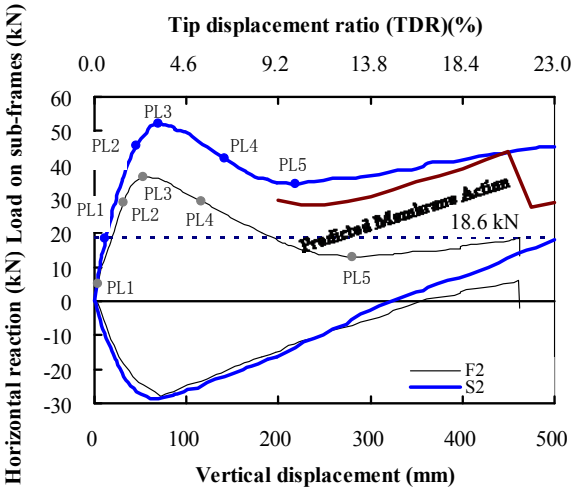

Fig. 8.20: Comparison of the load-displacement relationship of S2 to F2

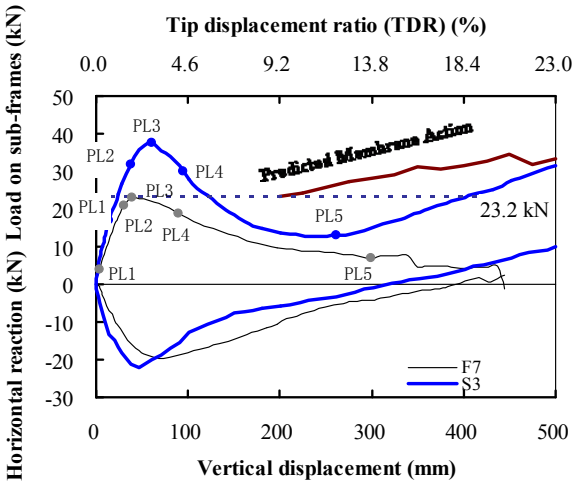

Fig. 8.21: Comparison of the load-displacement relationship of S3 to F7

8.8.2 Resistance Capacity Decomposition

Fig. 8.22 shows the contribution of the RC slab and beams in the resistant capacity of the S-series specimens in increasing the vertical displacement. For S1, initially, the RC slab only carried about 4.8 % of the resistant capacity. With the increasing

displacement, the contribution of the slab was increased to 31.2 % of the resistant capacity. After that, the slab component reduced to around 26.2 % due to the first crack forming in the slab. Next, the slab component increased to 38.6 % due to the plastic hinge forming in the BENAC. After the displacement reached 200.0 mm, the slab component significantly increased due to tensile membrane action developing in the slab.

In general, S2 and S3 had similar behavior to S1. Initially, 5.0 % and 5.4 % of the resistant capacity was carried by the RC slab for S2 and S3, respectively. When the vertical displacement reached 218.0 mm and 260.0 mm for S2 and S3 respectively, the slab component significantly increased due to the tensile membrane action development in the slab.

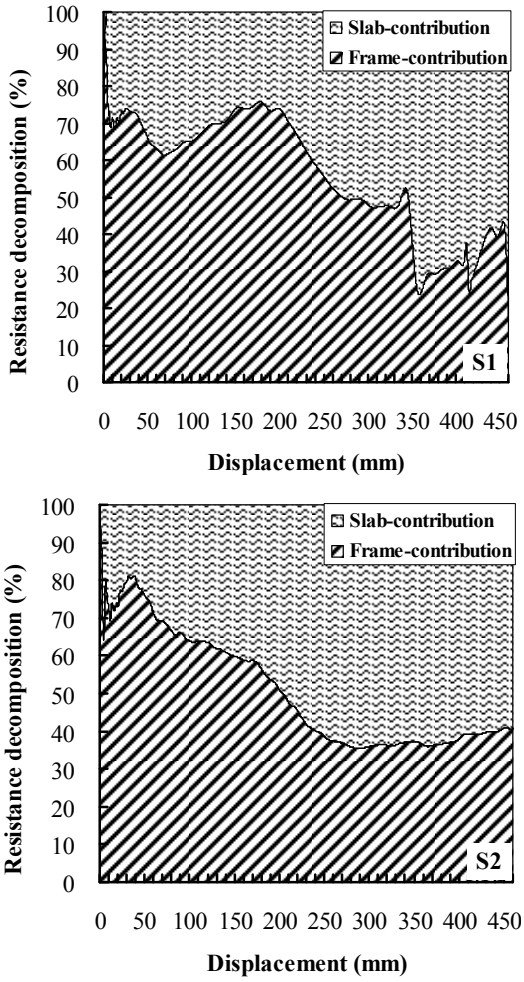

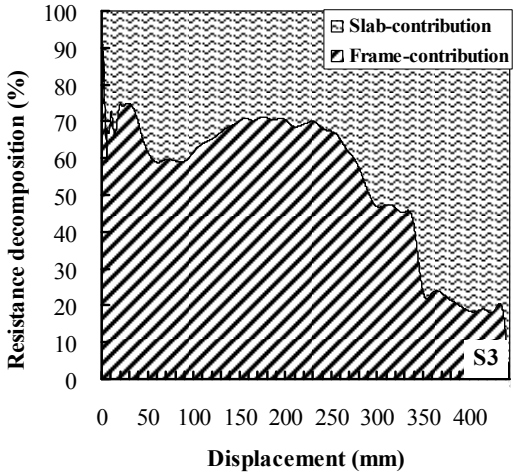

Fig. 8.22: Resistance decomposition of slab specimens

8.8.3 Energy Dissipation Capacity

Fig. 8.23 illustrates the relationship of the energy dissipation capacity (area under the load-displacement curves) and vertical displacement for all specimens. The total energy dissipated from Specimens F3, S1, F2, S2, F7 and S3 were 5.1 kN.m, 11.7 kN.m, 9.3 kN.m 20.0 kN.m, 4.8 kN.m and 10.7 kN.m respectively, at the end of each test. S1 increased the energy dissipation capacity by about 100.0 % compared with that of F3. For S2 and S3, the energy dissipation capacity increased by about 116.5 % and 121.6 % compared with F2 and F7, respectively. It should be noted that all of the tests of the S-series specimens were halted when the vertical displacement reached 500.0 mm due to safety concern.

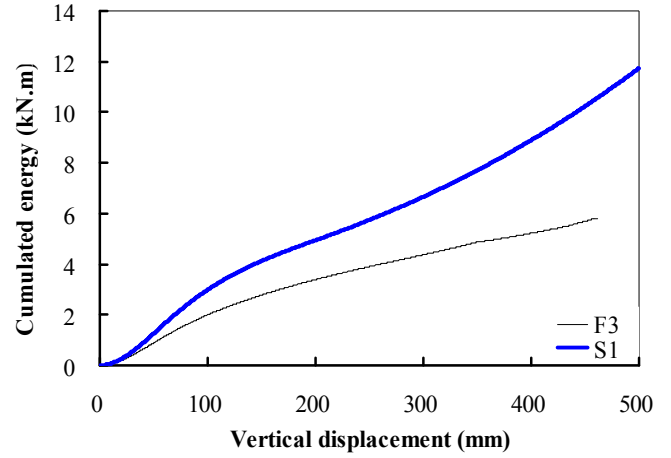

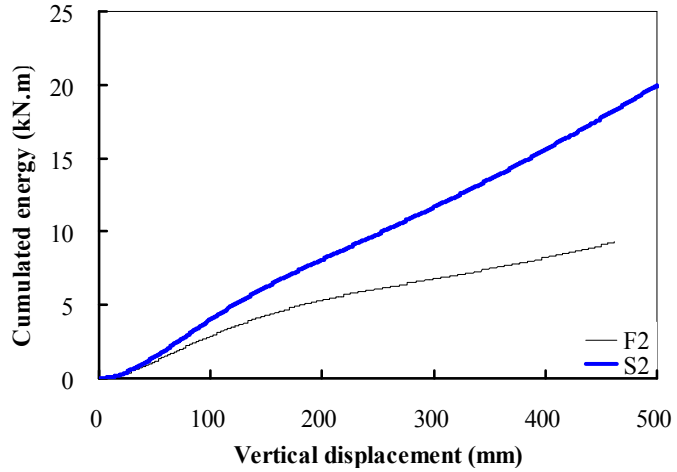

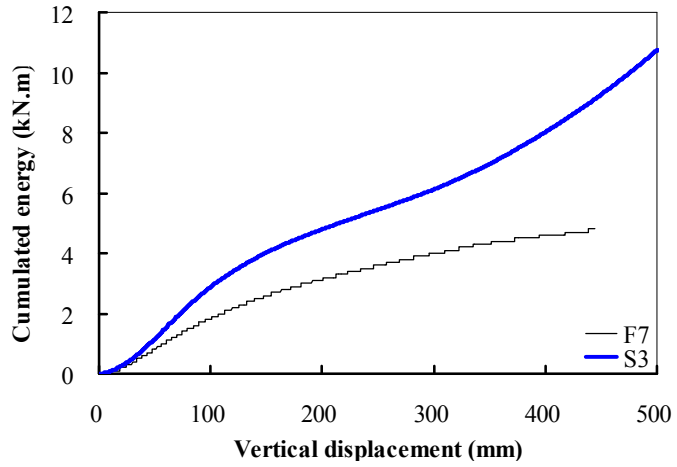

Fig. 8.23: Comparison of the cumulated energy capacity of the slab specimen with the corresponding frame specimen

8.9 Analytical Analysis to Capture Ultimate Capacity of the S-Series Specimens

Failure modes and the strain gauge results of the S-series specimens indicated that the increased ultimate capacity (first peak load) of the S-series specimens due to the RC slab could be decoupled into two parts: work as flange of the beam section (L-beam) and additional flexural strength provided by the slab itself. Therefore, in order to properly predict the ultimate strength of the S-series specimens, L-beam effects and the flexural strength provided by slab should be determined separately and the overall contribution of slab as the sum of these two actions.

8.9.1 Flexural Strength of the F- Series Specimens with L-Shape Beams

Due to limited instrumentation, the available test results could not determine the precise value of the effective flange width. Thus, the requirement for the effective flange width in Park and Paulay [P2] was used in the current analytical study. As an approximation, the slab reinforcement within a width of four times of the slab thickness each side of the web could be included within the tension steel of the beam (Park and Paulay [P2]). Thus, six R6 slab reinforcements were installed in the flange of the L-shape beam and included in the calculation. The ultimate moment capacity in the BENAC was increased as the flange in the tensile zone while the moment capacity in the BENC was assumed no change due to the flange being in compression. The partial constraint model proposed in **Chapter 5** was used to determine the ultimate capacity (first peak load) of the F-series specimens including flange effects. The results of F_u^{flange} are listed in **Table 8.4**.

$$F_u^{flange} = \frac{\xi M_a + M_u^{flange}}{l_n} \qquad (8\text{-}1)$$

where F_u^{flange} is the ultimate strength of the F-series specimens including the flange effect of the slab, M_a is the available bending moment at the BENC, M_u^{flange} is the ultimate bending moment of the BENAC including the flange, l_n is the clear span of the beam, and ξ is the rotational constraint factor (ξ=0.65 was used in this study).

Table 8.4: Comparison of the Predicted Ultimate Capacity with the Experimental Results for Slab Specimens

Specimen ID	$F_u^{measured}$ (kN)	F_u^{flange} (kN)	$F_u^{yield-line}$ (kN)	$F_u^{predicted}$ (kN)	$F_u^{predicted} / F_u^{measured}$
S1	39.1	30.2	4.8	35.0	0.90
S2	52.0	44.8	4.8	49.6	0.95
S3	37.5	29.2	4.9	34.1	0.91

8.9.2 Yield-Line Method to Determine the Additional Flexural Strength Provided by the Slab

The final failure modes of the S-series specimens indicated that the major yield line was diagonally connected to the two interfaces between the beam and the adjacent column. However, as shown in the slab reinforcement detailing (refer to **Fig. 8.2**), the top reinforcement in the slab was discontinuous and no top reinforcement was installed in the center of the slab. Therefore, only the two quarters of the slab near the adjacent columns had moment resistance.

Park and Gamble [P1] have concluded that for isotropic reinforced slabs, the ultimate moment resistance per unit width of the slab is equal in all directions and torsional moment at the yield line is zero. Therefore, the ultimate bending moment per unit

width acting at a general yield line m_{un} has same magnitude of the ultimate bending moment per unit width acting in the x and y directions.

As shown in **Fig. 8.24**, the effective length of the diagonal yield line is $\frac{\sqrt{l_x^2 + l_y^2}}{2}$ due to the top reinforcement in the slab being discontinuous. The total rotation of the half triangle segment close to the corner column refer to the yield line is $\frac{\delta\sqrt{l_x^2 + l_y^2}}{2l_x l_y}$. Hence, the internal work done is:

$$\sum m_{un}\theta_n l_0 = m_u \times \frac{\delta\sqrt{l_x^2 + l_y^2}}{l_x l_y} \times \frac{\sqrt{l_x^2 + l_y^2}}{2} = m_u \delta \frac{l_x^2 + l_y^2}{2l_x l_y} \qquad (8\text{-}2)$$

and external work done is:

$$\sum W_u \Delta = F_u^{yield-line} \times \delta \qquad (8\text{-}3)$$

where m_{un} is the ultimate bending moment per unit width at a yield line, θ_n is the relative rotation about the yield line of the two segments, l_0 is the length of the yield line; δ is the virtual small displacement in the direction of the load, W_u is the total load on a segment of the yield line pattern, and Δ is the downward movement of the centroid of a segment.

Therefore, the contribution of the slab due to the yield line can be determined by the virtual work equation

$$F_u^{yield-line} = m_u \times \frac{l_x^2 + l_y^2}{2 l_x l_y} \qquad (8\text{-}4)$$

where $F_u^{yield-line}$ is the flexural strength of the RC slab determined by the yield-line method.

For a yield line that runs at right angles to the reinforcement, the ideal ultimate moment of resistance per unit width due to that reinforcement is given by Park and Paulay [P2] and is shown in Eq. (8-5).

$$m_u = A_s f_y (d - 0.59 A_s \frac{f_y}{f_c^{'}}) \qquad (8\text{-}5)$$

where A_s is the area of tension steel per unit width, f_y is the yield strength of the reinforcement, and $f_c^{'}$ is the concrete compressive strength.

The results of $F_u^{yield-line}$ in S-series specimens are given in **Table 8.4**.

$$F_u^{predicted} = F_u^{flange} + F_u^{yield-line} \qquad (8\text{-}6)$$

where $F_u^{predicted}$ is the predicted ultimate strength of S-series specimens based on proposed the approaches.

As shown in the **Table 8.4**, good agreement was achieved between the measured results and the analytical results.

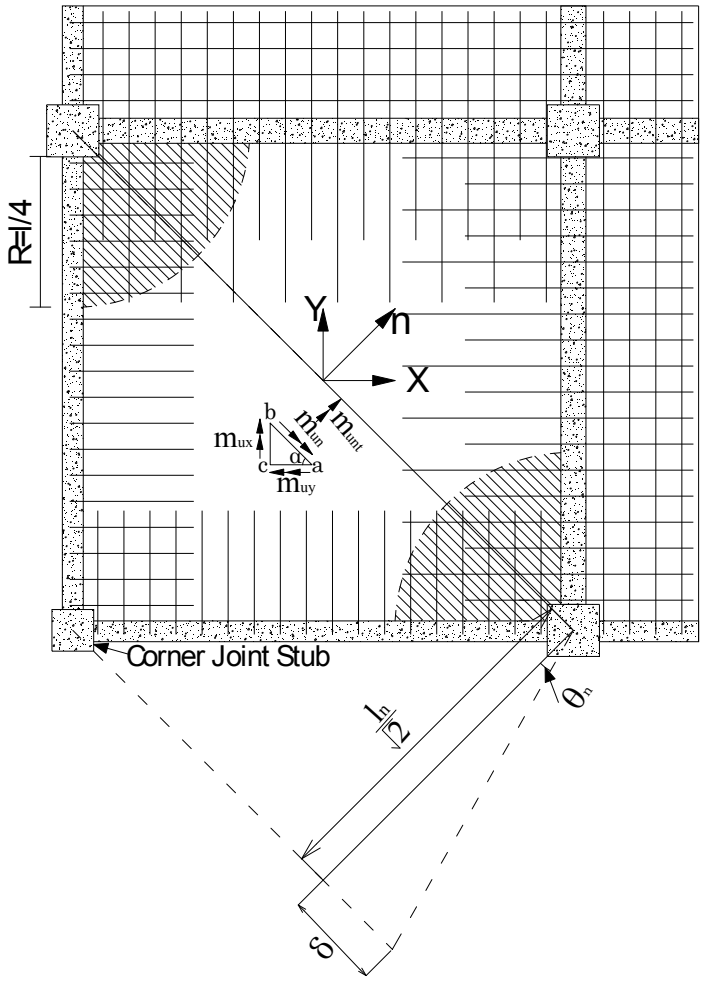

Fig. 8.24: Illustrate the yield-line method to determine the slab flexural resistance

8.10 Tensile Membrane Action on the Slabs

An obvious secondary ascending branch was observed in the load-displacement curve of the S-series specimens. Only tensile membrane action can explain this behavior due to the fact that limited catenary action was observed in the F-series specimens. So far, no existing analytical model can directly calculate the tensile membrane action of the two-way slab after losing one of the corner columns due to the special boundary and loading conditions. Thus, a simplified analytical analysis was proposed in this study to predict this behavior.

Tensile membrane action in the floor slabs will develop with large displacement if there is horizontal restraint at the perimeter of the floor slab or the slab is two-way spanning and is allowed a perimeter compressive restraining ring to form within the depth of the slab. A number of researchers, such as Park and Paulay [P2], have derived several analytical models to predict the tensile membrane action for a slab with or without horizontal constraints. However, in the present tests, one of the corner columns was lost due to extreme loading and concentrated vertical load was applied on the corner column to simulate the axial force previously carried by the corner column. Conversely, uniform loading was applied on the intact slab in the previous researches. Therefore, a simplified analytical model was derived based on the experimental observation and assumptions.

The following assumptions were used to derive the analytical model.

- Assuming tensile membrane action with a diagonal deformation.

- The concrete and top reinforcement in the slab carry no tension.

- The strain result illustrated that 75.0 % of the yield strain reached in the first bottom rebar near the adjacent column while 25.0 % yield strain was achieved in the first rebar near the corner column. Therefore, the strain in the slab rebar perpendicular with x or y direction was assumed linear distribution along with the edge beam and 75.0 % yield strain was assumed in the first rebar near the adjacent column and 25.0 % yield strain was assumed in the first rebar near the corner joint.

- A cantilever beam mechanism was assumed when the large displacement was

achieved in the tensile membrane action stage.

In the present analytical derivation, the slab reinforcement perpendicular to x direction is considered first. For the slab reinforcement perpendicular to y direction, it is similar.

As shown in **Fig. 8.25**, the tensile force of the ith rebar perpendicular with x direction was:

$$F_{ix} = A_s f_{si} = A_s(\frac{1}{4} f_y + \frac{1}{2} f_y(\frac{l_{nx} - S(i-1)}{l_{nx}})) = \frac{1}{2} A_s f_y(\frac{2l_{nx} - S(i-1)}{2l_{nx}}) \quad (8\text{-}7)$$

where A_s is the area of the slab reinforcement; f_{si} is the tensile stress of the ith rebar numbered from the adjacent column; S is the spacing of the slab reinforcement; l_{nx}, l_{ny} are the clear span of the beam in x and y direction respectively.

The vertical displacement in the ith rebar perpendicular with x direction was:

$$d_i = \frac{Si}{l_n + 0.5d_c} D_1 \quad (8\text{-}8)$$

where d_c is the width of the corner column, and D_1 is the vertical displacement in the corner column.

The vertical component of the tensile force of the ith rebar perpendicular with x direction was:

$$F_{ixv} = F_{ix} \frac{d_i}{\sqrt{d_i^{\,2} + (\frac{Si \times l_{ny}}{l_{nx}})^2}} \qquad (8\text{-}9)$$

The total vertical components in the slab rebar perpendicular with x direction were:

$$F_{xv} = \sum_{i=1}^{l_{nx}/s} F_{ivx} \qquad (8\text{-}10)$$

Similarly, the total vertical components in the slab rebar perpendicular with y direction were:

$$F_{yv} = \sum_{i=1}^{l_{ny}/s} F_{ivy} \qquad (8\text{-}11)$$

The tensile membrane action of the slab was:

$$F_{membrane} = F_{xv} + F_{yv} \qquad (8\text{-}12)$$

where $F_{membrane}$ is the predicted tensile membrane resistance in the slab.

The analytical membrane actions superimposed with the residual strength of the corresponding F-series specimens were compared with the measured results in the **Figs. 8.19**, **8.20** and **8.21**. The predicted results slightly over-estimate the test results for S1 and S3 while they under-estimate the test results of S2. In general, this simplified analytical model was expected to remain valid despite its simplicity. It should be noted that the flexural stiffness and torsional stiffness of the edge beams

following extreme cracking and concrete crushing will affect the development of the membrane action and was not included in this model due to limited data available.

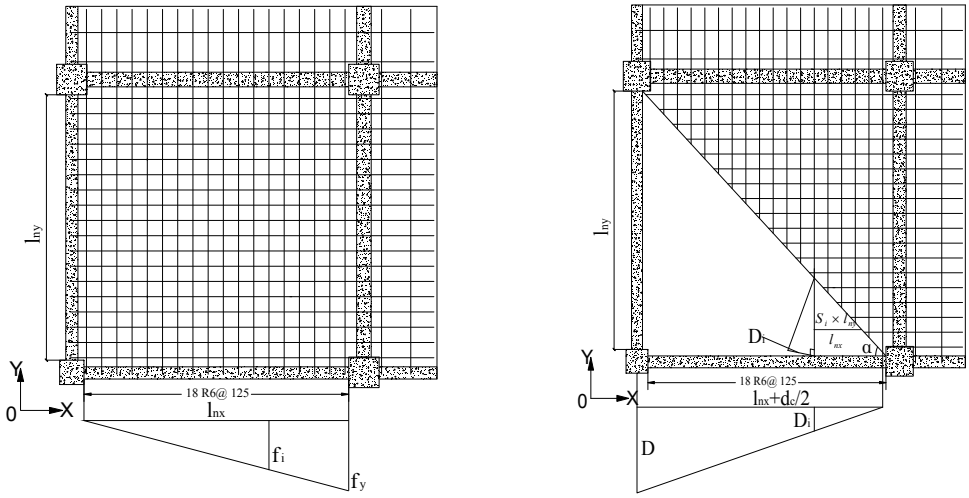

(a) (b)

Fig. 8.25: The simplified analytical method to capture the tensile membrane action of S1

8.11 Summary

The experimental study conducted in this research has derived the following conclusions:

1. As expected, seismic detailing could significantly improve the ultimate capacity of the substructures. The non-seismically detailed specimens F3 and F7 only reached 138.7 % and 99.1 % of the design axial load in the corner column specified by DoD [D1], respectively. However, seismically detailed F2 could reach up to 279.6 % of the design axial load in the corner column specified by DoD [D1] and could eliminate the possibility of progressive collapse if the corner column were lost (even if the value of DIF is '2.0').

2. Experimental results indicated that ignoring the contribution of the RC slab in resisting progressive collapse will be extremely conservative, especially for cast-in-situ structures. The ultimate load carrying capacity of S1, S2 and S3 (with slab) was increased by 51.6 %, 40.7 % and 63.0 % respectively as compared to the Specimens F3, F2 and F7 (without slab).

3. Top beam reinforcement near the fixed end fractured in the final test stage of the F-series specimens while a penetrating diagonal crack in the slab formed in the final test stage of the S-series specimens. The second ascending branch in the load-displacement curves of the S-series specimens indicated that tensile membrane action was developed in the slab due to limited catenary action as observed in the F-series specimens.

4. The proposed analytical method predicted the first ultimate capacity of the S-series specimens very well. Although the analytical results match the tensile membrane action developed in the slab reasonably, further experimental and analytical analysis are needed to refine the models.

CHAPTER 9

CONCLUSIONS AND COMMENTS ON FUTURE RESEARCH

9.1 Introduction

The performance of reinforced concrete beam-column substructure under the loss of a ground corner column scenario was investigated through experimental and analytical means in this study.

The study presented within this report consists of five main parts. In the first part of the report, seven RC beam-column substructures without slabs were subjected to a quasi-static loading regime. The variables in the test specimens include design detailing, span length and unequal span in the longitudinal and transverse directions.

In the second part of the report, an analytical approach, coupling yield strength, ultimate strength and corresponding displacements, was proposed to predict the load-displacement behavior of the substructures. A comprehensive parametric study was carried out based on the proposed model to investigate the influences of several critical parameters.

In the third part of the report, six RC beam-column substructures without slabs were subjected to a dynamic loading regime. The dimensions and reinforcement details of the dynamic specimen were similar to the quasi-static tested specimens. Moreover, the dynamic increase factors of the test specimens were evaluated by comparing the dynamic test results with the corresponding quasi-static test results.

In the fourth part of the report, the accuracy of analytical models (SDOF model and capacity curve model) was evaluated by comparing their results with test results. Moreover, the dynamic ultimate strength of the test specimens was determined by conducting incremental dynamic analytical analyses. The dynamic increase factors obtained from the analytical approach were compared with the values provided in the design guideline DoD [D1].

Finally, slab effects on the performance of the RC substructures for progressive collapse were evaluated by comparing the test results of the substructures without slabs with the corresponding specimens incorporating RC slabs.

Conclusions drawn from the experimental and analytical results are presented in the following section. Recommendations on future works are also presented.

9.2 Experimental Investigations

9.2.1 Quasi-Static Test of the RC Substructures without Slab

The conclusions drawn from the experimental investigation of seven RC substructures without slab subjected to quasi-static loading regime are as follows:

1. Specimens with seismic detailing saw a 41.5% increase in ultimate strength capacity compared to F3. This can be attributed to the increased amount of longitudinal beam reinforcement installed in the beam, which increased the flexural capacity of the beam section. Moreover, several transverse reinforcements were installed in the corner joint region, which allowed for plastic hinge development in the beam end adjacent to the corner joint.

2. As the transverse beam reinforcement ratio in the potential plastic hinge zone was increased from 0.23 % to 0.31 %, the strength of the tested specimen was enhanced by about 8.9 %. This was due to the shear failure that occurred in the plastic hinge zone which reduced the effectiveness of compressive arch action and resulted in a lower ultimate resistant capacity. However, when the transverse reinforcement ratio was increased from 0.31 % to 0.72 %, the strength of the tested specimen was only enhanced by 6.5 %. This indicates that the effect of the transverse reinforcement ratio in the potential plastic hinge zone for ultimate capacity is limited as long as the shear failure is not severe in the plastic hinge zone.

3. F5 reached an ultimate capacity of 26.8 kN while the design axial force of the corner column was 29.1 kN. Thus, F5 will totally collapse even if the dynamic increase factor is '1.0'. This confirmed that specimens with longer design spans are more vulnerable under similar distributed loads.

4. The plastic hinge properties of RC elements suggested in DoD [D1] is an adoption of the modeling parameters presented in ASCE 41-06 [A4]. The accuracy of these parameters was evaluated by comparing with the parameters obtained from the current tests. In general, the value of parameter "a" recommended in DoD [D1] is reasonable for a beam section controlled by flexural failure but it is too conservative if the beam section is controlled by the flexural and shear failure. Moreover, for parameters "b" and "c", the values suggested in DoD [D1] are extremely conservative. More studies are needed to assess these modeling parameters.

5. Although DoD [D1] has implemented significant modifications for tie strength design, no difference in design was proposed between the peripheral

tie near the corner column and the tie near the exterior column in DoD [D1]. As shown in the test results, the allowable tie strength determined based on the reinforcement details was larger than the required tie strength attained based on DoD [D1]. However, the measured horizontal tensile force (tie force) was much less than the allowable tie strength due to insufficient horizontal constraint provided by the corner joint. Thus, it is suggested that the catenary effect (tie strength method) to be neglected in practical design for buildings in resisting progressive collapse caused by losing a ground storey corner column.

6. Test results indicated that there are two ways to improve the performance of RC frames against progressive collapse caused by losing a corner column. Firstly, increase the flexural capacity of the beam section by amplifying the beam longitudinal reinforcement ratio for new buildings or by externally bonded composite materials (such as fiber-reinforced polymer) along the beam length for existing buildings. Secondly, upgrade the shear strength of the corner joint by installing more joint transverse reinforcement for new buildings or by externally wrapping composite materials (such as fiber-reinforced polymer) to confine corner joint for existing buildings. It should be emphasized that the failure due to rebar anchorage and splice is beyond the scope of this study.

9.2.2 Dynamic Test of the RC Substructures without Slab

The conclusions drawn from the experimental investigation of six RC substructures without slab subjected to dynamic loading regime are as follows:

1. The column removal apparatus was proved effective in dynamic tests as the measured duration of the column removal did not exceed 0.0035s, within 10% of the natural period of the substructures.

2. Peak accelerations measured in the corner column could reach up to 3.5 g in Specimen DF3 but the peak acceleration decreased upon moving away from the corner column.

3. The integration method could be utilized to determine the velocity and displacement responses only when acceleration results are available. However, baseline correction must be conducted before integration.

4. The peak value of the total vertical reaction force measured in the fixed supports was larger than the axial force of the corner column before its subsequent removal. This was due to the inertial force which developed after the sudden removal of the corner support.

5. No horizontal tensile force was recorded in the fixed support of DF3 and DF4. This indicated that catenary action did not develop to resist the progressive collapse during the tests of DF3 and DF4.

6. The test results confirmed that seismic detailing succeeded in increasing the resistant capacity of the structures against progressive collapse. Structures with longer design span lengths exhibited a higher vulnerability for progressive collapse compared to structures with shorter span lengths. Furthermore, more attention should be paid to structures subjected to a higher service load.

7. The dynamic as well as quasi-static behavior of tested specimens indicated that the dynamic increase factor is in the range of 1.14 to 1.38 for test specimens. The suggested value of '2.0' in DoD (2009) was over-conservative for the structural components with force-controlled behavior.

9.2.3 Experimental Investigate the Slab Effects on the Performance of RC Substructures for Progressive Collapse

The conclusions drawn from the experimental investigation of the slab effect on the performance of RC substructures for progressive collapse are as follows:

1. As expected, seismic detailing could significantly improve the ultimate capacity of the substructures. The non-seismically detailed specimens F3 and F7 only reached 138.7 % and 99.1 % of the design axial load in the corner column specified by DoD [D1]. However, seismically detailed F2 could reach up to 279.6 % of the design axial load in the corner column specified by DoD [D1] and could eliminate the possibility of progressive collapse if the corner column was lost (even the dynamic increase factor was '2.0').

2. Experimental results indicated that ignoring the contribution of the RC slab in resisting progressive collapse will be extremely conservative, especially for cast-in-situ structures. The ultimate load carrying capacity of S1, S2 and S3 (with slab) was increased by 51.6 %, 40.7 % and 63.0 % respectively as compared to the Specimens F3, F2 and F7 (without slab).

3. Top beam reinforcement near the fixed end fractured in the final test stage of the F-series specimens while a penetrating diagonal crack in the slab formed

in the final test stage of the S-series specimens. The second ascending branch in the load-displacement curves of the S-series specimens indicated that tensile membrane action was developed in the slab due to limited catenary action as observed in the F-series specimens. However, further experimental and analytical studies are needed to understand the detailed behavior of the membrane action of the slab for progressive collapse under the scenario of the loss of a corner column.

9.3 Analytical Investigations

9.3.1 Analytical Investigation of the RC Substructures without Slab under Quasi-static Loading Regime

The conclusions drawn from the analytical investigation of the RC substructures without slab subjected to quasi-static loading regime are as follows:

1. Comparisons made between the analytical and experimental results have shown good agreement. This demonstrates the applicability and accuracy of the proposed method to estimate the load-displacement curves of the RC substructures for progressive collapse caused by losing a corner column.

2. The parametric study based on the proposed method showed that the initial stiffness, yield strength and ultimate strength increased with an increase in the longitudinal reinforcement ratio. However, the residual strength decreased with an increase in the longitudinal reinforcement ratio.

3. The effect of the beam width on the initial stiffness, yield strength and ultimate strength of the substructures was limited. However, the residual strength increased with an increase in the width of the beam. It should be noted that increasing the beam depth significantly improved the overall performance of the substructures.

4. Increasing the clear span of the beam significantly decreased the initial stiffness, yield strength and ultimate strength of the specimen, but had no effect on the residual strength.

5. If the existing dimension of the column could not provide enough shear strength to allow the plastic hinge to be formed in the BENC, increasing the size of the corner column would improve the overall performance of the substructures. However, increasing the dimension of the corner column would cause no change in the performance of the substructures if the existing size of the column had enough strength to allow the plastic hinge to form in the BENC. Similar trends were observed for the influence of the joint transverse reinforcement ratio.

9.3.2 Analytical Investigation of the RC Substructures without Slab under Dynamic Loading Regime

The conclusions drawn from the analytical investigation of RC substructures without slab subjected to dynamic loading regime are as follows:

1. The SDOF method can accurately predict the displacement response of substructures in progressive collapse, as validated by the comparison between the analytical results and experimental data.

2. The residual strength of the substructure beyond the static ultimate strength should be considered in the SDOF models.

3. The damping ratio significantly influences the displacement response of the specimens. Large damping ratios (ζ=20%) were used in the current SDOF analysis because of the large damping observed in the experimental tests.

4. Comparing the value of the dynamic load increase factor (DLIF) obtained from SDOF with that suggested in DoD [D1], it was found that the proposed DIF values in DoD [D1] were over-conservative.

5. The capacity curve method can predict whether the test specimens will totally collapse, as well as predict the dynamic ultimate strength of the substructures without residual strength. However, it does not produce conservative results if the residual strength of the substructures is considered.

9.4 Recommendations for Future Research

It is not possible to provide a complete investigation in this study. Therefore the following research is recommended to obtain a better understanding in the behavior of the reinforced concrete frame under the loss of a corner column scenario as well as understanding the progressive collapse phenomenon itself.

9.4.1 Future Research about Experimental Investigations

The urgently needed future research studies for experimental investigation of the RC frames against progressive collapse are as follows:

1. Further experimental studies are needed to understand the effects of longitudinal reinforcement ratio, span depth ratio on the quasi-static and dynamic performance of the beam-column substructures without slabs after losing a corner column.

2. Further experimental studies are needed to investigate the quasi-static and dynamic performance of the reinforced concrete precast beam-column substructures after losing a corner column.

3. The influences of the slab longitudinal reinforcement ratio, slab thickness on the quasi-static and dynamic performance of the beam-column substructures with slabs after losing a corner column should be further studied.

4. The quasi-static and dynamic performance of flat plate or flat slab structures after losing a corner column should be studied.

5. The effect of the extent of the rotational constraint at the corner column on the quasi-static and dynamic performance of the substructures after losing a corner column should be studied.

6. Strengthening or repairing the reinforced concrete beam-column substructures (with or without slab) by externally bonded composite materials to resist progressive collapse caused by losing a corner column should be studied.

7. Quasi-static and dynamic tests of the reinforced concrete beam-column substructures (with or without slab) for progressive collapse caused by losing

several columns should be studied.

9.4.2 Future Research about Analytical Investigations

The urgently needed future research studies for analytical and numerical investigation of the RC frames against progressive collapse are as follows:

1. Further analytical analysis is needed to be developed to capture the dynamic performance of reinforced concrete substructures after losing a corner column.

2. Further analytical analysis is needed to capture the compressive and tensile membrane action developing in the slab to resist the progressive collapse.

3. Development of analytical design guidelines for the strengthening and repair of reinforced concrete substructures with externally bonded composite materials.

4. Further numerical tools should be refined and developed by validated by the above experimental results.

5. The design guidelines should be further refined with the above experimental and analytical analyses.

REFERENCES

[A1] Abruzzo J., Matta A., Panariello G., "Study of Mitigation Strategies for Progressive Collapse of a Reinforced Concrete Commercial Building" Journal of Performance of Constructed Facilities, ASCE, Vol. 20, No. 4, pp. 384-390, 2006.

[A2] ABAQUS Analysis User's Manual, 2006.

[A3] ACI Committee 318, "Building Code Requirements for Structural Concrete" American Concrete Institute, Farming Hills, Mich, 2008.

[A4] ASCE 41-06, "Standard-Minimum Design Loads for Buildings and Other Structures" SEI, 2007.

[A5] ASCE 7-10, "Standard- Minimum Design Loads for Buildings and Other Structures" SEI, 2010.

[A6] ASCE 7-95, "Standard- Minimum Design Loads for Buildings and Other Structures" SEI, 1996.

[B1] Bakir, P. G., and Boduroglu, H. M., "A New Design Equation for Predicting the Joint Shear Strength of Monotonically Loaded Exterior Beam-Column Joints" Engineering Structures, Vol. 24, No. 8, pp. 1105-1217, 2002.

[B2] Bao, Y. H., Kunnath, S. K., El-Tawil, S., and Lew, H. S., "Macromodel-Based Simulation of Progressive Collapse: RC Frame Structures" Journal of Structural Engineering, ASCE, Vol. 134, No. 7, pp. 1079-1090, 2007.

[C1] Calvi, G. M., Priestley, M. J. N., and Kowalsky, M. J., "Displacement-Based Seismic Design of Structures" IUSS Press, Pavia, Italy, 2008

[C2] CP 65, "Structural Use of Concrete, Part I. Code of Practice for Design and Construction" Singapore Standard, 1999.

[C3] Clark, L. A., and Speirs, D. M., "Tension Stiffness in Reinforced Concrete Beam and Slabs under Short-Term Load" Technical Report No 42.521, London: Cement and Concrete Association, 1978.

[C4] Corley G., "Learning from Disaster to Prevent Progressive Collapse" Civil Engineering, Institution of Civil Engineers, pp. 41-48, 2008.

[D1] Department of Defense, "Interim Antiterrorism/Force Protection Construction Standards" Guidance on Structural Requirements.

[F1] Fu, F. "Progressive Collapse Analysis of High-Rise Building with 3-D Finite Element Modeling Method" Journal of Constructional Steel Research, Vol. 65, pp. 1269-1278, 2009.

[G1] General Services Administration, "Progressive Collapse Analysis and Design Guidelines for new Federal Office Buildings and Major Modernization Projects" GSA, 2003.

[G2] Gilert, R. I., and Warner, R. F., "Tension Stiffness in Reinforced Concrete Slabs" Journal of Structural Division, Vol. 104 (ST12), pp. 1885-2000, 1978.

[G3] Gupta, B. A. K., and Maestrini, J. R., "Tension Stiffness Model for Reinforced Concrete Rebars" Journal of Structural Engineering, Vol. 116, No. 3, pp. 769-790, 1990.

[H1] Hines, E. M., "Seismic Performance of Hollow Rectangular Reinforced Concrete Bridge Piers with Confined Corner Elements" Ph.D, thesis, University of California (UCSD), San Diego, California, USA, 2002.

[H2] Hu, H-T., and Schnobrich, W. C., "Nonlinear Finite Element Analysis of Reinforced Concrete Plates and Shells Under Monotonic Loading" Computer and Structures, Vol. 38, No. 5/6, pp. 637-651, 1991.

[I1] ISC, "ISC Security Criteria for New Federal Office Buildings and Major Modernization Projects" Interagency Security Committee, Washington, DC, September, 2001.

[I2] Izzuddin, B. A., Vlassis, A. G., Elghazouli, A. Y., Nethercot, D. A., "Progressive Collapse of Multi-Storey Buildings due to Sudden Column Loss–Part Ⅰ: Simplified Assessment Framework" Engineering Structures, Vol. 30, No. 5, pp. 1308-18, 2008.

[K1] Kaewkulchai, G., and Williamson, E. "Dynamic Behavior of Planar Frames during Progressive Collapse" Proc., 16th Engineering Mechanics Conference, Univ. of Washington, Seattle, 2003.

[K2] Kim, J., and Park, J. "Design of Steel Moment Frames Considering Progressive Collapse" Steel and Composite Structures, Vol. 8, No. 1, pp. 85-98, 2008.

[M1] Marjanishvili, S. M., "Progressive Analysis Procedure for Progressive Collapse" Journal of Performance of Constructed Facilities, ASCE, Vol. 18, No. 2, pp. 79-85, 2004.

[M2] Mohamed, O. A., "Assessment of Progressive Collapse Potential in Corner Floor Panels of Reinforced Concrete Buildings" Engineering Structures, 31(3), pp. 749-757, 2009.

[M3] Marchand, K., Mckay, A., Stevens, D., J., "Development and Application of Linear and Non-linear Static Approaches in UFC 4-023-03" Structures 2009: Don't Mess with Structural Engineers@2009 ASCE, pp. 1729-1738, 2009.

[N1] National Research Council of Canada, National Building Code of Canada 1975, 1975, Ottawa, Canada.

[N2] National Research Council of Canada, National Building Code of Canada 1977, Ottawa, Canada, 1977.

[N3] National Research Council of Canada, National Building Code of Canada 1980, Ottawa, Canada, 1980.

[O1] Orton, S. L., "Development of a CFRP System to Provide Continuity in Existing Reinforced Concrete Building Vulnerable Concrete Frame Structures" PhD dissertation, University of Texas at Austin, Austin, TX, , 363 pp，2007.

[P1] Park, R., and Gamble, W. L., "Reinforced Concrete Slab" John Wiley & Sons, New York, pp.303-448, 1980.

[P2] Park, R, and Paulay, T., "Reinforced Concrete Structures" John Wiley and Sons, Inc, 769 pp, 1975.

[P3] Paulay, T. and Priestley, M. J. N., "Seismic Design of Reinforced Concrete and Masonry Buildings" John Wiley and Sons, Inc, 769 pp, 1992.

[P4] Park, R., "Tensile Membrane Behaviour of Uniformly Loaded Rectangular Reinforced Concrete Slabs with Fully Restrained Edges" Magazine of Concrete Research, Vol. 16, No. 46, pp. 39-44, 1964.

[P5] Priestley, M. J. N., "Performance Based Seismic Design" In: Proceedings of the 12th World Conference on Earthquake Engineering, Auckland, New Zealand. Paper No. 2831, 2000.

[P6] Priestley, M. J. N. and Grant, D. N., "Viscous Damping in Seismic Design and Analysis" Journal of Earthquake Engineering, Vol. 9 Special Issue, pp 229-255, 2005.

[P7] Prakhya and Morley, "Tension Stiffness and Moment-Curvature Relations for Reinforced Concrete Elements" ACI Structural Journal, Vol. 87, No.5, pp 597-605, 1990.

[P8] Pretlover, A., Ramsden, M., and Atkins, A., "Dynamic Effects of Progressive Failure of Structures" International Journal of Impact Engineering, Vol. 11, No.4, pp 539-541, 1991.

[Q1] Qian, K., and Li, B., "Performances of RC Interior Beam-Column Sub-assemblages under Loss of a Column Scenario" Journal of Performance of Constructed Facilities, ASCE, (to press).

[R1] Ruth, P., Marchand, K. A., Williamson, E. B. "Static Equivalency in Progressive Collapse Alternate Path Analysis: Reducing Conservatism while Retaining Structural Integrity" Journal of Performance of Constructed Facilities, ASCE, Vol. 20, No. 4, pp. 349-364, 2006.

[S1] Sasani, M., Bazan, M., and Sagiroglu, S., "Experimental and Analytical Progressive Collapse Evaluation of Actual Reinforced Concrete Structure" ACI Structural Journal, V.104, No.6, pp. 731-739, 2007.

[S2] Sasani, M., "Response of a Reinforced Concrete Infilled-frame Structure to Removal of Two Adjacent Columns" Engineering Structures, Vol. 30, pp. 2478-2491, 2008.

[S3] Sasani, M., and Sagiroglu, S., "Progressive Collapse of Reinforced Concrete Structures: A Multihazard Perspective" ACI Structural Journal, V.105, No.1, pp. 96-103, 2008.

[S4] Su, Y. P., Tian, Y., Song, X. S., "Progressive Collapse Resistance of Axially-Restrained Frame Beams" ACI Journal, V.106, No.5, pp. 600-607, 2010.

[S5] Saenz, L. P., "Discussion of equation for the stress-strain curve of concrete" (by Desai and Krishnan) ACI Structural Journal, Vol. 61, No.9, pp. 1229-1235, 1964.

[S6] Sun, F. F., and Xu, J. M., "Numerical Simulation of Progressive Collapse Behavior of Tall Core-outrigger Structures" The Third International Conference on Design and Analysis of Protective Structures, pp.84-93, 2010.

[S7] Schlaich, J., and Schafer, K. "Design and Detailing of Structural Concrete Using Strut-and-Tie Models" Journal of Structural Engineering, 69(6), pp.113-125, 1991.

[T1] Tan, L. Y., Krauthammer, T., and Yim, H. C., "Characterizing a Reinforced Concrete Connection for Progressive Collapse Assessment" The Third International Conference on Design and Analysis of Protective Structures, pp.64-73, 2010.

[T2] Tsai, M. H., "An Analytical Methodology for the Dynamic Amplification Factor in Progressive Collapse Evaluation of Building Structures" Mechanics Research Communications, pp.61-66, 2010.

[T3] Tsai, M. H., and Lin, B., H., "Investigation of Progressive Collapse Resistance and Inelastic Response for an Earthquake-Resistant RC Building Subjected to Column Failure" Engineering Structures, Vol. 30, pp.3619-3628, 2008.

[W1] Williams, A., "Tests on Large Reinforced Concrete Elements Subjected to Direct Tension" Technique Report No 42.562. Cement and Concrete Association, London, 1986.

[Y1] Yi, W. J., He, Q. F., Xiao, Y., and Kunnath, S.K., "Experimental Study on Progressive Collapse Resistant Behavior of Reinforced Concrete Frame Structures" ACI Journal, Proceedings V.105, No 4, pp.96-103, 2008.

[Y2] Yap, S. L., "Experimental and Analytical Study of Exterior Beam-Column Joint for Progressive Collapse" Master Thesis, Department of Civil Engineering Nanyang Technological University, Singapore, PP259, 2009.

APPENDIX A

DETERMINE THE AXIAL FORCE IN THE CORNER SUPPORT OF EACH SPECIMEN

Main steps:

Step1: Determine the bending moment demand of the beam in the prototype frame.

Step2: Determine the ratio of the bending moment demand to the yield capacity of the beam section in the prototype beam.

Step3: Determine the bending moment demand in the model frame based on the equivalent strain method.

Step4: Determine the required pressure applied on the model frame, which can produce required bending moment demand.

Step5: Determine the axial force in the corner support of each model frame.

The detailed configuration of the prototype corresponding model frames is given in **Table A.1.**

Table A.1: Co-relationship between the Prototype Frames with Corresponding Test Models in the Current Study (Unit: mm)

Test	Prototype frames				Model frames			
	Span-T	Span-L	Beam-T Dimensions	Beam-L Dimensions	Span-T	Span-L	Beam-T Dimensions	Beam-L Dimensions
F1	7200	7200	540×300	540×300	2400	2400	180×100	180×100
F2 and DF2	7200	7200	540×300	540×300	2400	2400	180×100	180×100
F3, DF1 and DF3	7200	7200	540×300	540×300	2400	2400	180×100	180×100
F4 and DF4	7200	7200	540×300	540×300	2400	2400	180×100	180×100
F5 and DF5	9000	9000	720×300	720×300	3000	3000	240×100	240×100
F6 and DF6	7200	9000	540×300	720×300	2400	3000	180×100	240×100
F7	7200	9000	540×300	630×300	2400	3000	180×100	210×100

Note: Span-T and Span-L represent span in the transverse and longitudinal direction, respectively
Beam-T and Beam-L represent transverse beam and longitudinal beam, respectively.

Step 1: Determine the bending moment demand of the beam of prototype frame.

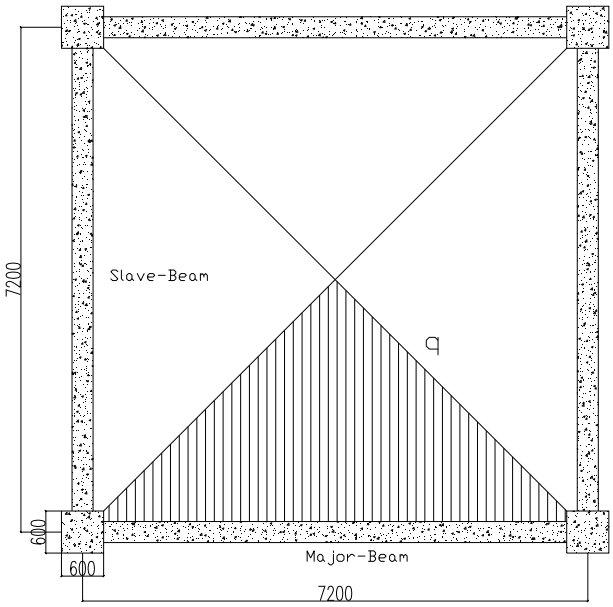

Fig. A1: Slab load distribution to beam of prototype slab

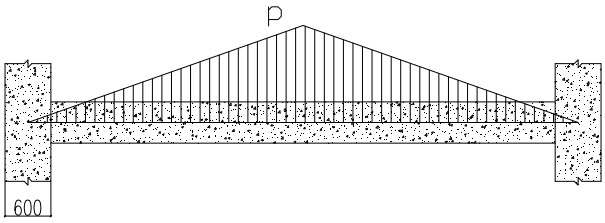

Fig. A2: Triangle line pressure on beam of prototype slab

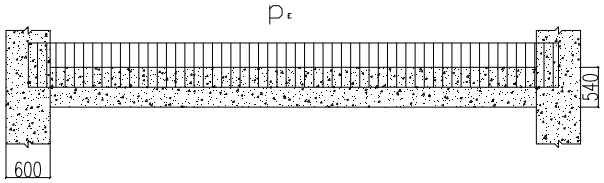

Fig. A3: Equivalent uniform line pressure on beam of prototype slab

The dead load due to slab self-weight is $0.21m \times 2450kg/m^3 \times 9.81N/kg = 5.05kpa$. The live load is taken to be 2.0 kPa at each storey level while the dead load consists of the self-weight of the building and 1.0 kPa additional dead load applied to the floors. The 1.0 kPa additional dead load accounts for items such as partitions, ceiling, mechanical ductwork, electrical items, plumbing, and so forth.

The dead load due to in-fill walls (two exterior walls and two half interior walls) is:

$$3(0.3m \times 5.5kN/m^3 \times 3.3m/7.2m) = 2.25kN/m^2 \qquad \text{(A-1)}$$

It should be clarified that the floor height is 3.3 m and the density of hollow brick is $550\,kg/m^3$.

The dead load due to RC beams (two exterior beams and two half interior beams) is:

$$3(0.3m \times 23.5kN/m^3 \times 0.54m/7.2m) = 1.59kN/m^2 \qquad \text{(A-2)}$$

According to DoD [D1], the design pressure at service condition is:

$$q_p = 1.2DL + 0.5LL = 1.2(5.05 + 1.0 + 2.25 + 1.59) + 0.5 \times 2 = 12.9kPa \qquad \text{(A-3)}$$

$$P_p = \frac{1}{2} q_p l_2 = 0.5 \times 12.9 \times 7.2m = 46.44kN/m \qquad \text{(A-4)}$$

$$P_{Ep} = \frac{5}{8} P_p = 29.02kN/m \qquad \text{(A-5)}$$

$$M_{Rp} = \frac{1}{12} P_{Ep} \times L^2 = 125.4kN.m \qquad \text{(A-6)}$$

where q_p is the uniform pressure on the prototype slab; P_p is the maximum value of triangle line pressure on the prototype beam; P_{Ep} is the equivalent uniform line pressure on the prototype beam; M_{Rp} is the bending moment demand on the prototype beam; M_{yp} is the yield bending moment on the prototype beam.

Step 2: Determine the ratio of the bending moment demand to the yield capacity of the beam section in the prototype beam.

$$M_{yp} = 260kN.m \qquad \text{(A-7)}$$

$$\frac{M_{Rp}}{M_{yp}} = \frac{125.4}{260} = 0.48 \qquad \text{(A-8)}$$

Step 3: Determine the bending moment demand of the model frame based on the same ratio of the demand to the yield capacity as the prototype frame.

$$M_{ym} = 9.67kN.m \qquad \text{(A-9)}$$

$$M_{Rm} = 0.48 \times 9.67kN.m = 4.64kN.m \qquad \text{(A-10)}$$

Step 4: Determine the line pressure of the model beam which can produce the required bending moment demand.

$$P_{Em} = \frac{12 \times M_{Rm}}{l^2} = 9.67kN/m \qquad \text{(A-11)}$$

$$P_m = \frac{8}{5} P_{Em} = 15.5kN/m \qquad \text{(A-12)}$$

$$q_m = \frac{2P_m}{l} = 12.9kPa \qquad \text{(A-13)}$$

where P_m is the maximum value of the triangle pressure on the model beam; P_{Em} is the equivalent uniform line pressure on the model beam; q_m is the uniform pressure on the model slab; M_{Rm} is the bending moment demand on the model beam; M_{ym} is the yield bending moment on the model beam.

It can be found that the ratio of the beam bending moment demand to its yield moment capacity of the model specimen is same as that in the prototype frame as long

as the total uniform pressure applied on the slab of the model specimen is same as its corresponding prototype slab.

Actually, this conclusion can also be drawn by stiffness equivalent method.

Assuming one model beam is one-third scale. Thus, the length, depth and the width of the beam are one third of that in the prototype beam.

$$M_{ym} = (\frac{1}{3})^3 M_{yp} \qquad \text{(A-14)}$$

The yield moment of model beam is 1/27 of that of prototype beam. The demand of bending moment of model beam is $kq_m l_m{}^3 = kq_m(\frac{l_p}{3})^3$. In order to obtain same ratio of the demand to the yield capacity, only ensure $q_m = q_p$.

Step 5: Determine the design axial force in the corner support of the tested specimens.

A.1. for DF3 and DF4

The design pressure is:

$$q_m = 1.2DL + 0.5L = 12.9\,kN/m^2 \qquad \text{(A-15)}$$

The design axial force is:

$$\frac{74.3kN}{4} = 18.6kN \qquad \text{(A-16)}$$

A.2. for DF1 and DF2

The design pressure is:

$$0.9q_m = 0.9(1.2DL + 0.5L) = 11.6\,kN/m^2 \qquad \text{(A-17)}$$

The design axial force is:

$$\frac{66.9kN}{4} = 16.7kN \qquad \text{(A-18)}$$

A.3. for DF5

The design pressure is:

$$0.8q_m = 0.8(1.2DL + 0.5L) = 10.3\,kN/m^2 \qquad \text{(A-19)}$$

The design axial force is:

$$\frac{92.9kN}{4} = 23.2kN \qquad \text{(A-20)}$$

A.4. for DF6

The design pressure is:

$$q_m = 1.2DL + 0.5L = 12.9\,kN/m^2 \qquad \text{(A-21)}$$

The design axial force is:

$$\frac{92.9kN}{4} = 23.2kN \qquad \text{(A-22)}$$